Understanding the role of van der Waals forces in solids from first principles

Dissertation
zur Erlangung des Grades
Doktorin der Naturwissenschaften (Dr. rer. nat.)
eingereicht im Fachbereich Physik
der Freien Universität Berlin

vorgelegt von
M.Sc.
Guo-Xu Zhang

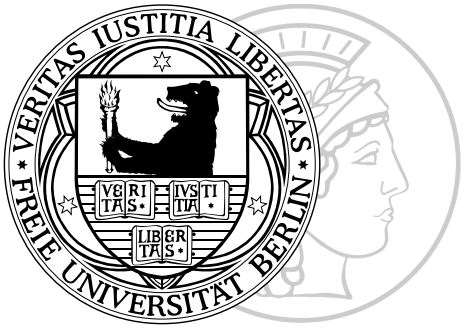

Berlin, 2014

Diese Arbeit wurde in der Zeit von April 2009 bis Januar 2014 unter der Betreuung von Prof. Dr. Matthias Scheffler und Dr. Alexandre Tkatchenko in der Abteilung Theorie am Fritz-Haber-Institut der Max-Planck-Gesellschaft durchgeführt.

Erster Gutachter (Betreuer): Prof. Dr. Matthias Scheffler
Zweiter Gutachter: Prof. Dr. Felix von Oppen
Tag der Disputation: 25. März 2014

致我最爱的父亲、母亲以及弟弟国强

ABSTRACT

The study of cohesion in solids is among the most fundamental research subjects in condensed-matter physics. The search for a deeper understanding of cohesion has lead to a steady progress in electronic-structure methods, enabling us to better understand structural, electronic, and mechanical properties of solids. The quantitative description of cohesion in solids requires solving the many-body Schrödinger equation and such exact treatment remains an unsolved problem. In this context, the correct treatment of cohesive properties (lattice constants, cohesive energies, and bulk moduli) requires an accurate description of the long-range electron correlation. In particular, van der Waals (vdW) interactions, being ubiquitous and arising from correlations between electrons, have been proposed to affect the cohesion in solids since a long time. This leads to two unsolved questions: (1) How to properly and effectively model vdW interactions in solids?, and (2) What is the quantitative role of vdW interactions in the cohesive properties of different types of solids? In this thesis, we address both questions by developing novel methods for vdW interactions in solids and assessing the role of the long-range vdW energy for a wide variety of non-metallic solids in the context of density-functional theory (DFT).

Among first-principles approaches to the many-body Schrödinger equation, DFT has become the method of choice for obtaining ground-state properties of molecules and materials. A great advantage of DFT is that it is in principle an exact theory and the complexity of the full many-body problem is replaced by the electronic exchange-correlation (XC) functional. However, this functional is only known approximately and all widely employed (semi-)local and hybrid functionals suffer from the so-called self-interaction errors and lack the long-range vdW energy tail, often yielding noticeable deviations from experimental data. This issue will be illustrated in my thesis by assembling a large database of 64 solids and employing the LDA, PBE, and M06-L functionals to study their cohesive properties. This assessment shows that none of these functionals is sufficient to describe the cohesion for a broad range of solids, leading us to propose that the missing long-range vdW interaction accounts for part of the deviations found in approximate XC functionals.

To assess the role of vdW interactions in solids, we develop the so-called DFT+vdW$^{\mathrm{TS+SCS}}$ method that accurately models the electrodynamic response effects in the polarizability and vdW coefficients. This method is essentially free of adjustable parameters; the only necessary ingredients are the electron density and reference polarizabilities for free (isolated) atoms in the gas phase. Together with a benchmark study based upon experimental and time-dependent DFT optical spectra, I show that the concept of *atoms-in-solids* can be successfully utilized to define polarizabilities for finite-gap materials. Remarkably, my analysis demonstrates the validity of the Clausius-Mossotti relation for linking the macroscopic dielectric function to the microscopic response in covalently-bonded semiconductors – a matter of long debate in the literature.

Upon the inclusion of long-range vdW interactions on top of the non-empirical PBE functional, a factor-of-two improvement is found in the cohesive properties with respect to the standard PBE values. I conclude that the vdW energy plays a crucial role in the cohesion of semiconductors and ionic solids. The proposed DFT+vdW$^{\mathrm{TS+SCS}}$ approach represents a promising way towards extending the applicability of standard density functionals, and thus will be useful for a wide variety of applications in molecules and materials.

ZUSAMMENFASSUNG

Die Bindungskräfte in Festkörpern sind von grundlegendem Interesse in der Physik kondensierter Materie. Eine quantitative Beschreibung von Kohäsion in Festkörpern bedarf der Lösung der Vielteilchen-Schrödinger-Gleichung, die allerdings meist nicht exakt lösbar ist. Für die Kohäsions-Eigenschaften ist eine genaue Beschreibung der langreichweitigen Korrelation der Elektronen maßgeblich. Insbesondere können van der Waals (vdW) Wechselwirkungen, die durch Korrelationen zwischen Elektronen auftreten, die Kohäsion in Festkörpern beeinflussen. Es stellen sich zwei Fragen: (1) Wie können vdW-Wechselwirkungen in Festkörpern präzise und effektiv modelliert werden?, und (2) Welche quantitative Rolle spielen sie? In dieser Arbeit werden beide Fragen behandelt, indem neue Methoden zur Beschreibung von vdW-Wechselwirkungen in Festkörpern entwickelt werden und die Rolle der langreichweitigen vdW-Energie für eine Vielzahl von nicht-metallischen Festkörpern im Kontext der Dichtefunktionaltheorie (DFT) untersucht wird.

Unter den *ab initio* Ansätzen zur Lösung der Schrödinger-Gleichung hat sich die DFT zur Methode der Wahl entwickelt, um die Grundzustands-Eigenschaften von Molekülen und Materialien zu bestimmen. Ein bedeutender Vorteil der DFT liegt darin, dass es sich im Prinzip um eine exakte Theorie handelt, wobei die Komplexität des vollen Vielteilchen-Problems durch das elektronische Austausch-Korrelations-Funktional ersetzt wird. Allerdings ist dieses Funktional nur näherungsweise bekannt und alle (semi-)lokalen und Hybrid-Funktionale, die breite Anwendung finden, sind mit sogenannten Selbstwechselwirkungsfehlern behaftet und berücksichtigen außerdem nicht die langreichweitigen vdW-Energiebeiträge, was oft zu merklichen Abweichungen im Vergleich zu experimentellen Messwerten führt. Diese Problematik wird in meiner Arbeit erläutert, indem die Bindungseigenschaften von 64 Feststoffen unter Verwendung von LDA, PBE und M06-L Funktionalen untersucht werden. Es wird gezeigt, dass keines der Funktionale ausreichend ist, um Kohäsion in Festkörpern für einen weiten Bereich von Materialien zu beschreiben. Wir folgern, dass dies zum Teil auf das Fehlen der vdW-Wechselwirkung zurückzuführen ist.

Zur Untersuchung der vdW-Wechselwirkungen in Festkörpern entwickeln wir die sogenannte DFT+vdW$^{\mathrm{TS+SCS}}$ Methode für eine genaue Modellierung der elektrodynamischen *response*-Effekte in der Polarisierbarkeit und den vdW-Koeffizienten. Diese Methode ist im Wesentlichen frei von anzupassenden Parametern; einzig die Elektronendichte und Referenz-Polarisierbarkeiten für freie Atome in der Gasphase werden benötigt. Zusammen mit einer Benchmark-Studie, die auf experimentellen und mit zeitabhängiger DFT bestimmten, optischen Spektren basiert, zeigen wir, dass das Konzept *atoms-in-solids* (Atome im Festkörper) erfolgreich verwendet werden kann, um Polarisierbarkeiten für Materialien mit endlicher Bandlücke zu definieren. Besonders bemerkenswert ist, dass meine Analyse die Gültigkeit der Clausius-Mossotti Relation für die Verknüpfung der makroskopischen dielektrischen Funktion mit der mikroskopischen Antwort in kovalent gebundenen Halbleitern zeigt – dies war Gegenstand langer Diskussionen in der Literatur. Durch die Einbeziehung von langreichweitigen vdW-Wechselwirkungen wird eine Verbesserung um einen Faktor zwei in der Beschreibung der Bindungs-Eigenschaften mit Bezug auf die entsprechenden Standard-PBE-Ergebnisse erreicht. Wir schließen daraus, dass die vdW-Energie eine entscheidende Rolle für die Kohäsion in Halbleitern und ionischen Festkörpern spielt. Die vorgestellte DFT+vdW$^{\mathrm{TS+SCS}}$ Methode zeigt einen vielversprechenden Weg auf, um die Anwendbarkeit von Standard-Dichtefunktionalen zu erweitern, und wird folglich für eine Vielzahl von Anwendungen in Molekülen und Materialien nutzbar sein.

Contents

1 Introduction

A prominent area of solid-state physics is the search for an understanding of cohesion in solids. Cohesion is an intrinsic property of matter that measures the binding experienced by one particle (atom, ion, or molecule) arising from the rest of the solid. The forces leading to cohesion are often classified into five idealized types according to the nature of bonding in a solid, namely ionic bonding, covalent bonding, metallic bonding, hydrogen bonding, and van der Waals (vdW) interactions. In realistic solids, the situation is typically more complex, with different forces all contributing to their cohesion. A prototypical example of vdW-bonded solids are noble-gas crystals, where the vdW energy provides the only stabilizing contribution to cohesion. In other solids, the role of the vdW energy is less clear. For example, the seminal textbook *Solid State Physics* by Ashcroft and Mermin [1] states "*the van der Waals part of the attractive interaction in ionic crystals makes a relatively small contribution to the cohesive energy in ionic crystals, of the order of 1 or 2 percent*". However, other published literature starting with the seminal work of Mayer [2] advocates a much larger contribution of vdW interactions to cohesion in ionic solids [3–7]. Nowadays, the study of cohesion in solids still receives significant attention due to its fundamental relevance for a wide range of condensed-matter applications and other related fields. Indeed, the importance of cohesive properties (e.g., the lattice constant, the bulk modulus, and the cohesive energy) can hardly be overestimated. For instance, the cohesive energy of different phases of a solid will ultimately account for its behavior under changing thermodynamic conditions, i.e., determine its phase diagram. The bulk modulus will determine how hard or soft the material is, i.e., its response to an externally applied pressure.

Many difficulties have been encountered in attempts to accurately determine cohesive properties using quantum-mechanical methods that are computa-

tionally feasible to be applied to solids. In particular, the qualitative and quantitative role of vdW interactions in the cohesive properties has frequently been a recurring question. It has long been recognized that vdW interactions may contribute to the cohesion of not only noble-gas and molecular crystals, but also many other crystalline solids. However, due to the difficulty of an accurate treatment of such interactions, it is typically assumed that they play a minor role in the cohesion of, e.g., ionic and covalently-bonded solids. It is now becoming clear that vdW interactions cannot be neglected for describing the structure, stability, and function of a wide variety of materials [8–11]. In particular, vdW interactions are ubiquitous and dependent upon the polarizability of valence electrons. An accurate description of vdW interactions has become an increasingly important effort to improve our understanding of a number of problems in physics, chemistry, and biology.

Since vdW interactions arise from electron density fluctuations, they are a quantum-mechanical phenomenon which require the solution of the many-electron Schrödinger equation. The description of vdW forces was first formulated in 1930 by R. Eisenschitz and F. London [12, 13] based on second-order perturbation theory. The leading term of the long-range part of these interactions is the instantaneous dipole-dipole interaction, exhibiting the well-known $-C_6R^{-6}$ asymptotic behavior for the vdW energy with interatomic separation R. The C_6 constant is called the dispersion coefficient, which characterizes the interaction strength between a given pair of atoms, ions, or molecules. An accurate calculation of C_6 coefficients plays a central role in studying vdW forces. This explains the existence of a large number of approaches devoted to the precise evaluation of C_6 values [14, 15].

Density-functional theory (DFT) is among the most widely used electronic-structure methods for modeling ground-state properties of molecules and condensed matter. The popularity of DFT arises mainly from its fair degree of accuracy at feasible computational cost for a wide range of practical applications. A great advantage of DFT is that this theory is in principle exact and the complexity of the many-body problem is replaced by the exchange-correlation (XC) functional, which must be approximated in practice. In the last few decades, DFT has been shown to be a very powerful technique for solving problems in quantum chemistry and condensed-matter physics, particularly for large systems. Unfortunately, approximate DFT functionals can yield large deviations from experiment in many situations. For instance, it is known that the commonly used XC functionals (i.e., local, semi-local, and hybrid functionals) do not uniformly show good performance for the prediction of

cohesive properties, when applied to a broad range of bulk solids, such as those considered in the present thesis. One prominent limitation of these functionals is that they are unable to describe the long-range electron correlation, and therefore lack the vdW energy tail. The reliable description of vdW interactions is one of the most significant challenges within the modern DFT framework.

In the last decade, many encouraging ideas and methods have been proposed for approximately accounting for vdW interactions based on DFT approaches (e.g., see recent review articles [8–11]). The basic requirement for any DFT-based vdW scheme is that it yields the correct R^{-6} decay for the interaction at long distances. Such a correction involves the addition of the vdW energy term to the DFT total energy. One popular way consists in adding the vdW energy by summing over all pairs of atoms using a multipolar expansion (termed as DFT+vdW in the thesis). The pair-wise vdW energy is often (but not always) evaluated with the leading $-C_6R^{-6}$ term, coupled with a damping function that is used to avoid singularities at short range and minimize double counting of correlation at intermediate range. The concept of DFT+vdW has gained great attention due to its ability to include vdW interactions in an effective way, and is becoming an increasingly active field of research. Several approaches have been developed, aiming at an improved evaluation of C_6 dispersion coefficients and the resulting vdW energies. Some of these methods have been shown to provide reliable dispersion coefficients when applied to a diverse range of small molecular systems.

Treating vdW interactions in more complex systems (such as large molecules and solids), is a very difficult task and remains challenging. It has been shown by numerous studies that the crystalline environment has a significant impact on the polarizability and C_6 dispersion coefficients. This can be best illustrated by a direct comparison of C_6 dispersion coefficients between in-crystal atoms (or ions) and isolated counterparts. A prototypical example of ionic crystals is alkali halides, e.g., sodium chloride (NaCl), whose free-atom and free-ion C_6 values are available from highly accurate *ab initio* calculations (Na–Na: 1556; Cl–Cl: 94.6; Na^+–Na^+: 1.6; Cl^-–Cl^-: 267; in hartree·bohr^6) [16, 17]. For isolated cations, their C_6 values are considerably smaller – much less polarizable – than those of neutral atoms, due to the less extended wave functions; in contrast, isolated anions are more polarizable, due to the expansion in their electron density tails. Turning to solids, it has been evident for many years that in-crystal dispersion coefficients differ from the corresponding free atoms or free ions values [17–19]. However, precisely modeling various crystalline effects that act in solids is a big challenge; and those effects, such as crystal-

field effect, overlap compression, and charge transfer, arise from both nearby and far-distance neighbors in the solid. Indeed, there is a large discrepancy in the evaluation of the dispersion coefficients for anions and cations of the alkali halides in the literature. It is clear that more efforts are needed to obtain environment-dependent vdW parameters. Two main problems are encountered in practical calculations: the neglect or only effective treatment of the electrodynamic response and the neglect of non-additive many-body vdW energy contributions beyond pair-wise approximations [20]. To overcome these obstacles, one has to develop a proper microscopic description of the frequency-dependent polarizability, rooted in local and nonlocal fluctuations, in which the full electrodynamic response of the system is accounted for.

The aim of this thesis is to gain a deeper understanding of the role of vdW interactions in the cohesion of various bulk solids, on the basis of accurate and efficient first-principles calculations. The present work employs the DFT+vdW concept to develop a new approach for treating vdW forces for "atoms-in-materials", particularly for large and complex systems. The first step towards our goal is to assess the performance of standard XC functionals applied to solids for describing their cohesive properties, using the full-potential all-electron Fritz-Haber-Institut *ab initio* molecular simulations (FHI-aims) package [21]. For a precise assessment of different functionals, two aspects need to be addressed: (i) a large database, which must contain cohesive properties of a diverse range of bulk materials, with reliable experimental data, measured at low temperature and extrapolated to zero temperature; (ii) the nuclear zero-point vibrational energy, which is known to contribute to cohesion in solids.

The second step is a benchmark study of vdW parameters and vdW energies based upon a combination of the DFT+vdW scheme with time-dependent density-functional theory (TDDFT) calculations of optical spectra of semiconductors and ionic crystals.

The third step is devoted to develop a general DFT-based model for accurately and efficiently studying vdW interactions from the microscopic theory of polarization. Finally, a database of 23 semiconductors is used for assessing the proposed DFT+vdW approach, and the role of long-range vdW interactions is evaluated using this method to obtain the cohesive properties of these solids.

The outline of this thesis is as follows:

Chapter 2 gives a textbook picture of cohesion in solids. The historical advances to understand the role of vdW interactions are reviewed, together

with existing challenges for a reliable treatment of cohesive properties from a theoretical point of view.

Chapter 3 summarizes the theoretical background used in this thesis. The formulation of DFT is given, together with the challenges for developing improved XC functionals. In particular, the state of the art for treating vdW interactions will be discussed, with regard to the advantages and shortcomings of the most popular methods.

In **Chapter 4**, the cohesive properties (lattice constants, cohesive energies, and bulk moduli) are investigated for a database of 64 solids using local and semi-local density functionals. Systematic deviations caused by these functionals will be carefully examined, especially regarding the relationships between pairs of the cohesive properties.

In **Chapter 5**, a benchmark study of vdW coefficients is performed using a combined DFT/TDDFT approach for six ionic and semiconductor solids. It is shown that the consideration of the chemical environment and the local field acting on a given atom in a dielectric medium, is crucial for an accurate treatment of vdW interactions in a solid.

Chapter 6 presents an extension of the Tkatchenko/Scheffler (TS) [22] method to large molecules and finite-gap solids by including electrodynamic response effects (DFT+vdW$^{\text{TS+SCS}}$), aiming at *ab initio* modeling and quantitative understanding of vdW interactions in complex systems. A brief discussion about the implementation of this method for solids is also given.

In **Chapter 7**, the proposed DFT+vdW$^{\text{TS+SCS}}$ method is assessed, in combination with the DFT/TDDFT benchmark study and available experimental information. Then, the applicability of the current approach is tested by extending it to 23 semiconductor solids. Finally, the role of vdW interactions in the cohesive properties is illustrated by adding long-range pair-wise interactions on top of the DFT-PBE functional.

In the final chapter, I shall summarize the main findings of the current work, together with an outlook for future studies.

2 TEXTBOOK PICTURE OF COHESION IN SOLIDS

The purpose of this chapter is to provide an overview of the current understanding of cohesion in crystalline solids. A central property of a crystal is its cohesive energy, E_0, which is the energy required to dissociate the constituent particles (atoms, ions or molecules) of a compound, e.g., AB, to infinite separation

$$\mathrm{AB(solid)} \rightarrow \mathrm{A(gas)} + \mathrm{B(gas)}. \tag{2.1}$$

The magnitude of E_0 tells us about the stability and bonding of a solid, and ultimately, it is the quantity that determines the equilibrium structure. To understand the cohesive energy as well as other related properties, one should look at the forces acting on the atoms upon forming a crystal. In the following, we shall begin with a description of the classification of solids on the basis of the nature of the interatomic and intermolecular forces operating between the particles, that is, the bonding types of crystals. Then, a brief history of the van der Waals (vdW) interaction contribution to cohesive energies will be outlined, as this is the main subject of this thesis. Finally, we will discuss cohesion in bulk solids, with regard to the relationships between different bulk quantities (lattice constant, cohesive energy, and bulk modulus), and conclude with the current challenges for the reliable prediction of cohesive properties in solids.

2.1 BONDING IN CRYSTALLINE SOLIDS

A crystal or crystalline solid is composed of atoms, ions, or molecules arranged in an ordered pattern that is repeated in three dimensions. The study of a crystal is based on investigating the microscopic arrangement of atoms inside it, which is closely related to an intrinsic property of a substance sticking

together, *cohesion*. Since the year 1913 [23], in which Bragg diffraction was first used to show characteristic patterns of reflected X-rays of crystalline solids, crystallography has begun its explosive growth. These patterns lead to a number of questions regarding the nature of cohesion in solids. What holds a crystal together? To what extent do the atoms in the solid resemble neutral atoms, held together by covalent bonds, and to what extent do they resemble ions, held together by electrostatic forces? Why does diamond have a tetrahedrally coordinated structure? Can the equilibrium geometry be modeled accurately, and how? In order to answer these questions, one first needs to have a clear understanding of different bonding scenarios. Loosely speaking, bonding in solids may be classified into five idealized types, namely ionic, covalent, metallic, hydrogen, and van der Waals (vdW) interactions. In realistic solids, the situation is typically more complex, with different forces all playing a role in their cohesion.

IONIC BONDING

Ionic bonding arises from the classical Coulomb attraction between two oppositely charged ions, and it is responsible for the formation of the so-called ionic crystals. Typically, among this family are compounds formed by alkali and alkaline-earth atoms in combination with halogens, in which there is a large difference in electronegativity between the components. The resulting crystal structures arise from optimal packing of differently sized ions, and mainly adopt a face-centered cubic (fcc) rock-salt lattice. A classic example of an ionic crystal is sodium chloride (NaCl). Doubly ionized elements from the IIA and VIA columns of the periodic table can also form ionic crystals, and almost all these compounds favor the sodium chloride structure.[1] Ionic solids are typically very stable and extremely brittle (soft), and the cohesive energy per atom is of the order of several electron volts.

COVALENT BONDING

While ionic bonding arises from an almost complete transfer of electrons between the atoms involved in a bond, covalent bonding is held by the sharing of electrons between the bonding participants through the overlap of orbitals on adjacent atoms. Typically, covalent bonding is strong and the cohesive energies are as large as several electron volts. In fact, purely covalent or ionic bonding is rare: many covalent compounds have some degree of ionic character, and

[1] Except for BeS, BeSe, and BeTe (zincblende), and BeO, MgTe (wurtzite).

vice versa. In solids, dominantly covalent bonding is found for the elements from the IVA column of the periodic table: carbon, silicon, germanium, and tin. These elements all crystallize in a tetrahedrally coordinated diamond structure. The crystals that contain elements from the IIIA and VA columns of the periodic table are partially ionic and partially covalent substances,[2] and they typically all adopt a zincblende structure. It is noteworthy that tetrahedrally coordinated structures (diamond, zincblende, and wurtzite structures) tend to be primarily covalently bonded. In addition to the crystal structure, continuous variation in the nature of the charge distribution can be found from the dominantly ionic IA–VIIA compounds through the progressively mixed bonding nature of IIA–VIA and IIIA–VA compounds over to the mainly covalent elements from the IVA column.

METALLIC BONDING

Metallic solids are held together by a "glue" of shared and delocalized electrons, resulting in metallic bonding. In metals, the outer valence electrons "separate" from the ion cores, but in contrast to ionic solids, there are no electronegative ions to bind them. As a consequence, they are not localized on one particular atom or pair of atoms, but free to hop between the ion cores, which are then embedded in a "sea" of electrons. The prime examples of metallic solids are the alkali metals of the IA column of the periodic table, in which the valence electrons can be considered as being separated from the core electrons. Metallic solids mainly crystallize in A1-fcc and A2-bcc (body-centered cubic) arrangements, adopting closed-packed structures. Although metallic bonding is typically less strong than ionic or covalent bonding, it can also amount to a few eV per atom. Particularly in transition metals, the filled d shells are not very tightly bound, such that the d electrons become more localized and lead to hybridization between localized and delocalized states.[3] This is reflected by the fact that transition metals are typically stable and hard (with large bulk modulus or compressibility), resulting from a mix of ionic, covalent, and metallic characters.

HYDROGEN BONDING

As well as interatomic forces, there are also intermolecular interactions in solids. Hydrogen bonding is the attraction between an electronegative atom

[2] The IIIA–VA compounds are conventionally considered as primarily covalent, as they are still less ionic in character.

[3] The hybridization in transition metals can be considered as partially covalent in nature.

and a covalently-bonded hydrogen atom that is bonded with an electronegative atom. It is often represented as A–H$\cdots$B, in which both A and B will be electronegative elements (e.g., C, N, O, and F). Compared with covalent or ionic bonds hydrogen bonds are weaker, but in some case the cohesive energy can be up to 1 eV per bond. In general, hydrogen bonding is discussed as an electrostatic interaction, between the partially positively charged hydrogen and the partially negatively charged electronegative elements. However, it can also show some covalent and vdW characters, being directional and stronger than vdW interactions. Therefore the modern picture of hydrogen bonding is much more complex — it is a mixture of electrostatics, induction, and dispersion effects. An example of such type of bonding in the solid state is water ice, where hydrogen bonds are responsible for the dominant intermolecular attraction.

VAN DER WAALS INTERACTION

van der Waals interaction (here used to signify London dispersion interaction) arises from fluctuating multipole moments in atoms and molecules. It is a purely quantum-mechanical phenomenon and exists ubiquitously in molecules and solids. Nowadays, it is becoming evident that vdW interactions are responsible for many phenomena in physics, chemistry, and biology. While vdW interactions are typically much weaker than ionic, covalent, or metallic bonding (the vdW energy rarely exceeds a few hundred meV per atom), the relatively small contribution of the vdW energy plays a major role in determining the structure and stability of a wide variety of materials. The prototypical examples of vdW interactions in solids are the solid noble gases residing in the VIIIA column of the periodic table, which all crystallize as fcc Bravais lattices. In fact, vdW interactions are the only attractive intermolecular forces that hold neutral atoms together. It was suggested that vdW interactions contribute considerably to the cohesion in many other molecular crystals as well [1, 24, 25]. In addition, they hold the layers of carbon in the graphite structure together and can also play a role in the cohesion of other type of bulk solids.

2.2 REVIEW OF VAN DER WAALS FORCES IN SOLIDS

It has long been recognized that vdW forces may contribute to bonding in solids [2, 26, 27], and thus can play a role in determining their cohesive, elastic, dielectric, lattice-dynamical properties, etc. The most direct evidence of the existence of vdW forces is the fact that noble gases can be condensed into the

solid state. The historical understanding of vdW forces in solids can be traced back to the 1920s, when the earliest X-ray measurements of the noble-gas solid structure showed the lattice to be fcc for neon [28], argon [29, 30], krypton [31], and xenon [32]. Thereafter, several studies have shown that the attractive vdW interactions can also contribute to the bonding in some ionic and metallic solids.

2.2.1 NOBLE-GAS CRYSTALS

The first explanation of a fluctuating dipole-dipole attractive potential was given by Fritz London [12, 13] from a quantum-mechanical treatment based on perturbation theory (see reviews by Margenau [33, 34] and the textbook by Kaplan [15]). Using second-order perturbation theory and assuming that the attracting particles (atoms, ions, or molecules) have spherical charge distributions,[4] the formula for the attractive energy between the two particles A and B at a large distance R_{AB} can be written as

$$E_{\mathrm{vdW}} = -\frac{C_6^{\mathrm{AB}}}{R_{\mathrm{AB}}^6}, \tag{2.2}$$

where the factor C_6, known as the dispersion coefficient, which depends on dipolar polarizabilities of isolated particles A and B, is the crucial quantity for an accurate determination of the energy. This attractive energy is frequently called the vdW dipole-dipole energy, dispersion energy, or simply the vdW energy.

Concerning the noble-gas solids, the correct theoretical treatment of vdW interactions has long been debated [35–38]. Early calculations predicted a hexagonal close-packed (hcp) structure [39–41], in disagreement with the fcc structure observed from experiment [36, 42–44]. Afterwards, a series of studies showed that the inclusion of three-body terms [45, 46], instead of only a two-body potential, yielded an fcc crystal structure for noble-gas solids in quantitative agreement with the experimental observations [47–53]. It has been acknowledged that many-body effects need to be considered to correctly describe the lattice constant, the cohesive energy, as well as, the bulk modulus of noble-gas crystals, which brought about significant progress in understanding the role of vdW interactions in the solid state.

[4] They have neither a permanent dipole nor any higher multipole, e.g., noble-gas atoms are spherically symmetrical.

2.2.2 ALKALI HALIDES

vdW interactions in ionic crystals were first studied by Born and Mayer [54] using the London approximation given by Eq. (2.2) for alkali halides. Mayer developed an approach to compute dispersion coefficients using the knowledge of absorption spectra and refractive-index data, and concluded that the vdW energy accounts for the stability of, e.g., the CsCl-type lattice for CsX (X=Cl, Br, I) crystals over the NaCl-type lattice [2]. This method was applied to other ionic solids, such as copper [55], silver and thallium halides [56]. In Mayer's approach, the free-ion polarizabilities reported by Pauling were used for cations and the values for anions were estimated from corresponding optical data. This was an important step for studying the vdW interactions in ionic solids. Following this work, it was realized that the crystalline environment has a large impact on the in-crystal polarizability, and later work focused on developing possible methods to improve upon the estimated results by Mayer.

May [3] proposed the possibility of much stronger vdW interactions than those predicted by Mayer [2] in order to explain the thermal phase transition of a CsCl crystal from the CsCl to NaCl structure. Tessman *et al.* [26] computed ionic polarizabilities from the fits of the experimental molar polarizabilities of alkali halides, and they showed that it is inappropriate to use free-ion polarizabilities of cations and anions for crystals. Subsequent improvements have been made in the polarizabilities since new optical data became available within improved accuracy of experimental measurements. Lynch [5] used optical data of potassium halides and silver chloride up to nearly 30 eV and computed vdW dipole-dipole coefficients using the method introduced by Mayer. He pointed out that it is difficult to separate the crystal polarizability into cationic and anionic contributions in an unambiguous way, and that local-field effects (which is the actual field acting on particles in a dielectric medium) play an important role in determining the vdW energy. Bakhshi revised Mayer's results for the copper, silver and thallium halides and emphasized that the vdW energy resulting from in-crystal polarizabilities is larger than that obtained from free-ion values [7]. As a result, the larger values of vdW energies, due to the larger vdW coefficients, yielded cohesive energies in better agreement with experiment than those reported by Mayer [55, 56].

The foregoing discussion thus reveals that there is considerable uncertainty in polarizability data used in the literature for calculating vdW energies. It has been evident from numerous studies of ionic solids that the polarizability and vdW coefficients depend on the structure and environment of the crystal [4,

5, 7, 26, 57–61]. More recently, since the beginning of 1980s, much work has been performed by Pyper, Fowler, Madden, *et al.* [17–19, 62–68] for accurate treatments of the polarizability and thus the resulting vdW energy in ionic solids, and this research area still remains active [22, 69–72].

2.2.3 NOBLE METALS

From the point of view of vdW interactions, metals are difficult to treat theoretically, because of the coexistence of localized and delocalized electronic states. It has long been recognized that the attractive vdW interaction between ions in a metal may contribute to the total cohesive energy [27]. However, the magnitude and the relative importance of this contribution remains an unresolved issue. For noble metals, estimates of the vdW energy have ranged from being of negligible importance to contributing roughly a third of the total cohesive energy, which is typically 3 to 4 eV per atom [24, 73–75]. This large variation reflects discrepancies in the estimate of the ionic polarizability and differences in the calculation of the conduction-electron screening of polarization forces [74, 76]. For example, copper and gold have been the subject of several studies [74, 75], with the vdW contribution to binding estimated as 0.2–0.6 eV for Cu and 0.6–1.2 eV for Au. Meanwhile, it was found that the inclusion of vdW interactions is necessary for obtaining reasonable structures observed from experiment for noble metals [75], and the same conclusion also applies to alkali metals [60, 77]. More recently, the need to include nonlocal correlation in density-functional theory (DFT) semi-local functionals has been discussed for heavy alkalis [71, 78, 79].

Therefore the following conclusions can be drawn regarding the understanding of vdW interactions in solids:

- van der Waals forces make a considerable contribution to the stability of noble-gas solids, ionic crystals, and noble metals, and thus play an important role in controlling phase transitions;
- although the van der Waals contribution to the total cohesive (binding) energy may not be the most significant component, it is typically important to determine the correct structure;
- the quantitative role of the van der Waals energy contribution in the cohesive properties (lattice constants, cohesive energies, and bulk moduli) has remained an unresolved question for many classes of solids;

- the large discrepancy in determining the van der Waals energy reflects the difficulty of obtaining the dynamic polarizability and the resulting C_6 dispersion coefficients for atoms (ions or molecules) in solids.

In order to address the above mentioned issues, it is necessary to have a reliable method for computing dispersion coefficients for atoms in solids. The work presented in this doctoral thesis is focused on qualitatively and quantitatively evaluating the influence of vdW interactions on the cohesive properties of ionic and covalently-bonded solids. We now turn to some of the elementary qualitative insights of various cohesive properties of bulk solids.

2.3 COHESIVE PROPERTIES

The relation between the properties of bulk materials and their electronic structure is a matter of considerable fundamental and applied interest. In particular, there have been significant efforts to understand structurally related properties of bulk solids from a total-energy point of view. These properties include the cohesive energy, the lattice constant, the bulk modulus, the shear modulus, Grüneisen parameters, and the critical pressure involved in pressure-induced phase transitions between different structures, to mention just a few. Here we only focus on the lattice constant, the cohesive energy, and the bulk modulus, and will introduce the basic theory of these properties in this section.

2.3.1 LATTICE CONSTANT

The equilibrium lattice constant of a solid can be measured via X-ray diffraction with high accuracy,[5] usually at finite temperature and extrapolated to absolute zero using thermal expansion data. Figure 2.1 shows the correlation between the experimental lattice constant and atomic weight for selected metals. It can be concluded that for a given type of solid, the lattice constant increases with the increase of nuclear charges, e.g., along the series of Li-Na-K-Rb, Rh-Pd-Ag, and W-Ir-Pt-Au-Pb. In principle, many properties of a crystalline solid can be related to its lattice constant, and some can be very sensitive to it. Thus the accuracy of the measured lattice constant from experiment or predicted one from theory is the key to other structurally related properties, such as the bulk modulus.

[5]For instance, the uncertainty for diamond crystal was $1.2 \times 10^{-6}\%$ in a recent X-ray measurement [80].

The equilibrium lattice constant is the one that minimizes the cohesive energy. From theoretical point of view, Kohn-Sham density-functional theory (KS-DFT) has become one of the most powerful tools for predicting ground-state properties and has long been used to calculate the equation of state (EOS), which reflects the dependence of the energy of a solid upon the lattice constant (or the volume of a unit cell) of the solid. Therefore the accuracy of the predicted lattice constant is a test of the accuracy of the KS-DFT approach (see more details of DFT in Section 3.2).

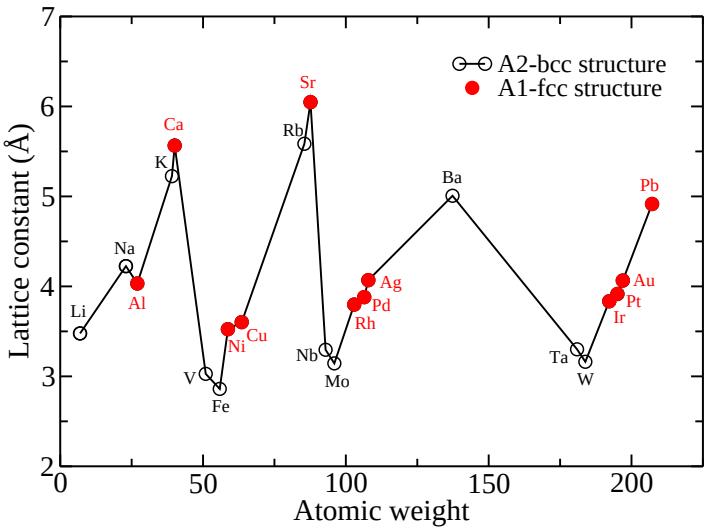

Figure 2.1: The experimental lattice constant as a function of atomic weight for selected main-group metals and transition metals.

2.3.2 Cohesive energy

The cohesive energy is defined as the difference between the energy per atom of bulk material at equilibrium and energy of the free atoms in their ground states

$$E_0 = \frac{1}{N}\left(E_{\text{total}} - \sum_i^N E_i\right), \tag{2.3}$$

where i symbolizes the constituent atoms of the solid and N equals the number of the atoms in a unit cell. This energy is one of the parameters used to understand the bonding nature of solids, and its magnitude tells us about the stability of a given solid. Along with the lattice constant, the cohesive energy allows us to calculate the transition pressure between different solid structures.

Empirical relations are an important tool for understanding solid-state properties. In many cases empirical relations do not give highly quantitative

results for each specific material, but they allow to understand qualitative trends. Empirical concepts, such as valence, empirical radii, electronegativity, ionicity and plasma frequency, are very often used to understand condensed-matter materials. These concepts are directly associated with the character of the bonding and thus provide means for explaining and classifying many fundamental properties of molecules and solids.

There have been quite a number of studies on the relationship between the cohesive energy and structural parameters, such as the distance between atoms in a solid. Aresti *et al*. [81] studied the zincblende solids and proposed an empirical expression for cohesive energy in terms of the nearest-neighbor separation d

$$E_0 d \approx \text{constant}. \tag{2.4}$$

Schlosser and co-workers also showed that the constant product of the cohesive energy with the nearest-neighbor distance is a good approximation for some families with common crystal structures, e.g., alkali chalcogenides and halides, group-II chalcogenides and halides, alkali hydrides, ammonium halides, and iron-group transition-metal oxides [82, 83].

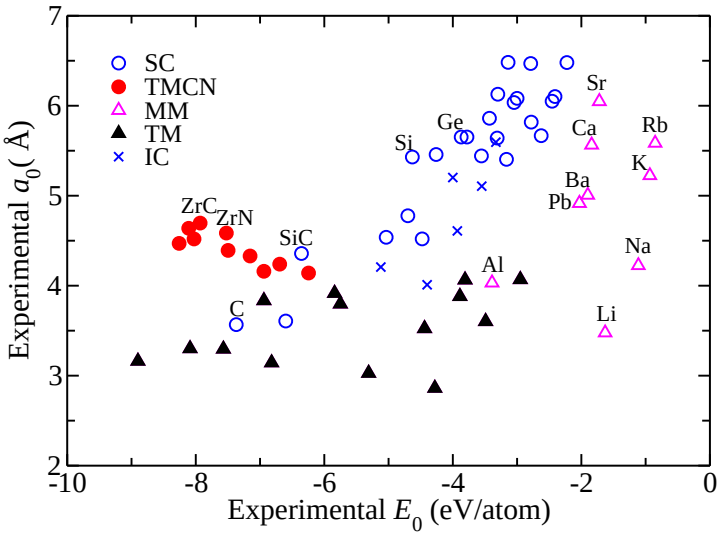

Figure 2.2: The experimental lattice constant as a function of cohesive energy for selected semiconductors, ionic crystals and metals. The definitions of five classes of solids are given as main-group metals (MM), transition metals (TM), simple semiconductors (SC), transition metal carbides and nitrides (TMCN), and ionic crystals (IC).

Figure 2.2 shows the lattice constants of selected non-molecular crystals versus their cohesive energies. The definitions of five classes of solids are given as main-group metals (MM), transition metals (TM), simple semiconductors

(SC), transition metal carbides and nitrides (TMCN), and ionic crystals (IC). It can be seen that the general tendency observed in experiment is replicated by the proposed empirical relations: there is a decrease in the cohesive energy upon going from smaller unit-cell volume crystals to larger ones, e.g., along the series of Li-Na-K-Rb, Al-Pb-Ba-Ca-Sr, and C-SiC-Si-Ge. However, this is only a very rough trend.

2.3.3 BULK MODULUS

The bulk modulus, B_0, characterizes the response of a material to an applied pressure, and is defined as

$$B_0 = -V\mathrm{d}P/\mathrm{d}V = V\mathrm{d}^2E/\mathrm{d}V^2, \tag{2.5}$$

where E is the total energy, P is the pressure, and V is the volume. Both theory and experiment suggest that the bulk modulus is a critical thermophysical and mechanical property, particularly in the area of high-pressure and high-temperature science [84]. A precise knowledge of this quantity thus is central to the EOS of any material.

The bulk modulus is commonly related to the geometrical properties of solids, such as the nearest-neighbor distance and the lattice constant, and trends can be found for the solids belonging to a similar bound group. It has been proposed that the equilibrium bulk modulus is inversely related to the structural parameters mentioned above. Anderson and Nafe [85] first proposed an empirical relationship between bulk modulus and unit-cell volume with the form of $B_0 \approx V_0^{-x}$, where x depends on the bonding type of the solid. Cohen and co-workers [86, 87] studied a number of covalent and ionic crystal, and deduced an analytical expression for the relationship between the bulk modulus and the nearest-neighbor separation d for diamond and zincblende structures

$$B_0 d^{3.5} = (1971 - 220\lambda) \approx \text{constant}, \tag{2.6}$$

where λ is an empirical ionicity parameter accounting for the effect of ionicity. This relationship is appropriate for group IVA (λ=0), IIIA–VA (λ=1), and IIB–VIA (λ=2). For the IA–VIIA rock-salt compounds, Cohen proposed the following relation

$$B_0 d^3 = 550 \approx \text{constant}. \tag{2.7}$$

A similar scaling of $B_0 d^{3.5}$ for the rock-salt structure was suggested by Schlosser [82, 83], and the cohesive energy was discussed in terms of d as well.

Figure 2.3 illustrates the correlations of the experimental lattice constants with the bulk moduli for the five studied classes of solids: SC, MM, TM, TMCN, and IC (as defined above). Together with Fig. 2.2, it can be concluded that for SC the crystals with smaller lattice constants tend to have a higher stability (more negative cohesive energy), while the bulk moduli increase as the unit cell becomes smaller. The same conclusion can be made for MM (group IA and IIA), TM (noble metals: Rh, Pd, and Ag; Ir, Pt, and Au), and IC. This correlation strongly depends on the crystal structure and the bonding character [82, 83, 85–87]. Cohen *et al.* [86, 87] investigated the contribution of covalency to the bulk modulus by using the so-called ionicity parameter λ in Eq. (2.6). Combined with Eq. (2.7), it shows that the bulk modulus is more sensitive to the structural change for covalent solids than ionic compounds, in good agreement with the experimental observations in Fig. 2.3. A likely origin for this is the increase of ionicity (λ) and loss of covalency in going from the group IVA to the almost fully ionic group IA–VIIA, with the sequence of IVA<IIIA–VA<IIB–VIA<IIA–VIA<IA–VIIA.

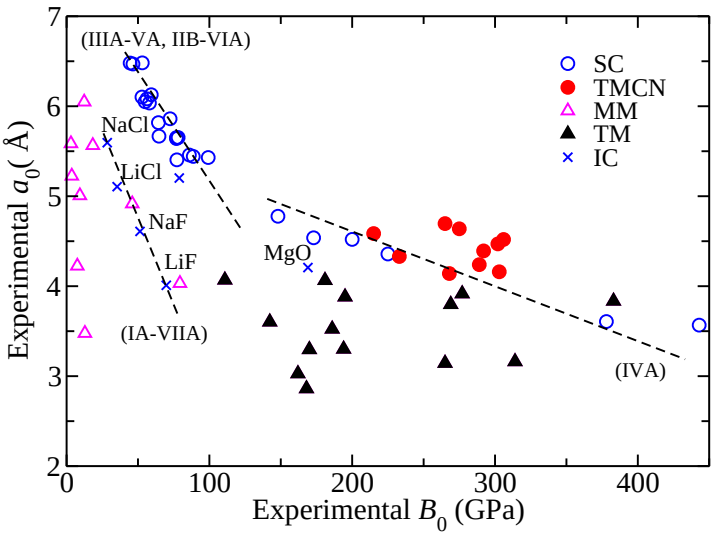

Figure 2.3: The experimental lattice constant as a function of the bulk modulus for selected semiconductors, ionic crystals and metals. The definitions of five classes of solids are given as main-group metals (MM), transition metals (TM), simple semiconductors (SC), transition metal carbides and nitrides (TMCN), and ionic crystals (IC). Dashed lines serve as a guide to the eye.

2.4 First-principles modeling of equilibrium properties

To go beyond simple qualitative understanding, the need for reliable and quantitative treatments is clear for describing bonding in solids and predicting equilibrium cohesive properties. Various kinds of difficulties have arisen in attempting to calculate and elucidate the cohesive and structural properties by quantum-mechanical methods. Firstly, to completely describe the physical behavior of electrons in a solid, one needs to compute the ground-state wave function of the system, which (in principle) might be achieved by solving the time-independent Schrödinger equation. However, this is not feasible for realistic system, as around 10^{23} electrons per cm^3 are involved in such a calculation for a solid. In a practical way, KS-DFT simplifies the difficulty to a tractable one-body problem (a single electron in a periodic potential), with the approximation solely made in the exchange-correlation (XC) energy functional term. Secondly, even though the effective single-particle Schrödinger equations are solved in a self-consistent manner, to develop accurate XC functionals for a diverse range of solids is still a big challenge. A brief description of the total-energy DFT method is given in this section, together with the current challenges for an accurate prediction of the cohesion in solids.

2.4.1 Total-energy calculations within KS-DFT

A central task for modeling ground-state properties of materials is to solve the non-relativistic time-independent Schrödinger equation (see Chapter 3, Section 3.1), with the Hamiltonian

$$H = T_{\mathrm{nucl}} + T_{\mathrm{elec}} + E_{\mathrm{n-e}} + E_{\mathrm{e-e}} + E_{\mathrm{n-n}}, \tag{2.8}$$

where the first two terms are for the kinetic energy of the nuclei and electrons respectively; the last three terms refer to the Coulomb attraction between electrons and nuclei, and the repulsion between electrons and between nuclei, respectively.

For realistic solids, solving the Schrödinger equation is an intractable problem, because of the electron-electron interaction that contains all the non-trivial many-body effects. Over several decades, total-energy DFT calculations have received great attention due to the growth of computing capability, and among modern computational methods, KS-DFT has no doubt become central to investigating ground-state properties, especially for large systems, e.g.,

biomolecules, solids, and surfaces. As the main tool of this thesis, KS-DFT will be introduced in Chapter 3.

Once the Schrödinger equation has been solved approximately, the total energy of a system can be determined and hence various other properties. For instance, the cohesive properties of a solid can be obtained using an EOS curve fitted to the energy versus volume. One of the most popular equation is the third-order Birch-Murnaghan EOS that has the form [88]

$$E(V) = E_0 + \frac{9V_0B_0}{16}\left\{\left(\left(\frac{V_0}{V}\right)^{\frac{2}{3}} - 1\right)^3 B_0' + \left(\left(\frac{V_0}{V}\right)^{\frac{2}{3}} - 1\right)^2 \left(6 - 4\left(\frac{V_0}{V}\right)^{\frac{2}{3}}\right)\right\}, \tag{2.9}$$

where V_0, E_0, B_0, and B_0' correspond to the equilibrium unit-cell volume, the cohesive energy, the bulk modulus (at V_0), and the pressure derivative of the bulk modulus (at V_0), respectively. This is also the EOS employed throughout the current work.

2.4.2 The (dis)agreement between theory and experiment

During the last decade KS-DFT [89] has had a rapidly growing impact not only on qualitative, but also quantitative predictions of materials properties [90–93]. The advantage of KS-DFT is that the formalism is in principle exact and the complexity is hidden in one term, the XC functional that determines the success or failure of approximate DFT calculations. Despite the great popularity and widespread use of DFT, it can still fail to predict properties quantitatively or even qualitatively for many systems. Some of the issues involved in practical calculations are summarized as follows.

Treatments of the exchange–correlation potential

Widely used local and semi-local approximations to the XC functional lead to systematic errors in cohesive properties of solids. For example, the local-density approximation (LDA) [89] and the gradient-corrected Perdew-Burke-Ernzerhof (PBE) [94] functionals, yield average errors of approximately 1–2% in lattice constants: LDA underestimates, while PBE overestimates with the errors systematically increasing with increasing nuclear charges [95–100]. In addition, the LDA functional severely overestimates the cohesive energies and underestimates the bulk moduli, with average errors around 20% and 16%, respectively. The results are improved when using PBE, particularly in the description of the cohesive energies (leading to 5.5% underbinding), however,

the error in the bulk moduli remains as large as 10%. Further developments have been attempted by adding additional semi-local information[6] beyond the first-order density gradient or including a fractional exact exchange in functional forms, which produces the meta-GGA [95, 101, 102] and hybrid functionals [103–105], respectively. Though these methods tend to describe some properties better than GGA functionals, they worsen the description of other properties. All of these (semi-)local and hybrid functionals share the same problem — long-range correlation, including the vdW energy tail, is not treated at all in these functionals. Methods for including vdW interactions in DFT are of great current interest, and presently these methods are being extended for describing the properties of bulk solids [22, 71, 72, 78, 79, 106–110].

Balance between accuracy and efficiency

The success of KS-DFT arises from the fact that clear approximations are made, and it performs remarkably well for many problems in chemistry and physics. Although recent developments in methodology and computing capability make it possible to carry out high-level quantum-chemical calculations, using coupled-cluster theory [111–114] or full configuration interaction (FCI) techniques, applications of these methods to solids are still in their infancy, mainly due to their massive computational resources required.[7] The first publication applying the FCI quantum Monte Carlo (FCIQMC) technique to realistic solids, which essentially enables one to capture the "exact" correlation energy, appeared in 2013 [110].

A more feasible way is to employ the so-called random-phase approximation (RPA) [115–117] for treating the electron correlation energy in solids. RPA calculations require the evaluation of the density response function; therefore they are more expensive than standard DFT calculations. Recent studies show that the usage of RPA yields significantly improved cohesive properties for a wide variety of solid-state systems over local and semi-local DFT approximations [107, 108], which also suggests that the long-range vdW forces may play an important role in the description of the cohesion in solids. However, a quantitative estimation of the long-range vdW contribution in

[6]The ingredients could be such as higher-order density gradients or the kinetic-energy density, which involves derivatives of the occupied Kohn-Sham orbitals (see details in Chapter 3, Section 3.3).

[7]The computational cost grows rapidly with the number of electrons N as well as the basis set size. Traditional full configuration interaction can be applied to at most some ten electrons with a small basis set; and coupled-cluster methods are also extremely expensive, scaling as N^7 [CCSD(T)].

different solids is lacking so far.

The importance of the nuclear zero-point vibrational energy

The final aspect to be addressed in this section is the contribution of the nuclear zero-point vibrational energy (ZPVE) effects, which need to be considered for comparing theoretical predictions with experimental measurements. The zero-point vibrational energy is the lowest possible vibrational energy for a quantum-mechanical system. According to the uncertainty principle, all physical systems undergo fluctuations even at zero temperature. The energy of the vibrational ground-state is often referred to as "zero-point vibration", while for a periodic solid, vibrations are characterized by normal modes, known as phonons [118]. The study of phonons is a subject of importance in solid-state physics, and a detailed discussion will be presented in Section 3.7.

There are several reasons why ZPVE should be taken into account in theoretical calculations of solids. Firstly, experimental lattice constants contain contributions from phonon zero-point vibrational energies; thus an unbiased comparison with experiment requires the inclusion of ZPVE in theory explicitly. Secondly, ZPVE influences not only the absolute energy, but also the EOS (energy versus unit-cell volume curve), as the phonon frequency changes with unit-cell volume, typically decreasing with increasing volume.[8] The ZPVE contribution is known to be inversely proportional to atomic mass, illustrating its greater importance for lighter atoms. Thus the inclusion of ZPVE effects becomes very important for an accurate comparison of theoretical and experimental lattice constants, cohesive energies, and bulk moduli. In addition, ZPVE tends to expand the lattice constant and reduce the stability of solids in most cases; therefore the neglect of ZPVE will introduce a systematic bias in the appraisal of different DFT functionals. Although recent calculations [96–98, 119] have been carried out for estimating the influence of ZPVE on lattice constants, a detailed study of the impact of ZPVE on bulk moduli and cohesive energies for a wide variety of bulk solids is still lacking. In this thesis, systematic calculations have been performed for 64 non-molecular solids, including metals and non-metals (covalent and ionic crystals). The methodology used for the phonon calculations will be introduced in Chapter 3 and the discussion of the results follows in Chapter 4.

[8] This is known as anharmonicity, the dependence of the phonon frequency on the unit-cell volume.

3 THEORETICAL BACKGROUND

This chapter focuses on introducing the theoretical methods used in this thesis to describe cohesive properties of solids. It starts with the derivation and formalism of density-functional theory (DFT), the most widely used electronic-structure method for (approximately) solving the many-body problem of quantum mechanics. The features of the DFT framework are given together with the challenges of developing approximate exchange-correlation (XC) functionals. In particular, an accurate treatment of long-range van der Waals (vdW) interactions represents a crucial theoretical challenge, as dispersion energy is ubiquitous in molecules and condensed matter, but not explicitly included in most DFT calculations that employ (semi-)local and hybrid XC functionals. Then, the state-of-the-art theoretical methods will be discussed for describing vdW interactions. Finally, the importance of vibrational contributions to cohesive properties of solids is addressed, followed by a description of approaches for phonon calculations.

3.1 THE SCHRÖDINGER EQUATION

One of the major targets of electronic-structure calculations is to solve the non-relativistic time-independent Schrödinger equation

$$\hat{H}\psi = E\psi, \tag{3.1}$$

where $\hat{H}$ is the Hamilton operator (Hamiltonian), which is described by coordinates of the particles in the system, and ψ and E are the wave function and the ground-state energy of the system, respectively. For a system consisting of M nuclei and N electrons, the distance between the i^{th} electron and I^{th} nucleus is represented by position vectors $\boldsymbol{r}_i$ and $\boldsymbol{R}_I$. The distance between

the i^{th} and j^{th} electron is described by vectors $\boldsymbol{r}_i$ and $\boldsymbol{r}_j$. For the I^{th} and J^{th} nuclei, $\boldsymbol{R}_I$ and $\boldsymbol{R}_J$ are used. The Hamiltonian, in atomic units,[1] is given by

$$\hat{H} = -\frac{1}{2}\sum_{I=1}^{M}\frac{\nabla_I^2}{M_I} - \frac{1}{2}\sum_{i=1}^{N}\nabla_i^2 - \sum_{i=1}^{N}\sum_{I=1}^{M}\frac{Z_I}{|\boldsymbol{r}_i - \boldsymbol{R}_I|} + \sum_{i=1}^{N}\sum_{j\neq i}^{N}\frac{1}{|\boldsymbol{r}_i - \boldsymbol{r}_j|} + \sum_{I=1}^{M}\sum_{J\neq I}^{M}\frac{1}{|\boldsymbol{R}_I - \boldsymbol{R}_J|}, \tag{3.2}$$

where Z_I is the charge of nucleus I, and M_I is the ratio of the mass of nucleus I to the mass of the electron. In short, the above Hamiltonian can be re-written as

$$\hat{H} = \hat{T}_{\text{nucl}} + \hat{T}_{\text{elec}} + \hat{V}_{\text{n-e}} + \hat{V}_{\text{e-e}} + \hat{V}_{\text{n-n}}, \tag{3.3}$$

where the first two terms describe the kinetic energy of the nuclei and electrons respectively; the final terms refer to the Coulomb attraction between electrons and nuclei, and the repulsion between electrons and between nuclei, respectively.

The solution to a non-relativistic time-independent Schrödinger equation involving the Hamiltonian,

$$\hat{H}\psi(\boldsymbol{r}, \boldsymbol{R}) = E\psi(\boldsymbol{r}, \boldsymbol{R}), \tag{3.4}$$

is the many-body wave function $\psi(\boldsymbol{r}, \boldsymbol{R})$, which describes wave-like motion and explicitly depends on the coordinates of all particles in the system, and E is the ground-state energy. Therefore solving the exact equation involves a problem with $(3N+3M)$ degrees of freedom. To turn the problem into a feasible enterprise (not only for the simplest hydrogen-atom case), approximations are required.

The first and the most common approximation is made to treat nuclei and electrons on a different footing, which is known as the Born-Oppenheimer approximation (BOA) [120]. The success of BOA lies in the large difference between the masses of the nucleus and the electron, M_I shown in Eq. (3.2), such that the electrons typically respond almost instantaneously to any change in the nuclear positions. In other words, one can consider the electrons as moving in the field produced by the fixed nuclei. Within this approximation, the nuclear kinetic-energy term can be neglected and the nuclear-nuclear repulsion term can be considered as a constant for a given set of coordinates. If one writes Eq. (3.3) with only the electronic term, the Hamiltonian becomes

$$\hat{H}_{\text{elec}} = \hat{T}_{\text{elec}} + \hat{V}_{\text{n-e}} + \hat{V}_{\text{e-e}}. \tag{3.5}$$

[1] In this thesis, unless otherwise stated, Hartree atomic units are utilized.

Solving the time-independent Schrödinger equation,

$$\hat{H}_{\mathrm{elec}}\psi_{\mathrm{elec}}(\boldsymbol{r},\boldsymbol{R}) = E_{\mathrm{elec}}\psi_{\mathrm{elec}}(\boldsymbol{r},\boldsymbol{R}), \tag{3.6}$$

one arrives at the electronic wave function $\psi_{\mathrm{elec}}(\boldsymbol{r},\boldsymbol{R})$ that describes the motion of electrons and depends on the electronic coordinates and the nuclear positions only parametrically. E_{elec} is known as the electronic total energy in Eq. (3.5), including the kinetic energy and Coulomb energies. The total energy is regained by adding the constant nuclear-nuclear repulsion term for the nuclei, and is written as

$$E_{\mathrm{total}} = T_{\mathrm{elec}} + E_{\mathrm{n-e}} + E_{\mathrm{e-e}} + E_{\mathrm{n-n}}. \tag{3.7}$$

The work presented in this thesis is entirely within BOA, in the following, the "total" and "elec" subscripts will be dropped for simplicity; and only electronic Hamiltonians and wave functions will be considered. Although the assumption of BOA remarkably reduces the complexity of solving the many-body Schrödinger equation, the resulting electronic Schrödinger equation is still extremely complex. Many approximate electronic-structure methods have been developed to solve the so-called "Schrödinger-like" equations. Density-functional theory (DFT) is currently among the most popular and most widely used quantum-mechanical methods, accounting for approximately 90% of all calculations today in condensed-matter physics, computational physics, and computational chemistry [90–93]. The formulation of DFT follows in the next section.

3.2 Basics of density-functional theory

One of the major reasons for the popularity of DFT lies in its excellent compromise between accuracy and feasibility. DFT avoids the expense of quantum-chemical methods, determining the energy directly from the electron density $n(\boldsymbol{r})$, rather than the many-electron wave function $\psi(\boldsymbol{r}_1,\boldsymbol{r}_2,\ldots,\boldsymbol{r}_N)$ (such as in Hartree-Fock and post-Hartree-Fock theories). Thus the many-body problem is shifted to the problem of solving a set of equations that depend solely upon the three spatial coordinates of the electron density.

3.2.1 The Thomas-Fermi theory

The concept of using the electron density rather than the wave function can be traced back to the work of Thomas [121] and Fermi [122] in 1927. In the original

Thomas-Fermi (TF) theory, the kinetic energy of electrons is approximated as an explicit functional of the density based on non-interacting electrons in a homogeneous gas. Within this model, the kinetic energy of electrons is expressed as

$$T[n(\boldsymbol{r})] = C_F \int n^{5/3}(\boldsymbol{r})\mathrm{d}\boldsymbol{r}, \tag{3.8}$$

where $C_F = \frac{3}{10}(3\pi^2)^{2/3} = 2.871$, and $n(\boldsymbol{r})$ defines the electron density and yields the total number of electrons N by integration

$$\int n(\boldsymbol{r})\mathrm{d}\boldsymbol{r} = N. \tag{3.9}$$

In the TF theory, the exchange and correlation among the electrons is neglected. When electron-nucleus and electron-electron interactions are included, the total energy is obtained

$$E_{\mathrm{TF}}[n(\boldsymbol{r})] = C_F \int n^{5/3}(\boldsymbol{r})\mathrm{d}\boldsymbol{r} - Z\int \frac{n(\boldsymbol{r})}{\boldsymbol{r}}\mathrm{d}\boldsymbol{r} + \frac{1}{2}\iint \frac{n(\boldsymbol{r})n(\boldsymbol{r}')}{|\boldsymbol{r}'-\boldsymbol{r}|}\mathrm{d}\boldsymbol{r}\mathrm{d}\boldsymbol{r}', \tag{3.10}$$

where the second and third terms correspond to the electron-nucleus and the Coulomb part of the electron-electron interactions, respectively. Although it is an important first step, the TF model remains a fairly crude approximation for most circumstances not only because of the poor description of the uniform gas in the representation of the kinetic energy, but also the complete neglect of exchange and correlation terms in the electron-electron interaction.

3.2.2 The Hohenberg-Kohn theorems

Modern density-functional theory, building upon the ideas of Thomas [121], Fermi [122], and many others, was born in 1964, with the work of Hohenberg and Kohn [123]. The approach of Hohenberg and Kohn (HK) is to formulate DFT as an exact theory of many-electron systems, where the Hamiltonian of interacting particles can be written as

$$\hat{H} = -\frac{1}{2}\sum_i \nabla_i^2 - \sum_i \upsilon_{\mathrm{ext}}(\boldsymbol{r}_i) + \sum_i \sum_{j\neq i} \frac{1}{|\boldsymbol{r}_i - \boldsymbol{r}_j|}; \tag{3.11}$$

$$\upsilon_{\mathrm{ext}}(\boldsymbol{r}_i) = -\sum_I \frac{Z_I}{|\boldsymbol{r}_i - \boldsymbol{R}_I|}. \tag{3.12}$$

Here $\upsilon_{\mathrm{ext}}(\boldsymbol{r}_i)$ is an external potential that includes interactions between electrons and nuclei. The HK approach is based upon two theorems [123]:

Theorem I: For any system of interacting particles in an external potential $v_{\text{ext}}(\boldsymbol{r})$, the total energy is determined uniquely (up to an additive constant) by the ground-state particle density $n_0(\boldsymbol{r})$.

Theorem II: A universal functional for the energy in terms of the density $n(\boldsymbol{r})$ can be defined, valid for any external potential $v_{\text{ext}}(\boldsymbol{r})$. For any particular potential, the exact ground-state energy of the system is the global minimum of this functional, and the density $n(\boldsymbol{r})$ that minimizes the functional is the exact ground-state density $n_0(\boldsymbol{r})$.

As a result, the energy functional has the following form

$$E[n(\boldsymbol{r})] = F_{\text{HK}}[n(\boldsymbol{r})] + \int v_{\text{ext}}(\boldsymbol{r}) n(\boldsymbol{r}) \mathrm{d}\boldsymbol{r}, \tag{3.13}$$

and the universal HK functional reads as

$$F_{\text{HK}} = T[n(\boldsymbol{r})] + V_{\text{e-e}}[n(\boldsymbol{r})], \tag{3.14}$$

where $T[n]$ is the kinetic-energy functional and $V_{\text{e-e}}[n]$ is the electron-electron interaction functional.

The HK theorems tell us there is a one-to-one correspondence between the external potential and the ground-state density. Thus a universal functional can be defined for any density, and by minimizing this functional one would find the exact density and energy of the true interacting many-body system: $E_0[n_0(\boldsymbol{r})] \leq E_0[n(\boldsymbol{r})]$.

The original proofs for these theorems are readily available (e.g., the original literature [123] or a standard textbook [124]), and thus will not be presented here. The HK theorems, however, are no nearer to a practical method, as the exact evaluation of the HK functional F_{HK} would require us to solve the many-electron Schrödinger equation. Assuming one has a functional that is a good approximation to $F_{\text{HK}}[n(\boldsymbol{r})]$ and that can be treated in a practical manner, a search for the density that minimizes this functional should then yield a good approximation to the ground-state density as well as the energy. This provides the fundamental concept upon which all practical DFT calculations are built up. The most practical scheme is known as the Kohn-Sham (KS) method, proposed by Kohn and Sham in 1965 [89].

3.2.3 THE KOHN-SHAM METHOD

Kohn and Sham developed a method based on the HK theorems that allows one to minimize the functional by varying $n(\boldsymbol{r})$ over all densities of N electrons. Essentially, the universal functional F_{HK}, given by Eq. (3.14), is separated into a set of energy components, each of which has a clear physical origin, and some of which have explicit forms. Approximation is only required for the components that cannot be readily evaluated.

KOHN-SHAM SYSTEM

" The Kohn-Sham system is defined as a fictitious system of ***non-interacting*** *particles (typically electrons) that generate the same density as any given system of interacting particles "* [125]:

$$n_{\mathrm{KS}}(\boldsymbol{r}) = n(\boldsymbol{r}).$$

Kohn and Sham considered a fictitious auxiliary system, aiming at modeling the true many-electron system. This fictitious system consists of independent electrons, each of which experiences the same external potential (denoted as the effective potential, which will be discussed in further detail in this section). This assumes that the ground-state density of a non-interacting system $n_{\mathrm{KS}}(\boldsymbol{r})$ is equal to the true ground-state density $n(\boldsymbol{r})$. Within this assumption, the ground-state wave function of the system can be written in terms of single-particle wave functions.

KOHN-SHAM HAMILTONIAN

From the HK theorem, one can determine the ground-state energy by minimizing the energy functional,

$$E[n(\boldsymbol{r})] = T[n(\boldsymbol{r})] + V_{\mathrm{e-e}}[n(\boldsymbol{r})] + \int v_{\mathrm{ext}}(\boldsymbol{r}) n(\boldsymbol{r}) \mathrm{d}\boldsymbol{r}, \tag{3.15}$$

where the sum of the first and second terms defines the universal functional F_{HK}. Kohn and Sham [89] wrote F_{HK} in three terms, so that the energy functional becomes

$$E[n(\boldsymbol{r})] = \underbrace{T_{\mathrm{s}}[n(\boldsymbol{r})] + \frac{1}{2} \iint \frac{n(\boldsymbol{r}) n(\boldsymbol{r}')}{|\boldsymbol{r} - \boldsymbol{r}'|} \mathrm{d}\boldsymbol{r} \mathrm{d}\boldsymbol{r}' + E_{\mathrm{xc}}[n(\boldsymbol{r})]}_{F_{\mathrm{HK}}} + \int v_{\mathrm{ext}}(\boldsymbol{r}) n(\boldsymbol{r}) \mathrm{d}\boldsymbol{r}. \tag{3.16}$$

In a concise manner, the energy functional can be expressed as

$$E[n(\boldsymbol{r})] = T_{\mathrm{s}} + V_{\mathrm{H}} + E_{\mathrm{xc}} + V_{\mathrm{ext}}, \tag{3.17}$$

- T_{s} is the kinetic energy of *non-interacting* electrons with the density $n(\boldsymbol{r})$; for such a system, the kinetic energy and the density can be described in terms of single-particle orbitals;

- V_{H} is the Hartree (or Coulomb) energy corresponding to the electron-electron interaction, equal to the classical electrostatic energy of the charge distribution $n(\boldsymbol{r})$, with the Hartree potential being

$$v_{\mathrm{H}} = \int \frac{n(\boldsymbol{r}')}{|\boldsymbol{r} - \boldsymbol{r}'|} \mathrm{d}\boldsymbol{r}'; \tag{3.18}$$

- E_{xc} is the non-trivial exchange-correlation energy that goes beyond the Hartree approximation;

- V_{ext} is the external potential energy acting on the electrons,

$$V_{\mathrm{ext}} = \int v_{\mathrm{ext}}(\boldsymbol{r}) n(\boldsymbol{r}) \mathrm{d}\boldsymbol{r}. \tag{3.19}$$

KOHN-SHAM EQUATIONS

The next step is to evaluate each term in Eq. (3.16). For a system of N electrons, one can construct the wave function from the single-particle orbitals $\psi_i(\boldsymbol{r})(i = 1, 2, \ldots, N)$ using a single Slater determinant. The kinetic energy and the electron density are then given by

$$T_{\mathrm{s}}[n] = -\frac{1}{2} \sum_{i=1}^{N} \langle \psi_i | \nabla^2 | \psi_i \rangle; \tag{3.20}$$

$$n(\boldsymbol{r}) = \sum_{i=1}^{N} |\psi_i|^2. \tag{3.21}$$

Writing Eq. (3.16) in terms of single-particle orbitals, one can arrive at the central equation in KS-DFT expressed as

$$\hat{h}_i^{\mathrm{KS}} \psi_i(\boldsymbol{r}) = \epsilon_i \psi_i(\boldsymbol{r}), \tag{3.22}$$

with the one-electron Hamiltonian being of the following form

$$\hat{h}_i^{\mathrm{KS}} = -\frac{1}{2}\nabla^2 + v_{\mathrm{H}}(\boldsymbol{r}) + v_{\mathrm{xc}}(\boldsymbol{r}) + v_{\mathrm{ext}}(\boldsymbol{r}). \tag{3.23}$$

At this stage, one can define an effective single-particle potential v_{eff},

$$v_{\mathrm{eff}} = v_{\mathrm{H}} + v_{\mathrm{xc}} + v_{\mathrm{ext}}, \tag{3.24}$$

with the exchange-correlation potential v_{xc} given by

$$v_{\mathrm{xc}}(\boldsymbol{r}) = \frac{\delta E_{\mathrm{xc}}[n(\boldsymbol{r})]}{\delta n(\boldsymbol{r})}. \tag{3.25}$$

Furthermore, one can rewrite the KS equation as

$$\left(-\frac{1}{2}\nabla^2 + v_{\mathrm{eff}}\right)\psi_i = \epsilon_i \psi_i. \tag{3.26}$$

Practical KS-DFT calculations involve searching for the electron density that minimizes this functional, such that the ground-state energy and the density can be obtained by solving the N single-particle equations. Note that v_{eff} is still a functional of the electron density $n(\boldsymbol{r})$ from its definition, hence these equations must be solved iteratively. Up to this point, the KS-DFT formalism is "exact" within the non-relativistic Born-Oppenheimer approximation. In fact, the only remaining part is the explicit evaluation of the exchange-correlation functional $E_{\mathrm{xc}}[n(\boldsymbol{r})]$, for which approximations are necessary.

3.3 Approximate exchange-correlation functionals

The KS equations expressed in Eq. (3.26) are so far exact within non-relativistic quantum mechanics: no approximations have yet been made, except for BOA. It should be noted that the kinetic energy T_{s} defined via Eq. (3.16), is not the *true* kinetic energy, but the *non-interacting* kinetic energy. Combining Eq. (3.15) with (3.16), one can re-write the exchange-correlation energy as

$$E_{\mathrm{xc}}[n(\boldsymbol{r})] = (T - T_{\mathrm{s}}) + (V_{\mathrm{e-e}} - V_{\mathrm{H}}), \tag{3.27}$$

where T and $V_{\mathrm{e-e}}$ represent the exact kinetic and electron-electron interaction energies, respectively; and V_{H}, the Hartree energy term, is the Coulomb self-energy of a stationary, non-quantized, distribution of electric charge of density

$n(\boldsymbol{r})$. Physically, E_{xc} contains contributions of exchange and correlation to the system energy followed below.

THE EXCHANGE ENERGY E_{x}

This term accounts for the fact that the wave function is anti-symmetric with respect to the exchange of any two particles' coordinates due to the Pauli exclusion principle. The difference in the electrostatic energy due to the anti-symmetrization, known as the exchange energy, can be written directly in terms of occupied KS orbitals as

$$E_{\mathrm{x}} = -\frac{1}{2}\sum_{ij}\iint \frac{\psi_i^*(\boldsymbol{r})\psi_i(\boldsymbol{r}')\psi_j^*(\boldsymbol{r}')\psi_j(\boldsymbol{r})}{|\boldsymbol{r}-\boldsymbol{r}'|}\mathrm{d}\boldsymbol{r}\,\mathrm{d}\boldsymbol{r}'. \tag{3.28}$$

The explicit calculation of E_{x} is computationally very expensive for solids, so approximations are needed in practice. Efficient approximations to the exchange energy often lead to a notorious deficiency in KS-DFT approaches, the so-called self-interaction error (SIE), which arises from the spurious interaction of an electron with itself and does not completely cancel in approximate DFT functionals. SIE is typically considered as the cause of many failures of KS-DFT, e.g., in charge transfer processes and transition states of chemical reactions [126].

THE CORRELATION ENERGY E_{c}

This term accounts for the fact that electrons are not independent, but correlated. The correlation energy is formally defined as the difference between the exact non-relativistic energy and the energy in the Hartree-Fock limit. By definition, the correlation energy has both potential and kinetic components, and the resulting physical effects are: (i) the potential energy is reduced; (ii) the kinetic energy is increased.

In contrast to the exchange energy, no general analytical expression is known for the electron correlation energy. It can only be calculated exactly by solving the many-electron Schrödinger equation of Eq. (3.2); therefore it is always approximated in practical calculations. Usually, the exchange and correlation terms are grouped together as

$$E_{\mathrm{xc}} = E_{\mathrm{x}} + E_{\mathrm{c}}. \tag{3.29}$$

Since the actual form of E_{xc} is unknown, to describe this term, one must

introduce approximate functionals based upon the electron density. In this section, we shall discuss the most popular formalism in the field of DFT functional development, climbing the so-called "Jacob's ladder" [90, 127] with the goal of obtaining an accurate total energy: the local (spin) density approximation, generalized gradient approximation, meta-generalized gradient approximation, hybrid functionals and the random-phase approximation. Of course, the computational cost grows as more ingredients are added for evaluating E_{xc}.

3.3.1 The local (spin) density approximation

The simplest approximation to the XC functional is the local-density approximation (LDA), which assumes the electron density can be treated locally as a uniform electron gas (UEG), so that the XC energy can be evaluated from the charge density at the point under consideration. LDA was first formulated by Kohn and Sham [89] and holds for systems with slowly varying densities. Within this approximation, the XC energy for a density $n(\boldsymbol{r})$ is written as

$$E_{\mathrm{xc}}^{\mathrm{LDA}}[n(\boldsymbol{r})] = \int n\left(\boldsymbol{r}\right) \epsilon_{\mathrm{xc}}^{\mathrm{unif}}[n(\boldsymbol{r})]\mathrm{d}\boldsymbol{r}, \tag{3.30}$$

where $\epsilon_{\mathrm{xc}}^{\mathrm{unif}}$ is the XC energy per electron of an electron gas with uniform density. The exchange-energy density of a UEG is known analytically, thus yielding a simple expression for the exchange energy [128]

$$E_{\mathrm{x}}^{\mathrm{LDA}}[n(\boldsymbol{r})] = -\frac{3}{4}\left(\frac{3}{\pi}\right)^{1/3} \int n^{4/3}(\boldsymbol{r})\mathrm{d}\boldsymbol{r}. \tag{3.31}$$

The exact functional form for the correlation energy density of a UEG is unknown (except in the limits of the infinitely-weak and infinitely-strong correlation cases) and has been numerically evaluated with quantum Monte Carlo (QMC) calculations in Ref. [129]. These data have then been used to parametrize an interpolated analytic form for $E_{\mathrm{c}}^{\mathrm{LDA}}$ in several ways, with the widely used parameterizations due to the work by Vosko *et al.* [130] and Perdew *et al.* [131, 132] found in most DFT computer codes. The local spin-density approximation (LSDA) is a straightforward generalization of LDA to include electron spin, written as $E_{\mathrm{xc}}^{\mathrm{LSDA}}[n_{\uparrow}, n_{\downarrow}]$, and it provides an improvement for systems where the spin of electrons is important.

Despite the fact that $n(\boldsymbol{r})$ of a system varies with position, L(S)DA performs remarkably well in practical applications. Its success, besides its validity for

very slowly varying densities, can be attributed to compensation between exchange and correlation holes [133], which explains to some extent its good performance in describing structural and elastic properties of both bulk solids and surfaces [134]. In fact, the prediction of geometries in LDA has been one of its great advantages. In many cases, LDA gives bond lengths of molecules and solids better than GGA functionals, as can be seen from the T-96 set of Scuseria and co-workers [135], which contains covalently-bonded diatomic molecules and simple polyatomic molecules. However, the LDA functional often leads to significant errors for the bonding of both molecules and solids. For instance, L(S)DA atomization energies (also known as cohesive energies in solids) are very inaccurate, typically off by 20–30%. Typically, it is found that L(S)DA yields overbinding — too large cohesive energies and too short bond lengths [98, 108, 136]. Therefore an accurate description of material properties requires functionals that go beyond L(S)DA.

3.3.2 The generalized gradient approximation

An improvement over L(S)DA can be made by introducing one additional ingredient to the energy functional, the density gradient $\nabla n(\boldsymbol{r})$, accounting for "non-locality" in realistic systems. This yields a group of functionals, called the generalized gradient approximation (GGA),

$$E_{\mathrm{xc}}^{\mathrm{GGA}}[n(\boldsymbol{r})] = \int n(\boldsymbol{r})\epsilon_{\mathrm{xc}}^{\mathrm{GGA}}[n(\boldsymbol{r}), \nabla n(\boldsymbol{r})]\mathrm{d}\boldsymbol{r}; \tag{3.32}$$

or more typically expressed as

$$E_{\mathrm{xc}}^{\mathrm{GGA}}[n(\boldsymbol{r})] = \int n(\boldsymbol{r})\epsilon_{\mathrm{xc}}^{\mathrm{unif}}F_{\mathrm{xc}}[n(\boldsymbol{r}), \nabla n(\boldsymbol{r})]\mathrm{d}\boldsymbol{r}, \tag{3.33}$$

where F_{xc} is known as the enhancement factor, a dimensionless parameter accounting for the gradient dependency, and $\epsilon_{\mathrm{xc}}^{\mathrm{unif}}$ is the XC energy density inherited from the LDA formalism. Note that XC functionals based on GGA are typically referred to as semi-local functionals, as the non-locality is only partially captured by the density gradient.

Unlike $\epsilon_{\mathrm{xc}}^{\mathrm{LDA}}$, the functional $\epsilon_{\mathrm{xc}}^{\mathrm{GGA}}$ lacks a uniquely justifiable form. Thus the form is often chosen to satisfy various physical constraints. However, it is impossible to satisfy every constraint simultaneously, such that the functional form is typically (but not always) chosen according to the nature of the system under consideration. This leads to many different parameterizations of GGA based on the choice of F_{xc}. Within the condensed-matter-physics community,

one of the most commonly used GGAs is that proposed by Perdew, Burke, and Ernzerhof [94], the PBE functional. It is a revised version of the PW91 [137] functional with a simplified form for the enhancement factor. Both of these functionals have no empirical parameters. To evaluate F_{xc}, it is generally split into its exchange and correlation terms. The PBE exchange can be expressed as

$$F_{\mathrm{x}}(s) = 1 + \kappa - \frac{\kappa}{1 + \mu s^2/\kappa}, \tag{3.34}$$

with κ and μ being constants, and s is defined as the dimensionless reduced density gradient, $|\nabla n|/2(3\pi^2 n)^{4/3}$. In contrast, the expression for the GGA correlation energy is more complex, due to the scaling relations and the treatment of spin polarization.

GGA functionals often show a better performance than LDA for molecular structures, hydrogen bonds, and other weakly bonded systems. However, it does not yield a uniform improvement over LDA for solids. Though PBE often gives lattice constants in better agreement with experiment, the same is not true for bulk moduli [98, 108, 136]. It has been found that the PBE functional describes reasonably good lattice constants, but exhibits a general behavior (opposed to LDA) of underbinding. Many variations to the functional form of F_{x} in Eq. (3.34) have been proposed to cure the shortcomings of PBE. For example, revPBE [138] changes one parameter on the exchange enhancement factor F_{x} by fitting exchange energies to reference data of atoms and molecules; RPBE [139] changes F_{x} aiming to improve the adsorption energy of small molecules on surfaces; PBEsol [140] recovers the second-order density gradient expansion for the UEG limit in the exchange term and describes geometries better for solids and surfaces, however, bulk moduli and cohesive energies are poorly predicted for some systems compared with PBE results [98, 99, 141, 142].

3.3.3 The meta-generalized gradient approximation

Adding more local ingredients beyond the first-order density gradient yields meta-GGA (or MGGA) functionals [95, 101, 102], which are located on the third rung of "Jacob's ladder". Besides ingredients already contained in GGAs, additional semi-local information could be higher-order density gradients and the kinetic-energy density, which involves derivatives of the occupied KS orbitals $\psi_i(\boldsymbol{r})$. A general form used for MGGA functionals is

$$E_{\mathrm{xc}}^{\mathrm{MGGA}}[n(\boldsymbol{r})] = \int n(\boldsymbol{r}) \epsilon_{\mathrm{xc}}^{\mathrm{MGGA}}[n(\boldsymbol{r}),\, \nabla n(\boldsymbol{r}),\, \nabla^2 n(\boldsymbol{r}),\, \tau(\boldsymbol{r}),\, \mu(\boldsymbol{r}), ..., \gamma(\boldsymbol{r})] \mathrm{d}\boldsymbol{r}, \tag{3.35}$$

where $\nabla^2 n(\boldsymbol{r})$ corresponds to the Laplacian of the density, $\tau(\boldsymbol{r}) = \frac{1}{2}\sum_{i}^{\text{occ}} |\nabla\psi_i(\boldsymbol{r})|^2$ is known as the non-interacting kinetic-energy density, and $\mu(\boldsymbol{r})$,...,$\gamma(\boldsymbol{r})$ represent other possible semi-local arguments (i.e., defined locally at $\boldsymbol{r}$) that could be used in MGGAs.

Several MGGA forms have been constructed on the basis of theoretical constraints (in some cases) in combination with fits to chemical data, and among those the highlights are the TPSS functional [95] and its revised version revTPSS [143, 144], and the M06-L functional [145, 146]. TPSS, devised by Tao, Perdew, Staroverov, and Scuseria, is a nonempirical MGGA functional. It predicts lattice constants slightly better than those of PBE, good surface energies, as well as good atomization energies [95, 135]. To further improve the performance on lattice constants, revTPSS was proposed but at the cost of worsening the energies compared with those of original TPSS [136]. Truhlar *et al.* developed MGGAs based on flexible functional forms parametrized on high-quality benchmark databases, and weak interactions for organic systems. MGGAs are also often coupled with fractional (0% to 100%) Hartree-Fock exchange. These functionals are known as hybrid MGGA functionals, such as the M06 family, including M06 [147], M06-2X [147], and M06-HF [148]. M06-L is the local MGGA (with 0% of Hartree-Fock exchange), and incorporates the ideas of physical constraints, modeling the exchange-correlation hole, and empirical fits in the functional form. At present most studies of the performance of M06-L are based on molecular systems, which shows better agreement with experiment than Becke-3-Lee-Yang-Parr (B3LYP) [104, 149] (the most widely used functional in the field of chemistry). In this thesis, we shall examine the performance of M06-L for a large database of crystalline solids, as presented in Chapter 4.

Although many improvements have been made to the XC functional, MGGAs still do not perform uniformly better than GGAs. Another point to highlight is that many MGGAs are constructed using experimental data to define the functional forms (except TPSS, which is a nonempirical MGGA), leading to the issue of many empirical parameters.

3.3.4 HYBRID FUNCTIONALS

So far with L(S)DA, PBE, and TPSS, the first three rungs of the nonempirical ladder are essentially completed. Further developments can be achieved by adding "nonlocal" terms into the XC energy, aiming at reducing self-interaction errors present in (semi-)local functionals. In principle, any exchange functional

can be combined with any correlation functional. As already mentioned above, a fraction of exact exchange (EXX) can be added to conventional GGAs or MGGAs. These functionals are known as hybrid functionals, originally proposed by Becke [103, 104]. A general form for hybrid GGAs can be written as [105],

$$E_{\mathrm{xc}}^{\mathrm{hybrid}} = \alpha E_{\mathrm{x}}^{\mathrm{EXX}} + (1-\alpha) E_{\mathrm{x}}^{\mathrm{GGA}} + E_{\mathrm{c}}^{\mathrm{GGA}} \tag{3.36}$$

where $E_{\mathrm{x}}^{\mathrm{EXX}}$ represents the exact exchange given by Eq. (3.28), and the coefficient α reflects the amount of the exact-exchange mixing, which can be defined semi-empirically or using perturbative arguments from the adiabatic connection formalism.

Hybrid functionals (such as B3LYP [104, 149]) have gained wide popularity in quantum chemistry, due to their improved predictions for many molecular properties (e.g., bond lengths, atomization energies and vibrational frequencies) relative to local and semi-local functionals. However, the application of hybrid schemes to extended systems is computationally challenging. Recently, a set of screened hybrid functionals, obtained by the use of a screened Fock exchange operator, such as HSE06 [150](revised from HSE03 [151] proposed by Heyd *et al.*) and HSEsol [142] (proposed by Kresse *et al.*), addressed this problem by separating the exchange interaction into a short-range (SR) and a long-range (LR) part. These developments allowed hybrid functionals to become popular in solid-state physics [106, 152–158].

The expression for the HSE XC energy is

$$E_{\mathrm{xc}}^{\mathrm{HSE}} = \alpha E_{\mathrm{x}}^{\mathrm{EXX,SR}}(\omega) + (1-\alpha) E_{\mathrm{x}}^{\omega\mathrm{PBE,SR}}(\omega) + E_{\mathrm{x}}^{\omega\mathrm{PBE,LR}}(\omega) + E_{\mathrm{c}}^{\mathrm{PBE}}, \tag{3.37}$$

where $E_{\mathrm{x}}^{\mathrm{EXX,SR}}$ is the SR exact exchange, $E_{\mathrm{x}}^{\omega\mathrm{PBE,SR}}$ and $E_{\mathrm{x}}^{\omega\mathrm{PBE,LR}}$ are the SR and LR components of the PBE exchange, and $E_{\mathrm{c}}^{\mathrm{PBE}}$ is the full PBE correlation. The parameter ω is known as the range-separation parameter, governing the extent of the SR interactions. The admixture constant α is set to be 0.25 that was derived from perturbation theory [159]. There are some improvements over traditional hybrids by introducing the range-separation concept to treat the exact exchange, with less computational cost. For instance, HSE06 was benchmarked for a variety of metallic, semiconducting, and insulating solids, and the results showed a substantial improvement over the standard LDA or GGAs for some cohesive properties as well as band gaps [153, 154]. However, there are still two issues concerning the use of hybrid functionals in solids. Firstly, metallic (including small-gap) systems cannot be treated well, in particular for the case of transition metals [142, 155, 157]. Secondly, in

general hybrid functionals cannot reproduce cohesive energies as well as PBE does [142, 155, 158]. An important reason is that the LR correlation in the XC energy is not included in any of hybrid functionals.

3.3.5 The random-phase approximation for electron correlation

The random-phase approximation (RPA) is located on the fifth rung of "Jacob's ladder", where the unoccupied orbitals and eigenvalues are involved. RPA is one of the oldest methods for computing the ground-state correlation energy of many-electron systems, and it treats long-range correlation seamlessly. Consequently, the vdW energy is naturally included in the RPA approach. The interested reader is referred to two recent review papers [160, 161] and references therein.

Some attractive features of RPA are the following:

- it is based on many-body perturbation theory and is free from empirical parameters;
- it dramatically improves over semi-local density functionals for non-covalent interactions [161, 162];
- it can be coupled with exact exchange, and sometimes is able to capture some static correlation [160, 161];
- it is computationally feasible for molecules with over 100 atoms.

RPA is presently among the best choices for predicting properties of molecules, solids, and surfaces. It has been shown that the RPA approach predicts accurate lattice constants and bulk moduli for a diverse range of bulk solids, including semiconductors, insulators, as well as metals, with mean absolute relative errors (MAREs) being 0.4% and 4% for the two properties respectively [108].[2] However, cohesive energies are typically disappointing (with even more underbinding than PBE) [108]. A very recent development going beyond RPA, the renormalized second-order perturbation theory (rPT2) [163] approach, has shown great promise in resolving the underbinding problem in standard RPA. While this is only based upon some preliminary results of the cohesive energies of small copper clusters, a systematic investigation of this issue is greatly needed. In addition, RPA (and its variants) calculations are more demanding than conventional DFT calculations due to the evaluation of the response function. Thus the

[2] RPA outperforms both LDA and PBE approximately by 1% and 6% for lattice constants and bulk moduli respectively, obtained from a database of 24 solids [108].

computational cost needs to be addressed for its widespread use in future applications.

The original scheme was first formulated by Bohm and Pines during the years between 1951 and 1953 [115–117]. There have been many developments beyond standard RPA in the last half century, and a more detailed discussion of this method will follow in Section 3.4.2.

The success of RPA (and beyond) tells us that the long-range correlation energy is critical for approaching the "heaven" of chemical accuracy (within 1 kcal/mol for energetics). This motivates the need for adding the long-range vdW energy on top of local and semi-local KS-DFT calculations and assessing potential methods that are feasible for complex materials.

3.4 Methods for treating van der Waals interactions

Generally, the term "vdW interactions" can refer to different types of interatomic and intermolecular interactions, e.g., electrostatics, induction, and dispersion. The term "dispersion energy" is often used interchangeably with "vdW energy", and corresponds to the attractive interaction between fluctuating multipoles. In this thesis, we follow this convention. vdW interactions arise from the correlated motion of electrons; thus the vdW energy constitutes a large part of the long-range electron correlation energy. These interactions are inherently quantum mechanical in nature, the exact treatment of which must be performed using many-electron quantum mechanics. Here we will only focus on the discussion of DFT-based vdW inclusive theories, upon which this thesis is founded. The quantum-chemical wave function approaches (e.g., coupled-cluster and configuration-interaction methods) are not yet feasible for practical calculations of solids.[3]

3.4.1 Interaction between fluctuating dipoles

Dispersion interactions were explained by London [12, 13] from a quantum-mechanical treatment based on second-order perturbation theory, and are also known as London (dispersion) forces in his honor. The long-range multipolar expansion for the pair-wise vdW energy is frequently written in terms of

[3]The computational cost grows rapidly with the number of electrons N as well as the basis set size. Traditional full configuration interaction can be applied to at most some ten electrons with a small basis set; and even coupled-cluster methods are extremely expensive, scaling like N^7. The reader is referred to Refs. [111–114, 164–167] for more information.

interatomic separation R as a series with coefficients C_n denoted as *dispersion coefficients* [15, 168]

$$E_{\mathrm{vdW}} = -\sum_{n=6,8,10,\ldots}^{\infty} \frac{C_n}{R^n}. \tag{3.38}$$

THE C_6 DISPERSION COEFFICIENT

The first nonvanishing term of the above expression, $C_6 R^{-6}$, corresponds to the interaction between two fluctuating dipoles, and is typically (but not always) the dominant contribution. Therefore in many applications, vdW interactions can be approximated by the first term of the multipolar expansion, with the error rapidly diminishing as the distance increases. This explains the fact that there are a large number of methods aiming to evaluate C_6 dispersion coefficients accurately.

In order to compute the vdW energy, the necessary ingredients are the dynamic dipolar polarizability and C_6 dispersion coefficients. Both of them are dependent upon the *oscillator strength* [169] distribution that describes the transition from state ψ_0 to state ψ_n, as defined by

$$f_{n0} = \frac{2}{3}\omega_{n0}|d_{n0}|^2, \tag{3.39}$$

where ω_{n0} is the transition frequency between the two states, and d_{n0} is the associated dipole-moment matrix element.

According to second-order perturbation theory, the C_6 dispersion coefficient of the dipole-dipole interaction between two isolated particles A and B can be expressed as

$$C_6^{\mathrm{AB}} = \frac{3}{2}\sum_{n,m\neq 0} \frac{f_{n0}^{\mathrm{A}} f_{m0}^{\mathrm{B}}}{\omega_{n0}^{\mathrm{A}}\omega_{m0}^{\mathrm{B}}(\omega_{n0}^{\mathrm{A}} + \omega_{m0}^{\mathrm{B}})}. \tag{3.40}$$

Thus the difficulty of a straightforward evaluation of the perturbation expression arises from the requirement of complete knowledge of all excited states. In practice, a more convenient mathematical form to Eq. (3.40) can be expressed in terms of the dynamic dipolar polarizability, yielding the so-called Casimir-Polder formula [170].

DIPOLAR POLARIZABILITY

Polarizability is an intrinsic property of matter, and it measures the change in the charge distribution of an atom (ion or molecule) with respect to an applied electric field. The quantity of primary interest here is the dipolar polarizability,

the response of the dipole moment to the electric field, from which one can obtain C_6 dispersion coefficients. We note that the field can be either external or internal, stemming from other atoms or electrons inside a molecule or material. For more details, the reader is referred to a comprehensive review article [171].

According to second-order perturbation theory, the average dynamic polarizability is defined as

$$\alpha(i\omega) = \sum_{n\neq 0} \frac{f_{n0}}{\omega_{n0}^2 + \omega^2}, \tag{3.41}$$

where the oscillator strength f_{n0} is given by Eq. (3.39). The above definition allows Eq. (3.40) to be rewritten in terms of dynamic polarizabilities, arriving at the Casimir-Polder formula

$$C_6^{\mathrm{AB}} = \frac{3}{\pi} \int_0^\infty \alpha_{\mathrm{A}}(i\omega)\alpha_{\mathrm{B}}(i\omega)\mathrm{d}\omega, \tag{3.42}$$

where the integrand contains the averaged dipolar polarizability as a function of imaginary frequency.[4] This integral expression is often used as a starting point for developing various approximate methods to determine C_6 dispersion coefficients.

On the experimental side, the dynamic polarizability can be obtained from dielectric-function measurements [172], Rayleigh scattering [173], molecular beam methods [174, 175], and other related methods. Thus an accurate theoretical treatment of the polarizability can improve our understanding of many properties, such as the dielectric constant and the refractive index (see Table 3.1 and more discussion below in Section 3.5). Once the dynamic polarizability and the resulting dispersion coefficients are known, the next question is how to calculate the vdW energy in practical calculations.

Table 3.1: The relationship between the dipolar polarizability α and other physical quantities, where V is the unit-cell volume of a crystal.

Quantity	Relation to α
Dielectric constant, ε	$\frac{\varepsilon-1}{\varepsilon+2} = \frac{4\pi\alpha}{3V}$ *
Refractive index, n	$\frac{n^2-1}{n^2+2} = \frac{4\pi\alpha}{3V}$ *
dispersion coefficient, C_6	Eq. (3.42)

* Valid for dilute systems and ionic and semiconductor solids with cubic symmetry.

[4] The equivalence of Eqs. (3.40) and (3.42) can be obtained by means of the definite integral: $\frac{2}{\pi}\int_0^\infty \frac{ab}{(a^2+x^2)(b^2+x^2)}\mathrm{d}x = \frac{1}{a+b}$.

3.4.2 Inclusion of the long-range vdW energy in DFT

Numerous promising ideas have been proposed for including the vdW energy in DFT calculations motivated by the need to treat large and complex molecular and condensed-matter systems. As discussed in Section 3.3, many commonly used exchange-correlation functionals (LDA, GGAs, etc.) provide a route to the inclusion of electron-correlation effects in an effective way, with a relatively low computational cost. The basic concept for any DFT-based vdW method is to add an additional term that accounts for the missing *long-range correlation energy* to the DFT energy, as simply expressed by

$$E_{\rm tot} = E_{\rm DFT} + E_{\rm vdW}, \tag{3.43}$$

where $E_{\rm DFT}$ is the KS-DFT total energy computed with a given (semi-)local or hybrid XC functional. Many DFT-based vdW methods have been developed, which differ from one another in the way of obtaining the polarizability as well as coupling with the underlying functional. Here we focus on the most widely used methods, namely, RPA, vdW-DF, and DFT+vdW; for an extended discussion, we refer the reader to recent review articles by Grimme [8], Johnson *et al.* [9], Tkatchenko *et al.* [10], and Klimeš and Michaelides [11].

Random-phase approximation

RPA [115–117] explicitly computes the electron correlation energy, and it can be formulated within different theoretical frameworks.[5] Presented here is the formulation based on the adiabatic-connection fluctuation-dissipation theorem (ACFDT), with the RPA correlation energy written on the imaginary frequency axis as follows

$$E_{\rm c}^{\rm RPA} = \frac{1}{2\pi}\int_0^\infty {\rm d}\omega {\rm Tr}\left[\ln(1-\chi^0(i\omega)\upsilon) + \chi^0(i\omega)\upsilon\right], \tag{3.44}$$

where υ is the Coulomb potential, and $\chi^0(i\omega)$ is the non-interacting density response function of the KS system, having an explicit form in terms of single-particle orbitals $\psi_i(\boldsymbol{r})$, orbital energies ϵ_i, and Fermi occupation factors f_i

$$\chi^0(\boldsymbol{r},\boldsymbol{r}',i\omega) = 2\sum_{i,j}(f_i - f_j)\frac{\psi_i^*(\boldsymbol{r})\psi_j(\boldsymbol{r})\psi_j^*(\boldsymbol{r}')\psi_i(\boldsymbol{r}')}{\epsilon_i - \epsilon_j - i\omega}. \tag{3.45}$$

[5] RPA can be derived from many-body perturbation theory or from coupled-cluster theory, which will not be discussed, but redirected to, e.g., a very recent review by Ren *et al.*, Ref. [160].

Within this approach, the XC energy in RPA is obtained by coupling the exact exchange energy together with the RPA correlation energy

$$E_{\mathrm{xc}}^{\mathrm{RPA}} = E_{\mathrm{x}}^{\mathrm{EXX}} + E_{\mathrm{c}}^{\mathrm{RPA}}. \tag{3.46}$$

Note that RPA is very commonly used in a post-processing fashion, that is, the exchange and correlation terms for the RPA total energy are evaluated using KS orbitals (LDA, PBE, etc.).

The inclusion of the correlation energy within RPA can yield better agreement with experiment than (semi-)local functionals. RPA provides excellent bond lengths, very good heats of formation, accurate adsorption and surface energies for some systems [176]. In addition, RPA remedies part of problems associated with LDA or GGAs for cohesive properties of solids, showing the significance of the long-range correlation energy in extended systems. RPA predicts accurate lattice constants and bulk moduli (with MAREs of 0.4% and 4% respectively) for insulators, semiconductors, and metals [107, 108]. Still, several shortcomings of RPA need to be pointed out. Firstly, consistent improvements of all cohesive properties remain a big issue. Although RPA provides a well-balanced description of lattice constants and bulk moduli, cohesive energies are even more underestimated with respect to PBE results (MAE 0.30 eV versus 0.17 eV per atom) [107, 108]. Attempts have been made to go beyond standard RPA (such as RPA+SOSEX [177], RPA+rSE [178], and rPT2 [163]), however, insofar systematic studies on a broad range of materials are still lacking [160, 162]. Furthermore, calculations of RPA and beyond require the evaluation of the KS response function, and thus are more expensive than standard DFT computations.

VDW-DF FUNCTIONAL

The so-called van der Waals density functional (vdW-DF), originally developed by Langreth, Lundqvist and co-authors, aims to approximate the nonlocal correlation energy from the electron density. The growing family of vdW-DFs (vdW-DF-04 [179], vdW-DF-09 or VV09 [180], vdW-DF-10 or vdW-DF2 [181], VV10 [182], etc.) share the same root – the correlation energy is split into two contributions: (i) a long-range part, $E_{\mathrm{c}}^{\mathrm{nl}}$, which is a nonlocal two-point functional of the electron density; (ii) a short-range part from a local or semi-local density functional. In the general vdW-DF framework, the XC energy takes the form

$$E_{\mathrm{xc}} = E_{\mathrm{x}}^{0} + E_{\mathrm{c}}^{0} + E_{\mathrm{c}}^{\mathrm{nl}}, \tag{3.47}$$

where E_x^0 and E_c^0 are the exchange and correlation terms from (semi-)local functionals respectively, and E_c^{nl} is the nonlocal part accounting for long-range vdW interactions. The quantity E_c^0 is typically chosen to give the correlation energy in the uniform density limit. Moreover, E_c^{nl} is constructed to vanish for a uniform electron density, such that no double-counting appears in the UEG limit [179].

The simplest form for the nonlocal correlation energy in vdW-DF reads

$$E_c^{nl} = \frac{1}{2} \iint d\boldsymbol{r} d\boldsymbol{r}' n(\boldsymbol{r}) \phi(\boldsymbol{r}, \boldsymbol{r}') n(\boldsymbol{r}'), \tag{3.48}$$

where the correlation kernel $\phi(\boldsymbol{r}, \boldsymbol{r}')$ depends upon $|\boldsymbol{r} - \boldsymbol{r}'|$, and the charge density and density gradients at $\boldsymbol{r}$ and $\boldsymbol{r}'$. The interaction kernel $\phi(\boldsymbol{r}, \boldsymbol{r}')$ is governed by two properties: at what separation the interaction appears and the difference in electron density at interacting points. Note that the "choice" of the kernel function is one of the most important aspects of the evaluation of different variants of vdW-DFs [182–185]. For the mathematical derivation, we refer the reader to the original papers [182–185], where the numerical evaluation of the kernel function was also discussed.

The vdW-DF functional has a number of features. For instance, the E_c^{nl} term accounts for two-body contributions to the vdW energy at long distances, but neglects non-additive many-body contributions, such as the three-body Axilrod-Teller [45] terms those can become significant in realistic materials [20, 186]. Deriving an expression for the three-body correction is possible, however, at the expense of significantly increased computational cost.

In addition, the accuracy of the vdW-DF framework at short and intermediate ranges depends not only upon the quality of the E_c^{nl} component, but also on the combination of E_x^0 and E_c^0. Improvements have been found when using the vdW-DF-04 functional within revPBE exchange [109], and vdW-DF-10 [181] and VV10 [182] within PW86R exchange.

The nonlocal vdW-DF functional has been applied to a broad range of molecules and materials [187], and has already provided useful predictions for weakly interacting systems, such as molecular complexes, polymer crystals, and molecules adsorbed on surfaces. Recently it has also been examined for bulk crystals [71, 79]. These studies have shown that many challenges still remain, particularly in more complex systems, including solids. For instance, vdW-DFs overestimate lattice constants for solids as well as binding distances for gas-phase dimers in comparison with their experiment, and they underestimate bulk moduli and cohesive energies (only slightly better than

PBE) [71]. In addition, it was found that the errors obtained from various vdW-DF descendants are very sensitive to choices of each terms in the functional form given by Eq. (3.47). While the vdW-DF functional divides the correlation energy into two parts based on particular treatment, other ways of splitting the correlation are also possible.

DFT+VDW

Within this approach, termed as "DFT+vdW", one can write a general form of adding the long-range pair-wise vdW energy to the DFT energy as

$$E_{\mathrm{DFT+vdW}} = E_{\mathrm{DFT}} - \frac{1}{2}\sum_{\mathrm{A}}\sum_{\mathrm{B}} f_{\mathrm{damp}}(R_{\mathrm{AB}})\frac{C_6^{\mathrm{AB}}}{R_{\mathrm{AB}}^6}. \tag{3.49}$$

E_{DFT} is still obtained from standard KS-DFT calculations, employing a local, semi-local or hybrid XC functional. Having determined C_6^{AB} coefficients for interacting atom pair A and B (with an interatomic distance R_{AB}), the leading term of the vdW energy of the system can be estimated as a sum of pair-wise potentials $C_6^{\mathrm{AB}} R_{\mathrm{AB}}^{-6}$ over all interacting pairs. In addition, a damping function f_{damp} is used to avoid singularities at short distances and ameliorate double-counting of correlation at intermediate distances [8–11].

Different variants of the DFT+vdW approach have been proposed, differing in the way they define the damping function or obtain C_6 dispersion coefficients. The most popular ones are those introduced by Grimme (DFT-D1, DFT-D2 and DFT-D3) [70, 188, 189], Becke and Johnson (XDM) [190–192], as well as, Tkatchenko and Scheffler (TS) [22].

In the first two methods by Grimme (DFT-D1/2), the C_6 dispersion coefficients are calculated by making use of ionization potentials and static polarizablities of isolated atoms as inputs [70, 188]. The two main disadvantages of these approaches are the *fixed* dispersion coefficients independent upon chemical environment and the *empirical* parameters invoked in damping functions. The latest version, DFT-D3 [189], was proposed to improve over DFT-D1/2, by using new sets of cutoff radii and dispersion coefficients determined from KS-DFT and time-dependent density-functional theory (TDDFT) calculations. In this approach, the environmental dependence of C_6 coefficients is captured by considering the coordination number of a given atom with its bonding partners. A range of C_6 reference values are precalculated that correspond to different hybridization states for each pair of atoms. Based on the coordination of an atom, the C_6 dispersion coefficient is interpolated

accounting for different chemical environments. Despite the simplicity of this approach, DFT-D3 has been shown to provide reliable dispersion coefficients when applied to small molecular systems. A MARE of 8.4% was found on a database of 174 pairs of molecular C_6 coefficients [189], referenced to data of Meath and co-authors derived from experimental dipole oscillator strength distribution (DOSD) [193–196].

The environmental dependence of dispersion coefficients has also been addressed by Becke and Johnson [190–192, 196, 197] in their exchange-dipole moment (XDM) method. In this approach, dispersion coefficients vary with the chemical environment through the Hirshfeld partitioning (e.g., see Ref. [196–199]) of the dipole-moment density into atomic terms, in combination with the relationship between polarizability and volume. Thus the inputs required in XDM are KS or HF orbitals, the density of a system, and the polarizability of free atoms. The XDM approach has advantages over empirical schemes, with no empirical fitting of C_6 coefficients and a well-defined partitioning scheme using the electron density. The big challenge in the XDM approach is how to precisely quantify atomic volumes and the exchange hole (approximating the XC hole), which are known to affect results to some extent [11, 102, 200, 201]. Nevertheless, the overall accuracy of the C_6 coefficients computed using this model is still reasonable, with a MARE of 12.2% for the 174-pairs molecular C_6 data of Meath and co-workers [189, 196]. In addition to the determination of C_6 coefficients, the damping function remains an empirical component in the XDM method, with one [190, 196] or two free parameters [197]. Concerning the computational cost, calculations with XDM are more demanding compared with the DFT-D-type approaches (similar to the cost with hybrid functionals). This is due to the requirement of HF orbitals (preferable to KS orbitals according to the authors) for evaluating dipole moments.[6]

The approach used in this thesis is the Tkatchenko/Scheffler (TS) [22] method, employing the electron density to evaluate system-dependent C_6 dispersion coefficients for atoms-in-materials. The idea of this method is to compute the relative rather than absolute polarizability and C_6 dispersion coefficients of atoms inside a molecule (or a solid), referenced to highly accurate free-atom values. Similar to the XDM approach, molecular polarizability and C_6 coefficients are decomposed by making use of the Hirshfeld partitioning scheme and the direct relationship between polarizability and volume. The TS

[6]Becke and Johnson [190–192, 196, 197] initially chose to use HF, instead of KS orbitals, with the aim of avoiding the long-range deficiency of LDA and GGAs potentials for evaluating the exchange hole that is sensitive to orbital behavior at long distances.

method computes the vdW energy for atoms in molecules via the summation of pair-wise interactions from the ground-state electron density, thus adding no additional computing time to standard KS-DFT calculations. In the TS scheme, C_6 dispersion coefficients vary according to the chemical environment of atoms in molecules; in particular, hybridization effects are accurately accounted for. This can be shown from its remarkable performance on a database of 1225 intermolecular C_6 coefficients, with a MARE of 5.5% when compared with reliable experimental data [22]. The TS approach can be readily used and compatible with a range of XC functionals (LDA, GGAs, MGGAs, and hybrid functionals). Last but not least, although damping functions remain as a shared "drawback" in the DFT+vdW family of methods, TS is less empirical than other approaches, with only a single adjustable parameter s_R that adapts the damping function to a particular XC functional. As one of the main methods used in this thesis, details of the TS approach will be presented in next section.

3.4.3 The concept of "atoms-in-materials": the TS approach

Adding pair-wise interatomic $C_6 R^{-6}$ terms to the DFT energy was introduced in the previous section, denoted as DFT+vdW in this thesis. A serious shortcoming of many DFT+vdW approaches to the vdW energy is their empirical nature, as the vdW parameters (i.e., the polarizability, the C_6 coefficient, and the vdW radius) do not depend on the electronic structure. To improve this situation, Tkatchenko and Scheffler [22] developed a method to obtain accurate C_6 dispersion coefficients and vdW radii R^0 directly from the ground-state electron density.

The C_6 dispersion coefficient for a pair of spherically symmetric atoms (ions or molecules) A and B can be expressed in terms of frequency-dependent dipolar polarizabilities $\alpha_{\mathrm{A/B}}(i\omega)$ through the Casimir-Polder formula given by Eq. (3.42). Several useful expressions can be derived for C_6^{AB} with a simplified model for $\alpha(i\omega)$. An important derivation is the London formula, expressed in terms of the static polarizability and effective frequency of interacting particles. Using the leading term in the Páde series [202], the polarizability of atom A at imaginary frequencies reads as

$$\alpha_{\mathrm{A}}(i\omega) = \frac{\alpha_{\mathrm{A}}^0}{1 + (\omega/\omega_{\mathrm{A}})^2}, \tag{3.50}$$

where α_{A}^0 is the static polarizability and ω_{A} is an effective frequency. Upon substitution in the Casimir-Polder integral, this yields the London formula [12,

13]

$$C_6^{\mathrm{AB}} = \frac{3}{2}[\omega_{\mathrm{A}}\omega_{\mathrm{B}}/(\omega_{\mathrm{A}} + \omega_{\mathrm{B}})]\alpha_{\mathrm{A}}^0\alpha_{\mathrm{B}}^0. \tag{3.51}$$

For A=B, one finds

$$\omega_{\mathrm{A}} = \frac{4}{3}\frac{C_6^{\mathrm{AA}}}{(\alpha_{\mathrm{A}}^0)^2}. \tag{3.52}$$

Combining Eqs. (3.51) with (3.52) and expressing C_6^{AB} in terms of homomolecular parameters, one arrives at

$$C_6^{\mathrm{AB}} = \frac{2C_6^{\mathrm{AA}}C_6^{\mathrm{BB}}}{(\frac{\alpha_{\mathrm{B}}^0}{\alpha_{\mathrm{A}}^0}C_6^{\mathrm{AA}} + \frac{\alpha_{\mathrm{A}}^0}{\alpha_{\mathrm{B}}^0}C_6^{\mathrm{BB}})}. \tag{3.53}$$

ATOMS-IN-MATERIALS

The TS approach starts from high-level reference data for free atoms taken from self-interaction corrected TDDFT calculations in Ref. [16], and uses the direct relation between polarizability and volume [203] to define vdW parameters for atoms in molecules (or solids). This is achieved by the definition of the effective volume, referenced to free-atom values [22]. Changes in the effective volume rescale the vdW parameters through the Hirshfeld partitioning [196–199] of the electron density for an atom inside a molecule,

$$\begin{aligned} \frac{V_{\mathrm{A}}^{\mathrm{eff}}}{V_{\mathrm{A}}^{\mathrm{free}}} &= \frac{\int r^3 w_{\mathrm{A}}(\boldsymbol{r})n(\boldsymbol{r})\mathrm{d}^3\boldsymbol{r}}{\int r^3 n_{\mathrm{A}}^{\mathrm{free}}(\boldsymbol{r})\mathrm{d}^3\boldsymbol{r}}, \\ w_{\mathrm{A}}(\boldsymbol{r}) &= \frac{n_{\mathrm{A}}^{\mathrm{free}}(\boldsymbol{r})}{\sum_{\mathrm{B}} n_{\mathrm{B}}^{\mathrm{free}}(\boldsymbol{r})}, \end{aligned} \tag{3.54}$$

where $n(\boldsymbol{r})$ is the total electronic density, $n_{\mathrm{A}}^{\mathrm{free}}(\boldsymbol{r})$ is the density of the free atom, $w_{\mathrm{A}}(\boldsymbol{r})$ is the Hirshfeld atomic partitioning weight for a given atom A, r is the distance from the nucleus of atom A, and the sum over B runs over all atoms of the system, taken as free atoms and placed at their positions in the molecule. Both $n(\boldsymbol{r})$ and $n_{\mathrm{A}}^{\mathrm{free}}(\boldsymbol{r})$ are computed from standard DFT calculations. The effective vdW parameters are then determined by making use of the direct

relation between the volume V and the polarizability α

$$\begin{aligned} \frac{\kappa_{\mathrm{A}}^{\mathrm{eff}}}{\kappa_{\mathrm{A}}^{\mathrm{free}}}\frac{\alpha_{\mathrm{A}}^{\mathrm{eff}}}{\alpha_{\mathrm{A}}^{\mathrm{free}}} &= \frac{V_{\mathrm{A}}^{\mathrm{eff}}}{V_{\mathrm{A}}^{\mathrm{free}}}; \\ \frac{\omega_{\mathrm{A}}^{\mathrm{eff}}}{\omega_{\mathrm{A}}^{\mathrm{free}}}(\frac{\kappa_{\mathrm{A}}^{\mathrm{eff}}}{\kappa_{\mathrm{A}}^{\mathrm{free}}})^2\frac{C_{6\mathrm{AA}}^{\mathrm{eff}}}{C_{6\mathrm{AA}}^{\mathrm{free}}} &= (\frac{V_{\mathrm{A}}^{\mathrm{eff}}}{V_{\mathrm{A}}^{\mathrm{free}}})^2; \\ \frac{R_{\mathrm{eff}}^{0}}{R_{\mathrm{free}}^{0}} &= (\frac{V_{\mathrm{A}}^{\mathrm{eff}}}{V_{\mathrm{A}}^{\mathrm{free}}})^{1/3}. \end{aligned} \tag{3.55}$$

In this way, C_6 dispersion coefficients become functionals of the electron density. In the above equations, there are two additional unknowns. First, κ is the proportionality constant between V and α, written as $\kappa_{\mathrm{A}}^{\mathrm{free}}$ and $\kappa_{\mathrm{A}}^{\mathrm{eff}}$ for free atoms and atoms in materials, respectively. Second, ω_{A} is the effective frequency. In the TS method, $\frac{\omega_{\mathrm{A}}^{\mathrm{eff}}}{\omega_{\mathrm{A}}^{\mathrm{free}}}(\frac{\kappa_{\mathrm{A}}^{\mathrm{eff}}}{\kappa_{\mathrm{A}}^{\mathrm{free}}})^2$ is assumed to be unity. It has been shown that this choice is appropriate for a large variety of molecules. A MARE of 5.5% was found for 1225 intermolecular C_6 dispersion coefficients [22], with respect to the values determined from experimental dipole oscillator strength distribution data [193–196]. It is noteworthy that this assumption can be derived from the quantum harmonic oscillator model, which shall be presented in Chapter 6.

The vdW energy and the damping function

Once the polarizability and C_6 dispersion coefficients are determined, the vdW energy can be computed by summing pair-wise interatomic C_6R^{-6} terms over all pairs of atoms. In the TS approach, the vdW energy is written as

$$E_{\mathrm{vdW}} = -\frac{1}{2}\sum_{\mathrm{A}}\sum_{\mathrm{B}} f_{\mathrm{damp}}(R_{\mathrm{AB}}, R_{\mathrm{AB}}^{0})\frac{C_6^{\mathrm{AB}}}{R_{\mathrm{AB}}^6}, \tag{3.56}$$

where R_{AB} is the interatomic distance between atoms A and B, R_{AB}^0 is the vdW radius, C_6^{AB} is the corresponding coefficient, and f_{damp} is the damping function. In principle, the accuracy of any DFT-based vdW method depends solely on the coefficients used and the choice of the damping function. Considering that the C_6 coefficients in the TS approach are calculated from the Hirshfeld-volume partitioning based on the electron density, the damping function is the only ingredient that requires introducing empirical parameters.

There are two reasons for using a damping function in the vdW energy expression. Firstly, the R^{-6} term diverges at short distances. Secondly, although the long-range correlation tail is completely missing, short-range correlation

effects are already contained in local and semi-local density functionals. By using a damping function that equals unity at sufficiently large distances and zero at small distances, double-counting effects are minimized.

There are several damping functions suggested in the literature [38, 70, 188, 189, 195, 204–207], and some representative ones are given in Appendix D. A Fermi-type function is used in the TS method

$$f_{\mathrm{damp}}(R_{\mathrm{AB}}, R^0_{\mathrm{A}}, R^0_{\mathrm{B}}) = \frac{1}{1+\exp[-d(\frac{R_{\mathrm{AB}}}{s_R R^0_{\mathrm{AB}}}-1)]}, \tag{3.57}$$

where R_{AB} is the interatomic distance, $R^0_{\mathrm{AB}} = R^0_{\mathrm{A}} + R^0_{\mathrm{B}}$ is the sum of the effective atomic vdW radii of atoms A and B, and d and s_R are free parameters that need to be chosen.

The vdW radii require a careful treatment, and it should be noted that they are not experimental observables. There is a rigorous theoretical definition for noble-gas atoms, namely that the vdW radius, R^0_{AB}, corresponds to half of the equilibrium distance of a rare-gas dimer where the Pauli repulsion balances the London dispersion attraction. For other elements, consistent definition is to choose the distance where the electron-density contour value of a spherical free atom equals that of the noble-gas atom in the same row of the periodic table, and it will correspond to the vdW radius. This was proposed in the TS method as the free-atom reference for the vdW radius [22].

The d parameter adjusts the damping function's steepness, and has been shown to have a negligible influence on the structural and energetic properties of molecules [70, 188, 189, 205]. A choice of $d = 20$ offers a good compromise and minimizes double-counting effects [22, 70]. The scaling factor s_R adapts the damping function to a particular DFT functional, and is the only freely adjustable parameter in the TS method. The s_R parameter scales vdW radii and reflects the range of the electron correlation covered by a given functional in terms of the distance. The values of s_R coupling to different functionals in the TS method (which were determined from the S22 database [208]) are tabulated in Appendix D.

To summarize, the TS approach computes the vdW energy for atoms-in-materials from the ground-state electron density and accurately includes the local chemical environment by utilizing the Hirshfeld partitioning of the electron density. This method yields remarkably accurate C_6 dispersion coefficients for a diverse range of small molecules (5.5% accuracy). Concerning the computational time, there is a negligible additional cost beyond standard

DFT calculations. However, TS lacks the description of the long-range electrodynamic response, which arises from interactions with more distant fluctuating dipoles and becomes crucial for large systems (including solids) [20]. Nevertheless, the TS method improves the prediction for weakly-bonded small systems over local and semi-local density functionals, and we will show that it is an important first step towards further developments for more complex systems, such as large molecules, bulk solids, and surfaces [20, 72, 209].

3.4.4 Challenges of computing accurate vdW energy

So far the state of the art for the treatment of vdW interactions in DFT has been reviewed, now we shall address the remaining challenges for the three different methods (i.e., RPA, vdW-DF, and DFT+vdW) when applied to solid-state materials. RPA is a natural way for accounting for vdW interactions from many-body theory. RPA calculations suggest that nonlocal correlations are important for accurate predictions in many applications, and their inclusion can yield cohesive properties of solids in better agreement with experiment. However, the improvements are not consistent among the cohesive properties of solids (semiconductors, ionic crystals, and metals) [107, 108]. The high computational cost due to the evaluation of the response function limits its application for large systems, including solids. Turning to vdW-DF family, the big advantage of these methods over other pair-wise approaches is that long-range vdW interactions are included in the XC functional; thus the charge redistribution due to electron correlations is taken into account. Unfortunately, vdW-DFs do not offer a good performance for a wide range of applications, mainly due to the challenge of combining the nonlocal correlation with an exchange functional.

The simplicity and low computational cost of DFT+vdW approaches make them easy to use; thus they have become quite popular [8, 10, 11]. It should be noticed that remarkable performance of DFT+vdW methods (e.g., DFT-D3, XDM, and TS) has been acknowledged on structural and energetic properties for a diverse range of molecular systems. In contrast, knowledge of the use of those methods for condensed-matter materials is rather limited, reflecting the difficulty in obtaining reliable polarizability and C_6 dispersion coefficients for atoms in solids. Within the DFT+vdW framework, it is clear that efforts are required to (i) accurately and efficiently compute environment-dependent vdW coefficients from the electron density of a system; and (ii) employ a damping function that can be related to the electron density (instead of only

being fitted to theoretical data of the S22 test set). In practice, both of these aspects are not trivial for realistic systems. In particular, capturing environment effects in solids requires a proper understanding of the connection between the microscopic polarizability and the macroscopic dielectric properties, which will be the topic of the next section.

3.5 Polarization of a dielectric medium

In classical electromagnetism, electric polarization of dielectrics is the vector field that expresses the shift of dipoles in response to an applied electric field. When a dielectric is placed in a time-dependent external field, the medium will adapt to the perturbation by varying the positions of positive nuclei and negative electrons. The resulting displacement generates electromagnetic fields; thus the system consists of coupled motions of oppositely charged particles. As a consequence, the charge density will be distorted, producing electric polarization. Polarization describes how a material responds to an applied electric field and the way the material influences the electric field, and thus can be used to study the forces that result from this response acting on constituent atoms of the dielectric material [210]. This phenomenon is known as dielectric polarization and the reader is referred to standard textbooks, e.g., by Jackson [211], and lecture notes by Dresselhaus [212] for a detailed discussion.

3.5.1 Electric polarization in Maxwell's equations

Electric polarization ($\mathbf{P}$)

Supposing a dielectric medium contains many particles (atoms or molecules) in an average continuum approximation for describing the polarization and no multipole moment is present. By definition, the electric dipole moment induced per unit volume of the dielectric is called the electric polarization (or polarization density, or simply polarization) of the dielectric

$$\mathbf{P}(\boldsymbol{r}) = \sum_i N_i \langle \mathbf{p}_i \rangle, \tag{3.58}$$

where $\mathbf{p}_i$ is the dipole moment of the i^{th} type of individual particle in the dielectric medium, the average is taken over a small volume centered at position $\boldsymbol{r}$ and N_i is the average number per unit volume of the i^{th} type of particle at the point $\boldsymbol{r}$.

In practice, it is necessary to establish a connection between the applied

electric field **E** producing the polarization **P** and the resulting magnitude of the polarization. In a homogeneous and isotropic dielectric medium, a linear relationship exists between them, with a coefficient of proportionality

$$\mathbf{P} = \chi_e \mathbf{E}. \tag{3.59}$$

The coefficient χ_e is called the electric susceptibility of the medium, and it is time-dependent quantity and can be related to the relative permittivity via

$$\varepsilon = 1 + 4\pi\chi_e. \tag{3.60}$$

Electric displacement (D)

The electric displacement is a quantity that is used to connect the polarization or electric susceptibility with the macroscopic Maxwell's equations, and its definition is given by

$$\mathbf{D}(\boldsymbol{r}) = \mathbf{E}(\boldsymbol{r}) + 4\pi\mathbf{P}(\boldsymbol{r}). \tag{3.61}$$

Together with Eqs. (3.59) – (3.61), one arrives at the expression of **P** in terms of **E** at position $\boldsymbol{r}$:

$$\mathbf{P}(\boldsymbol{r}) = \frac{\varepsilon - 1}{4\pi}\mathbf{E}(\boldsymbol{r}). \tag{3.62}$$

Dielectric function (ε) and atomic polarizability (α)

The above relations deal with the polarization density and the relative permittivity (also called the dielectric constant for the static zero-frequency value) in terms of the applied macroscopic electric field. The relative permittivity is a function of the frequency of the applied field, also called the dielectric function $\varepsilon(\omega)$.[7] In general, the fundamental electronic excitation spectrum of a substance is described in terms of the complex frequency-dependent dielectric function given by

$$\varepsilon(\omega) = \varepsilon_1(\omega) + i\varepsilon_2(\omega). \tag{3.63}$$

Either the real part or the imaginary part contains all the desired response information, as they can be related to each other by the causality condition: the real part of the dielectric function in the imaginary frequency axis *iu* can be

[7] Here the spatial arguments are omitted for simplicity.

obtained by performing the Kramers-Kronig transformation

$$\varepsilon_1(iu) = 1 + \frac{2}{\pi}\int d\omega \frac{\varepsilon_2(\omega)}{\omega^2 + u^2}, \tag{3.64}$$

under the condition that the absorption spectra has been measured or calculated over a large enough spectral range.

The microscopic counterpart to the relative permittivity is the polarizability α, defining the induced dipole moment in response to the electric field that produces the dipole moment. For instance, if the electric dipole moment induced at atom i is proportional to the electric field $\mathbf{E}$, the coefficient gives the atomic polarizability

$$\mathbf{p}_i = \alpha_i \mathbf{E}. \tag{3.65}$$

For a crystal of N atoms in a unit volume V, supposing that the average continuum of polarization is valid (as introduced in the beginning) one can then write the polarization density as

$$\mathbf{P} = \sum_{i=1}^{N} \mathbf{p}_i / V = \sum_{i=1}^{N} \alpha_i \mathbf{E}/V. \tag{3.66}$$

Polarization is an intrinsic property of matter, and it plays a very important role in evaluating many properties, including polarizability, dielectric constant, refractive index, and dispersion coefficients. It should be remarked that a proper connection is required between the polarizability and the dielectric function, such that a bridge between macroscopic and microscopic scales can be built. To achieve this target, one has to look at the macroscopic and microscopic fields that act on a particle in an actual material.

3.5.2 Local field and the Clausius-Mossotti relation

In a dielectric medium, an individual particle (atom, ion, or molecule) not only feels the external macroscopic field, but also the internal microscopic field generated by the dipoles induced by the electric field coming from other particles. The effective electric field, the macroscopic field plus the fields from all other dipoles, is frequently called the local field, $\mathbf{E}^{\mathrm{loc}}$, and the proper evaluation of this is crucial for studying the interactions between constituent atoms in a molecule or a crystal.

Considering a crystal of N polarizable atoms with the unit-cell volume V subject to an external field $\mathbf{E}$, the local field acting on atom i at position $\boldsymbol{r}$ can be

expressed as a summation of two components

$$\mathbf{E}_i^{\mathrm{loc}}(\boldsymbol{r}) = \mathbf{E}(\boldsymbol{r}) + L\mathbf{P}(\boldsymbol{r}), \tag{3.67}$$

where $\mathbf{P}$ is the polarization density, i.e., the dipole moment per volume given by Eq. (3.58). The constant L is known as the Lorentz factor, which is related to ionicity and crystal symmetry and varies from 0 to $4\pi/3$, yielding the two limits for the relation between the dipolar polarizability α and the dielectric function ε. In the case $L = 0$, in which the local field is simply the macroscopic applied electric field in the medium, gives rise to the Drude-Sellmeier model; and substituting Eq. (3.66) with Eq. (3.62), one finds the polarizability for the unit cell of a crystal in terms of the dielectric function as

$$\frac{\alpha}{V} = \frac{\mathbf{P}}{\mathbf{E}} = \frac{\varepsilon - 1}{4\pi}. \tag{3.68}$$

In the case $L = 4\pi/3$, which yields the local field $\mathbf{E}^{\mathrm{loc}} = \mathbf{E} + 4\pi\mathbf{P}/3$, the Clausius-Mossotti (CM) relation is recovered

$$\frac{\alpha}{V} = \frac{\mathbf{P}}{\mathbf{E}^{\mathrm{loc}}} = \frac{3}{4\pi}\frac{\varepsilon - 1}{\varepsilon + 2}. \tag{3.69}$$

It has been shown in numerous studies of the local field,[8] that Eq. (3.68) is valid for free electrons in a metal, which can be qualitatively understood by the fact that a free electron has a uniform charge distribution and therefore can merely feel the average field in a dielectric medium. In contrast, Eq. (3.69) is exact for non-overlapping atoms in cubic solids.

In the following, we derive the Clausius-Mossotti relation[9] between microscopic polarizability α and the dielectric function ε. In doing so, the so-called *Lorentz sphere*, a sphere large enough to contain sufficiently many neighboring atoms but small compared with the wavelength of electromagnetic radiation, is employed, as depicted in Fig. 3.1. Thereby, the electric field that an individual atom feels in a dielectric medium can be divided into two regions: the nearby region within the sphere and the far away region that can be described by a continuous medium. Based upon this consideration, one can

[8] Among these we would like to mention the work by Mott [213, 214], Darwin [215, 216], de Wette [217, 218], and Tessman [26].

[9] Also known as Lorentz-Lorenz formula, when the polarizability is formulated in terms of the refractive index n by making use of the relation $n = \sqrt{\varepsilon}$.

divide the local field given by Eq. (3.67) into three components

$$\mathbf{E}^{\text{loc}} = \mathbf{E} + \mathbf{E}_{\text{in}} - \mathbf{E}_{\text{sph}}. \tag{3.70}$$

This first component $\mathbf{E}$ is the applied macroscopic electric field, containing all external sources of the applied field and the field due to the surface charge density outside the sample. The second term $\mathbf{E}_{\text{in}}$ arises from the induced dipoles inside the sphere and can be taken into account through a dipole-interaction term. The last component $\mathbf{E}_{\text{sph}}$, frequently called Lorentz (cavity) field, is considered to eliminate the contribution from the continuous dielectric medium within the cavity by subtracting a term due to the polarization of a spherical medium. If one treats the polarized elements as point dipoles and assumes a lattice of cubic symmetry, $\mathbf{E}_{\text{sph}}$ will be the macroscopic field due to a uniformly polarized medium, with the magnitude $4\pi\mathbf{P}/3$. The above assumption of cubic symmetry at each lattice site, makes the contribution from nearby dipoles within the sphere cancel out, so that $\mathbf{E}_{\text{in}} = 0$. Now, the local field in a dielectric medium can be expressed as

$$\mathbf{E}^{\text{loc}} = \mathbf{E} + \frac{4\pi}{3}\mathbf{P}, \tag{3.71}$$

which leads to the well-known Clausius-Mossotti equation, also called the Lorentz-Lorenz relation. Note that the above expression for the local field is just reformulating Eq. (3.67) with the Lorentz factor $L = 4\pi/3$ being equal in all directions. It has been extensively shown that the CM relation is very successful for connecting macroscopic and microscopic properties [18, 26, 62, 63, 67, 219–221]. Most calculations in non-metallic solids use the Lorentz effective field, and many properties of solids, e.g., lattice vibrations and oscillator strengths in ionic crystals, depend on the magnitude of the effective field.

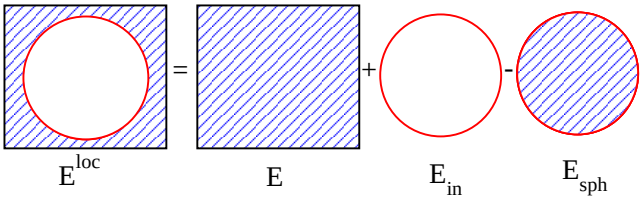

Figure 3.1: Contributions to the local field acting on a particle (atom, ion, or molecule) inside in a cavity surrounded by a continuous dielectric medium: the macroscopic electric field $\mathbf{E}$ from the dielectric medium, the microscopic field due to all other particles inside the cavity $\mathbf{E}_{\text{in}}$, and the "double counting" field due to the dielectric medium within the cavity $\mathbf{E}_{\text{sph}}$.

The validity of the use of the CM relation for obtaining microscopic

properties has been debated for a long time when applied to realistic solids. The CM relation clearly fails in the case of free electrons in a metal, where instead one must employ the Drude-Sellmeier model given by Eq. (3.68). Another issue arises from the fact that most solids, even non-metallic ones, do not obey the point dipole or cubic symmetry assumptions used in the derivation of the CM relation. In particular, Mott [213, 214], Darwin [215, 216], Bonneville [222–224], and many others, have argued that the overlap of electronic charge distributions will lead to reduction of the Lorentz factor L from $4\pi/3$. In this thesis, we will present a benchmark study for several cubic solids, ionic crystals (NaCl and MgO) and semiconductors (C, Si, Ge, and GaAs), using time-dependent DFT calculations to obtain the optical spectra and the dielectric function. By applying the CM relation to all solids studied, the frequency-dependent polarizabilities can be calculated. Our purpose is to examine the applicability of the CM equation in covalently-bonded solids, where the overlap (hybridization) is important. We will show that the CM relation holds for all of the systems considered, and detailed results will be discussed in Chapter 5.

Although numerous studies (including this thesis) have shown the success of using the Clausius-Mossotti relation for describing many properties of non-metallic materials, one may immediately note that the calculation of the Lorentz field relies upon the assumption of point dipoles within a cubic lattice, limiting the transferability to more general materials, such as non-cubic crystals [217]. Further aim of this work is thus to develop a method that can generalize the CM model to treat non-cubic solids. This can be accomplished from the microscopic equations for interacting dipoles.

According to classical electrodynamics, the polarization density (dipole moment per unit volume) in a system of N polarizable atoms interacting with an applied electric field $\mathbf{E}$ satisfies the equation

$$\mathbf{P}(\boldsymbol{r}) = \alpha(\boldsymbol{r})\mathbf{E} + \alpha(\boldsymbol{r}) \int \mathbf{T}(\boldsymbol{r} - \boldsymbol{r}')\mathbf{P}(\boldsymbol{r}')\mathrm{d}\boldsymbol{r}'. \tag{3.72}$$

Explicitly, the induced dipole moment μ_i at atom i is given by

$$\mu_i = \alpha_i[\mathbf{E}_i + \sum_{i \neq j}^{N} \mathbf{T}_{ij}\mu_j], \tag{3.73}$$

where $\mathbf{E}_i$ is the constant applied electric field, α_i is the dipolar polarizability tensor of atom i. The dipole-dipole interaction tensor (or propagator) $\mathbf{T}_{ij}$ is

defined as

$$\mathbf{T}_{ij} = \nabla_{\boldsymbol{r}_i} \otimes \nabla_{\boldsymbol{r}_j} V(r_{ij}), \tag{3.74}$$

where $V(r_{ij})$ is the Coulomb potential at the distance r_{ij} between atoms i and j, and $\boldsymbol{r}_i$ and $\boldsymbol{r}_j$ are their corresponding positions. One of the aims of the microscopic theory is to find an expression for the dipole interaction tensor valid for model charge distributions. In this thesis, we shall present a method based on classical electrodynamics, in which the dipolar polarizability is defined by modeling the interaction between a collection of coupled quantum harmonic dipole oscillators. This will be the subject of Chapters 6 and 7.

3.5.3 Model for cluster polarizability

An alternative way of computing the polarizability for atoms-in-materials is to use the cluster extrapolation (CE) model, in which the polarizability is defined in terms of *atoms*, instead of *unit cells*, as in the CM approach. This can be achieved by performing cluster calculations within the framework of TDDFT.

van der Waals interaction between two clusters

The ingredients in determining dispersion coefficients for atoms in molecules or solids have been introduced in Section 3.4.3, as given by Eqs. 3.50 – 3.53. An extension to the case between large molecules or clusters would be to sum over contributions from individual polarizable entities by using the approximation of additivity for the screened polarizability [225, 226].

Additivity procedure

The total molecular polarizability is frequently approximated by summing over the contributions from individual entities, e.g., covalent bonds or atoms. We shall illustrate this procedure for silicon to derive the general expressions for inter-cluster dispersion coefficients. In the case of a finite cluster cut from Si bulk (A4-diamond structure) and saturated with hydrogen atoms, symbolized as $\mathrm{Si}_i\mathrm{H}_j$, there are four types of tetra-coordinated silicon atoms, the "bulk-like" silicon atoms, and surface silicon atoms bonded to one, two, or three H atoms. To model bulk properties, one needs to use a cluster that contains sufficient "bulk-like" silicon atoms. One can employ an additivity procedure to estimate the static polarizability [225, 226], i.e., the total polarizability of the cluster is given by the sum over the contributions from the averaged individual components. Therefore the total static polarizability of a semiconductor cluster

Si_iH_j can be written as

$$\alpha^{\text{cluster}} \simeq i\,\overline{\alpha_{\text{Si}}} + j\,\overline{\alpha_{\text{H}}}, \tag{3.75}$$

where *i* and *j* are the numbers of Si and H atoms in the cluster, respectively, and $\overline{\alpha_{\text{Si}}}$ and $\overline{\alpha_{\text{H}}}$ denote the average static polarizabilities.

In second-order perturbation theory, the C_6 coefficients are additive [15], and the inter-cluster coefficient is then expressed by the sum of all interatomic contributions

$$C_6^{\text{cluster}} = \sum_{\text{A}} \sum_{\text{B}} C_6^{\text{atom}}. \tag{3.76}$$

Combining with the Casimir-Polder integral, one finally arrives at

$$C_6^{\text{cluster}} = i^2 C_6^{\text{SiSi}} + j^2 C_6^{\text{HH}} + 2ij C_6^{\text{SiH}}, \tag{3.77}$$

with

$$C_6^{\text{SiH}} = \frac{2C_6^{\text{HH}} C_6^{\text{SiSi}}}{(\frac{\alpha_{\text{Si}}}{\alpha_{\text{H}}} C_6^{\text{HH}} + \frac{\alpha_{\text{H}}}{\alpha_{\text{Si}}} C_6^{\text{SiSi}})}. \tag{3.78}$$

On the basis of the above Eqs. (3.75) – (3.78), the atomic static polarizability, together with the C_6 dispersion coefficients between, e.g., Si atoms, can be extracted by performing TDDFT calculations for a set of clusters. In this thesis, calculations are performed for C, Si, and Ge clusters using the CE approach, and technical details and corresponding results shall be presented in Chapter 5.

3.6 Time-dependent density-functional theory

3.6.1 Time-dependent Kohn-Sham formalism

Time-dependent density-functional theory extends ground-state DFT to the treatment of time-dependent properties, including excitations. The time-dependent analogue of the Hohenberg-Kohn-Sham theory was first formally developed by Runge and Gross in 1984 [227]: in a time-dependent quantum problem, all observables are functionals of the time-dependent electron density $n(\boldsymbol{r}, t)$ (under certain conditions), which is known as the Runge and Gross (RG) theorem. For the formal derivation we refer the reader to the original paper [227] and textbooks [228–230].

The time-dependent electronic Schrödinger equation is written as

$$i\frac{\partial}{\partial t}\Psi(\boldsymbol{r}, t) = \hat{H}(\boldsymbol{r}, t)\Psi(\boldsymbol{r}, t), \tag{3.79}$$

in which the Hamiltonian and wave function evolve with time. The RG theorem

implies there is one-to-one correspondence of the time-dependent external potential and time-dependent density, by which one can construct the time-dependent KS equation

$$i\frac{\partial}{\partial t}\psi_i(\boldsymbol{r},t) = \left(-\frac{1}{2}\nabla^2 + v_{\text{eff}}^{\text{TD}}(\boldsymbol{r},t)\right)\psi_i(\boldsymbol{r},t), \tag{3.80}$$

where $v_{\text{eff}}^{\text{TD}}$ is the effective single-particle potential extended from Eq. (3.24) and evolving with time

$$v_{\text{eff}}^{\text{TD}} = v_{\text{H}}(\boldsymbol{r},t) + v_{\text{xc}}(\boldsymbol{r},t) + v_{\text{ext}}(\boldsymbol{r},t). \tag{3.81}$$

The time-dependent density can thus be computed from the time-dependent KS orbitals by solving Eq. (3.80), $n(\boldsymbol{r},t) = \sum|\psi_i(\boldsymbol{r},t)|^2$. As in the static DFT case (see Section 3.3), the exact functional form of the time-dependent exchange-correlation potential,

$$v_{\text{xc}}(\boldsymbol{r},t) = \frac{\delta E_{\text{xc}}[n(\boldsymbol{r},t)]}{\delta n(\boldsymbol{r},t)}, \tag{3.82}$$

is unknown, and thus has to be approximated. The first and simplest functional is the adiabatic local-density approximation (ALDA), where the value of potential v_{xc} at position $\boldsymbol{r}$ and time t is equal to that of a static UEG at that time, with density $n(\boldsymbol{r},t)$. This approximation can also be extended to adiabatic GGA, MGGA, and hybrid functionals [231].

One of the most prominent applications of TDDFT is to calculate excited-state energies of atoms, molecules, and solids, based on the linear response of the system to a time-dependent electric field, that is, how the electron density changes in response to time-varying external potential. This allows the treatment of response properties such as dynamic polarizabilities and thus dispersion coefficients as well. Practical calculations employ the adiabatic approximation, and almost all use the same approximation of the XC potential for both the ground-state and the excited-state calculations. Thus the accuracy of any TDDFT calculation is also limited by the approximation used for the XC functional.

3.6.2 Linear-response theory

The key quantity in the linear-response theory is the response function $\chi(\boldsymbol{r},\boldsymbol{r}',t-t')$, which describes the change of the density δn at $(\boldsymbol{r},t)$ in response

to a small change of the external potential δv_{ext} at $(\boldsymbol{r}', t')$

$$\begin{aligned} \delta n(\boldsymbol{r}, t) = \iint \chi(\boldsymbol{r}, \boldsymbol{r}', t - t') \delta v_{\text{ext}}(\boldsymbol{r}', t') \mathrm{d}\boldsymbol{r}' \mathrm{d}t'; \\ \chi(\boldsymbol{r}, \boldsymbol{r}', t - t') = \frac{\delta n(\boldsymbol{r}, t)}{\delta v_{\text{ext}}(\boldsymbol{r}', t')}. \end{aligned} \tag{3.83}$$

In the KS TDDFT framework, δv_{ext} is substituted using the effective time-dependent potential $\delta v_{\text{eff}}^{\text{TD}}$ (defined by Eq. (3.81)) evaluated to first order in the perturbing potential

$$\delta v_{\text{eff}}^{\text{TD}}(\boldsymbol{r}, t) = \delta v_{\text{H}}(\boldsymbol{r}, t) + \delta v_{\text{xc}}(\boldsymbol{r}, t) + \delta v_{\text{ext}}(\boldsymbol{r}, t), \tag{3.84}$$

and the density response function is rewritten as

$$\chi_{\text{KS}}(\boldsymbol{r}, \boldsymbol{r}', t - t') = \frac{\delta n(\boldsymbol{r}, t)}{\delta v_{\text{eff}}^{\text{TD}}(\boldsymbol{r}', t')}. \tag{3.85}$$

In order to relate the KS response to the true response, it is convenient to define an XC kernel as the functional derivative of the time-dependent XC potential with respect to the time-dependent density evaluated at the ground-state density [228]

$$f_{\text{xc}}[n_0](\boldsymbol{r}, \boldsymbol{r}', t - t') = \frac{\delta v_{\text{xc}}(\boldsymbol{r}, t)}{\delta n(\boldsymbol{r}', t')} \, |_{n=n_0} \, . \tag{3.86}$$

Combining Eqs. (3.83) to (3.86) and taking time-frequency Fourier transforms, one arrives at a Dyson-like equation for the interacting response function

$$\begin{aligned} \chi(\boldsymbol{r}, \boldsymbol{r}', \omega) = \chi_{\text{KS}}(\boldsymbol{r}, \boldsymbol{r}', \omega) + \\ \int \mathrm{d}\boldsymbol{r}_1 \mathrm{d}\boldsymbol{r}_2 \chi_{\text{KS}}(\boldsymbol{r}, \boldsymbol{r}_1, \omega) \left(\frac{1}{\boldsymbol{r}_1 - \boldsymbol{r}_2} + f_{\text{xc}}(\boldsymbol{r}_1, \boldsymbol{r}_2, \omega) \right) \chi(\boldsymbol{r}_2, \boldsymbol{r}', \omega), \end{aligned} \tag{3.87}$$

with the independent-particle response function written in terms of the KS energies and orbitals through Eq. (3.45). The previous equation is formally the central equation of TDDFT linear-response theory, with χ_{KS} obtained from the ground-state KS calculation. Thus any evaluation of the true response function of an interacting system will involve a two-step calculation: one first needs to calculate the independent-particle response function, finding all occupied and unoccupied KS orbitals at the ground-state KS potential; afterwards the interacting response function is computed using the Dyson-like equation given by Eq. (3.87) with an approximated XC kernel. In this thesis, we shall focus

on linear-response calculations for two situations: (i) extended systems and (ii) finite systems.

3.6.3 TDDFT IN EXTENDED SYSTEMS

Concerning solids, the optical response properties provide important information, including energy band structure, impurity levels, excitons, lattice vibrations, etc. From experimental measurements, such as transmission, absorption, and reflectivity, one can deduce the frequency-dependent complex dielectric function. On the theory side, it is the microscopic dielectric function $\varepsilon(\boldsymbol{r}, \boldsymbol{r}', \omega)$, which is directly accessible in *ab initio* calculations.

Within the linear-response theory, the inverse of the microscopic dielectric function of a periodic system is linked to the response function (in momentum space)

$$\varepsilon^{-1}_{\mathbf{G},\mathbf{G}'}(\mathbf{q}, \omega) = \delta_{\mathbf{G},\mathbf{G}'} + v_{\mathbf{G},\mathbf{G}'}(\mathbf{q})\chi_{\mathbf{G},\mathbf{G}'}(\mathbf{q}, \omega), \tag{3.88}$$

where $\mathbf{q}$ is a vector in the first Brillouin zone, $\mathbf{G}$ and $\mathbf{G}'$ are reciprocal lattice vectors, and v is the bare Coulomb interaction. In a long-wavelength limit ($\mathbf{G} = \mathbf{G}' = 0$), the macroscopic dielectric function $\varepsilon_{\mathrm{M}}(\mathbf{q}, \omega)$ can then be obtained by inverting the resulting matrix of the microscopic $\varepsilon^{-1}_{\mathbf{G},\mathbf{G}'}(\mathbf{q}, \omega)$ [232, 233]

$$\varepsilon_{\mathrm{M}}(\mathbf{q}, \omega) = \lim_{\mathbf{q}\to 0} \frac{1}{\varepsilon^{-1}_{00}(\mathbf{q}, \omega)}, \tag{3.89}$$

by which optical phenomena are described.

In a practical calculation, the response function is most readily calculated using Eq. (3.87); the essential ingredient, in addition to the XC functional for the ground-state density, is the XC kernel, f_{xc}, which is defined in Eq. (3.86) and contains all non-trivial many-body effects. The simplest approximation for $f^{\mathrm{ALDA}}_{\mathrm{xc}}$ yields very good results for finite systems, however, it fails to describe absorption spectra of solids, especially for systems such as wide-band gap semiconductors [228–230, 234]. Two reasons typically accounts for this discrepancy: $f^{\mathrm{ALDA}}_{\mathrm{xc}}$ lacks self-energy corrections and excitonic effects (electron-hole interactions), causing a redshift and underestimation of the low-energy part in the spectrum. Within many-body perturbation theory, the *GW* approximation [235] is used to obtain accurate quasiparticle (removal and addition) energies and a subsequent solution of the Bethe-Salpeter equation (BSE) [236] offers a way of including the electron-hole interaction. The above two-step approach leads to much better overall agreement with experiment. However, the two-particle nature of BSE requires solving four-point equation;

thus the calculations are much more demanding than standard KS-DFT. Keeping the efficiency of TDDFT and reproducing reliability of the BSE framework have been of great interest for the calculation of excitations. Several attempts have been made and we refer the reader to Refs. [234, 237–241]. In particular, we would like to mention the nanoquanta kernel (developed by Sottile *et al.* [240]), which includes the long-range contribution (LRC) to the XC kernel and yields considerable success for optical spectra of semiconductors and insulators with bound and strong excitons [231, 242–244]. In this work the optical spectra of small-gap (Si, Ge, and GaAs) and wide-gap (C, MgO, and NaCl) solids have been calculated using TDDFT with the nanoquanta kernel implemented in the computer code Vienna *ab initio* simulation package (VASP) [245, 246] (in collaboration with VASP contributor Joachim Paier [72]), and the computational details and corresponding results will be presented in Chapter 5.

3.6.4 TDDFT IN FINITE SYSTEMS

To obtain response properties of finite systems, the Sternheimer approach [247] is often used. This method is based upon the solution of a set of self-consistent equations for each frequency that only depends on occupied states, and thus has the advantage of making calculations feasible for large systems (see, e.g., Ref. [248–250] for extended discussion). According to perturbation theory, for a given perturbative potential, one can find first-order perturbations to wave functions through solving the Sternheimer equation

$$\left[\hat{H}^{(0)} - \varepsilon^{(0)}\right] \psi^{(1)} = -\left[\hat{H}^{(1)} - \varepsilon^{(1)}\right] \psi^{(0)}, \tag{3.90}$$

where $\hat{H}^{(0)}$ and $\psi^{(0)}$ denote the unperturbed Hamiltonian and wave function, and $\hat{H}^{(1)}$ and $\psi^{(1)}$ are corresponding first-order perturbed quantities. The variation of the electron density can be formulated in terms of the variation of wave functions

$$n^{(1)}(\boldsymbol{r}) = \sum_{m}^{\text{occ.}} \left[\psi^{*(0)}(\boldsymbol{r})\psi^{(1)}(\boldsymbol{r}) + \psi^{*(1)}(\boldsymbol{r})\psi^{(0)}(\boldsymbol{r})\right]. \tag{3.91}$$

Within the TDDFT framework, the frequency-dependent response of Eq. (3.90) is rewritten as

$$\left[\hat{H}^{(0)} - \varepsilon_m \pm \omega + i\eta\right] \psi^{(1)}(\boldsymbol{r}, \pm\omega) = \hat{H}^{(1)}(\pm\omega)\psi^{(0)}(\boldsymbol{r}), \tag{3.92}$$

where ω is the frequency of the perturbative potential, and η is a positive infinitesimal perturbation, which is used for obtaining the correct position of the poles of the response function and thus the polarizability.

The Sternheimer approach has been successfully applied to calculations of static and dynamic properties, such as polarizabilities and vibrational modes. In Section 3.5.3, the cluster extrapolation model has been illustrated for computing the C_6 dispersion coefficient between two finite systems. The cluster calculations have been performed within the Octopus code [251, 252], an open source package for the simulation of both ground-state and excited-state processes. The results will be presented in Chapter 5, together with a comparison with those obtained from the periodic TDDFT calculations using the VASP code.

3.7 PHONONS

A phonon is a quasi-particle representing the quantization of vibrational modes of a crystalline lattice [118]. The study of phonons (or lattice vibrations) is of great importance in solid-state physics [253–255], as it can explain many physical properties of materials, such as sound velocity, thermal properties, elastic properties, etc. Phonons can be understood by perturbing atoms around equilibrium positions $\{\boldsymbol{R}_i^0\}_i$ of the nuclei in the lattice, with the Hamiltonian given by

$$\hat{H} = \sum_i \frac{\hat{p}^2}{2M_i} + \underbrace{E_0 + \frac{1}{2}\sum_{i,j} V(\boldsymbol{R}_i - \boldsymbol{R}_j)}_{\text{adiabatic approximation}}, \tag{3.93}$$

where the last two terms are contributions of the adiabatic potential energy based on the Born-Oppenheimer approximation (see Section 3.1), with $\boldsymbol{R}_i = \boldsymbol{R}_i^0 + \mathbf{u}_i$ representing the position of the i^{th} atom under the displacements $\mathbf{u}_i$. Thus the aim of lattice dynamics is to solve equations of motion for the displacement vectors $\mathbf{u}$.

3.7.1 THE HARMONIC APPROXIMATION

In a crystalline solid, supposing that the amplitude of atomic displacements is small compared with interatomic distances, the potential energy can be expanded in a Taylor series

$$E = E_0 + \sum_{i\alpha} \frac{\partial E}{\partial \mathbf{u}_{i\alpha}} + \frac{1}{2}\sum_{i\alpha,j\beta} \Phi_{i\alpha,j\beta}\mathbf{u}_{i\alpha}\mathbf{u}_{j\beta} + \dots, \tag{3.94}$$

where **u** is the vector of atomic displacement from equilibrium geometry, i and j label atoms, and α and β label Cartesian coordinates. At equilibrium the forces $-\partial E/\partial \mathbf{u}_{i\alpha}$ are zero on all atoms so linear terms vanish; the second-order term $\Phi_{i\alpha,j\beta}$ is the force constant matrix, given as the second derivative $\partial^2 E/\partial \mathbf{u}_{i\alpha}\partial \mathbf{u}_{j\beta}$. Under the condition of small displacements, one can further omit higher terms than second order. This leads to the harmonic approximation (HA) based on the knowledge of just one fundamental matrix, $\Phi_{i\alpha,j\beta}$. One can also define the force constant matrix in reciprocal space and obtain the dynamical matrix, written as

$$D_{i\alpha,j\beta}(\mathbf{k}) = \frac{1}{\sqrt{M_i M_j}} \sum \Phi_{i\alpha,j\beta} e^{-i\mathbf{kR}}. \tag{3.95}$$

Thus properties of phonons in a periodic system can be described by finding eigenvalues of the dynamical matrix D, where phonon frequencies are given by the square root of the eigenvalues

$$\omega^2(\mathbf{k})\mathbf{u}_{i\alpha}(\mathbf{k}) = \sum D_{i\alpha,j\beta}(\mathbf{k})\mathbf{u}_{j\beta}(\mathbf{k}). \tag{3.96}$$

After the frequencies are found, thermodynamic properties are determined using the resulting density of states. For a N-atom harmonic system, the dimension of the dynamical matrix is $3N \times 3N$ at each wavevector **k**, and all wavevectors are coupled, such that the calculation becomes complicated. In practice one often treats lattice vibrations of a crystal in a supercell by making a set of small displacements of the atoms and evaluating the forces exerted on the other atoms.

3.7.2 PHONONS: SUPERCELL APPROACH WITH FINITE DISPLACEMENT

A frequently employed method for calculating phonons of a solid is based on the supercell (direct) method. In this approach, finite displacement calculations are carried out by displacing the atoms in a supercell, which directly give all the elements of the force constant matrix, representing the interactions between pairs of atoms. The relation between forces and force constants can be written as

$$F_{i\alpha} = -\sum_{j\beta} \Phi_{i\alpha,j\beta}\mathbf{u}_{j\beta}. \tag{3.97}$$

As pointed by Kresse and coworkers [256], the practical evaluation of forces within supercell method requires a summation over periodic image cells via Eq. (3.97). Hence, the force acting on an atom i at position α arises from displacements $\mathbf{u}_{j\beta}$ of all supercell atoms, together with those from periodic

images. The phonon frequencies are then obtained from solutions of the eigenvalue problem. Note that a supercell with periodic boundary conditions should be large enough, such that calculations of a dynamical matrix for all atom pairs is sufficient to give phonons at all wavevectors. Thus the supercell size needs to be treated as a convergence parameter in a practical calculation. Moreover, the use of symmetry of crystal, i.e., repeating primitive unit cells, can reduce the number of force evaluations and save computational cost. In *ab initio* calculations, the displacement $\mathbf{u}_{j\beta}$ is taken as an input, and then the forces are computed explicitly.

In this thesis, phonon calculations are performed for a broad range of solids using the methodology introduced above. A specific discussion about the computational settings and the results will be presented in Chapter 4.

3.7.3 The quasi-harmonic approximation

Phonon frequencies are known to be dependent on the unit-cell volume of a crystal, which leads to anharmonicity. In other words, phonons affect the equation of state (energy versus unit-cell volume curve) of a solid. Anharmonic effects can play an important role in many systems [257]; thus one is frequently interested in the influence of lattice vibrations on energy curves $E(V)$. While an explicit evaluation of anharmonic contributions in actual crystals turns out to be very hard, a more feasible way is to employ the quasi-harmonic approximation (QHA) that can account partially for effects of anharmonicity. Here the word "quasi-harmonic" is used for an approximation that introduces volume dependence of phonon frequencies, in which the harmonic approximation is assumed to hold for each volume.

3.7.4 Free energy in the quasi-harmonic approximation

If one aims to evaluate the phonon contribution to the energy at finite temperature, one should employ the Helmholtz free energy. For a solid in the harmonic approximation, the Helmholtz free energy can be expressed as the sum of electronic and vibrational terms relevant to volume and temperature effects

$$F(T,V) = E_0(V) + \underbrace{\frac{1}{2}\sum_i \hbar\omega_i(V) + k_B T \sum_i \ln\left(1 - e^{-\frac{\hbar\omega_i}{k_B T}}(T,V)\right)}_{\text{harmonic approximation}}, \qquad (3.98)$$

where the first term is the internal energy contribution, the second term is the zero-point vibrational energy, and the last term is the vibrational energy at finite temperature. The phonon frequency ω_i, defined in Eq. (3.96), is evaluated at a given volume V for each harmonic vibrational mode i. Knowing the volume-dependent frequency of vibrations, one can determine the equilibrium volume by minimizing the energy. Moreover, many properties of solids, e.g., phonon spectrum and thermal properties, can be obtained.

4 Assessing the performance of density functionals applied to solids

This chapter presents an overview of the description of cohesive properties (including lattice constants, cohesive energies, and bulk moduli) for 64 non-molecular solids using local and semi-local functionals (LDA, PBE GGA, and M06-L meta-GGA), along the three lowest rungs of the "Jacob's ladder" of density functionals [90, 127]. The calculations are carried out using the full-potential all-electron electronic-structure FHI-aims code [21], which employs numeric atom-centered orbitals. We shall first illustrate the influence of the zero-point vibrational energy on the three cohesive properties and show that it can play an important role in certain solids. Then, a detailed discussion of the performance of the three functionals will follow in comparison with reliable reference data from experiment. In particular, these density functionals are examined regarding the correlation of errors between pairs of cohesive properties. While the three functionals yield good performance for certain systems and properties, none of them can be considered reliable for all the investigated solids. We discuss the possible improvements required to increase the reliability of density functionals for solids.

4.1 Motivation

Density-functional theory (DFT) in the Kohn-Sham (KS) framework [89] has proven to be a very useful tool in condensed-matter physics and quantum chemistry [90–93]. In particular, the favorable ratio of accuracy to computational cost makes it a powerful method for predicting a wide

range of ground-state properties of large systems. A great advantage of KS-DFT is that the formalism is in principle exact and the complexity of the many-body problem is replaced by the description of the density-functional approximation (DFA) for the exchange-correlation (XC) energy term. Despite the remarkable success of KS-DFT, approximate density functionals often yield significant deviations from experiment for describing structural, electronic, mechanical, and optical properties of molecules and materials in many situations. Developing reliable and efficient XC functionals that are applicable to a broad range of systems is a great ongoing challenge.

For constructing improved functionals, it is helpful to have a deeper understanding of the errors arising from commonly used DFAs. Cohesive properties (lattice constants, bulk moduli, and cohesive energies) can be used as probes to identify and understand the performance of current functionals applied to solid-state materials. For instance, the local-density approximation (LDA), the generalized gradient approximation (GGA), and the meta-GGA (or MGGA) overall predict reasonable geometries for bulk solids, with an average error of 1–2%, while they can yield large deviations from experiment for both cohesive energies and bulk moduli of solids. It is noteworthy to mention that systematic trends are found behind the errors using these methods. Thus investigating the relationships between errors in different properties can help to improve our understanding of density functionals as well as cohesive properties themselves.

What are some of the challenges in DFT calculations for practical applications in solids? First, lattice constants are systematically underestimated by LDA and overestimated by most GGAs [96–100, 119, 142]. The LDA functional [89] is located on the first rung of "Jacob's ladder" [90, 127]. It is a very successful approximation for many systems, especially for those where the electron density is slowly varying such as semiconductors and transition metals. Still, there are many features that LDA fails to describe. For instance, LDA lattice constants are typically too small, up to 5% when compared with experiment. GGAs are on the next rung of "Jacob's ladder" and are an extension of LDA to account for the nonhomogeneity effects by introducing the gradient of the electron density. They have been successful in improving over LDA for certain properties, e.g., geometries. Most GGAs predict reasonable lattice constants but still overestimate them approximately by 2%.[1]

[1]Reliable lattice constants can be determined experimentally with the relative accuracy less than 0.1%. For instance, the uncertainty for diamond crystal was 1.2×10^{-6}% in a recent X-ray measurement [80].

Another problem of DFT applied to solids is the difficulty for approximate functionals to predict quantitatively reliable cohesive properties uniformly [96–99, 141, 142]. Since the most widely used Perdew-Burke-Ernzerhof (PBE) [94] GGA overcorrects lattice constants with respect to LDA, numerous studies have been performed in the field of functional development for solids in recent years. A simple modification of PBE is the PBEsol functional [140], which differs from PBE only in two parameters and is designed specifically to improve over PBE for equilibrium properties of bulk solids and their surfaces. By restoring the gradient expansion for exchange, PBEsol lattice constants are systematically lower than PBE by 1–2%, however at the expense of cohesive energies being less accurate [98, 99, 136, 141, 142]. The MGGA family [95, 101, 102], located on the third rung of the ladder, is a natural way to improve accuracy further by making use of the kinetic-energy densities, the electron density and its gradient in the XC approximation. For some systems MGGAs can perform well for cohesive properties [96–99, 136, 141]; whereas more generally it has been found that an improvement of the lattice constant is accompanied by a worsening of the bulk modulus, the cohesive energy, or both; overall MGGA functionals produce little improvement over GGAs. The Tao-Perdew-Staroverov-Scuseria (TPSS) functional [95, 135], a non-empirical MGGA method, predicts lattice constants slightly shorter than those of PBE, and the improvement in bulk moduli is rather limited. The revised TPSS (revTPSS) proposed recently [143, 144] alleviates the lattice-constant error, however, both TPSS and revTPSS worsen cohesive energies compared with PBE [119, 136]. In conclusion, no existing LDA, GGA, or MGGA functional is sufficient to accurately describe all the cohesive properties of a broad range of solids at the same time (see Table 4.1).

Two main effects are typically used to explain deficiencies in current local and semi-local functionals: the presence of self-interaction errors (SIE) and the lack of long-range van der Waals (vdW) interactions [90–93]. As already reviewed in Section 3.3, further improvements in functional design can be achieved by developing hybrid functionals and the random-phase approximation (RPA) approach, the fourth and fifth rungs of "Jacob's ladder", respectively. Hybrid functionals have been proposed by adding a fraction of exact exchange to conventional GGAs or MGGAs, aiming at reducing SIE present in semi-local functionals [103, 104]. In particular, range-separation of the exchange interaction has allowed the hybrid scheme to become popular in solid-state physics. HSE06 [150], among the most widely used screened hybrid functionals, often shows superior performance over LDA, GGAs, or MGGAs in describing some bulk properties such as lattice constants and

Table 4.1: The mean error (ME) and mean absolute error (MAE) in theoretical lattice constants a_0 (Å), cohesive energies E_0 (eV/atom), and bulk moduli B_0 (GPa) of bulk solids with respect to their experimental data reported in the literature * using density functional approximations along "Jacob's ladder". The mean relative error (MRE, %) and mean absolute relative error (MARE, %) are given in parentheses, corresponding to the percentage with respect to the experimental cohesive data.

		LDA	PBE	PBEsol	TPSS	revTPSS	HSE06	RPA
a_0	ME	−0.058	0.051	−0.005	0.035	0.014	0.031	0.016
		(−1.3)	(1.0)	(−0.2)	(0.7)	(0.3)	(0.6)	(0.4)
	MAE	0.058	0.055	0.029	0.043	0.032	0.033	0.019
		(1.3)	(1.0)	(0.7)	(0.9)	(0.7)	(0.7)	(0.4)
B_0	ME	24	−2.2	12.6	−4.9	−0.9	−3.8	−1.1
		(15.4)	(−3.4)	(6.0)	(−7.7)	(−4.3)	(−5.0)	(0.4)
	MAE	24.8	12.8	15.8	7.9	8.7	7.3	4.0
		(16.3)	(9.5)	(9.3)	(9.7)	(9.0)	(4.0)	(3.5)
E_0	ME	0.74	−0.15	0.21	−0.11	0.01	−0.23	−0.30
		(18)	(−4.3)	(6.0)	(−2.0)	(1.2)	(−6.1)	(−7.3)
	MAE	0.74	0.17	0.28	0.17	0.21	0.25	0.30
		(18)	(4.5)	(6.5)	(4.7)	(5.7)	(6.5)	(7.3)

* LDA, PBE, and PBEsol lattice constant and bulk modulus data are taken from Ref. [98, 99] (60 solids), and their cohesive energies are from Ref. [108] (24 solids); TPSS and revTPSS data are from Ref. [136] (20 solids), HSE06 are from Ref. [142] (30 solids), and RPA are from Ref. [108] (24 solids).

band gaps [106, 152–158]. However, it cannot treat metallic (including small-gap) systems well and reproduce experimental cohesive energies as well as PBE does [142]. Along "Jacob's ladder" [90, 127], RPA is the only approach that treats the long-range correlation seamlessly. Recent RPA calculations performed by Kresse *et al.* [108] show that a proper treatment of the long-range correlation, which is beyond the reach of LDA, GGAs, MGGAs, and hybrid functionals, can yield rather good agreement with experiment for the cohesive properties of solids. RPA provides a well balanced prediction of lattice constants and bulk moduli for a diverse range of solids (including semiconductors, ionic crystals, and metals), with relative accuracy of 0.4% and 4%, respectively [108]. However, there are also shortcomings using RPA: the computational cost is greatly increased with respect to LDA or PBE [160, 161] and cohesive energies are further underestimated compared with those values obtained from PBE calculations [108].

While common DFAs often yield large deviations of theoretical cohesive properties from experiment, the deviations are not just random and clear systematic trends can be seen for many systems. It was found, particularly along the same series of solids (elements in the same row or column of the

periodic table), the overestimation (underestimation) of lattice constants is linked to the underestimation (overestimation) of bulk moduli, as well as cohesive energies. Grabowski and co-authors [258] have demonstrated the correlation between the deviations from experiment of the lattice constants and the bulk moduli of nine fcc metals (noble metals, together with Al and Pb). Particularly for PBE, an increase of the error with the number of *d* electrons among the 4*d* and 5*d* transition metals is apparent. Grabowski *et al.* proposed an "*ab initio*" error bar, with LDA and PBE being the upper and lower boundaries respectively, with respect to experiment. However, a systematic study is still lacking on the relationships between the deviations for pairs of cohesive properties. Considering the different performance of DFAs applied to different classes of systems, a large solid-state database is required and the analysis of the predictive capability of density functionals should be performed according to the bonding type of solids. Such an analysis could lead to new insights into the cohesion of solids.

Cohesive properties measured in experiment always include vibrational contributions even at 0 K. The nuclear zero-point vibrational energy (ZPVE) effects thus need to be considered for an unbiased comparison between theory and experiment [253–255]. As discussed in Section 2.4, ZPVE influences cohesive properties (lattice constants, cohesive energies, and bulk moduli) of solids, and it is inversely proportional to nuclear mass and most of the time increases the unit-cell volume of bulk crystals [96–98, 119]. It has been shown that the increase of the theoretical lattice constant caused by the ZPVE contribution can be as large as 2% for very light solids such as LiH [142], which is comparable in magnitude to the spread in theoretical calculations and larger than typical uncertainties ($<$0.1%) in experimental measurements.

In this thesis, numerical results of the cohesive properties are reported at the LDA, GGA, and MGGA levels for 64 non-molecular solids with cubic symmetry, covering metals, semiconductors, and ionic crystals, calculated using the all-electron Fritz Haber Institute *ab initio* molecular simulations (FHI-aims) package [21]. It is the first systematic application showing the all-electron accuracy of this code for a broad range of solids. We also investigate the performance of the three functionals used here from the perspective of examining the relationships between the errors in different properties. The MGGA functional we choose is M06-L, which was proposed by Zhao and Truhlar [145] and is designed to incorporate the spin kinetic-energy density in an empirical way in the XC functional. M06-L was reported to outperform other semi-local functionals for a combination of thermochemistry, thermochemical

kinetics, metallochemical and non-covalent interactions, bond lengths, and vibrational frequencies [145, 146]. However, there are very few studies applying this functional to bulk solids; thus it would be useful to know its performance for a wide range of materials, particularly for heavy elements from the third and forth rows of the periodic table. This chapter is organized as follows: Section 4.2 gives the technical details of the calculations performed for this study, including the description of the solid database and computational settings; while Section 4.3 presents the results and discussion.

4.2 TECHNICAL DETAILS

4.2.1 DATABASE

Our database comprises 64 non-molecular solids with cubic structures: 24 metals and 40 non-metals (semiconductors and insulators). The structures cover: A1 (fcc, 13 solids), A2 (bcc, 11 solids), A4 (diamond, four solids), B1 (rock-salt, 16 solids), and B3 (zincblende, 20 solids), as shown in Fig. 4.1. To show trends clearly, we divide the 64 solids into five classes as follows (see Table 4.2): main-group metals (MM), transition metals (TM), simple semiconductors (SC), ionic crystals (IC), and transition metal carbides and nitrides (TMCN). MM includes groups IA and IIA, together with aluminum and lead; TM covers periods 4–7 of the periodic table; SC represents the solids of groups IVA, IIIA–VA, and IIB–VIA; the six ionic crystals are LiCl, LiF, NaCl, NaF, MgO, and MgS; and there are 10 compounds in the TMCN class (TMC and TMN, TM = Ti, Zr, Hf, V, and Nb). The full list of the solids studied here is shown in Tables C.2 to C.7, with the calculated and experimental cohesive data, as well as the relevant literature cited.

Table 4.2: The definitions of five classes of solids are given as main-group metals (MM), transition metals (TM), simple semiconductors (SC), transition metal carbides and nitrides (TMCN), and ionic crystals (IC).

Type of solid	Type of structure	Number of solids
MM	A1, A2	9
TM	A1, A2	15
SC	A4, B3	24
IC	B1	6
TMCN	B1	10

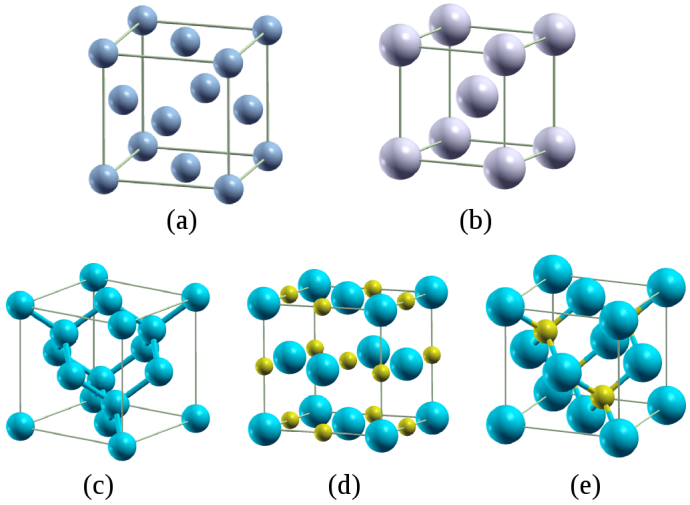

Figure 4.1: The unit-cell structures of (a) A1-fcc, (b) A2-bcc, (c) A4-diamond, (d) B1-rock-salt, and (e) B3-zincblende.

4.2.2 Computational method

All calculations were carried out with the FHI-aims package [21], which implements full-potential, all-electron electronic-structure theory with numeric atom-centered basis functions. For each solid, the equilibrium volume V_0 and bulk modulus B_0 were determined by fitting cohesive energies per unit cell at 7–11 points in a range of $V_0 \pm 20\%$ to a third-order Birch-Murnaghan equation of state (EOS) [88] shown in Eq. (2.9). The unit-cell volumes V are related to the lattice constants a by the expressions $V = a^3/4$ for the fcc, diamond, and zincblende structures, or $V = a^3/2$ for the bcc structure. The cohesive energy, defined as the energy per atom required to atomize the crystal, was evaluated using the LDA, PBE, and M06-L functionals from the energies of the crystal and the constituent free atoms. The spin-restricted formalism was employed for bulk crystals, with two exceptions (the ferromagnetic metals: Fe and Ni), and the spin-unrestricted formalism for open-shell atoms (no fractional occupancies were allowed). A $20 \times 20 \times 20$ $(16 \times 16 \times 16)$ Monkhorst-Pack grid [259] was used in the primitive unit cell of metals (non-metals). The basis sets and k-point meshes in reciprocal space are fully converged. Relativistic effects are more important for heavy elements; here for consistency a scalar-relativistic treatment using the scaled zero-order regular approximation [260] was employed for all solids. It should be pointed out spin-orbit effects (which can be important in open-shell systems) are not included. Philipsen and Baerends [261] have compared the scalar-relativistic and fully relativistic

calculations of the cohesive properties of 11 solids in four columns of the periodic table and found out spin-orbit effects hardly alter cohesive energies, lattice constants, and bulk moduli and the mean absolute contributions are about 0.03 eV, 0.005 Å, and 1 GPa, respectively. They showed that the spin-orbit contributions are non-negligible only for the cohesive energies and the lattice constants of Au and Bi (see Table C.1 of Appendix C). Therefore the scalar-relativistic treatment is sufficient to capture the relativistic effects in most solids considered here.

The FHI-aims all-electron code offers accurate and efficient implementation of DFT with (semi-)local and hybrid functionals to obtain ground-state properties of periodic and cluster systems, up to systems with thousands of atoms [21]. For periodic solids, the performance of FHI-aims can be seen when comparing the present results with those reported using the WIEN2k code [262], which is based upon the full-potential linearized augmented plane-wave and local orbitals method to solve KS equations and is normally regarded as the reference for solid-state studies. For the same database of 55 solids, excellent agreement is found with the reported WIEN2k values using both the LDA and PBE functionals [98, 99], with mean absolute deviations of 0.003 Å for the lattice constants and 0.5 GPa for the bulk moduli. For the analysis of the calculations, the following statistical quantities will be used throughout the work: the mean error (ME), the mean absolute error (MAE), the mean relative error (MRE, in %), and the mean absolute relative error (MARE, in %), all of which are determined by comparing with reliable experimental values measured at low temperatures and/or extrapolated to 0 K.

The phonon calculations were performed using phonopy [253] interface with the FHI-aims package [263] and a work flow of phonon calculations is sketched in Fig. 4.2. The supercell approach was combined with the quasi-harmonic approximation (see Section 3.7), i.e., at a set of volumes harmonic vibrational frequencies are determined using DFT calculations and the resulting zero-point vibrational energies are added to ground-state energies at each volume V. Figure 4.3 shows the effect of zero-point vibrations for the case of diamond. A comparison between PBE and ZPVE-corrected PBE binding curves (energy versus lattice constant) shows, besides a decrease of the cohesive energy, that the zero-point vibrational energy yields an expansion of the lattice constant due to the phonon anharmonicity.

In the FHI-aims package, the force-constant approach is employed to calculate phonon spectra and the vibrational density of state (DOS), $g(V, \omega)$, and

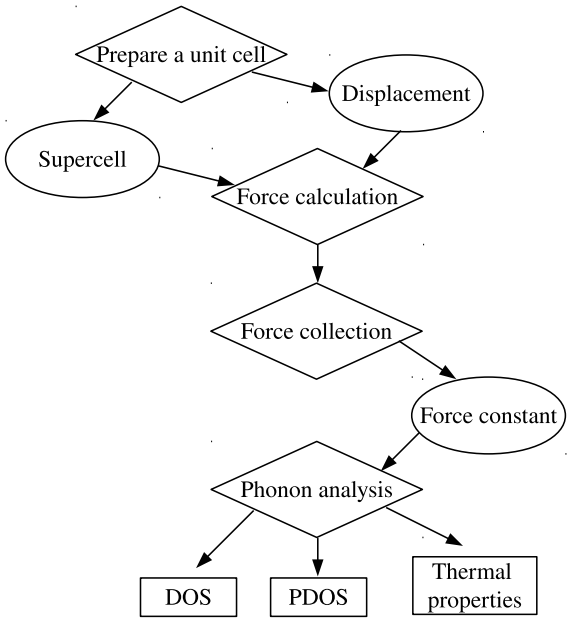

Figure 4.2: A schematic representation of phonon calculations in the framework of phonopy.

ZPVE is estimated as the frequency integration over the vibrational DOS

$$\mathrm{ZPVE} = \frac{1}{2}\int \hbar\omega \mathrm{g}(V,\omega)\mathrm{d}\omega. \tag{4.1}$$

A systematic test on the supercell size was carried out and it is found that a choice of a $2 \times 2 \times 2$ supercell with a $8 \times 8 \times 8$ Monkhorst-Pack grid is sufficient to ensure the convergence of zero-point vibrational energies for all the solids studied here (see an example of diamond bulk shown in Figs. A.3 and A.4). With the finite-displacement approach, one may adjust the value of the small finite displacement δ used to calculate the force response in the three Cartesian directions. From the phonon calculations in this work, it can be concluded that a reasonable variation in δ has only a small impact on the estimated ZPVE. Taking diamond as an example, the change in ZPVE is less than 1×10^{-3} eV/atom when varying δ from 1×10^{-3} to 1×10^{-1} Å, as tabulated in Table A.1. In addition, it was found that the effect of the specific DFT functional on the ZPVE is negligible for these systems; thus the ZPVE was calculated at the PBE level and added on top of the ground-state DFT total energies for all the three functionals.

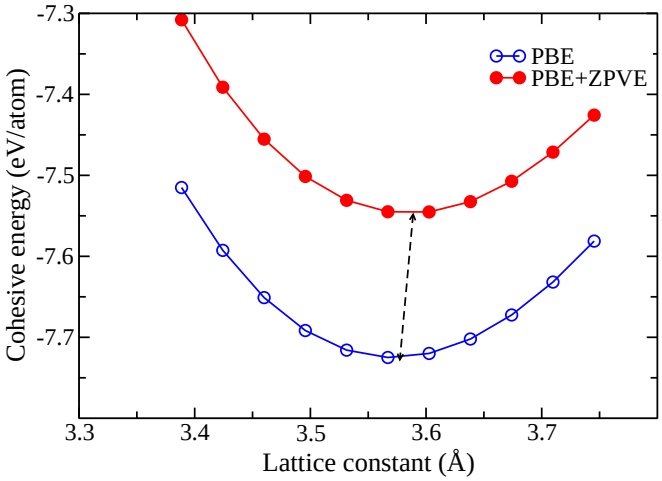

Figure 4.3: Binding curves (cohesive energy versus lattice constant) of the diamond crystal: neglecting zero-point vibrational effects (blue line, empty circles) and including the zero-point vibrational energy (ZPVE, red line, solid circles). The calculations were performed within the PBE functional. The dashed line illustrates the shift in the equilibrium.

4.3 Results and discussion

4.3.1 ZPVE contributions to the cohesive properties

Figures 4.4 and 4.5 show the ZPVE contributions (with respect to experimental cohesive data) to the lattice constants a_0, the cohesive energies E_0, and the bulk moduli B_0 of selected metals and non-metallic solids respectively, together with available theoretical values reported from previous work [141, 142, 264]. A statistical summary is given in Table 4.3 for the 64 solids studied. The results show that including zero-point vibrations has an even stronger effect on the bulk modulus than the lattice constant and the cohesive energy. For 24 metals, the average contributions are about 0.2%, 0.7%, and 1.4% for a_0, E_0, and B_0, respectively. In addition, the ZPVE effect is inversely proportional to nuclear mass, e.g., along the series of Li-Na-Al-K, and is found to be negligible for "heavy" solids. When only considering the "light" metals, located on the second to fourth rows of the periodic table, the averaged contribution is almost twice as large as the value calculated for the whole group of metals. In particular, for bulk Li, the lattice constant expands by 0.7% and the bulk modulus softens considerably by $\sim 4\%$.

For non-metallic solids, ZPVE contributions become more pronounced. A set of 40 solids shows average contributions of 0.3% for the lattice constant, 1.1% for the cohesive energy, and 2.2% for the bulk modulus. For ionic crystals, the effect

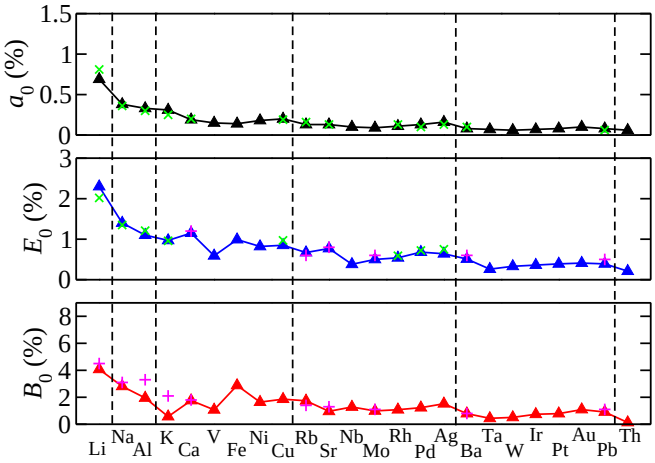

Figure 4.4: Zero-point vibrational contributions to the lattice constants a_0, cohesive energies E_0, and bulk moduli B_0 of selected metals. The values are shown as a percentage with respect to the experimental cohesive properties: solid curves are obtained from the present *ab initio* phonon calculations using the PBE functional, pink pluses are taken from Ref. [264], and green crosses are from Ref. [141]. Dashed lines serve as a guide to the eye.

is particularly strong. The largest contribution occurs for LiF, with changes of ∼1% (0.04 Å) for a_0 and ∼8% (5.6 GPa) for B_0, which are typically more than numerical errors from theoretical predictions, and even might be comparable to the contribution due to long-range correlation interactions [72]. This suggests that for non-metallic solids, especially ionic crystals, the inclusion of ZPVE can become vital for an accurate treatment of systems where long-range vdW forces are of interest.

As confirmed from the present study, ZPVE tends to increase the lattice constant and reduce the bulk modulus and its inclusion improves the predictions of the LDA functional and worsens those of PBE. Thus neglecting zero-point vibrations will lead to a bias in the appraisal of different DFAs. In this thesis, the ZPVE contribution will always be included for the discussion of functional performance.

4.3.2 Performance of LDA, PBE, and M06-L functionals

Having assessed the effect of ZPVE, we can now study the performance of local and semi-local density functionals applied to the 64 solids. The calculated a_0, E_0, and B_0 using the LDA, PBE, and M06-L functionals, together with their experimental values, are tabulated in Tables C.2 to C.7. The statistical data of ME and MAE are shown in Table 4.4 for the three cohesive properties studied here, with the relative errors marked in parentheses. To illustrate the

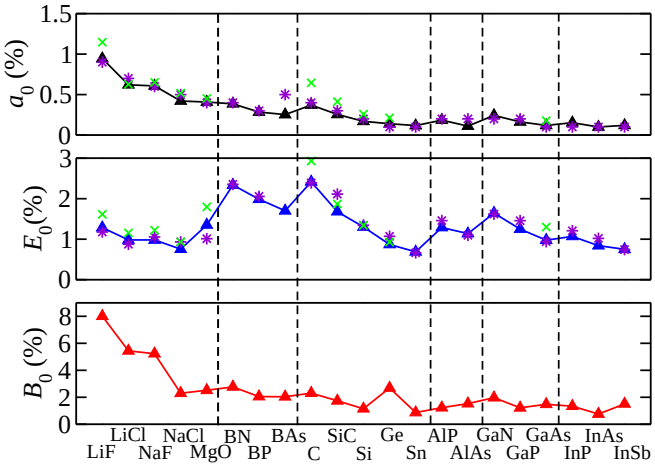

Figure 4.5: Zero-point vibrational contributions to the lattice constants a_0, cohesive energies E_0, and bulk moduli B_0 of selected non-metallic solids. Solid lines are obtained from the present *ab initio* phonon calculations using the PBE functional, green crosses are taken from Ref. [141], and purple stars are from Ref. [142].

Table 4.3: Zero-point vibrational contributions to the lattice constants a_0 (Å), cohesive energies E_0 (eV/atom), and bulk moduli B_0 (GPa) of 64 solids (24 metals, 40 non-metals with six ionic crystals included) using the PBE functional. The values in parentheses are the corresponding percentage with respect to the reported experimental cohesive properties. The 24 metals are divided into two groups: nine elements from periods 2 to 4, and 15 elements from periods 5 to 7 of the periodic table.

	a_0	E_0	B_0
All metals (24)	0.007	0.023	1.53
	(0.17%)	(0.73%)	(1.37%)
Periods 2-4 (9)	0.011	0.029	1.66
	(0.29%)	(1.13%)	(2.07%)
Periods 5-7 (15)	0.004	0.020	1.45
	(0.10%)	(0.47%)	(0.94%)
Non-metals (40)	0.012	0.054	3.39
	(0.25%)	(1.11%)	(2.18%)
Ionic crystals (6)	0.026	0.044	2.86
	(0.55%)	(1.06%)	(4.35%)

performance of the three functionals for different types of solids, we also plot the relative errors in the bulk moduli and the cohesive energies as a function of those in the lattice constants for a given type of solid in Figs. 4.6 and 4.7, respectively. The corresponding MAREs are presented in Table 4.5 in terms of classes of solids, properties, as well as functionals. The data sets shown in these tables and figures shall be used for discussion throughout this chapter.

Let us first discuss the performance of the LDA functional. A well-known

Table 4.4: The mean error (ME) and mean absolute error (MAE) in the calculated lattice constants a_0 (Å), cohesive energies E_0 (eV/atom), and bulk moduli B_0 (GPa) of the 64 solids (24 metals, 34 semiconductors, and six ionic crystals) with respect to experimental data using the LDA, PBE, and M06-L density functionals. The mean relative error (MRE, %) and mean absolute relative error (MARE, %) are given in parentheses, corresponding to the percentage with respect to the reported experimental cohesive properties. All quantities include zero-point vibrational effects.

	ME			MAE		
	a_0	E_0	B_0	a_0	E_0	B_0
LDA	−0.064	0.854	12.66	0.064	0.854	15.85
	(−1.39)	(19.24)	(8.25)	(1.39)	(19.24)	(10.91)
PBE	0.056	−0.120	−10.41	0.062	0.223	14.25
	(1.08)	(−3.06)	(−9.68)	(1.22)	(5.87)	(11.72)
M06-L	0.031	0.174	−4.48	0.074	0.269	12.57
	(0.54)	(6.55)	(−1.98)	(1.41)	(8.88)	(13.43)

trend is confirmed by the current work, namely that LDA underestimates lattice constants, overestimates bulk moduli, and considerably overestimates cohesive energies in most cases. According to the MAREs of the three properties summarized in Table 4.5, one can clearly observe that LDA yields different performance for different classes of solids. For the SC class, it predicts the lattice constants and the bulk moduli in good agreement with experiment, however at the expense of poor prediction of the cohesive energies. In comparison, for metals (groups MM and TM), LDA yields large deviations for all the three properties. The performance for ionic crystals is moderate at the LDA level, when compared with MM and TM.

Turning to the PBE functional, one can see the opposite trend to LDA: the lattice constants are too large, the bulk moduli are too small, and the cohesive energies are underestimated with a MARE of ∼6% (versus ∼20% by LDA) for the 64 solids. Overall, PBE improves the agreement with experiment compared with the LDA functional. In particular for metals, the superiority of PBE over LDA becomes more prominent in the predictions of all three properties. This is important, because LDA is the functional for metallic electrons. Thus real metals are not "ideal". For semiconductors and ionic crystals, PBE yields large deviations from experiment for the lattice constants as well as the bulk moduli, though the cohesive energies are still reasonably predicted at this level. A characteristic feature of the PBE functional found in the current study is the increase of the error with increasing lattice constant, as can be seen, e.g., along the series of C-SiC-Si-Ge-Sn, BN-BP-BAs, and AlP-AlAs-AlSb. For certain systems, the bulk moduli and the cohesive energies follow the same trend, and

further discussion will be presented in Section 4.3.3 for a deeper understanding of errors in the cohesive properties found in (semi-)local DFAs.

Table 4.5: The mean absolute relative error (MARE, %) in the calculated lattice constants a_0, cohesive energies E_0, and bulk moduli B_0 of the 64 solids divided into five classes (see main text for definitions) with respect to experimental data using the LDA, PBE, and M06-L density functionals. All quantities include zero-point vibrations.

	LDA			PBE			M06-L		
	a_0	E_0	B_0	a_0	E_0	B_0	a_0	E_0	B_0
MM	3.08	20.25	13.24	0.88	9.00	5.97	3.04	36.33	31.39
TM	1.66	25.13	17.75	1.04	6.39	8.49	0.95	7.97	9.14
SC	0.63	19.34	4.71	1.61	5.68	16.13	1.74	2.77	13.24
IC	1.51	8.12	8.97	1.87	5.75	14.45	0.27	3.03	4.87
TMCN	1.20	15.95	14.59	0.50	2.84	9.59	0.55	3.76	9.50
All metals	2.19	18.61	16.06	0.98	7.37	7.54	1.73	18.61	17.48
All solids	1.39	19.24	10.91	1.22	5.87	11.72	1.41	8.88	13.43

Turning to the M06-L functional, its overall performance lies between LDA and PBE on the predictions of the cohesive properties. However, no consistent trend can be identified. For most semiconductors, M06-L overestimates the lattice constants and underestimates the cohesive energies as well as the bulk moduli. In particular for main-group metals, M06-L severely overbinds: the lattice constants are too small, and cohesive energies as well as the bulk moduli are too large. For transition metals, the M06-L functional performs equally well as PBE does, as can be seen from Table 4.5. On the other hand, the current work suggests that M06-L significantly improves the performance on the cohesive properties of ionic crystals in comparison with LDA and PBE, and for these systems it slightly overestimates the lattice constants, and reasonably predicts the cohesive energies and the bulk moduli, with the corresponding MAREs of 0.3%, 3%, and 4.9%, respectively.

Figures 4.6 and 4.7 show a comparison of the LDA, PBE, and M06-L functionals for describing the cohesive properties of the five classes of solids. Among the three functionals, LDA predicts the best lattice constants and bulk moduli for semiconductors, however, the cohesive energy remains a big issue at this level, with a MARE of $\sim$20% for the 34 solids in this group. While PBE outperforms LDA on the prediction of the cohesive energies for semiconductors, it worsens both the lattice constants and the bulk moduli. In fact, the improved performance of PBE over LDA can be mainly seen in its better description of the cohesion in the systems having (semi-)metallic nature. As depicted in Figs. 4.6 and 4.7, compared with LDA, all the cohesive

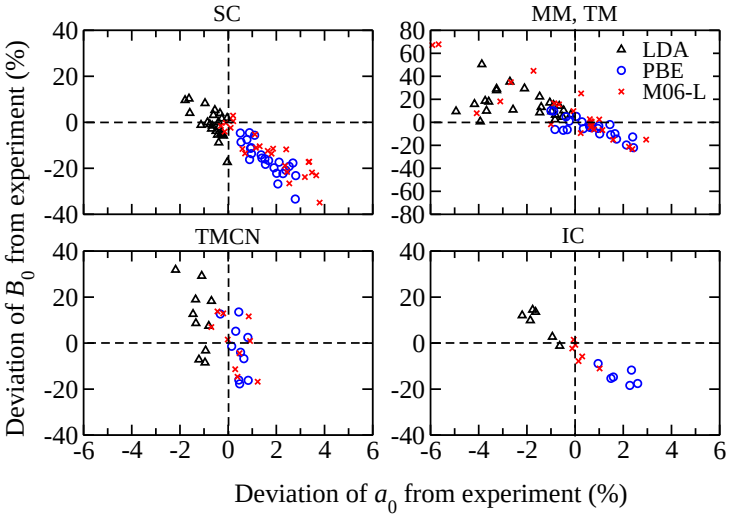

Figure 4.6: Correlation between the deviations of the bulk moduli B_0 (%) and those of the lattice constants a_0 (%) using the LDA, PBE, and M06-L functionals. The definitions of the five classes of solids are given as main-group metals (MM), transition metals (TM), simple semiconductors (SC), transition metal carbides and nitrides (TMCN), and ionic crystals (IC). All quantities include zero-point vibration effects.

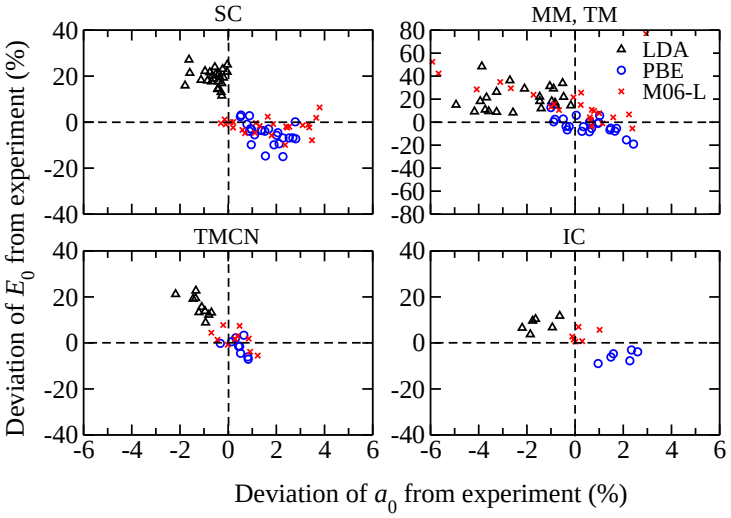

Figure 4.7: Correlation between the deviations of the cohesive energies E_0 (%) and those of the lattice constants a_0 (%) using the LDA, PBE, and M06-L functionals.

properties obtained from PBE are in much better agreement with experiment for the MM, TM, and TMCN groups. On the other hand, the M06-L MGGA functional also improves over LDA for TM and TMCN (though its performance is slightly worse than PBE). However, M06-L yields significant deviations from experiment for the main-group metals, in consistent with the study by Truhlar and coworkers [146]. The MAREs are calculated to be about 3%, 36%, and

31% for the lattice constants, cohesive energies, and bulk moduli, respectively, as given in Table 4.5. Thus it can be concluded that the M06-L functional outperforms LDA for the systems in which a "mixed" bonding nature (metallic, covalent, and/or ionic) becomes prominent in their cohesion (e.g., TM and TMCN). In comparison with PBE, an improved performance of M06-L is found for light-mass semiconductors. For instance, for the light solids (such as C, Si, BN, BP, and AlP), the cohesive properties obtained from M06-L are in good agreement with experiment; in particular, the bulk moduli are as good as the LDA values, whereas PBE yields the worst performance among the three functionals; and the cohesive energies are greatly improved at the M06-L level, compared with the LDA results. When going to heavier systems, one can hardly find any improvement by using M06-L over PBE. This can be seen for the case of GaSb, InSb, ZnTe, CdTe, etc., where M06-L yields worse predictions than PBE. Note that similar performance can also be observed for the ionic crystals. The M06-L MGGA functional significantly improves the description for the six ionic compounds that have medium mass, with a MARE of only 0.3% for the lattice constants versus those of 1.5% and 1.9% by LDA and PBE, respectively. Our study suggests a diverse performance of (semi-)local DFAs on the cohesive properties, strongly dependent upon the bonding nature of the solid considered. Further discussion shall be focused on the relationship between pairs of the cohesive properties, that is, a_0/B_0 and a_0/E_0.

4.3.3 Correlations between the errors in cohesive properties

Much attention has been paid in the literature to the understanding of relationships of the cohesive energy and the bulk modulus with geometrical properties of various types of solids. It is well established that the equilibrium cohesive energy and the bulk modulus are inversely related to the lattice constant (or the nearest-neighbor distance), as depicted in Figs. 2.2 and 2.3. The inverse relation can be explained by the volume dependence of the total energy (the equation of state) causing a monotonous decrease of bulk moduli with increasing volume. There are some analytical expressions reported in the literature for several families of cubic solids, e.g., simple semiconductors (groups IVA, IIIA–VA, and IIB–VIA), ionic crystals (groups IIA–VIA and IA–VIIA), and metals (groups IA and IIA, and noble metals), based upon empirical approaches. Despite the fact that empirical methods are often not able to yield highly accurate results, they can still be very useful, particularly for illustrating trends in properties of a wide variety of materials.

According to the empirical expressions of $E_0 d \approx$ constant and $B_0 d^x \approx$ constant given by Eqs. (2.4), (2.6), and (2.7),[2] it can be seen that the overestimation (underestimation) of the lattice constant (nearest-neighbor distance) should correspond to the underestimation (overestimation) of the bulk modulus or the cohesive energy. As a matter of fact, overall all commonly used DFAs can predict this trend (see Table 4.1). In contrast, whether (and how) errors between theory and experiment in those properties can be linked to one another or not is much less known and remains an interesting question.

Figures 4.6 and 4.7 show the relative errors in the bulk moduli and the cohesive energies as a function of those in the lattice constants, using the LDA, PBE, and M06-L functionals for the 64 solids divided into five classes. It can be seen that most data points fall in the quadrants II and IV of the Cartesian plane, showing that the shorter the lattice constants predicted, the larger the bulk moduli and cohesive energies, and vice versa. This indicates that LDA, PBE, and M06-L can broadly predict the observed experimental trends (the inverse relationships of bulk moduli and cohesive energies with lattice constants). If one further looks into the errors concerning a given type of solids, large differences can be found for specific functionals. For SC and IC, a nearly monotonous dependence is observed for the deviations from experiment of the bulk moduli upon those of the lattice constants using all three functionals tested, that is, the overestimated lattice constants is accompanied by the underestimated bulk moduli. Also seen is a better (linear) correlation between the errors from the PBE calculations, in comparison with, e.g., LDA, applied to the SC compounds, where half of the values fall in the quadrant III, in disagreement with the empirical study based on experimental observations. To directly illustrate this issue, we performed fitting of experimental and theoretical cohesive data against the nearest-neighbor distance d using the expression $B_0 = Cd^x$, where C is regarded as a constant. Table 4.6 shows the fitting results for the solids of groups IVA, IIIA–VA, IIB–VIA, and IA–VIIA; also presented are the linear fitting results of the relative errors between predicted (using the three functionals) and experimental values. Overall, the PBE functional yields the most consistent results compared with experiment, and it is the method that reproduces systematic trends in the cohesive properties of solids better than the other two approaches.

Turning to metals, for the MM and TM groups an apparent scatter of the errors is found from both the LDA and M06-L calculations, and the inversely

[2]Here d represents the nearest-neighbor distance in a crystal and x is an empirical parameter relevant to crystal structure and bonding nature (see Section 2.3 and Ref. [81–83, 85–87]).

Table 4.6: Fits of the experimental and calculated bulk modulus B_0 against the nearest-neighbor distance d using the expression $B_0 = Cd^x$, where C is a constant. Deviations of the bulk modulus (ΔB_0) and the nearest-neighbor distance (Δd) from corresponding experimental data (Expt.) are fitted to a linear relation, and the last column gives standard deviations (Dev.) for the slope k from linear fitting using DFAs.

		$B_0 = Cd^x$		$\Delta B_0 = k\Delta d$	
Group		C	x	k	Dev.
IVA	Expt.	2176	-3.66		
	PBE	2391	-3.94	-12.03	**2.28**%
	M06-L	2391	-3.89	-9.44	3.16%
	LDA	2401	-3.87	-33.37	21.18%
IIIA–VA	Expt.	1811	-3.48		
	PBE	1975	-3.72	-9.18	**7.85**%
	M06-L	2002	-3.70	-7.05	9.23%
	LDA	1994	-3.65	3.24	52.99%
IIB–VIA	Expt.	984	-3.00		
	PBE	1364	-3.49	-9.55	8.28%
	M06-L	1626	-3.61	-5.91	7.72%
	LDA	1085	-3.08	-4.95	21.53%
IA–VIIA	Expt.	456	-2.68		
	PBE	516	-2.95	-7.02	13.45%
	M06-L	575	-2.99	-11.36	35.65%
	LDA	530	-2.78	-6.57	12.20%

correlated behavior is only captured using the PBE functional. This also reflects the poor performance of LDA and M06-L, particularly in the description of main-group metals. Finally, for the TMCN group, there is no clear trend shown by any method used here. This is not surprising, as experiment does not exhibit clear correlations between any pair of cohesive properties (see Figs 2.2 and 2.3), mainly due to the mixed nature of metallic, covalent, and ionic bondings in these solids [265, 266].

The above findings suggest that the errors in cohesive properties obtained from DFT calculations are correlated and system dependent. In general, PBE shows superior performance to LDA, due to the inclusion of the density gradient term for satisfying "non-locality" in realistic systems. Therefore the improvement of PBE over LDA will become more prominent for the systems with relatively inhomogeneous densities, e.g., main-group metals with one or two *s* electrons in the outer shell,[3] for which both LDA and M06-L yield large deviations. Likewise, for the solids with relatively slowly varying densities,

[3]In comparison with transition metals, the valence electrons of main-group metals have more freedom to "migrate" from the ion cores.

such as semiconductors and some transition metals, the cohesive properties are better predicted within LDA rather than PBE (except for the cohesive energies). When it comes to the M06-L functional, the present study shows that it can perform well for "light" solids. This can be ascribed to the fact that the functional form in M06-L is obtained by fits to molecular systems, thus it can describe the mid-range interactions to some extent, which can be seen from its good performance for the ionic crystals considered here.

Furthermore, our work suggests that investigating the relationships between errors in cohesive properties can help us to understand performance and capability of DFAs. In particular, it is found that the system-dependent behavior of the cohesive properties is best reproduced at the PBE level. Indeed, by using the PBE functional an increase of errors in bulk moduli is accompanied by that in lattice constants for most solids in the current database. This is consistent with the finding by Grabowski and co-authors, who have discussed the dependence of errors produced by the LDA and PBE functionals for fcc metals [258]. The behavior of the increasing errors with mass can also be observed in lattice constants. In Fig. 4.8, the deviations of the calculated lattice constants from experiment are plotted as a function of their experimental values for 24 metals and 40 non-metals for all the three functionals. One can see the monotonous relationship, indicating that the systematic error increases as the crystal unit-cell volume increases, is better reproduced by PBE rather than LDA or M06-L. The trend is more pronounced in non-metals than metals, in good agreement with experiment (see Figs. 2.2 and 2.3). For 40 non-metals, a nearly linear behavior is captured using PBE, while two separate regions are found using M06-L.

Note that for those solids with a large unit-cell volume (heavy nuclear mass) in the current database, the M06-L method yields worse performance for the prediction of the cohesive properties than PBE does, whereas the opposite trend is found for light solids. This is a strong indication that long-range vdW interactions are responsible for part of deviations caused by modern DFAs. Indeed, all widely employed local and semi-local (and even hybrid) functionals suffer from the presence of self-interaction errors and the lack of the long-range vdW energy tail, often leading to noticeable deviations from experiment in describing material properties. Using hybrid functionals and including the long-range correlation in DFAs should improve the prediction of density functionals for reproducing experimental data [8–11]. Given that the use of hybrid functionals reduces the impact of SIE, the role of long-range vdW interactions is less clear, particularly for solid-state materials [71, 79]. The

importance of both aspects has been recently illustrated in our study of six ionic and semiconductor solids using accurate dielectric functions of those solids. Upon the inclusion of the long-range vdW interaction on top of PBE-GGA as well as HSE06 hybrid functional, a significant improvement was found in the cohesive properties over original PBE or HSE06 [72]. The present work suggests that the M06-L functional is able to capture some intermediate interactions by construction, as observed from its good performance in light solids, whereas it lacks the long-range correlation. This can be seen from the poor prediction of the cohesion using M06-L for heavy solids. Moreover, the worse-description of the cohesive properties for heavy solids using M06-L than PBE tells us the non-empirical PBE functional reproduces experimental trends much better and can be used for developing more advanced approaches that correctly account for the long-range correlation energy.

4.4 SUMMARY

In this chapter, the cohesive properties of 64 solids have been studied using the first three rungs of "Jacob's ladder" of density-functional approximations (LDA, GGA, and MGGA) within the FHI-aims package. It has been shown that the zero-point vibrational contributions can be significant for certain solids and properties. In particular, ZPVE can influence the bulk modulus more than the lattice constant as well as the cohesive energy, as can be seen from the relative change in those properties. Furthermore, ZPVE plays a larger role for non-metals and light solids.

For the cohesive properties, the present study reproduces the well-known trends of the LDA and PBE functionals. LDA delivers the best prediction on the lattice constants and bulk moduli of covalently-bonded systems, however, the cohesive energies are considerably overestimated with a MARE of $\sim$20%. PBE gives the best overall performance compared with LDA and M06-L, especially for metals and transition metal carbides and nitrides. The MGGA functional M06-L gives a better description than PBE does for certain semiconductors and ionic crystals, but yields poor prediction on bulk moduli.

By comparing the DFT results to experimental studies and empirical observations, we discuss the cohesive properties in terms of the relationships of the cohesive energy and the bulk modulus with the lattice constant. As expected, all three functionals are capable of broadly reproducing the experimental trends. However, systemic differences are observed in the deviations of the DFT results from the experimental data. Given the empirical

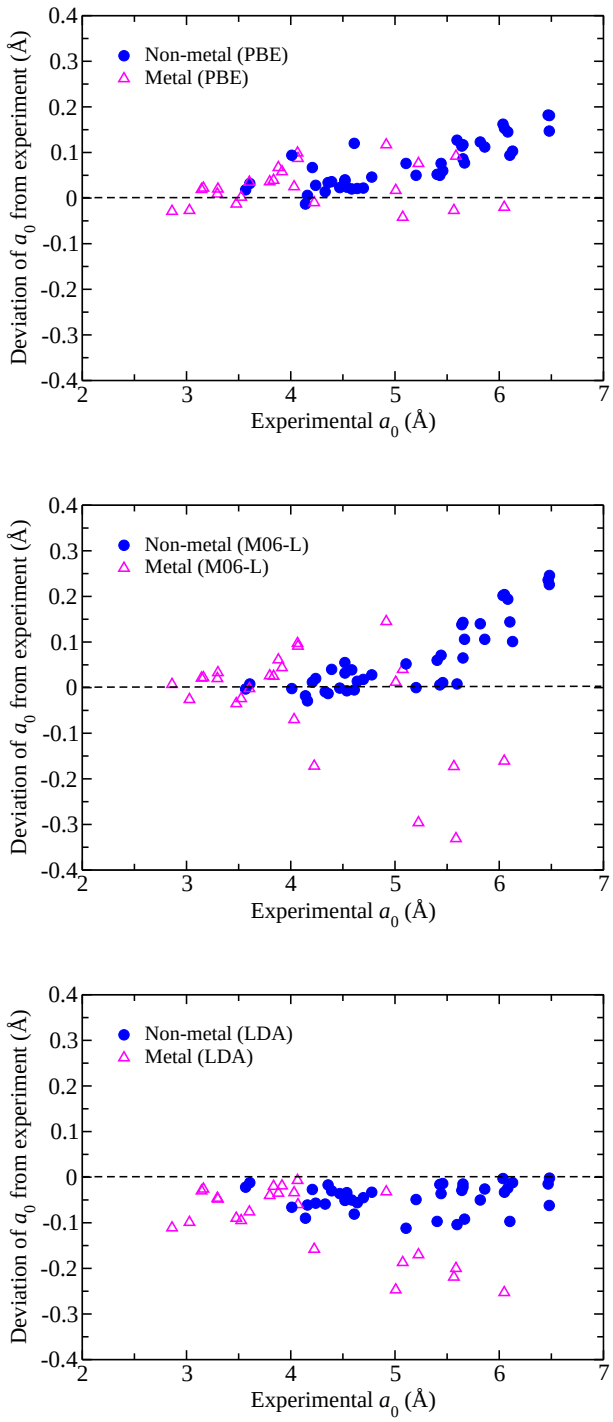

Figure 4.8: Deviations of DFT lattice constants (Å) from experiment for 24 metals and 40 non-metals versus their experimental lattice constants (Å) using the PBE, M06-L, and LDA functionals.

relationships between the lattice constant and both the bulk modulus and the cohesive energy, we expect the deviations of the bulk moduli and the cohesive energies to be inversely related to those of the lattice constants. The PBE functional reproduces this behavior better than LDA or M06-L.

Overall, none of the functionals tested here can be considered better than the others when applied to a broad range of solids, but the observed trends among different types of interactions and groups of atoms can certainly be helpful for developing DFT functionals. We note that the lack of long-range vdW interactions may account for some of the deviations seen in the three functionals employed in this work. The M06-L functional already captures mid-range correlation interactions, which can be seen from its good performance for ionic solids, whereas it is less clear how it could be improved further, especially given its highly empirical nature. PBE represents a natural functional for adding long-range electron correlation because of its systematic behavior for the cohesive properties of solids. The next chapter is focused on establishing benchmark data of the polarizability and C_6 dispersion coefficients using time-dependent DFT calculations and assessing the importance of vdW interactions in ionic and semiconductor solids.

5 Benchmark study of vdW coefficients in semiconductors and ionic solids: Combined DFT/TDDFT approach

The study of long-range van der Waals (vdW) interactions in solids requires the knowledge of the dynamic polarizability of all atoms (or ions) in the material, including local-field effects. In this chapter, the polarizability is determined from the calculated optical spectrum of solids within the framework of time-dependent density-functional theory (TDDFT), invoking the Clausius-Mossotti (CM) relation between the dielectric function and the polarizability. The CM relation was shown to be very successful for connecting microscopic and macroscopic properties of many ionic crystals with cubic symmetry. However, the validity of the use of this formula in covalently-bonded solids is much less clear. To assess this, the cluster extrapolation model is employed for obtaining the frequency-dependent polarizability and C_6 dispersion coefficients. Subsequently, we use the obtained vdW parameters for computing the vdW energy based on the summation of pair-wise interatomic contributions, and add the resulting vdW energy to the DFT energy of the system. The validation of this DFT/TDDFT methodology is discussed for a few semiconductors and ionic crystals (C, Si, Ge, GaAs, NaCl, and MgO), followed by an assessment of the role of long-range vdW interactions in the cohesive properties of these solids.

5.1 MOTIVATION

The dielectric function of solids plays an important role in many physical processes. The fundamental electronic excitation spectrum is generally described in terms of a complex electronic dielectric function $\varepsilon(\omega) = \varepsilon_1(\omega) + i\varepsilon_2(\omega)$, in which the real part ε_1 corresponds to the refraction of the electromagnetic radiation as it passes through the medium and the imaginary part ε_2 describes absorption. Much effort has been made to obtain accurate dielectric functions experimentally and theoretically [220, 231, 234, 239, 243, 267–270]. The real and imaginary parts of the macroscopic dielectric function $\varepsilon_{\mathrm{M}}(\mathbf{q},\omega)$ can be derived from measurements of such as refraction, reflection, and absorption spectra over a large enough spectral range, and they are related to one another by a Kramers-Kronig transformation. From a theoretical point of view, the inverse microscopic dielectric function of a crystal is connected to the response function (linear-response regime): $\varepsilon^{-1}_{\mathbf{G},\mathbf{G}'}(\mathbf{q},\omega) = 1 + v_{\mathbf{G},\mathbf{G}'}(\mathbf{q})\chi_{\mathbf{G},\mathbf{G}'}(\mathbf{q},\omega)$, where $\mathbf{q}$ is a vector in the first Brillouin zone, $\mathbf{G}$ and $\mathbf{G}'$ are reciprocal lattice vectors, and v is the bare Coulomb interaction. In a long-wavelength limit, the macroscopic dielectric function can be readily obtained from the microscopic $\varepsilon_{\mathbf{G},\mathbf{G}'}(\mathbf{q},\omega)$ via the relation of $\varepsilon_{\mathrm{M}}(\mathbf{q},\omega) = \lim_{\mathbf{q}\to 0} \frac{1}{\varepsilon^{-1}_{00}(\mathbf{q},\omega)}$, in which the electronic components ε_1 and ε_2 can be compared with experimental measurements if they are available.

An accurate calculation of the optical-absorption spectrum of solids requires proper treatments of both electron-electron and electron-hole effects. A well-established method for yielding good results of dielectric functions is so-called the two-step approach within the framework of many-body perturbation theory, i.e., the *GW* approximation [235] for the self energy and the solution of the Bethe-Salpeter equation (BSE) [236] for the electron-hole interaction. Such a calculation is, however, computationally very demanding. Time-dependent density-functional theory (TDDFT), as already introduced in Section 3.6, represents an advantageous way of computing reliable excitations of solids with less computational requirement than the above scheme. In the linear-response TDDFT, the response function (yielding the inverse microscopic dielectric function $\varepsilon^{-1} = 1 + v\chi$) is described by Dyson-like formula

$$\chi = \left[1 - (v + f_{\mathrm{xc}})\chi_{\mathrm{KS}}\right]^{-1} \chi_{\mathrm{KS}}, \tag{5.1}$$

where χ_{KS} is the independent-particle Kohn-Sham (KS) response function and

v is the bare Coulomb interaction.[1] To evaluate the response function χ of materials, the challenge is how to find good approximations for the time-dependent exchange-correlation (XC) potential v_{xc} and its density derivative (the so-called XC kernel $f_{\mathrm{xc}} = \delta v_{\mathrm{xc}}/\delta n$). The simplest approximation is the time-dependent local-density approximation (TD-LDA), using LDA for v_{xc} and the adiabatic local-density approximation (ALDA) for f_{xc}; thus $f_{\mathrm{xc}}^{\mathrm{ALDA}}$ is local both in time (frequency-independent) and in space. It has been shown that TD-LDA often yields good results for excitation energies of finite systems. However, this is not the case for the optical spectrum of solids — the quasiparticle gap is too small and the bound exciton is completely missing [228, 230, 234]. Extensive discussion has been made to go beyond TD-LDA in the literature for tackling those issues and improvements can be found through the inclusion of long-range nonlocal terms and dynamic effects in the XC kernel (which must be a strongly nonlocal functional of the density and also frequency-dependent) [234, 237–241]. Recent advances in developing (static and dynamic) nonlocal kernel allow to compute reliable optical spectra of solids within linear-response TDDFT [231, 242–244]. The kernel employed in this thesis is the so-called nanoquanta (NQ) [240] kernel, which has the asymptotic form of a long-range contribution (LRC) [239, 242] kernel (decaying in the momentum space as $1/q^2$) and includes electron-hole interactions by utilizing a nonlocal exchange term $f_{\mathrm{x,nl}}$ into Eq. 5.1 for the full response function. The implementation of NQ has been done in the code of Vienna *ab initio* simulation package (VASP) [245, 246], in which both the response function and the dielectric function are represented in reciprocal space and the projector augmented-wave (PAW) method is used.

One of the main goals of studies of the dielectric response is to relate macroscopic observables such as the dielectric function to microscopic quantities such as the polarizability of the constituent particles forming a material, provided that the "particle" is properly defined in the material. To establish a connection between them, one has to analyze the electric polarization in a dielectric medium. At optical frequencies, the local (or effective) field acting on atoms or ions in a crystal can be written as $\mathbf{E}^{\mathrm{loc}} = \mathbf{E} + L\mathbf{P}$, where $\mathbf{E}$ is the macroscopic electric field, $\mathbf{P}$ is the polarization density (dipole moment per unit volume), and the constant L is known as Lorenz factor that is related to ionicity and structure of the solid [26, 220–222]. Substituting the local field into Eq. (3.66) and combining with Eq. (3.62), one can arrive at a general form for the unit-cell

[1] Here the position and frequency arguments are omitted for simplicity.

polarizability in terms of the dielectric function with a constant Lorentz factor

$$\alpha_{\text{cell}} = V\frac{\varepsilon - 1}{L(\varepsilon - 1) + 4\pi}, \tag{5.2}$$

where V is the unit-cell volume of the crystal. Two limiting cases are $L = 0$ and $L = 4\pi/3$, yielding the Drude-Sellmeier (DS) formula and the Clausius-Mossotti (CM) relation, respectively

$$\alpha_{\text{cell, DS}} = V\frac{\varepsilon - 1}{4\pi}; \tag{5.3}$$

$$\alpha_{\text{cell, CM}} = V\frac{3}{4\pi}\frac{\varepsilon - 1}{\varepsilon + 2}. \tag{5.4}$$

As discussed in Section 3.5.2, the DS formula is exact for the free-electron gas, where an electron merely feels the average macroscopic field composed of a uniformly distributed medium. In contrast, the CM relation becomes accurate for dilute, isotropic, and homogeneous systems, in which the particles can be regarded as non-overlapping point dipoles. In such situations, the polarizability can be described in terms of individual components forming the material. These systems include liquids, gases, polycrystals, amorphous materials, and "idealized" ionic crystals. Among numerous studies of Eq. (5.4) applied to non-metallic systems, the discussion is mainly about the deviation of the Lorentz factor L from its usual value of $4\pi/3$, which is exact only if induced dipoles are treated as points, i.e., there is no overlap between any pair of atoms or ions. It was shown that the CM relation is a very good approximation for many ionic crystals with cubic symmetry [26, 219] (see Section 3.5.2 for more discussion and citations therein). This can be explained by the fact that in ionic crystals anions are much more polarizable than cations, such that the induced dipole moment mainly depends on anions, between which there is no significant overlap.

Unlike ionic crystals, the validity of employing the CM formula for relating the dielectric function to the polarizability is much less clear in covalently-bonded materials [1, 24, 211]. In particular, Mott [214] and Pantelides [271] proposed that CM fails to describe systems where the overlap between neighboring atoms is nonnegligible. In this thesis, to shed light on this problem, we performed TDDFT optical-absorption spectrum calculations for ionic and covalent solids. The dynamic polarizability and C_6 dispersion coefficients are then obtained using the CM relation and the Casimir-Polder integral, respectively. To assess the validity of the use of the CM relation, an alternative

cluster extrapolation (CE) model is utilized. We discuss how the overlap between constituent atoms affects the local field in a dielectric medium.

Unlike the CM model, in which the polarizability is defined per unit cell, the CE approach treats the total polarizability and dispersion coefficients by summing over atomic components, as described in Section 3.5.3. Given that both α and C_6 coefficients are dependent on the lattice constant of a crystal, particular care has been taken to study the role of variation in the interatomic distance, and a new set of unit-cell-volume-dependent $\alpha(V)$ and $C_6(V)$ are generated for the semiconductors studied here. A detailed description of the CM and CE approaches follows in the next section.

5.2 Technical details

5.2.1 Optical-absorption spectra

In the CM model, the first step for obtaining the polarizability and C_6 dispersion coefficients of atoms in solids is to compute the dielectric function from the optical-absorption spectrum. In this section, the calculation of the dielectric function $\varepsilon(\mathbf{q}, \mathbf{q}', \omega)$ using the computational code VASP [245, 246] shall be addressed for diamond-type solids.[2] The optical spectra have been computed using the linear-response theory of TDDFT (see Section 3.6) for a series of unit-cell volumes within $\pm 20\,\%$ of the experimental volume, using the same approach as in Ref. [231] (see the computational details reported in Appendix B). Two XC functionals were employed: the ALDA and Heyd-Scuseria-Ernzerhof (HSE) functional [150, 151]. For the HSE functional, the parameter μ defines the length scale for the separation of the nonlocal and semi-local exchange, and it is empirically set to 0.2–0.3 Å^{-1}. In the present study, a value of $\mu = 0.3\,\text{Å}^{-1}$ was chosen for all solids, as it was found to best reproduce their experimental absorption spectra. Moreover, to include the effective XC kernel from the nonlocal exchange term, we follow the approach described in Refs. [239, 240, 242, 244], employing the nanoquanta kernel, which enables us to reproduce some excitonic effects in bulk materials within the TDDFT framework.

Figure 5.1 shows the imaginary part of the dielectric function $\varepsilon_2(\omega)$ obtained from the TD-HSE and TD-LDA calculations for Si bulk (at the experimental lattice constant), in comparison with its experimental absorption

[2] Th calculation of optical spectra using Vienna *ab initio* simulation package (VASP) was in collaboration with VASP contributor Joachim Paier (see Ref. [72]).

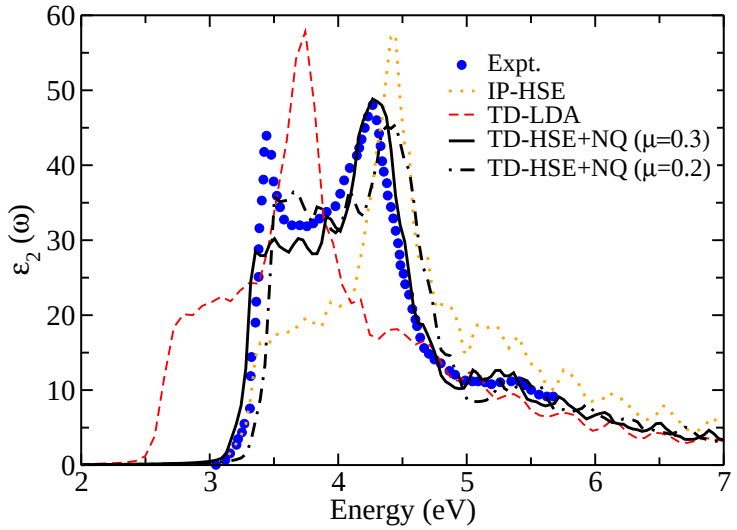

Figure 5.1: The optical-absorption spectrum of Si bulk using TD-HSE ($\mu = 0.3$ Å^{-1}) with the nanoquanta (NQ) kernel (full black line) and in the independent-particle (IP) approximation (orange small dots). The TD-LDA result is shown using the red dashed line, TD-HSE ($\mu = 0.2$ Å^{-1}) is shown by the black dot-dashed line, and the experimental spectrum is shown by blue dots, taken from Ref. [270]. All calculations were performed at the experimental lattice constant.

spectrum [270]. It is found that neither TD-LDA nor IP-HSE (in the independent-particle approximation) is able to reproduce the experimental optical spectrum and that the excitonic peak is completely absent in both cases. The inclusion of a long-range contribution to the XC kernel within the TD-HSE scheme (μ = 0.3 Å^{-1}) improves the agreement with experiment, yielding a redshift of the spectrum and a pronounced increase of the intensity at low energies with respect to IP-HSE (where many-electron effects have been entirely neglected). Note that extending the range of the nonlocal exchange part of the HSE functional (μ = 0.2 Å^{-1}), the first peak becomes more apparent (showing excitonic effects), however, at the expense of worsening the position. Thus it can be concluded that the interaction range of the HSE functional is slightly too short to correctly account for the electrostatic interaction in the weakly-bound exciton such as in Si bulk. Nevertheless, our calculations reproduce the results reported in a previous study [231] using equivalent computational settings, and agree with the conclusion that when combined with TD-HSE, the NQ nonlocal exchange kernel is able to partially capture excitonic effects and yield reasonably good optical spectra of solids.

Also calculated are the optical spectra of C and Ge (see Appendix B) and the above finding holds for both of them. Turning to the static dielectric constant, the corresponding results for C, Si, and Ge are reported in Table 5.1,

together with those for GaAs, NaCl, and MgO (which will be discussed in next sections). The TD-LDA approach overestimates the dielectric constants of the solids considered here, while the TD-HSE+NQ results agree much better with the experimental data. The current study suggests that TD-HSE is a reliable approximation for modeling optical properties of semiconductors and ionic crystals studied here.

Table 5.1: Calculated static dielectric constants from TD-LDA, TD-HSE ($\mu = 0.3$ Å^{-1}) in the independent-particle (IP) approximation and including the electron-hole interaction within the nanoquanta (NQ) kernel. All data are calculated at the experimental volumes and experimental values are taken from Ref. [272].

	TD-LDA	TD-HSE		Expt.
Solid		IP	NQ	
C	5.8	5.2	5.6	5.7
Si	13.2	10.9	11.3	11.9
Ge	23.5	–	15.9	16.0
GaAs	14.0*	10.6	10.9	10.9
MgO	–	–	2.8	3.0
NaCl	–	–	2.3	2.3

* The value is taken from Ref. [231].

In the CM approach, the next step is to obtain the dielectric function on the imaginary-frequency axis from the imaginary part on the real axis, $\varepsilon_2(\omega)$, by performing a Kramers-Kronig transformation via Eq. (3.64). The frequency-dependent polarizability can then be calculated using the CM relation shown in Eq. (5.4). The corresponding results will be presented in the next sections, together with the validation of this method.

5.2.2 Cluster extrapolation model

An alternative way of calculating vdW parameters is to employ the cluster extrapolation model. In this approach, the central approximation is the additivity of the polarizability, i.e., the polarizability is defined in terms of atomic fragments and the total polarizability of a cluster equals the sum of all atomic constituents (the reader is referred to Section 3.5.3 for more details). Here we will elucidate this method for Si, but the same procedure and conclusions also apply to C and Ge. For the case of hydrogen-saturated Si clusters, a set of 30 Si_iH_j clusters ranging from SiH_4 to $Si_{172}H_{120}$,[3] were cut from Si bulk at the experimental volume (a few examples are given in Fig. 5.2).

[3]The geometries of those clusters were initially used in Ref. [226].

The change in the lattice constant has been studied by varying the distance between bonded Si atoms. The geometries were optimized (only for the relaxation of saturating hydrogen atoms) from self-consistent DFT calculations employing the PBE [94] functional, implemented in the Fritz Haber Institute *ab initio* molecular simulations (FHI-aims) package [21]. In the case of finite systems (atoms, molecules, or clusters), it is more convenient to use a real-space approach. Using the optimized geometries, linear-response equations of the electron density to a perturbative potential were solved using the self-consistent Sternheimer approach [247], as implemented in the Octopus code [251] with the ALDA parametrization for the XC potential. For the real-space regular grid, a spacing of 0.275 Å was chosen to ensure convergence, and a radius of 4.5 Å was used for constructing the simulation box by adding spheres around each atom. With the above computational setting, the polarizability and C_6 dispersion coefficients of the clusters were obtained through the formulation described in Section 3.5.3.

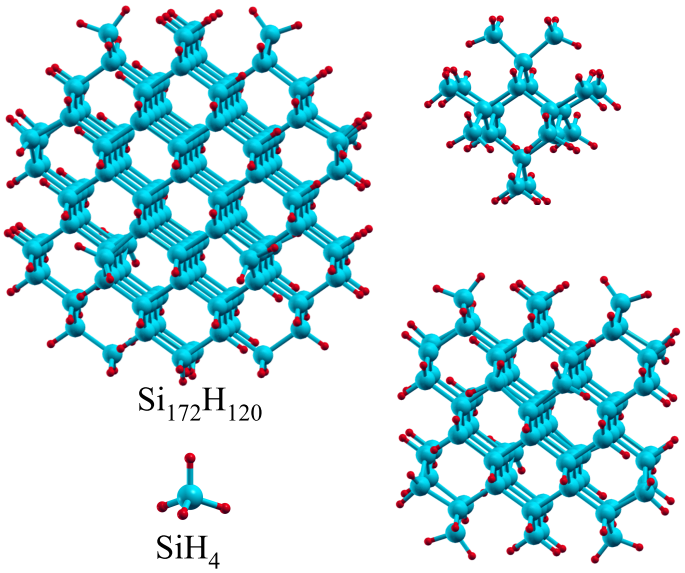

Figure 5.2: Four hydrogen-saturated Si-cluster geometries of a set of 30 clusters ranging from SiH_4 to $Si_{172}H_{120}$. The big (blue) spheres represent Si atoms, while the small (red) spheres show H atoms.

The additivity of the polarizability

The approximation used in the CE approach is that the total polarizability of a cluster is the sum of contributions from the "averaged" constituent components

of each species, i.e., $\alpha^{\mathrm{cluster}} \simeq i\,\overline{\alpha_{\mathrm{Si}}} + j\,\overline{\alpha_{\mathrm{H}}}$. To verify this, least-squares fitting was employed to obtain the atomic polarizabilities of the hydrogen and silicon atoms, α_{H} and α_{Si}; then, the dispersion coefficients of hydrogen–hydrogen and silicon–silicon interactions, C_6^{HH} and C_6^{SiSi}, can be further determined via Eqs. (3.77) and (3.78). Different fitting methods have been tested by using different sets of clusters, among which the cluster size grows from SiH_4 to $Si_{172}H_{120}$.

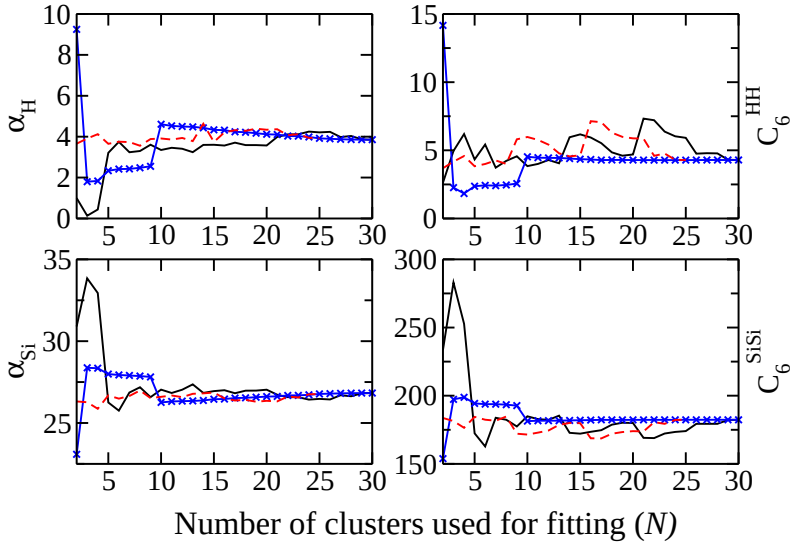

Figure 5.3: Least-squares fitting results for the polarizability (left panels, bohr^3) and C_6 (right panels, hartree·bohr^6) per atom (Si or H) to a set of N hydrogen-saturated Si clusters (Ref. [72]). The solid black curve shows the fitting results starting from the smallest cluster (SiH_4). The dashed red curve starts from the $Si_{17}H_{36}$ cluster. The crossed blue curve starts from the largest $Si_{172}H_{120}$ cluster.

Figure 5.3 shows the fitting results of the Si clusters obtained in three different ways, starting the fitting procedure from the smallest cluster (SiH_4), the middle one ($Si_{17}H_{36}$), as well as, the largest one ($Si_{172}H_{120}$). The fitting was carried out using different sets of clusters that start from the above three clusters, i.e., the largest (smallest or middle-sized) two, three, and so on, until all 30 clusters were included in the fitting procedure. It was found that all of the fitted parameters (namely α_{H}, α_{Si}, C_6^{HH}, and C_6^{SiSi}) show very good convergence as long as more than 10 clusters are used in the training set. Encouragingly, the procedure starting from the largest cluster (the crossed blue curve plotted in Fig. 5.3) gives the most reliable results, in the sense that the four quantities saturate quickly with the number of clusters used for fitting. In this case, the root-mean-square deviations (RMSDs) obtained are: α_{H} (0.23 bohr^3, 5.6%), C_6^{HH} (0.06 hartree·bohr^6, 1.4%), α_{Si} (0.17 bohr^3, 0.6%), and C_6^{SiSi} (0.24 hartree·bohr^6,

0.1%).[4] It can be concluded that the additivity of the polarizability employed in the CE model is a good approximation for the semiconductor clusters, and no matter which combination of clusters is utilized for fitting (more than 10 clusters at least), a negligible variation is found for both α_{Si} and C_6^{SiSi}.

THE EFFECT OF SATURATING HYDROGEN ATOMS

As the quantities we wish to obtain are α_{Si} and C_6^{SiSi}, one needs to first determine the parameters of the saturating hydrogen atoms. To estimate the effect of hydrogen atoms on obtaining the parameters of Si atoms, the largest cluster, $Si_{172}H_{120}$, was chosen, with different combinations of α_{H} and C_6^{HH} being fixed parameters (which were determined from the least-squares fits using different numbers of clusters, as presented in Fig. 5.3). The polarizability and C_6 dispersion coefficients of Si atoms were further computed using Eq. (3.75) and Eqs. (3.77) and (3.78), respectively. The corresponding results are shown in Fig. 5.4: the fitted parameters of hydrogen and silicon atoms as a function of the number of clusters used for fitting. It can be found that the variation of C_6^{HH} is negligible, as long as more than 17 clusters are used in the fitting procedure that starts from the largest cluster (see Fig. 5.4). In contrast, there is a noticeable change in α_{H}, with a variation of $\pm 10\%$ with respect to the average value. However, such a variation does not lead to noticeable uncertainties for the parameters of Si atoms (α_{Si} and C_6^{SiSi}), showing the negligible effect of saturating hydrogen atoms on the evaluation of the quantities of interest here. The RMSDs of α_{Si} and C_6^{SiSi} are remarkably small: 0.15 bohr^3 and 0.24 hartree·bohr^6, respectively. Finally, the parameters of $\alpha_{\mathrm{H}} = 4.24$ bohr^3 and $C_6^{\mathrm{HH}} = 4.28$ hartree·bohr^6, obtained from the least-squares fitting using the 17 largest clusters, were used for determining the polarizability and dispersion coefficients of Si atoms in the CE model.

THE EFFECT OF CLUSTER SIZE

Having determined the vdW parameters of hydrogen atoms, the last aspect we want to address is how the fitting procedure used in the CE approach depends on the cluster size. To illustrate this, one should compare the polarizability and dispersion coefficients of Si atoms for different sizes of clusters. In Fig. 5.5, we show the values of α_{Si} and C_6^{SiSi} as a function of the number of Si atoms in a set of 30 Si_iH_j clusters, where the parameters of $\alpha_{\mathrm{H}} = 4.24$ bohr^3 and $C_6^{\mathrm{HH}} = 4.28$ hartree·bohr^6 were taken for hydrogen atoms and fixed. It can

[4] The root-mean-square deviation (RMSD) is defined as $\sqrt{\frac{\sum_{i=1}^{n}(x_i-\bar{x})}{n}}$.

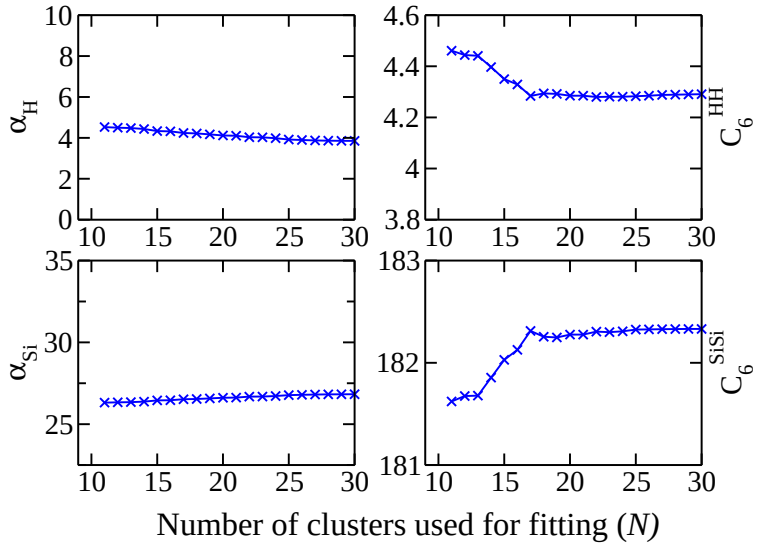

Figure 5.4: Calculated polarizabilities (left panels, bohr^3) and C_6 dispersion coefficients (right panels, hartree·bohr^6) per atom for the cluster of $Si_{172}H_{120}$, where α_H and C_6^{HH} were determined from least-squares fitting using different numbers of hydrogen-saturated Si clusters N (Ref. [72]).

be immediately seen that there are negligible changes of α_{Si} as well as C_6^{SiSi} for the clusters larger than $Si_{22}H_{40}$, indicating that the choice of the largest cluster, $Si_{172}H_{120}$, is very accurate for the present study. On the other hand, one can further look at the types of Si atoms surrounded by different numbers of hydrogens in a given cluster: "bulk-like" silicon without hydrogen and "surface" silicon bonded to one, two, or three hydrogens. As presented in Fig. 5.5, individual clusters show noticeable deviations of the polarizability and C_6 from those of most other clusters, when they contain many "surface" silicons connected to three hydrogens, e.g., $Si_{106}H_{120}$. This also verifies that the largest cluster is the most reliable one, as there is no silicon bonded to three hydrogens, but many "bulk-like" silicon atoms in this cluster.

Up to this point, it can be concluded that the additivity model of Eq. (3.75) is a good approximation, the use of which provides a way for evaluating polarizabilities and C_6 dispersion coefficients in semiconductors. In the following sections, the results obtained from the CE approach, together with those from CM, will be discussed.

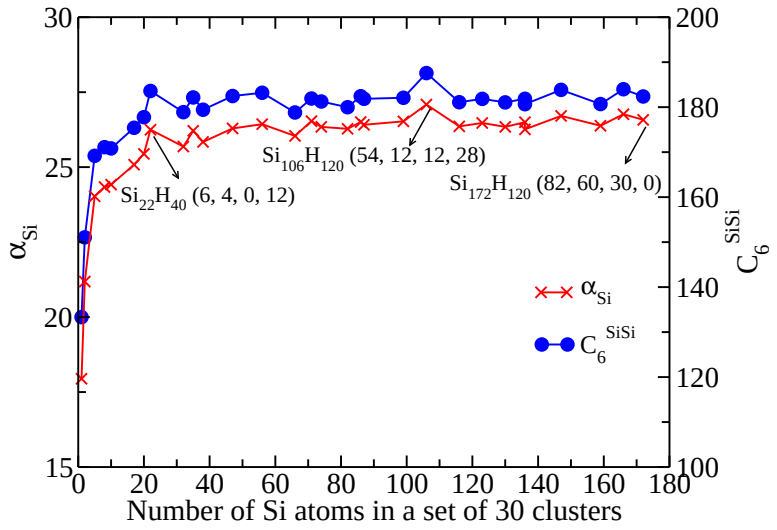

Figure 5.5: The polarizability (left axis red, bohr^3) and dispersion coefficients (right axis blue, hartree·bohr^6) as a function of the number of Si atoms in different sizes of clusters. The values marked in parentheses indicate numbers of different types of Si atoms in the tetra-coordinated cluster: "bulk-like"atoms, and "surface" atoms bonded to one, two, or three hydrogens, respectively.

5.3 Results and Discussion

5.3.1 Dependence of vdW parameters on the lattice constant

The polarizability of atoms or ions in solids varies according to local coordination and bonding in the solid. As it was evident that the polarizability of ions in ionic crystals depends upon the lattice constant [26, 59, 61], Fowler, Pyper, and co-authors investigated the volume-dependent polarizabilities for a series of ionic solids [17–19, 64–66, 68]. In this thesis, we extend this work to covalently-bonded solids by performing periodic and cluster TDDFT calculations based on the CM and CE models. As described in the previous section, in the CM approach, the frequency-dependent polarizabilities were obtained from the periodic TDDFT calculations of the optical-absorption spectra at a range of unit-cell volumes. Then, the C_6 dispersion coefficients were computed by performing the Casimir-Polder integral. In the CE model, the clusters were cut from a bulk crystal with the lattice constant varied around the equilibrium volume, and the corresponding polarizability and C_6 coefficients were determined from Eq. (3.75), and Eqs. (3.77) and (3.78), respectively.

The calculated vdW parameters of C, Si, and Ge are tabulated in Tables B.1 and B.2, as functions of the lattice constants of those solids. The results derived from the CM relation are reported using both the TD-HSE and TD-LDA

approaches, together with those obtained from TD-LDA based on the CE model. We follow with the discussion for each solid below.

DIAMOND

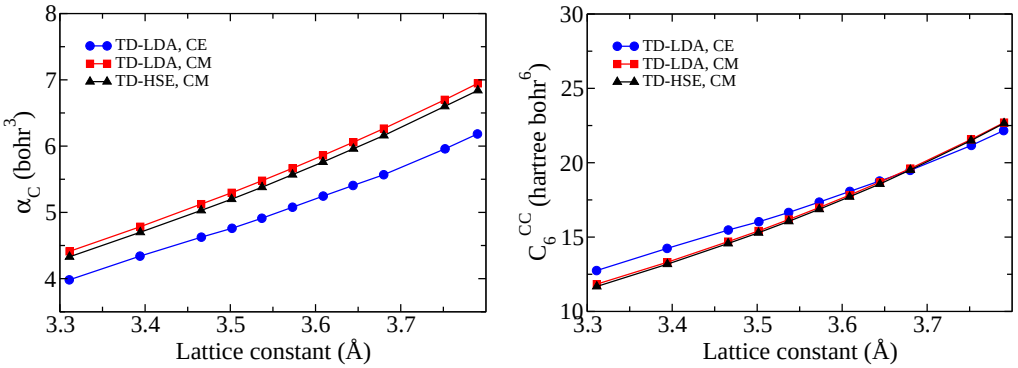

Figure 5.6: Calculated static polarizabilities (left panel) and C_6 dispersion coefficients (right panel) as a function of the lattice constant for diamond bulk using the TD-HSE and TD-LDA approaches from the Clausius-Mossotti (CM) and cluster extrapolation (CE) models.

The in-crystal static polarizabilities and C_6 dispersion coefficients are plotted in Fig. 5.6 as a function of the lattice constant of diamond using the CM and CE approaches. It can be seen that both α_{C} and C_6^{CC} increase with the lattice constant of the unit cell, showing a linear dependence in the studied volume range. Periodic calculations (employing LDA and HSE functionals) show that the vdW parameters obtained from TD-LDA are larger than those from TD-HSE, in line with the results of the static dielectric constant (plotted in Fig. B.2). The deviations between the TD-LDA and TD-HSE values are found to be 3% and 1% for the polarizability and C_6 dispersion coefficient, respectively. The comparison of the calculated dielectric constant with the corresponding experimental data tells us that TD-HSE yields better agreement with experiment. When the CE model is used instead of CM, a nearly linear dependence is observed as well. When comparing the two models, one finds a difference of $\sim$10% (with respect to the CM values) for α_{C} at the experimental lattice constant (3.567 Å) using the same functional (TD-LDA). This can be attributed to the fact that the values of the polarizability and C_6 dispersion coefficients of C and H atoms are of the same magnitude and both are quite small. As a consequence, the effect of the saturating hydrogens will become important and thus non-negligible, which means even a small change in the value of α_{H} or C_6^{HH} may lead to a noticeable change in α_{C}. In contrast

to the static polarizability, our study shows that the influence of hydrogen on the estimated C_6^{CC} becomes much less important, as C_6 is an integrated quantity that relies on the dynamic polarizability. As can be seen in Fig. 5.6, the difference between the C_6 coefficients obtained using the CE and CM approaches is reduced to less than 2% at the equilibrium lattice constant. Considering that both CM and CE rely on a number of approximations, the agreement between them is remarkable. Our study suggests that, in addition to dilute systems (gases and liquids) and ionic crystals, the CM relation also holds for covalently-bonded semiconductors, and that using this relation allows one to calculate the polarizability and dispersion coefficients of atoms in non-metallic solids.

SILICON

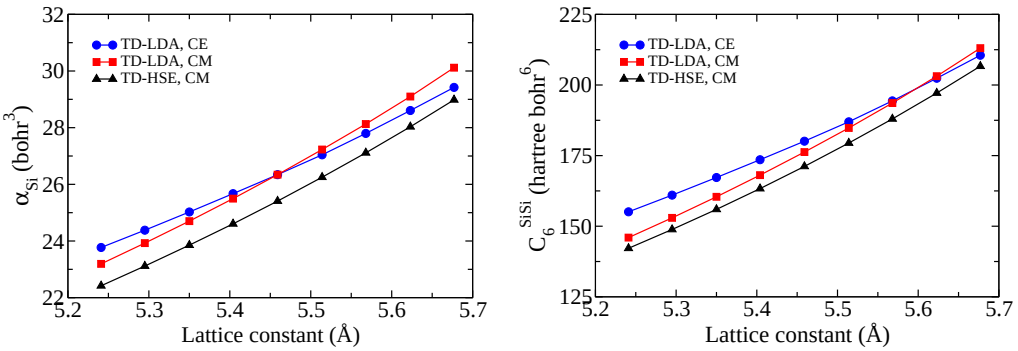

Figure 5.7: Calculated static polarizabilities (left panel) and C_6 dispersion coefficients (right panel) as a function of the lattice constant for Si bulk using the TD-HSE and TD-LDA approaches from the CM and CE models.

The calculated α_{Si} and C_6^{SiSi} dispersion coefficients are plotted in Fig. 5.7 as a function of the lattice constant of Si bulk using the CM and CE methods. It is apparent that the static polarizability follows the same trend as C_6 dispersion coefficients using the two models: both of them increase with the lattice constant and a nearly linear dependence is observed. For periodic calculations, the values computed within TD-LDA are larger than those within TD-HSE, and the same to the static dielectric constant results shown in Fig. B.3. The same as the case of diamond, the comparison with experiment shows TD-HSE leads to more reliable dielectric constant than TD-LDA. When comparing the CE and CM approaches, one finds that the cluster calculations yield larger values for the polarizabilities and C_6 dispersion coefficients at small unit-cell volumes but smaller values at large volumes, indicating that the deviation between the

two models decreases when approaching the equilibrium volume and then increases again. Note that the maximum deviations between CM and CE are found to be less than 0.5 bohr^3 (2%) for α_{Si} and 9.0 hartree·bohr^6 (6%) for C_6^{SiSi}. We therefore conclude that the two approaches yield good agreement for the polarizability and C_6 dispersion coefficients of Si bulk.

GERMANIUM

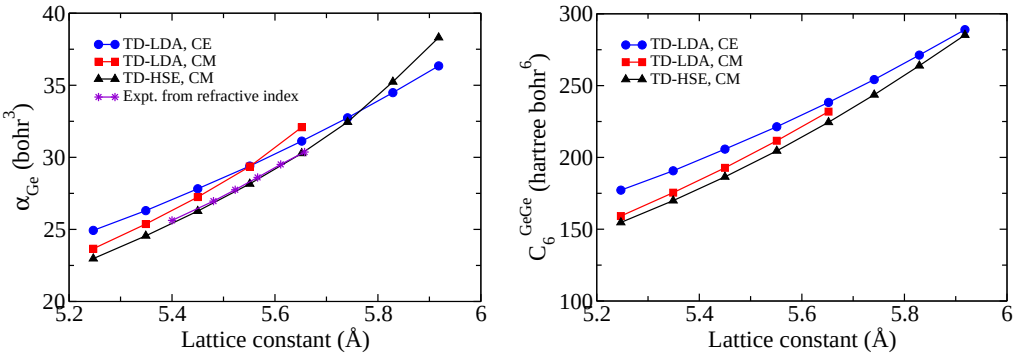

Figure 5.8: Calculated static polarizabilities (left panel) and C_6 dispersion coefficients (right panel) as a function of the lattice constant for Ge bulk using the TD-HSE and TD-LDA approaches from CM and CE models. The experimental curve was obtained using the refractive-index data from Ref. [267].

Figure 5.8 shows the polarizability and C_6 dispersion coefficients as a function of the lattice constant of Ge using the CM and CE approaches, together with those obtained from the experimental dielectric function applying the CM relation (marked by purple stars). Similar to C and Si, the polarizability and dispersion coefficient increase with the unit-cell volume when using both the CM and CE methods. Among the three solids studied here, Ge is the only system for which experimental data is available for the volume-dependent dielectric function, as investigated by Cardona's group [267]. In their work, the authors measured the refractive index of Ge (as well as GaAs) with varying pressure, and then extrapolated to the pressure- and volume-dependent static dielectric constant $\varepsilon(V)$. We compare our TDDFT calculations with experiment and find that the volume dependence of $\varepsilon(V)$ and $\alpha(V)$ are remarkably well reproduced at the TD-HSE level, as can be seen in Figs. 5.8 and B.4. This demonstrates once again that using the CM relation upon TD-HSE calculations yields the most reliable dielectric function, polarizablity, and C_6 dispersion coefficient among the methods used in the current study.

THE CLAUSIUS-MOSSOTTI RELATION APPLIED TO COVALENT SOLIDS

To understand the success of the CM relation for general solids beyond rare-gas and ideal ionic crystals, we employ the Tkatchenko/Scheffler (TS) [22] method to compute the polarizability and C_6 dispersion coefficients for atoms in the semiconductors considered here. The TS approach computes the vdW parameters using the ground-state electron density and accurately takes into account the local chemical environment surrounding each atom (the reader is referred to Section 3.4.3 for full details of TS). However, it does not include electrodynamic screening effects [20]. For example, the TS method yields α_{Si} of 35 bohr^3 and C_6^{SiSi} of 280 hartree·bohr^6 for Si bulk – less than a 10% decrease from the corresponding free-atom values. Thus it can be concluded that the reduction in the polarizability of semiconductors arises mainly from the electrodynamic screening. As motivated at the start of this chapter, Eq. (5.2) connects the dielectric function to the unit-cell polarizability by including the collective electrodynamic screening from all the dipoles in the crystal. For crystals with cubic symmetry (which holds for all the solids studied in this work), the Lorentz factor is $L = 4\pi/3$, which yields the CM relation given by Eq. (5.4). The Lorentz factor is merely modified due to short-range effects that are closely related to ionicity (or covalency) and crystal symmetry. We therein conclude that the short-range overlap/hybridization effects play a minor role in modifying the polarizabilities of C, Si, and Ge, and this explains the success of the CM relation for semiconductors.

Having assessed the TD-HSE calculations, we now can utilize the resulting vdW parameters (the polarizability and C_6 coefficients) with the DFT+vdW method for computing the vdW energy.

5.3.2 THE ROLE OF THE VDW ENERGY IN IONIC AND SEMICONDUCTOR SOLIDS

In the DFT+vdW approach, the vdW energy is obtained by summing over all pair-wise interactions via $C_6 R^{-6}$ terms, and added on top of the DFT energy, as discussed in Section 3.4.2. Here the TS approach [22] is employed, with the vdW parameters computed from TD-HSE.

Table 5.2 summarizes the cohesive properties (lattice constants a_0, bulk moduli B_0, and cohesive energies E_0) obtained from the third-order Birch-Murnaghan equation of state (EOS) [88] curve using different DFT functionals for C, Si, and Ge, together with the experimental values. The zero-point vibrational energy (ZPVE) is added to the electronic energies at each volume for

every functional, using quasi-harmonic approximation. All DFT calculations, except HSE06, were performed within full-potential all-electron FHI-aims package [21]. Instead, the HSE06 calculations were carried out using the VASP code [245, 246].

For the (semi-)local and hybrid density functionals, the considered cohesive properties follow the well-known trends: the lattice constants with LDA are too small, the bulk moduli are large, and the cohesive energies are considerably overestimated; while the PBE functional shows an opposite tendency: the lattice constants are too large, the bulk moduli and cohesive energies are underestimated. Overall, HSE06 predicts the cohesive properties in best agreement with experiment, though a noticeable underbinding is found for Ge. The HSE06 functional partially cures self-interaction errors in LDA and GGAs, leading to a significant improvement on the electronic structure for a variety of semiconducting and insulating solids over standard XC functionals [153, 154]. The present study suggests that HSE06 indeed yields improved results for the lattice constants and bulk moduli of semiconductors and ionic solids. However, lattice constants are still somewhat overestimated, while the bulk moduli are underestimated in HSE06 calculations. Furthermore, the HSE06 method leads to underestimated cohesive energies, typically very similar to the PBE functional.

Turning to DFT+vdW approaches, the cohesive properties of C, Si, and Ge were obtained from Birch-Murnaghan EOS fits, with vdW energies included. The vdW contributions (in percentage) to the cohesive properties are tabulated in Table 5.3. As expected, the vdW contribution increases from C to Ge. When the vdW energy is added to the PBE and HSE06 functionals, the overall performance for the cohesive properties of C, Si, and Ge are in better agreement with experiment, with the largest effect found for Ge. For the PBE+vdW calculations, the errors in all the cohesive properties are reduced by a factor of two with respect to PBE . The same improvement is obtained for the HSE06+vdW method, except for the bulk moduli, where the errors remain roughly the same but change the sign (overestimation for HSE06+vdW *versus* underestimation for HSE06).

For diamond, both PBE+vdW and HSE06+vdW yield slight overbinding (see Table 5.2). This can be ascribed to the anharmonic zero-point energy [273], which plays an important role in the description of the EOS curve for light solids but is not accounted for in the current study. For Si and Ge, the PBE+vdW cohesive properties are consistently improved with respect to the PBE results (e.g., the binding curves of Ge plotted in Fig. 5.9). The vdW contribution is

Table 5.2: Calculated cohesive properties of C, Si, and Ge: lattice constants a_0 (Å), cohesive energies E_0 (eV/atom), and bulk moduli B_0 (GPa). The quasi-harmonic zero-point energy was calculated using the PBE phonon spectrum for every functional.

		a_0	E_0	B_0
C	LDA	3.546	−8.76	457
	PBEsol	3.568	−8.10	440
	PBE	3.585	−7.55	423
	HSE06	3.561	−7.43	456
	PBE+vdW	3.576	−7.74	429
	HSE06+vdW	3.554	−7.60	464
	Expt.	3.567	−7.37	443
Si	LDA	5.412	−5.23	96
	PBEsol	5.443	−4.88	93
	PBE	5.481	−4.49	88
	HSE06	5.444	−4.52	97
	PBE+vdW	5.459	−4.77	91
	HSE06+vdW	5.425	−4.78	100
	Expt.	5.430	−4.62	99
Ge	LDA	5.630	−4.54	69
	PBEsol	5.681	−4.11	65
	PBE	5.770	−3.69	56
	HSE06	5.691	−3.68	71
	PBE+vdW	5.718	−3.98	73
	HSE06+vdW	5.653	−3.96	84
	Expt.	5.652	−3.87	76

shown to be system-dependent, increasing along the series of C, Si, and Ge for all the properties studied here; those contributions are 0.34%, 0.4%, and 1.0% to the lattice constants; 2.7%, 5.4%, and 7.8% to the cohesive energies; and 1.4%, 3.0%, and 22.4% to the bulk moduli, respectively. In particular, our results suggest that the influence of vdW interactions becomes most important for the bulk moduli. For the Ge bulk, the change of 1% in the lattice constant, due to the inclusion of long-range vdW interactions, is accompanied by ∼22% change in the bulk modulus. We thus conclude that vdW forces in the studied semiconductors are responsible for part of the errors found in GGA or hybrid functional for describing the cohesive properties, and they can be crucial for certain solids and properties.

BINARY SOLIDS: NACL, MGO, AND GAAS

We have also examined long-range vdW interactions in three binary solids. Here two ionic crystals (NaCl and MgO) and one semiconductor (GaAs) are

Table 5.3: The vdW contributions obtained from PBE+vdW to the cohesive properties with respect to their experimental values (%): lattice constants a_0, cohesive energies E_0, and bulk moduli B_0.

	a_0	E_0	B_0
C	0.3	2.7	1.4
Si	0.4	5.4	3.0
Ge	1.0	7.8	22.4
MgO	0.7	3.5	8.9
GaAs	1.5	8.2	15.9
NaCl	2.9	6.0	25.0

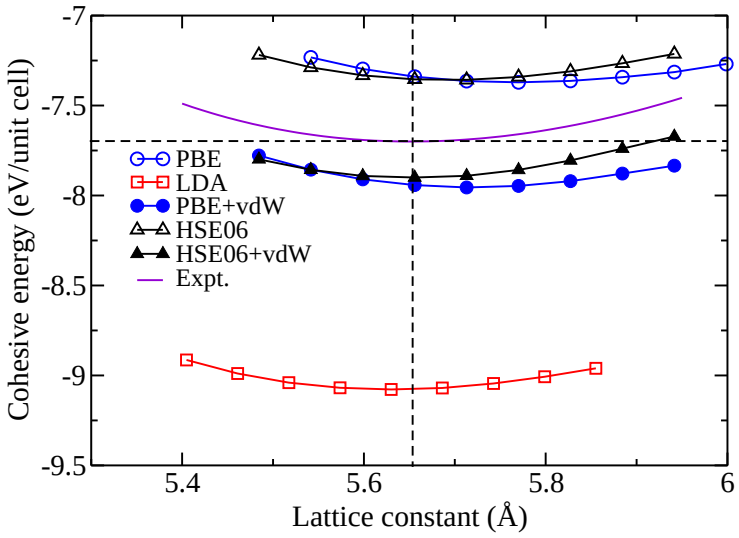

Figure 5.9: The calculated binding curves of Ge bulk employing DFT functionals (LDA, PBE, and HSE06) and DFT+vdW approaches (PBE+vdW and HSE06+vdW). The experimental equilibrium lattice constant and cohesive energy are marked by dashed lines, while the extrapolated experimental binding curve is shown as a purple solid line.

considered. The cohesive properties of those solids are tabulated in Table 5.4, using PBE and HSE06 functionals, together with DFT+vdW on top of the two functionals. For the three solids, PBE yields large deviations from experiment, in particular for NaCl, in which the relative errors are found to be 2.3%, 6%, and 18% in the lattice constant, the cohesive energy, and the bulk modulus, respectively. Although HSE06 predicts better lattice constants and bulk moduli than PBE, this is not the case for cohesive energies. When the vdW energy is added on top of PBE and HSE06, it is found that all the properties are significantly improved with respect to pure PBE or HSE06. The vdW energy contributes around 0.2 eV/atom to the cohesive energy and 9–16 GPa to the

bulk modulus for GaAs, NaCl, and MgO.

Table 5.4: Calculated cohesive properties of MgO, GaAs, and NaCl: lattice constants a_0 (Å), cohesive energies E_0 (eV/atom), and bulk moduli B_0 (GPa). The quasi-harmonic zero-point energy is calculated using the PBE phonon spectrum for every functional.

		a_0	E_0	B_0
MgO	PBE	4.271	−4.91	145
	HSE06	4.223	−4.83	161
	PBE+vdW	4.241	−5.09	160
	HSE06+vdW	4.203	−5.00	177
	Expt.	4.207	−5.12	169
GaAs	PBE	5.755	−3.12	59
	HSE06	5.693	−3.12	71
	PBE+vdW	5.669	−3.39	71
	HSE06+vdW	5.631	−3.39	83
	Expt.	5.648	−3.31	76
NaCl	PBE	5.723	−3.07	23
	HSE06	5.689	−3.07	23
	PBE+vdW	5.562	−3.27	30
	HSE06+vdW	5.543	−3.27	32
	Expt.	5.595	−3.31	28

5.4 SUMMARY

In this chapter, a combined DFT/TDDFT approach was presented for computing the polarizability and C_6 dispersion coefficients for "atoms-in-solids". We obtained accurate vdW coefficients in ionic and semiconductor solids using TDDFT optical-absorption spectra and the Clausius-Mossotti relation for linking the dielectric function to the polarizability. In combination with the cluster extrapolation model as well as available experimental data, we showed that local-field effects are of great importance in the accurate treatment of polarization, and that the CM relation is a good approximation for computing the polarizability and C_6 dispersion coefficients for atoms in semiconductors.

When the long-range vdW energy is included, the DFT+vdW method leads to an improvement of the cohesive properties of ionic (NaCl, MgO) and semiconductor (Si, Ge, and GaAs) solids. Note that a well-known tendency found for most GGAs and hybrid functionals is that they consistently underestimate cohesive energies and bulk moduli, and overestimate lattice constants for a wide variety of semiconductors, ionic solids, and metals (as

illustrated in Chapter 4). We thus conclude that our findings about the importance of the long-range vdW energy are very likely to be valid beyond the benchmark semiconductors and ionic solids presented in this chapter. Given that this combined DFT/TDDFT approach is computationally demanding (due to the calculation of response function in the reciprocal space), our further aim is to develop an accurate and efficient DFT-based method that can compute reliable vdW energies for a wide variety of materials. This can be achieved from a direct evaluation of the polarizability and C_6 dispersion coefficients by combining the TS method with classical electrodynamics, which is the subject of the next chapter.

6 DFT+vdW APPROACH INCLUDING ELECTRODYNAMIC RESPONSE FOR NON-METALLIC SOLIDS

This chapter describes the methodology for computing the long-range van der Waals (vdW) energy with the inclusion of the electrodynamic response and coupling it with standard density-functional theory (DFT) calculations. As introduced in Section 3.4.3, the Tkatchenko/Scheffler (TS) [22] method computes the vdW energy from the ground-state electron density, and it is presently among the best choices for the study of vdW interactions in molecular systems. However, TS lacks the description of the long-range electrodynamic response, which becomes crucial for large systems. An extension of the TS approach to solids is proposed by including electrodynamic response effects in the effective atomic polarizabilities obtained from TS. A brief discussion of implementation details will be given at the end of this chapter.

6.1 THE POINT-DIPOLE MODEL

When atoms interact in a molecule or a solid, dipolar fluctuations of the system will differ from those of free atoms, as the "embedded" atom is influenced by interactions not only with its local environment, but also with more distant fluctuating dipoles. Therefore an accurate calculation of the polarizability requires consideration of both short- and long-range effects. This can be achieved through modeling the environment as a dipole field of quantum harmonic oscillators and solving the classical electrodynamics self-consistent screening (SCS) equations. The point-dipole model will be introduced as a starting point and a more general model will be presented afterwards.

The point-dipole model is one of the simplest choices to treat the polarization of extended systems [274–280]. In this model, a molecule (or a solid) is considered as an arrangement of N atoms, each of which is described by a polarizable dipole. According to classical electrodynamics, the polarization density (dipole moment per unit volume) in such a system satisfies the equation

$$\mathbf{P}(\boldsymbol{r}) = \alpha(\boldsymbol{r})\mathbf{E} + \alpha(\boldsymbol{r}) \int \mathbf{T}(\boldsymbol{r} - \boldsymbol{r}')\mathbf{P}(\boldsymbol{r}')\mathrm{d}\boldsymbol{r}', \tag{6.1}$$

where $\mathbf{E}$ is the constant applied electric field, α is the local polarizability tensor, and $\mathbf{T}$ is the dipole-dipole interaction tensor (propagator). Explicitly, for a molecule, the induced dipole moment μ_i at atom i is given in terms of the applied electric field E_i by

$$\mu_i = \alpha_i[\mathbf{E}_i + \sum_{i \neq j}^{N} \mathbf{T}_{ij}\mu_j], \tag{6.2}$$

where α_i is the atomic polarizability tensor of atom i. The dipole field tensor, $\mathbf{T}_{ij}$, has the following expression

$$\mathbf{T}_{ij} = \nabla_{\boldsymbol{r}_i} \otimes \nabla_{\boldsymbol{r}_j} V(r_{ij}), \tag{6.3}$$

where $V(r_{ij})$ is the Coulomb potential for a system of point charges at the distance r_{ij} between atoms i and j, with $\boldsymbol{r}_i$ and $\boldsymbol{r}_j$ representing the atomic positions. To compute the polarizability, it is convenient to rearrange Eq. (6.2) into a single matrix equation, in the abbreviated notation

$$\mathbf{A}\mu = \mathbf{E}, \tag{6.4}$$

where $\mathbf{A}$ is a $3N \times 3N$ matrix containing the inverse of atomic polarizability tensors along the 3×3 diagonals, while non-diagonal components correspond to coupled dipole interaction tensors. The inversion of $\mathbf{A}$ produces the matrix $\mathbf{B}$ and the induced dipole moment can be rewritten as

$$\mu = \mathbf{B}\mathbf{E}, \tag{6.5}$$

with

$$\mathbf{B} = \mathbf{A}^{-1} = \left(\alpha^{-1} + \sum \mathbf{T}\right)^{-1}. \tag{6.6}$$

With the above formulation, solving Eq. (6.2) will give rise to the polarizability tensor that contains all the interactions with other atoms of the system. For a

molecule, the molecular polarizability is just the response to an uniform field, becoming a sum over all 3×3 submatrices $\mathbf{B}_{ij}$

$$\mu_{\mathrm{mol}} = \left[\sum_{i}^{N} \sum_{j}^{N} \mathbf{B}_{ij} \right] \mathbf{E} = \alpha_{\mathrm{mol}} \mathbf{E}, \tag{6.7}$$

which after contraction yields a 3×3 matrix corresponding to the polarizability tensor. Finally, the averaged molecular polarizability can be determined by diagonalizing α_{mol} to obtain the three principal components and taking the trace.

The point-dipole approximation in Eq. (6.2) is exact for treating the induced dipole moment at large interacting distances. However, it is well-known that this approach leads to infinite molecular polarizability due to the divergence of the dipole interaction tensor $\mathbf{T}_{ij}$ as the interatomic distance r_{ij} is decreased. In reality, atoms should be characterized by dipole-density distributions that lead to finite molecular polarizabilities. This more realistic situation can be described by a collection of quantum harmonic oscillators (QHOs).

6.2 Coupled quantum harmonic oscillators

There have been a number of modified point-dipole models that aim at simulating the damping effect mentioned above, by changing either the dipole field tensor [278] or the polarizability tensor [281]. The idea of the method presented here is to extend the description of point-polarizable dipoles to model a dipole field of quantum harmonic oscillators extended in space and described by dipole-density distributions. The difference between the current approach and the ones proposed in the literature is that by construction our method can naturally avoid the singularity of the polarizability at short distances, and that all the ingredients needed in our method are determined using the electron density from self-consistent electronic structure calculations. The formulation presented here is mainly based on the recent study in our group [20], together with the earlier work of Mayer [279, 280].

Rewriting Eq. (6.3), one finds

$$\mathbf{T}_{ij} = \nabla_{\boldsymbol{r}_i} \otimes \nabla_{\boldsymbol{r}_j} V(r_{ij}) = (r_{ij}^2 \mathbf{I} - 3\boldsymbol{r}_{ij} \otimes \boldsymbol{r}_{ij})/r_{ij}^5, \tag{6.8}$$

where r_{ij} is the distance between atoms i and j, $\boldsymbol{r}_{ij} \otimes \boldsymbol{r}_{ij}$ represents the position tensor product with 3×3 Cartesian components connecting atom i to j, and $\mathbf{I}$ is

the identify matrix. Clearly, the Coulomb potential $V(r_{ij})$ diverges as $r_{ij} \to 0$, and so does $\mathbf{T}_{ij}$.

The problem can be solved via renormalization of the tensor expression. If one considers the dipole field modeled as a collection of QHOs, each of which is represented as a Gaussian distribution of the form $n(\boldsymbol{r}) = \left(\pi^{3/2}R^3\right)^{-1} \exp\left[-r^2/(2\sigma)^2\right]$ (with σ the width of the distribution), the interaction between two atoms is then replaced by two Gaussian distributions rather than two point dipoles. The Gaussian distribution is taken to renormalize the tensors, given by $\mathrm{erf}[r_{ij}/\sigma_{ij}]/r_{ij}$, where $\sigma_{ij} = \sqrt{\sigma_i^2 + \sigma_j^2}$ is an effective width related to the Gaussian widths of interacting atoms i and j. As a result, the Coulomb potential has a renormalized form of $W(r_{ij}) = \mathrm{erf}[r_{ij}/\sigma_{ij}]/r_{ij}$, damped at short distances. The dipole propagator $\mathbf{T}_{ij}$ is then given by

$$\mathbf{T}_{ij} = \nabla_{\boldsymbol{r}_i} \otimes \nabla_{\boldsymbol{r}_j} W(r_{ij}) = \frac{3\boldsymbol{r}_{ij} \otimes \boldsymbol{r}_{ij} - r_{ij}^2 \mathbf{I}}{r_{ij}^5} \left[\mathrm{erf}\left(\frac{r_{ij}}{\sigma_{ij}}\right) - \frac{2}{\sqrt{\pi}} \frac{r_{ij}}{\sigma_{ij}} e^{-\left(\frac{r_{ij}}{\sigma_{ij}}\right)^2} \right] - \frac{4}{\sqrt{\pi}} \frac{1}{(\sigma_{ij})^3} \frac{\boldsymbol{r}_{ij} \otimes \boldsymbol{r}_{ij}}{r_{ij}^2} e^{-\left(\frac{r_{ij}}{\sigma_{ij}}\right)^2}. \tag{6.9}$$

The width σ_{ij} of the Gaussian function is derived from the dipole self-energy, i.e., the zero-distance limit of the classical dipole-dipole interaction for a given frequency of the electric field: $-\frac{1}{2}\lim_{r_{ij}\to 0} \mathbf{p}_i \mathbf{T}_{ij} \mathbf{p}_i = \frac{1}{2}\mathbf{p}_i[(\sqrt{2/\pi}/3{\sigma_{ij}}^3)\mathbf{I}]\mathbf{p}_i$. Under the condition $\mathbf{T}_{ii} = -\alpha_i^{-1}$, one can further write the isotropic atomic polarizability in terms of the Gaussian width

$$\alpha_{\mathrm{iso}} = 3\sqrt{\frac{\pi}{2}}\,(\sigma_{ij})^3\,. \tag{6.10}$$

Based on the above model, the divergence of dipole-dipole interactions is eliminated. Note that Eq. (6.10) is important from a theoretical point of view: it relates the Gaussian width to the atomic polarizability that is solely influenced by local environment effects, thus providing an efficient way to estimate other related properties of atoms. Therefore we stress that the coupled QHOs require hybridized polarizabilities as an input, which ensures that the short-range hybridization/overlap effects are accounted for. This can be achieved by making use of the TS method introduced in Section 3.4.3 and the implementation is the topic of the next section.

6.3 IMPLEMENTATION DETAILS

As introduced in the previous section, we now have a method for computing polarizability for a system of coupled QHOs. One can further write the polarizability tensor based on the SCS equation (Eq. 6.2) as

$$\alpha_i^{\mathrm{SCS}}(\boldsymbol{r}, i\omega) = \alpha_i^0(\boldsymbol{r}, i\omega) + \alpha_i^0(\boldsymbol{r}, i\omega) \sum_{i \neq j}^{N} \mathbf{T}_{ij} \alpha_j^{\mathrm{SCS}}(\boldsymbol{r}', i\omega). \tag{6.11}$$

where $\alpha_i^{\mathrm{SCS}}(\boldsymbol{r}, i\omega)$ is the fully screened atomic polarizability tensor (for a given frequency of the electric field) that we wish to obtain through solving the SCS equation, and α_i^0 is defined as an input tensor.

The scheme proposed here is to take α_i^0 from the TS method, i.e., $\alpha_i^0 = \alpha_i^{\mathrm{TS}}$, and proceed with the SCS step via the above equation, such that both the short-range hybridization captured by TS and the electrodynamic screening captured by SCS, are taken into account accurately and efficiently [20].

If one considers Eq. (6.4) for a molecule of N atoms, the matrix $\mathbf{A}$ reads

$$\mathbf{A} = \begin{pmatrix} \alpha_1^{-1} & \mathbf{T}_{12} & \dots & \mathbf{T}_{1N} \\ \mathbf{T}_{21} & \alpha_2^{-1} & \dots & \mathbf{T}_{2N} \\ \dots & \dots & \dots & \dots \\ \mathbf{T}_{N1} & \mathbf{T}_{N2} & \dots & \alpha_N^{-1} \end{pmatrix}, \tag{6.12}$$

where α_i represents the polarizability tensor of atom i, taken as α_i^{TS} with its isotropic value on the diagonal, and $\mathbf{T}_{ij}$ is the dipole tensor connecting atoms i and j $(i, j = 1, 2, \dots, N)$, as expressed in Eq. (6.9). Note that both α and $\mathbf{T}_{ij}$ are 3×3 matrices.

For a periodic system, due to periodic boundary conditions, a given atom not only interacts with the neighboring atoms in the same unit cell, but also those from its image cells. Thus Eq. (6.12) becomes

$$\mathbf{A} = \begin{pmatrix} \alpha_1^{-1} + \sum \mathbf{T}_{11'} & \mathbf{T}_{12} + \sum \mathbf{T}_{12'} & \dots & \mathbf{T}_{1N} + \sum \mathbf{T}_{1N'} \\ \mathbf{T}_{21} + \sum \mathbf{T}_{21'} & \alpha_2^{-1} + \sum \mathbf{T}_{22'} & \dots & \mathbf{T}_{2N} + \sum \mathbf{T}_{2N'} \\ \dots & \dots & \dots & \dots \\ \mathbf{T}_{N1} + \sum \mathbf{T}_{N1'} & \mathbf{T}_{N2} + \sum \mathbf{T}_{N2'} & \dots & \alpha_N^{-1} + \sum \mathbf{T}_{NN'} \end{pmatrix}, \tag{6.13}$$

where i' and j' denote the atoms from the image cell $(i', j' = 1', 2', \dots, N')$. The interactions of an atom with its own images are contained in the diagonals and those with the images of other atoms are located in the non-diagonal parts. The

B matrix is defined as the inversion of **A**. After diagonalization, one can obtain the three principle components of the total polarization matrix for a molecule or a crystal, and the average value corresponds to the average of the trace, as given by

$$\alpha^{\mathrm{SCS}} = (\alpha_{\mathrm{xx}} + \alpha_{\mathrm{yy}} + \alpha_{\mathrm{zz}})/3. \tag{6.14}$$

Each atom i is characterized by its position $\boldsymbol{r}_i = \{x_i, y_i, z_i\}$. In principle, to implement the above procedure, one needs only the element name and its coordinates as the input, such that the effective polarizability α_i^{TS} obtained from the TS approach can be utilized.

To obtain the C_6 dispersion coefficient, frequency-dependent dipolar polarizability calculations must be carried out. In this thesis, the Gauss-Legendre integral approach was taken, and a converged integral can be obtained by using 20 frequencies. The resulting polarizability $\alpha^{\mathrm{SCS}}(i\omega)$ now contain both short-range (via the TS approach) and electrodynamic (via the SCS equation) screening.

So far, the proposed DFT+vdW$^{\mathrm{TS+SCS}}$ methodology has been introduced. To assess the accuracy and applicability of this method, calculations are performed for a wide variety of semiconductors, as described in the next chapter.

7 THE ROLE OF VDW FORCES IN THE COHESIVE PROPERTIES OF 23 SEMICONDUCTORS

In this chapter, the validity of the DFT+vdW$^{\text{TS+SCS}}$ method introduced in Chapter 6 will be assessed in comparison with time-dependent density-functional theory benchmark data for the vdW parameters (the polarizability and C_6 dispersion coefficients) of C, Si, and Ge. Then, the broad applicability of this approach will be demonstrated for 20 binary semiconductors. Thereafter, the influence of the vdW energy on the cohesive properties will be carefully discussed for all 23 solids.

7.1 VERIFICATION OF THE DFT+VDW$^{\text{TS+SCS}}$ METHOD FOR THE VDW PARAMETERS OF C, SI, AND GE

As introduced in previous chapters, the key quantities in the study of van der Waals (vdW) interactions are the dispersion coefficients. The required ingredient to compute the C_6 dispersion coefficient is the dynamic dipolar polarizability at imaginary frequencies $\alpha(i\omega)$, which is used in the Casimir-Polder integral. One possibility is to directly model the polarizability from microscopic theory of polarization (see Chapter 6). An alternative way is to first obtain the macroscopic dielectric function $\varepsilon_{\text{M}}(\omega)$ theoretically or experimentally and then use the connection between the polarizability and the dielectric function based upon the Clausius-Mossotti (CM) relation for finite-gap systems.

Obtaining accurate vdW parameters, including the polarizability and C_6 dispersion coefficients, is a very demanding task for atoms in solids both experimentally and theoretically. This explains the fact that reliable data are still

lacking for practical calculations of vdW energies in condensed-matter systems, which motivated a part of the current thesis. Aiming at accurately yet efficiently treating vdW interactions in solids, we proposed a DFT-based vdW approach in the previous chapter, termed as DFT+vdW$^{\text{TS+SCS}}$.[1] To assess this approach, we shall first apply it to simple semiconductors, and then extend to binary semiconductors. We will use the available experimental data to validate the method developed here.

7.1.1 Experimental polarizabilities from the single oscillator model

In addition to the two approaches discussed in Chapters 5 and 6, we have computed the polarizability and C_6 dispersion coefficients using experimental refractive-index data based on the single oscillator (SO) approximation. It is worthy of mentioning again that there is very limited experimental knowledge about the vdW parameters for solids; thus the comparison between theory and experiment is important. To the best of our knowledge, the SO model, having been applied to more than 100 different types of condensed-matter systems, is the only available experimental source of data that can be used to obtain the polarizabilities for a wide range of solids. In this method, a simple connection between the refractive index $n(\omega)$ and two SO parameters (E_0 and $E_{\rm d}$) is introduced as

$$n^2(\omega) - 1 = \frac{E_{\rm d} E_0}{E_0^2 - \omega^2}, \tag{7.1}$$

where ω is the photon energy, E_0 is the single oscillator energy, and $E_{\rm d}$ is the dispersion energy, which is a measure of the strength of interband optical transitions [220].[2] Note that the SO parameters have fundamental physical significance: E_0 can be considered as an "effective" energy gap related to the direct band gap, and $E_{\rm d}$ is an interband strength parameter, which is closely related to the chemical-bonding nature of the material. It is clear that the performance of the SO model relies greatly upon the accuracy of experimental optical spectra. In reality, reliable optical-spectrum measurement is a difficult task, as a large enough spectral energy range must be measured, which is rarely done.

[1] Note that "DFT+vdW" is a concept that computes vdW parameters and then includes the resulting long-range vdW energy to the standard DFT energy within LDA, GGAs, etc. (e.g., with the PBE functional, PBE+vdW). The superscript of "DFT+vdW" is used to specify a given method for computing vdW parameters, unless otherwise stated.

[2] Experimental verification of the single oscillator approximation can be seen by plotting $1/(n^2-1)$ versus ω^2, with a linear relation being found for all materials studied in a reasonable range [220].

In the following, the vdW parameters for the three model systems (C, Si, and Ge) will be discussed using four different methods, among which the TD-HSE results are taken as the reference for the polarizabilities and C_6 dispersion coefficients, as explained in Chapter 5.

7.1.2 VDW PARAMETERS AT THE EQUILIBRIUM LATTICE CONSTANT

To assess the proposed DFT+vdW approach, four schemes were employed for obtaining the vdW parameters, namely TD-HSE, SO, TS, and TS+SCS. For the SO method, the dielectric function is obtained via Eq. (7.1) using the reported SO parameters (see Table D.2) for each solid. The four schemes are summarized below:

- TD-HSE: obtains the dielectric function from TDDFT calculations and uses the CM relation (see Chapter 5)
- SO: obtains the dielectric function from experimental refractive-index data and uses the CM relation (see Section 7.1)
- TS: directly computes the polarizability from the DFT electron density (see Section 3.4.3)
- TS+SCS: uses the effective atomic polarizability from the TS method and solves the classical electrodynamics self-consistent screening (SCS) equations (see Chapter 6)

Table 7.1: Calculated static polarizabilities (bohr^3/unit cell) of C, Si, and Ge. Four approaches are employed: TD-HSE, the single oscillator (SO) model using experimental optical spectra, the Tkatchenko/Scheffler (TS) method, and TS coupled with self-consistent screening equations (TS+SCS). All data are calculated at the experimental volumes.

	TD-HSE	SO	TS	TS+SCS
C	11.1	11.0	21.8	14.1
Si	50.0	50.8	69.6	47.7
Ge	60.6	60.7	77.9	53.6

The calculated static polarizabilities are tabulated in Table 7.1 for C, Si, and Ge using the four approaches, and the corresponding curves are plotted in Fig. 7.1, together with the C_6 dispersion coefficients on the right-hand side. The TDDFT calculations are considered as the reference. It can be seen that there is excellent agreement between the SO and the TD-HSE results for

the static polarizabilities of all the three solids. However, the SO approach leads to noticeable underestimation of C_6 coefficients when compared with the TD-HSE values. This may be attributed to the integrated nature of the dispersion coefficient, requiring a large enough spectral range in experimental measurements, which is rarely available in practice.

Turning to the two DFT-based methods, there is a large reduction in both the polarizability and C_6 dispersion coefficients upon using the TS+SCS approach when compared with TS. Upon the inclusion of electrodynamic screening in TS+SCS, better agreement with the TD-HSE results is found for the diamond-type solids, as depicted in Fig. 7.1. For C and Si, the TS+SCS and TD-HSE values are in excellent agreement, whereas an underestimation (12% with respect to the TD-HSE value) is observed for Ge using the TS+SCS model. As described in Chapter 6, TS+SCS is based on mapping the system onto the atom-centered quantum harmonic oscillator (QHO), and thus is only valid for non-metallic systems. This may account for the deviation seen in the low band-gap semiconductor, such as Ge.

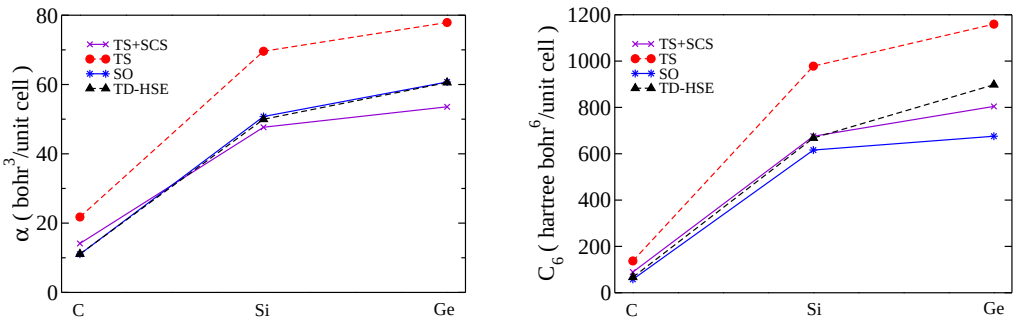

Figure 7.1: Calculated static polarizabilities (left panel) and C_6 dispersion coefficients (right panel) of C, Si, and Ge using the TD-HSE, SO, TS, and TS+SCS approaches. All data are calculated at the experimental volumes.

7.1.3 Dependence of vdW parameters on the lattice constant

The dependence of the polarizability and C_6 dispersion coefficients on the unit-cell volume has been demonstrated in Chapter 5, and capturing this behavior is necessary for an accurate treatment of cohesive properties of solids. The calculated polarizabilities and C_6 coefficients are plotted as functions of the lattice constants of C, Si, and Ge in Figs. 7.2 – 7.4, respectively. Five methods are compared: TD-HSE and TD-LDA using the CM relation, TD-LDA from the cluster extrapolation (CE) model, TS, and TS+SCS. The numerical results of the static polarizabilities and the C_6 coefficients (e.g., using the TD-HSE and

TS+SCS methods) are presented in Tables D.3 and D.4, respectively.

It is found that both the polarizability and C_6 dispersion coefficients increase with increasing lattice constant (except when using TS), showing a linear dependence over the studied volume range. The same conclusion holds for the other four methods used for the three solids. Here we emphasize that the TD-HSE values are considered as reference data. Comparing TS with TD-HSE, one finds that TS considerably overestimates the polarizabilities and C_6 coefficients. Apart from giving too large values for the vdW parameters, the TS approach cannot reproduce their volume dependence. A comparison of TS+SCS with TD-HSE shows good agreement between them for the three model systems. In contrast to the TS scheme, TS+SCS improves the agreement with TD-HSE by more than a factor of two. Thus it can be concluded that the electrodynamic screening, which is missing in the original TS method, has an important impact on vdW parameters, and an accurate treatment of vdW interactions requires the inclusion of both short- and long-range environment effects. It should be mentioned that an increase in the lattice constant results in an increased deviation of the vdW parameters obtained using TS+SCS from the TD-HSE reference data, in particular for Si and Ge, as can be seen in Figs 7.3 and 7.4. This can be ascribed to the fact that the band gap decreases with increasing lattice constant. Accordingly, when the system becomes metallic at sufficiently large unit-cell volume, the TS+SCS model based upon coupled QHO is no longer valid.

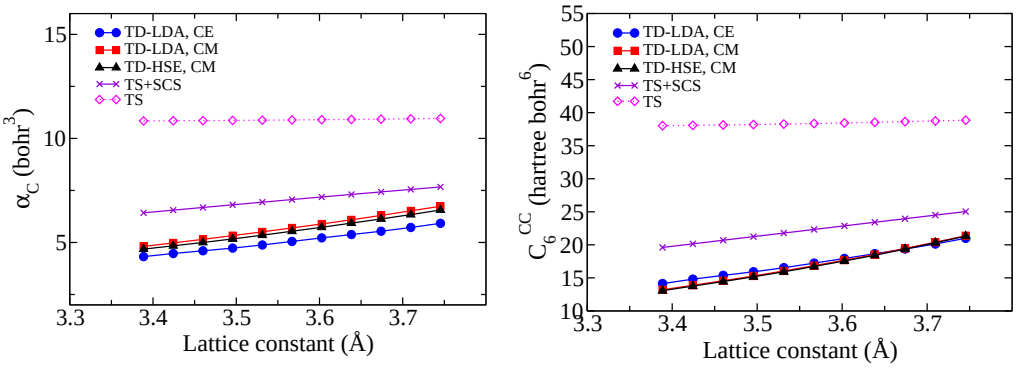

Figure 7.2: Calculated static polarizabilities (left panel) and C_6 dispersion coefficients (right panel) per atom as a function of the lattice constant of diamond using five methods: TD-HSE and TD-LDA using the Clausius-Mossotti (CM) relation, TD-LDA using the cluster extrapolation (CE) model, TS, and TS+SCS.

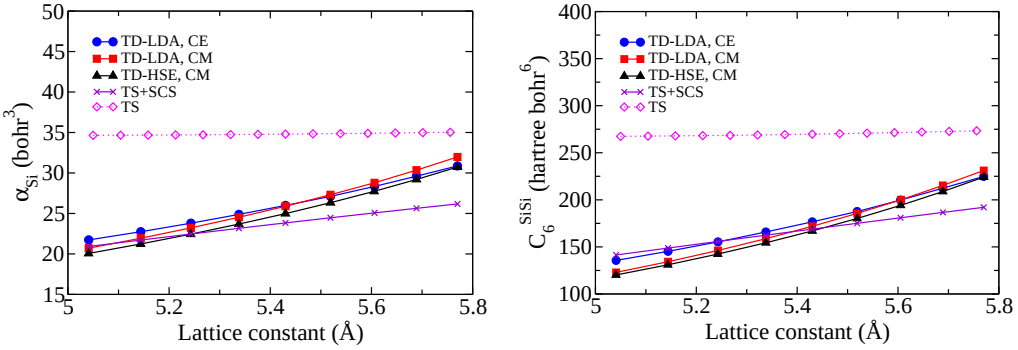

Figure 7.3: Calculated static polarizabilities (left panel) and C_6 dispersion coefficients (right panel) per atom as a function of the lattice constant of silicon.

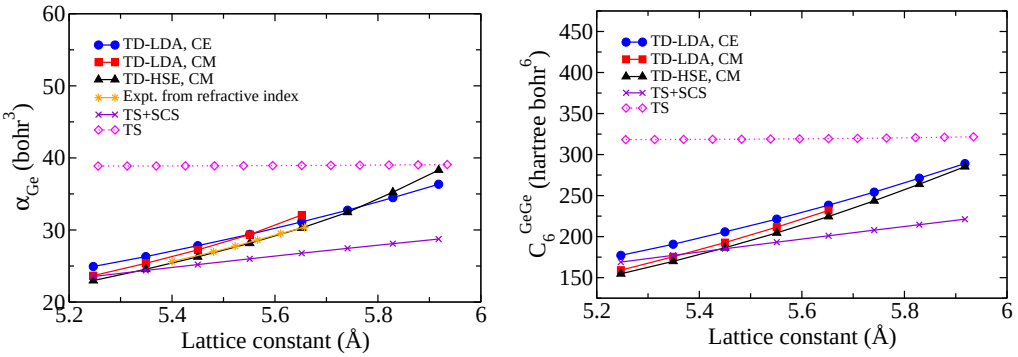

Figure 7.4: Calculated static polarizabilities (left panel) and C_6 dispersion coefficients (right panel) per atom as a function of the lattice constant of germanium. The experimental data are taken from Ref. [267] by Cardona and co-authors.

7.1.4 Screened vdW energy

Having assessed reliable vdW parameters, we can now compute the vdW energy using the DFT+vdW method introduced in Section 3.4.3. In this framework, the vdW energy is computed by summing over all the pair-wise interactions via $C_6 R^{-6}$ terms, and then is added to the DFT energy. It should be noted again that in this context "DFT" denotes the specific exchange-correlation (XC) functional employed in a DFT calculation (e.g., the PBE functional, corresponding to "PBE+vdW"), and the superscript of "DFT+vdW" specifies the method for computing vdW parameters. The present DFT calculations were performed using the PBE functional [94], implemented in the FHI-aims all-electron package [21]. The zero-point vibrational energy (ZPVE) was added to the ground-state energy at each volume within the harmonic approximation,

as it can affect the cohesion of solids.[3]

Table C.8 summarizes the cohesive properties (lattice constants, cohesive energies, and bulk moduli) of C, Si, and Ge determined from the Birch-Murnaghan equation of state fits, employing PBE, PBE+vdW^{TS}, and PBE+vdW^{TS+SCS}, together with experimental values. As already shown in Chapter 5, the cohesive properties of the three solids are consistently better predicted with the inclusion of the vdW energy on top of the PBE energy, using the C_6 dispersion coefficients computed from the combined DFT/TDDFT approach. Turning to the two DFT+vdW methods, in which the vdW parameters are determined from either the TS+SCS or the TS schemes, the contributions of the vdW energies to the cohesive properties are tabulated in Table 7.2 and depicted in Fig. 7.5. It can be seen that the vdW contribution

Table 7.2: The vdW contribution to the cohesive properties of C, Si, and Ge using the two DFT+vdW methods, TS and TS+SCS coupled with the PBE functional: lattice constants a_0 (Å), cohesive energies E_0 (eV/unit cell), and bulk moduli B_0 (GPa). The numbers in parentheses are the corresponding absolute relative values with respect to experiment (%).

	a_0		E_0		B_0	
	TS+SCS	TS	TS+SCS	TS	TS+SCS	TS
C	0.008	0.019	−0.182	−0.199	4.57	7.56
	(0.24)	(0.54)	(2.47)	(2.71)	(1.03)	(1.71)
Si	0.042	0.024	−0.285	−0.278	6.05	1.71
	(0.77)	(0.43)	(6.16)	(6.01)	(6.10)	(1.72)
Ge	0.060	0.030	−0.262	−0.287	7.02	5.63
	(1.07)	(0.53)	(6.77)	(7.42)	(9.11)	(7.31)

increases from C to Ge when using the PBE+vdW^{TS+SCS} method for all the properties studied here: 0.2%, 0.8%, and 1.1% to the lattice constants; 2.5%, 6.2%, and 6.8% to the cohesive energies; and 1.0%, 6.1%, and 9.1% to the bulk moduli, respectively. This is consistent with the TD-HSE results shown on the left-hand side of Fig. 7.5, though an underestimation (with respect to the TD-HSE value) of the vdW energy is observed for Ge using TS+SCS. This is most likely due to the semi-metallic nature of Ge, as discussed before. The increasing contribution of vdW interactions can be explained by the fact that the solids become more polarizable in the sequence of C-Si-Ge. In contrast, this feature of vdW interactions cannot be correctly reproduced using the TS method. Firstly, due to the lack of the long-range screening, the volume-dependence

[3]The reader is redirected to Section 4.3 for a detailed discussion of the influence of ZPVE upon cohesive properties of solids.

is not captured in the TS approach for the polarizability and C_6 dispersion coefficients. Secondly, the vdW radius (through the damping function that decays exponentially with separation) affects the vdW energy even more than the C_6 dispersion coefficients. Thus care needs to be taken in obtaining both screened C_6 and vdW radius. Our study suggests the TS+SCS method can accurately treat both short- and long-range environment effects. So far, it has

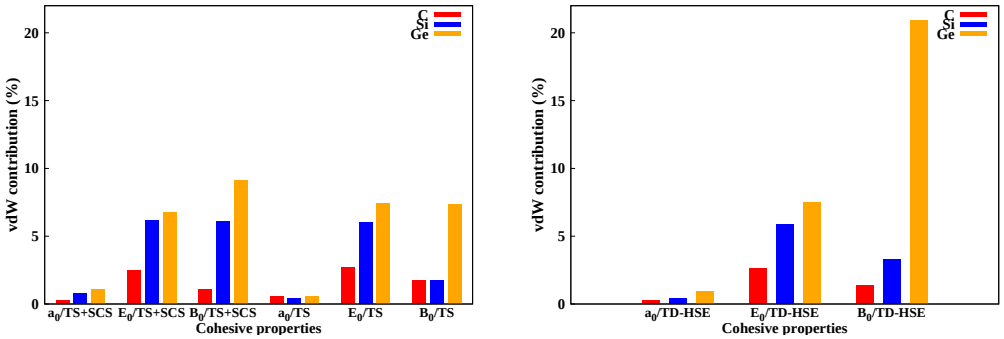

Figure 7.5: The vdW contribution to the cohesive properties (lattice constants a_0, cohesive energies E_0, and bulk moduli B_0) of C, Si, and Ge using the PBE+vdW$^{\text{TS+SCS}}$ and PBE+vdW$^{\text{TS}}$ methods. The corresponding PBE+vdW$^{\text{TD-HSE}}$ results are shown on the right-hand side.

been verified that the DFT+vdW$^{\text{TS+SCS}}$ approach is an efficient yet accurate way to deal with long-range vdW interactions in diamond-type solids, with low computational cost and reasonable accuracy. Screening effects are shown to play a very important role in studying vdW interactions in solids. The focus of the next section is to illustrate this by applying the DFT+vdW$^{\text{TS+SCS}}$ method to binary compounds.

7.2 VDW INTERACTIONS IN BINARY SEMICONDUCTORS

As presented in Chapter 4, for some of zincblende semiconductors, local and semi-local density functionals can yield significant deviations in the cohesive properties from experimental data. In the zincblende structure, the arrangement of atoms is the same as the diamond structure, but with two different elements at the lattice sites. This ensures that all the approximations (e.g., cubic symmetry and finite gap) used for treating C, Si, and Ge remain valid for this class of solids as well. Therefore these binary compounds can be considered as probes for examining the applicability of the proposed DFT+vdW$^{\text{TS+SCS}}$ approach for a variety of solids with increasing complexity.

7.2.1 IIIA–VA COMPOUNDS

We have chosen 13 semiconductors from the IIIA–VA group: BN, BP, BAs, AlP, AlAs, AlSb, GaN, GaP, GaAs, GaSb, InP, InAs, and InSb. The experimental cohesive properties of the above solids are plotted in Fig. 7.6, showing the inverse correlation of the lattice constants with the bulk moduli (left panel) as well as the cohesive energies (right panel).

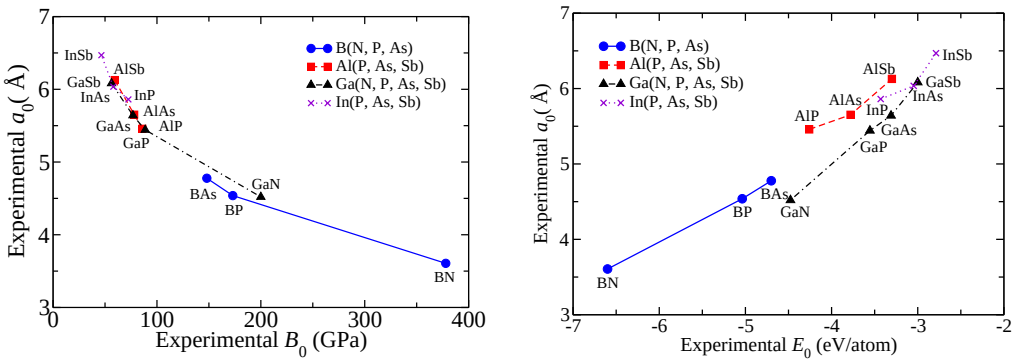

Figure 7.6: The experimental lattice constant a_0 as a function of the bulk modulus B_0 (left panel) and the cohesive energy E_0 (right panel) of the IIIA–VA group semiconductors. Lines are drawn to guide the eye.

As already discussed in Chapter 4, the deviation of the calculated lattice constants from experimental values increases with increasing nuclear mass, and this trend is consistently reproduced by the PBE functional rather than the LDA or M06-L functional. The same conclusion can be made for bulk moduli and cohesive energies. In the previous section, it has been shown that for diamond-type crystals the vdW contribution to the cohesion increases in the order of C-Si-Ge. This, together with the fact that the errors in the cohesive properties increase with system size when using the PBE functional, suggests that the increased deviation is due to the more important role of long-range vdW interactions for heavier semiconductors. To elucidate this, we compare the polarizability and C_6 dispersion coefficients obtained from the TS+SCS method for the IIIA–VA group solids ordered by increasing mass, as depicted in Fig. 7.7. It can be seen that both the polarizability and dispersion coefficients increase along the column of the periodic table.

Furthermore, the volume dependence has been studied, as plotted in Fig. D.1, with vdW energies computed using the volume-dependent vdW parameters at each value of the lattice constant. The vdW contribution to the cohesive energies, computed as the difference between PBE and PBE+vdW$^{\text{TS+SCS}}$ results, is depicted in Fig. 7.8 with respect to the experimental data. It can be clearly

seen that the vdW contribution increases with an increase in the mass, e.g., along the series BN-BP-BAs, AlP-AlAs-AlSb, GaN-GaP-GaAs-GaSb, as well as, InP-InAs-InSb; the average contribution being about 7% of the experimental cohesive energies .

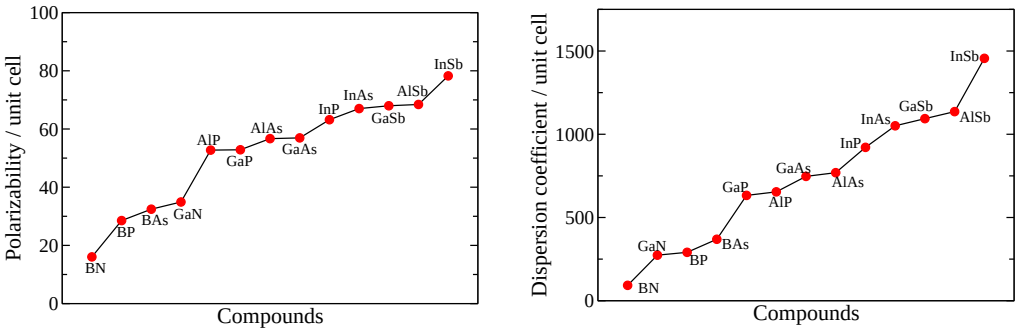

Figure 7.7: Calculated static polarizabilities (bohr^3) and C_6 dispersion coefficients (hartree·bohr^6) per unit cell for 13 IIIA–VA group solids using the TS+SCS method. All values are calculated at the experimental unit-cell volumes.

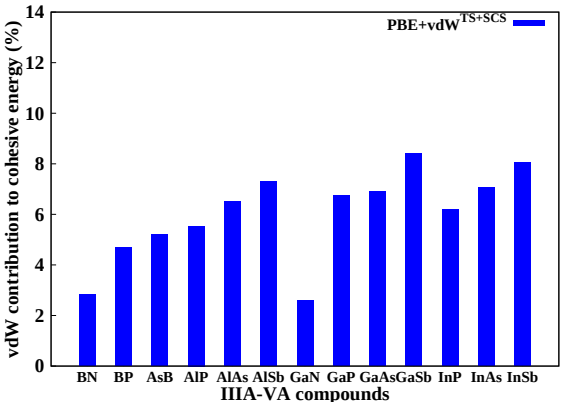

Figure 7.8: The vdW contribution to the cohesive energies of the IIIA–VA group solids using the DFT+vdW^{TS+SCS} method.

7.2.2 IIB–VIA COMPOUNDS

Six solids were studied in the IIB–VIA group: ZnS, ZnSe, ZnTe, CdS, CdSe, and CdTe. The experimental cohesive properties of the above compounds are plotted in Fig. 7.9: the lattice constant versus the bulk modulus as well as the cohesive energy.

To have an overview of the performance of the proposed TS+SCS model for the polarizability, we compare it with the SO model that is based upon experimental information. In the present database, there are 10 solids for which

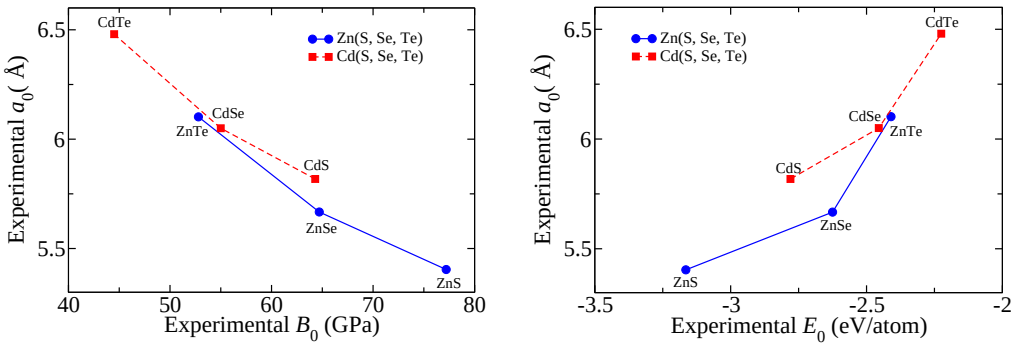

Figure 7.9: The experimental lattice constant a_0 as a function of the bulk modulus B_0 (left panel) and the cohesive energy E_0 (right panel) of the IIB–VIA group semiconductors. Lines are drawn to guide the eye.

the SO parameters are available from experimental refractive-index data [220]. The static polarizabilities and dispersion coefficients have been compared using four approaches: the SO model, the DFT-based TS+SCS and TS methods, together with the TD-HSE benchmark, which is only available for the diamond-type solids and GaAs, as shown in Fig. 7.10. The TD-HSE values are accurate, but have a high computational cost. The SO model yields a good prediction for the static polarizability, however, C_6 dispersion coefficients are underestimated due to the limited spectral range of experimental measurements. The TS approach is found to overestimate both the polarizability and dispersion coefficients, in line with its neglect of the electrodynamic screening. Finally, the TS+SCS method yields good results at a rather low computational cost: the vdW parameters are considerably reduced with respect to the TS results (due to the inclusion of the electrodynamic response), resulting in much better agreement with the available TDDFT benchmark data. It is also important to mention that all the above methods show similar trends for both the polarizability and C_6 dispersion coefficients.

The polarizability and C_6 dispersion coefficients obtained from the TS+SCS method are compared for the IIB–VIA group solids in Fig. 7.11. As for the IIIA–VA solids, an increase of the polarizability and C_6 dispersion coefficients is found along the same column of the periodic table, indicating that the vdW energy increases with the unit-cell volume. The volume dependence of the vdW parameters of the above compounds is shown in Fig. D.1. The vdW contribution to the cohesive energies, i.e., the change between the PBE and PBE+vdW$^{\text{TS+SCS}}$ results, is depicted in Fig. 7.12. The same conclusion can be made as for the IIIA–VA group that the vdW contribution becomes more important for heavy semiconductors. An average contribution of 8% is

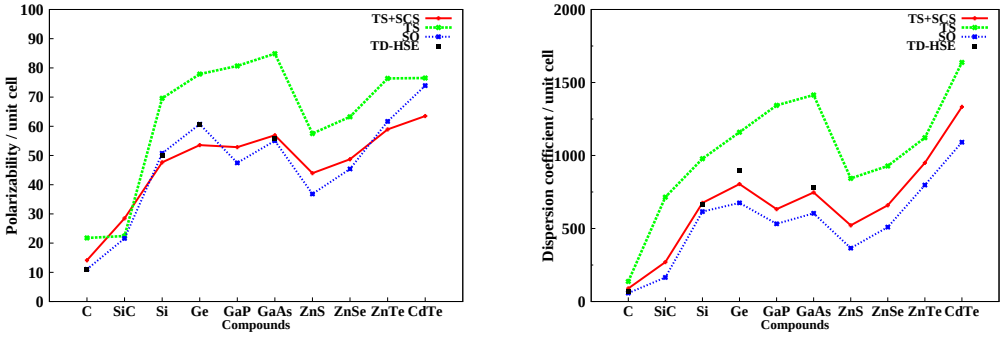

Figure 7.10: Calculated static polarizabilities (bohr^3) and C_6 dispersion coefficients (hartree·bohr^6) per unit cell for ten semiconductor solids using TD-HSE, TS, and TS+SCS, together with the SO model determined from the experimental optical spectra. All values are calculated at the experimental unit-cell volumes.

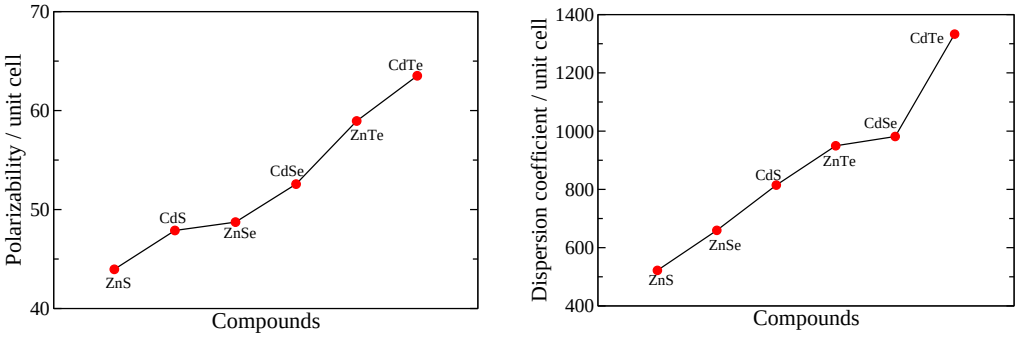

Figure 7.11: Calculated static polarizabilities (bohr^3) and C_6 dispersion coefficients (hartree·bohr^6) per unit cell of six IIB–VIA group solids using the TS+SCS model. All values are calculated at the experimental unit-cell volumes.

obtained with respect to experiment for IIB–VIA semiconductors.

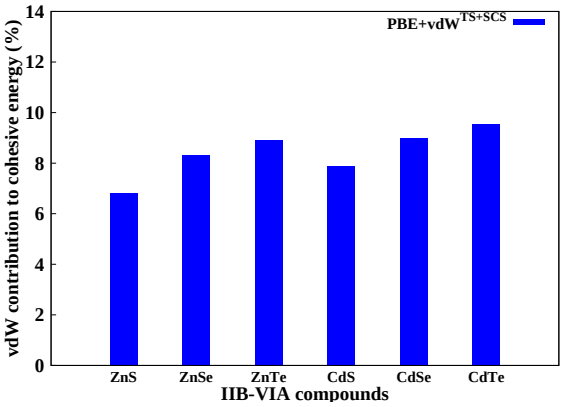

Figure 7.12: The vdW contribution to the cohesive energies of the IIB–VIA group solids using the DFT+vdW$^{\text{TS+SCS}}$ method.

7.3 Cohesive properties with the inclusion of the vdW energy

As already mentioned at the start of this chapter, (semi-)local XC functionals yield large deviations for the cohesive properties of the presently studied semiconductor solids. A plot of DFT versus experimental cohesive properties is shown in Fig. 7.13, illustrating the performance of the three functionals employed in this thesis, while the errors are summarized in Table 7.3.

In general, LDA underestimates lattice constants and overbinds in nearly all cases, while PBE and M06-L show the opposite trend. LDA leads to the best predictions of the lattice constants and the bulk moduli. The M06-L and PBE functionals have similar statistical errors in the lattice constants, though the former performs slightly better for light-mass solids but worse for heavy ones. This is most likely due to a better description of middle-range correlation and the lack of long-range correlation in the M06-L functional form [145, 146]. For the bulk moduli, the mean absolute relative errors (MAREs) are about 4%, 12%, and 16% for LDA, M06-L and PBE, respectively. Turning to the cohesive energies, those evaluated using the LDA functional are dramatically overestimated, with the MAE being 0.7 eV/atom or 19% of the experimental value. Both PBE and M06-L, cure a large part of this error, with the MAEs of 0.2 eV or 5.8% and 0.1 eV or 2.6%, respectively.

Interestingly, a characteristic feature of the PBE functional is an increased error with increasing lattice constant (or mass), as can be seen, e.g., along the series AlP-AlAs-AlSb, GaN-GaP-GaAs-GaSb, as well as, InP-InAs-InSb. This also applies to the bulk moduli and the cohesive energies.

Turning to the PBE+vdW$^{\text{TS+SCS}}$ method, the cohesive properties, obtained from the fits to the Birch-Murnaghan equation of state, are summarized in Tables C.9 to C.12 for the IIIA–VA group semiconductors and Table C.13 for the IIB–VIA group. The PBE and PBE+vdW$^{\text{TS+SCS}}$ results are compared with respect to experiment. The errors are summarized in Table 7.3.

Figure 7.14 shows the relative errors in the bulk moduli (left panel) and the cohesive energies (right panel) versus those in the lattice constants for 23 semiconductor solids (including C, Si, SiC, and Ge), using the LDA, PBE, and M06-L functionals, together with the PBE+vdW method. As can be clearly seen in the plots, the inclusion of long-range vdW interactions systematically improves the lattice constants, the cohesive energies, and the bulk moduli, in better agreement with experiment. The MAREs are 0.7%, 3.2%, and 8.4% for the lattice constants, cohesive energies, and bulk moduli, and the corresponding

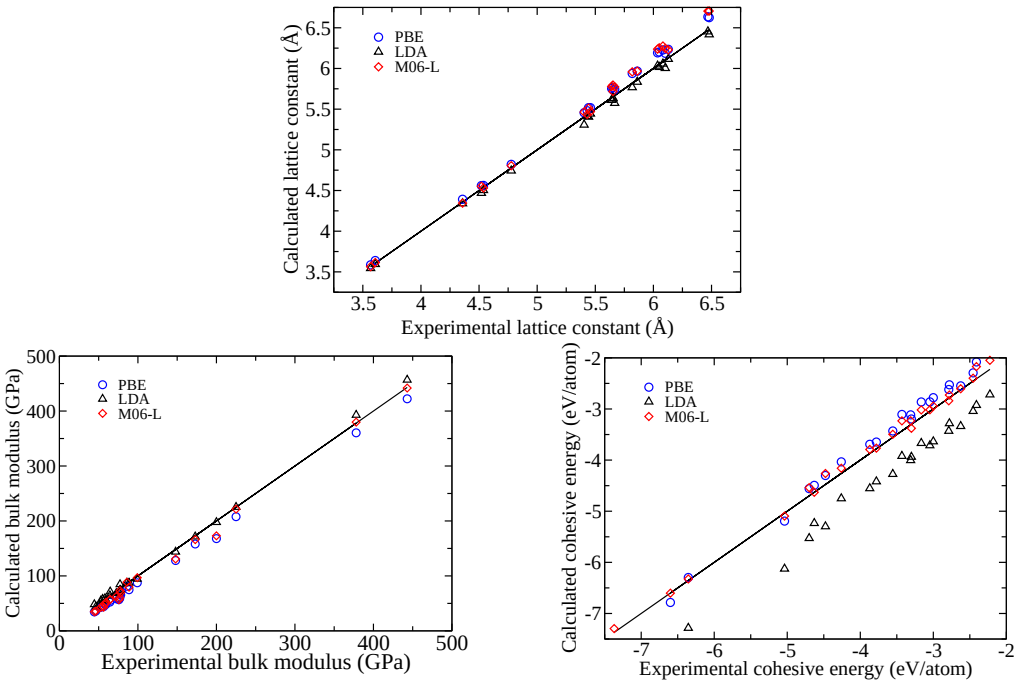

Figure 7.13: Calculated and experimental lattice constants a_0, bulk moduli B_0, and cohesive energies E_0 of 23 semiconductors using the PBE, LDA, and M06-L functionals.

Table 7.3: Mean error (ME) and mean absolute error (MAE), in the lattice constants (a_0, Å), cohesive energies (E_0, eV/atom), and bulk moduli (B_0, GPa) of 23 semiconductor solids. The mean relative error (MRE, %) and mean absolute relative error (MARE, %) are given in parentheses, corresponding to the percentage with respect to the reported experimental cohesive properties. All quantities include zero-point vibrational effects.

	ME			MAE		
	a_0	E_0	B_0	a_0	E_0	B_0
LDA	−0.035	0.72	0.72	0.035	0.72	3.98
	(−0.65)	(19.09)	(0.09)	(0.65)	(19.09)	(4.09)
M06-L	0.096	−0.070	−9.01	0.098	0.09	9.39
	(1.61)	(−2.14)	(−11.96)	(1.65)	(2.61)	(12.25)
PBE	0.087	−0.14	−13.94	0.087	0.19	13.94
	(1.52)	(−4.95)	(−15.50)	(1.52)	(5.81)	(15.50)
PBE+vdW$^{\text{TS+SCS}}$	0.042	0.09	−8.12	0.042	0.13	8.12
	(0.73)	(1.81)	(−8.43)	(0.73)	(3.22)	(8.43)

vdW contributions are 0.8%, 6.8%, and 7.1%, respectively. The improvement of PBE+vdW$^{\text{TS+SCS}}$ over PBE for such a wide range of solids is noteworthy, as it accounts for half of the error obtained from the PBE functional, demonstrating the importance of long-range vdW interactions. While the PBE functional is

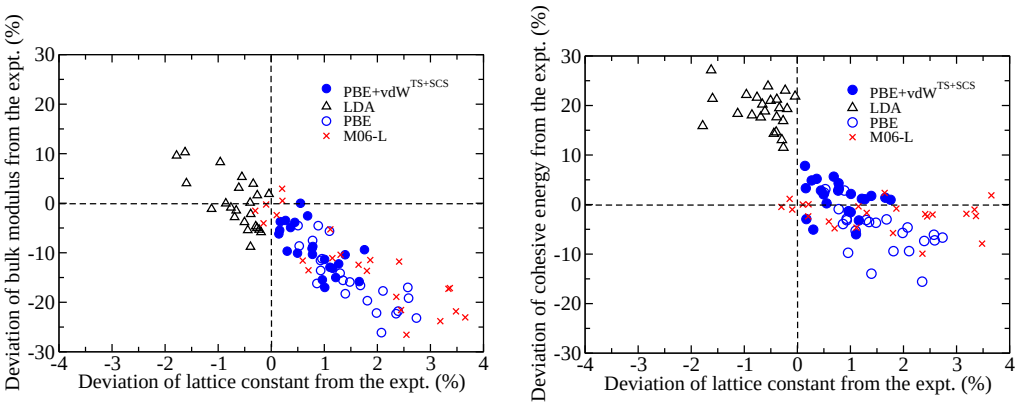

Figure 7.14: Deviations of the bulk moduli B_0 (left panel) and the cohesive energies E_0 (right panel) with those of the lattice constants a_0 using the LDA, PBE, and M06-L functionals, together with the PBE+vdW$^{\text{TS+SCS}}$ method. All quantities contain the influence of zero-point vibration effects.

already one of the most widely used methods for solids due to its reasonable accuracy for diverse properties, the accuracy of PBE greatly increases when coupling with an accurate vdW method, such as the DFT+vdW$^{\text{TS+SCS}}$ approach. The remaining deviations from experiment highlight the need for better exchange functionals, reducing self-interaction errors.

7.4 Summary

In this chapter, we have shown the role of vdW interactions in the cohesive properties for a database of 23 semiconductors by employing the DFT+vdW$^{\text{TS+SCS}}$ method proposed in this thesis. Firstly, this method was verified for diamond-type crystals, which are the model systems where accurate reference data of polarizabilities and dispersion coefficients were taken from the TDDFT calculations carried out using the HSE functional in Chapter 5. Four approaches (namely TD-HSE, TS, TS+SCS, and SO) were used for calculating polarizabilities and C_6 coefficients of C, Si, and Ge, and it was shown that the TS+SCS method outperforms the other three concerning accuracy and computational cost: it yields good agreement with TD-HSE reference data and requires negligible computational time compared with conventional DFT calculations. A comparison between TS and TS+SCS tells us that the long-range electrodynamic screening, which is accounted for in TS+SCS, has a significant impact on the vdW coefficients for atoms in solids.

Furthermore, we demonstrated the applicability of the DFT+vdW$^{\text{TS+SCS}}$

method by extending it to binary zincblende semiconductors. The TS+SCS method predicts the correct dependence of vdW parameters upon the unit-cell volume, that is, polarizabilities and C_6 coefficients increase with the lattice constant. The vdW energies were computed using the vdW parameters (obtained from TS+SCS) via the summation of pair-wise interactions, and added on top of the DFT total energies carried out using the PBE functional. For the 23 semiconductors, the averaged contributions of the vdW interactions are found to be approximately 1% to lattice constants and 7% to both bulk moduli and cohesive energies, which accounts for half of the error found for PBE functional. It can be concluded that vdW interactions play an important role in semiconductors and are crucial for an accurate treatment of the cohesion in solids. The current study shows that the DFT+vdW$^{\text{TS+SCS}}$ approach proposed here provides an accurate and efficient way for coupling vdW energies with DFT calculations. The inclusion of long-range vdW interactions improves the applicability of currently used semi-local density functionals, and thus should improve their performance for a wide variety of applications.

8 CONCLUSIONS AND OUTLOOK

Cohesion is an intrinsic property of matter, the study of which has remained a theoretical challenge for a long time. The lack of detailed understanding of the role of van der Waals (vdW) interactions prevents us from developing a completely satisfactory picture of cohesion in solids. In this doctoral thesis several existing challenges for the accurate treatment of vdW interactions are addressed by employing first-principles electronic-structure methods.

The work presented here aims at a deeper understanding of the importance of long-range vdW interactions in the description of cohesion in non-metallic bulk solids. The first challenge we encountered was exploring computational tools that should be affordable for the calculation of complex solid-state materials, and presently density-functional theory (DFT) represents the best compromise between the accuracy and computational cost towards our goal. Despite the fact that DFT lacks the long-range correlation tail in its (semi-)local and hybrid exchange-correlation (XC) functionals, it offers an effective route for including the long-range vdW energy on top of these functionals (yielding the DFT+vdW method). Therefore part of my thesis was devoted to the assessment of the widely used density functionals applied to solids for describing their cohesion. Care has been taken to construct a database of a broad range of solids with reliable experimental reference data as well as the inclusion of the nuclear zero-point vibrational energy. The limitations of using local and semi-local XC functionals for obtaining the cohesive properties (lattice constants, cohesive energies, and bulk moduli) of bulk materials have been demonstrated from a study of 64 non-molecular crystals, including semiconductors, ionic crystals, metals, and transition metal carbides and nitrides. The calculations were carried out using the full-potential all-electron FHI-aims package [21], and its all-electron accuracy was shown for a broad range of systems. The capabilities of approximate XC functionals for the prediction of cohesive properties were

discussed on the first three rungs of "Jacob's ladder" [90, 127], i.e., the LDA, PBE GGA, and M06-L MGGA. Overall, these three functionals lack the long-range electron correlation and thus do not simultaneously describe all three cohesive properties well.

The central ingredients for studying the vdW interactions are the dispersion coefficients, which requires the knowledge of the frequency-dependent polarizability for atoms in materials. In practice, it can be obtained in two ways: the first one consists in obtaining the dielectric function through the calculation (or the measurement) of the optical spectrum of solids and utilizing the relation between the macroscopic dielectric function and the microscopic polarizability. The second way involves the direct evaluation of the polarizability from the microscopic theory of polarization.

Time-dependent density-functional theory (TDDFT) calculations were performed to obtain the optical spectra of six covalent and ionic solids (C, Si, Ge, GaAs, NaCl, and MgO). By employing the Clausius-Mossotti (CM) relation for these finite-gap systems, the frequency-dependent polarizability was calculated, obtaining the benchmark data of C_6 dispersion coefficients and vdW energies. Together with an independent assessment using the cluster extrapolation model, our study demonstrates that the CM relation is a reasonably good approximation for linking the dielectric function and the polarizability in semiconductor solids, an issue of long debate in the literature. The inclusion of long-range vdW energies using the DFT+vdW scheme leads to an overall improvement of the cohesive properties of ionic and semiconductor solids. It was shown that vdW interactions have an especially large impact on bulk moduli. Furthermore, the importance of including long-range vdW interactions not only to those (semi-)local density functionals but also hybrid functionals was illustrated using HSE06 (HSE06+vdW) for computing the cohesive properties of the solids studied.

As most GGAs and hybrid functionals consistently yield underbinding for a wide range of semiconductors, metals, and ionic crystals (see Chapter 4), we thus conclude that our findings about the role of the long-range vdW energy in cohesion are very likely to be valid for a variety of solids and other properties, such as phase transition pressures. Further research then focused on obtaining an accurate but more efficient (compared with TDDFT) method for computing vdW interactions for non-metallic solids. We proposed a solution based on computing the frequency-dependent polarizability and C_6 dispersion coefficients from classical electrodynamics model with quantum-mechanical polarizabilities obtained from the Tkatchenko/Scheffler approach, yielding the

so-called DFT+vdW$^{\text{TS+SCS}}$ method.

Finally, we applied the DFT+vdW$^{\text{TS+SCS}}$ method to a database of 23 semiconductors. The validity of this method was demonstrated by its good agreement with TDDFT reference polarizability and C_6 dispersion coefficients for C, Si, and Ge solids. The comparison of TS+SCS vdW parameters with TS ones underlines the importance of the electrodynamic screening in the treatment of vdW interactions for bulk solids, and demonstrates that the inclusion of both local and nonlocal environment effects for "atoms-in-solids" enables us to capture the correct dependence of the vdW parameters on the unit-cell volume. Furthermore, the transferability of the DFT+vdW$^{\text{TS+SCS}}$ method was addressed by studying zincblende-structure binary semiconductors. Over the whole database of 23 semiconductors, the average contribution of long-range vdW interactions was found to be 1% to the lattice constants, accompanied by 7% to both the bulk moduli and the cohesive energies.

The work presented here demonstrates the importance of developing accurate methods for vdW interactions for understanding cohesive properties of solids. It was shown that the importance of vdW interactions typically increases for heavier solids and they should be included if one aims at an accurate treatment of materials properties. This thesis enables us to conclude that the lack of the long-range vdW interactions in the local, semi-local, and hybrid functionals, is responsible for an important part of deviations found in DFT calculations when applied to solids. For example, the PBE+vdW approach yields a factor of two improvement in the cohesive properties of ionic and semiconductor solids when compared with the standard PBE functional. We stress that the computational cost of the DFT+vdW approach is the same as that of a conventional DFT calculation, therefore this method can be used in a wide variety of applications.

The results presented in the thesis represent a step towards a better understanding of the cohesion in bulk solids. For developing an understanding of complex materials, further studies should be focused on fundamental properties of various functional materials, e.g., organic molecules and their hybrid interfaces, nanoscale molecular complexes, and organic molecular crystals. Here, we shall discuss some further necessary developments of the DFT+vdW approach. Of particular interest are applications and extension of the DFT+vdW$^{\text{TS+SCS}}$ method to ionic and metallic solids, which remains a difficult challenge due to the need to use gradient information in the definition of the polarizability. Secondly, we note that while the cohesive energies of the 23-semiconductor database calculated using PBE+vdW are indeed in better

agreement with experiment than pure PBE results, they are "overcorrected", with an average overestimation of 0.13 eV/atom or 3% in relative terms. Two reasons can account for this deviation: the short- and mid-range interactions covered by the PBE functional and the omission of the many-body energy in the current theory. The first aspect can be improved by coupling the DFT+vdW^{TS+SCS} method to hybrid functionals (e.g., HSE06), which will be an important next step for assessing our method. Concerning the second aspect, despite the fact that many-body effects are likely to have a small impact on vdW forces in cubic semiconductors, the inclusion of those effects (e.g., the repulsive three-body non-additive terms [45, 46]) will certainly reduce the overbinding, and thus may reproduce experimental cohesive energies better. Indeed, one must include many-body vdW interactions in order to deal with more complex compounds, such as non-cubic and molecular solids [20, 25]. Our final remark is that the current theory is based on a model of interacting dipoles, while shorter-range multipole-multipole interactions are ignored. Such effects may play a role for certain systems (e.g., high-pressure phases of ice [282]), and need to be addressed in the future.

Appendices

A STRUCTURAL DETAILS AND CONVERGENCE TESTS

DFT total energy calculation:

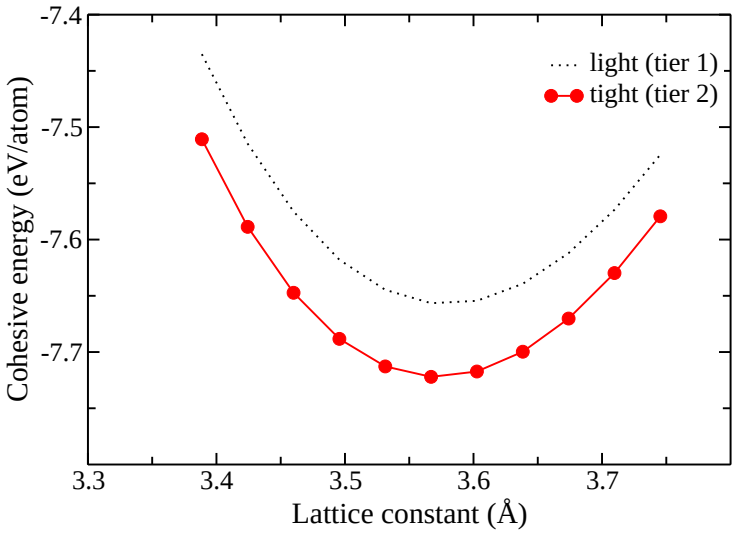

Figure A.1: Basis sets convergence of the calculated cohesive energy (eV/atom) for diamond bulk using the PBE functional.

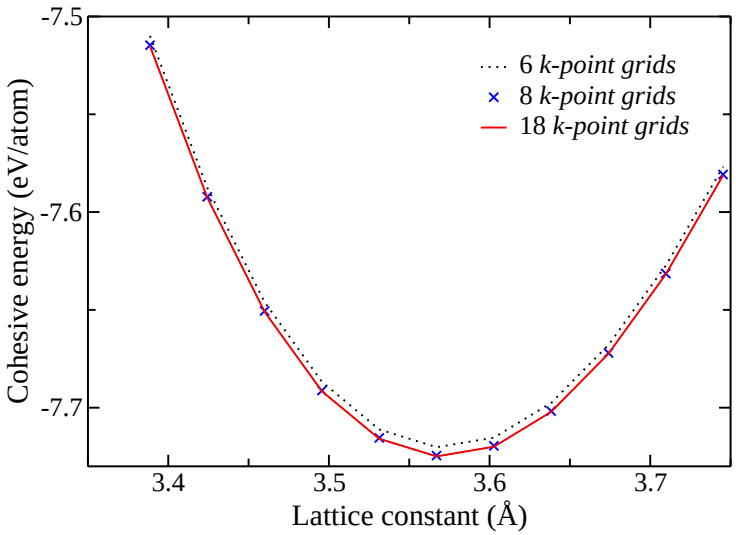

Figure A.2: k-point grids convergence of the calculated cohesive energy (eV/atom) for bulk diamond using the PBE functional.

Phonon calculations:

For the phonon calculations with the finite-displacement approach, there is one adjustable parameter: the finite displacement δ used to gather the force response in all the Cartesian directions. The convergence of the zero-point vibrational energy was achieved by varying the displacement (from 0.001 to 0.1 Å) via phonopy [253, 263] interface with the FHI-aims package [21]

Table A.1: The calculated zero-point vibrational energy versus finite displacement δ used in the phonon calculations of bulk diamond.

δ (Å)	0.001	0.005	0.01	0.02	0.1
ZPVE (eV)	0.180816	0.180817	0.180812	0.180788	0.1812

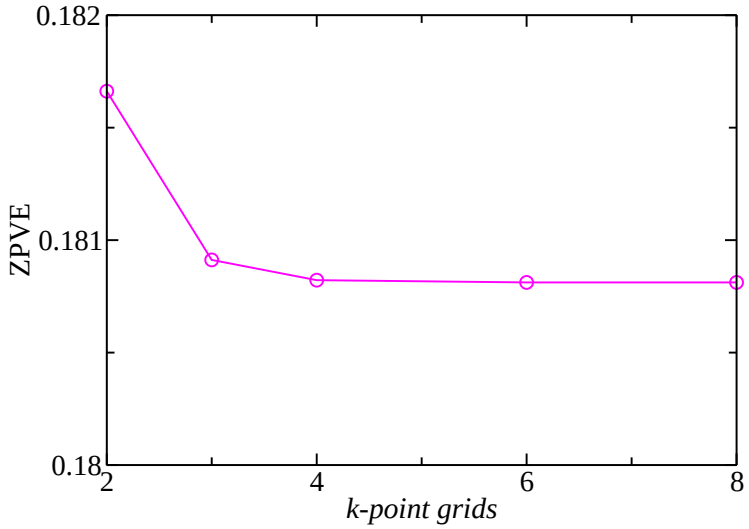

Figure A.3: The calculated zero-point vibrational energy (eV/atom) for diamond crystal at the experimental lattice constant (3.567 Å) versus the k-point grids used in the phonon calculations.

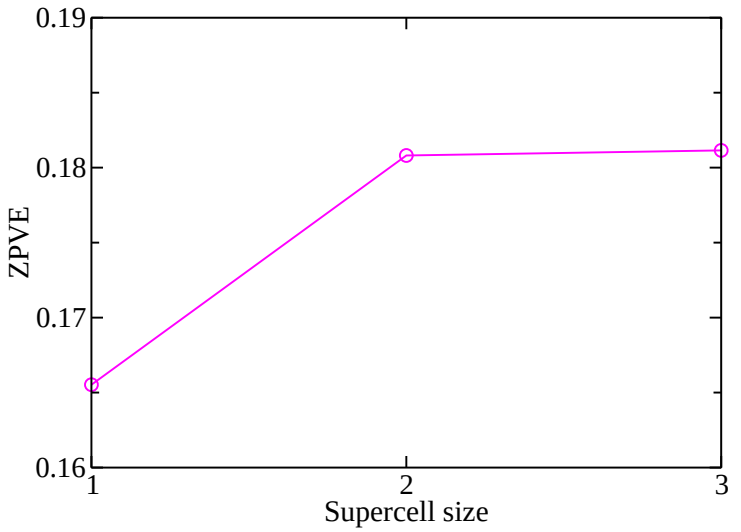

Figure A.4: The calculated zero-point vibrational energy (eV/atom) for diamond crystal at the experimental lattice constant (3.567 Å) versus different supercell size used in the phonon calculations.

B Optical spectra

Computational details:
The optical spectra of the six ionic and semiconductor solids presented in Chapter 5 were obtained using the Vienna *ab initio* simulation package (VASP) [245, 246], employing time-dependent Kohn-Sham density-functional theory in its linear-response formulation. For the calculations of C, Si, and Ge, only outer valence s and p electrons were used for the self-consistent field and excited-state calculations. The respective [He], [Ne], and [Ar]$3d^{10}$ electrons were treated as core electrons and kept frozen in the configuration determined as the PAW core potential. For the low band-gap case of Ge, the importance of $3d$ electrons as valence electrons was carefully checked, and no noticeable change was found in the spectra. Concerning the kinetic energy cutoff, the default values of 414, 245.7, and 173.8 eV have been used for C, Si, and Ge, respectively. Calculations using a 40 % higher cutoff did not affect the quality of the spectra over the entire volume range, and thus confirms that the convergence was reached. Gaussian smearing using a width of 0.05 eV was used throughout this work. For the present calculations "shifted k meshes" (e.g., as described in Ref. [231]) was employed to achieve k-point convergence, and 12 conduction bands were used. TD-LDA calculations for C and Si used $32 \times 32 \times 32$ k points; for Ge (with a smaller band-gap), a mesh of $56 \times 56 \times 56$ k points was chosen in order to obtain sufficiently converged results. TD-HSE+NQ calculations for C and Si employed the same mesh as used for TD-LDA, while a reduced mesh of $40 \times 40 \times 40$ k points were chosen for the Ge TDHSE+NQ spectrum, due to the larger computational requirement for setting up the nonlocal nanoquanta kernel. Turning to binary solids, frozen [He] (for O), [Ne] (for Cl, Na, Mg) and [Ar]$3d^{10}$ (for Ga, and As) core states were employed. Similar to the diamond-type solids, 12 conduction bands and a $32 \times 32 \times 32$ k-point mesh were used for the excited state calculations of NaCl, MgO, and GaAs. The plane-wave kinetic energy cutoffs for NaCl, MgO, and GaAs were 350, 400, and 210 eV, respectively.

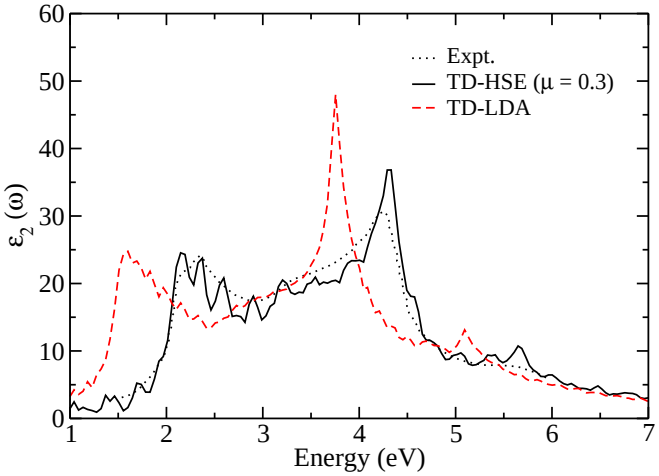

Figure B.1: Optical-absorption spectra of Ge using TD-HSE (μ=0.3 Å^{-1}) including electron-hole interactions (full black line). The TD-LDA result is shown using the red dashed line, and the experiment is shown by black dots (Ref. [243]).

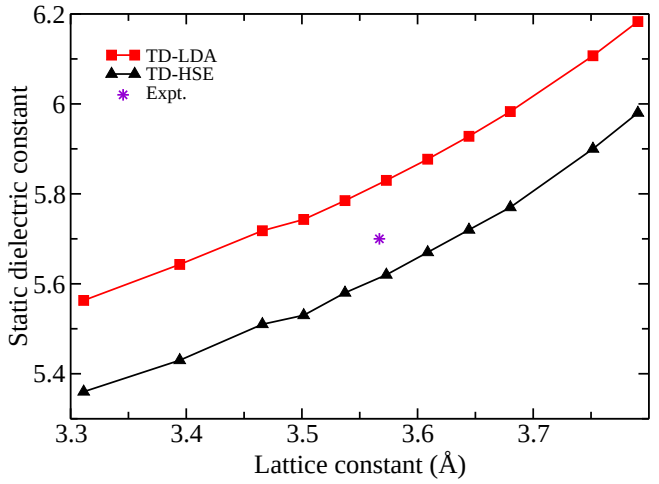

Figure B.2: Calculated static dielectric constants as a function of the lattice constant (Å) of diamond from the TD-HSE and TD-LDA periodic calculations.

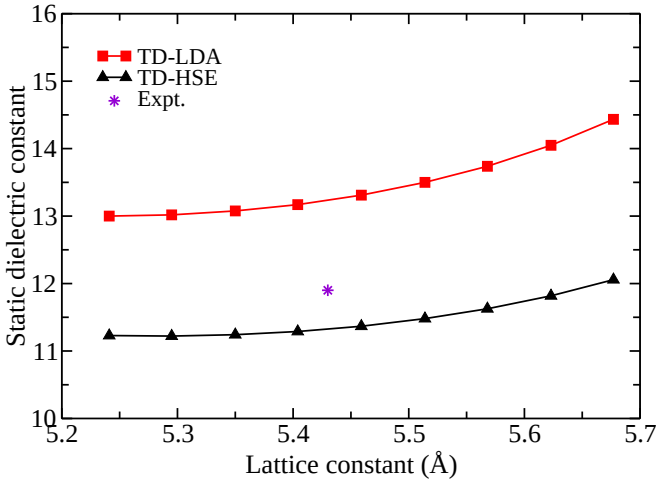

Figure B.3: Calculated static dielectric constants as a function of the lattice constant (Å) of silicon from the TD-HSE and TD-LDA periodic calculations.

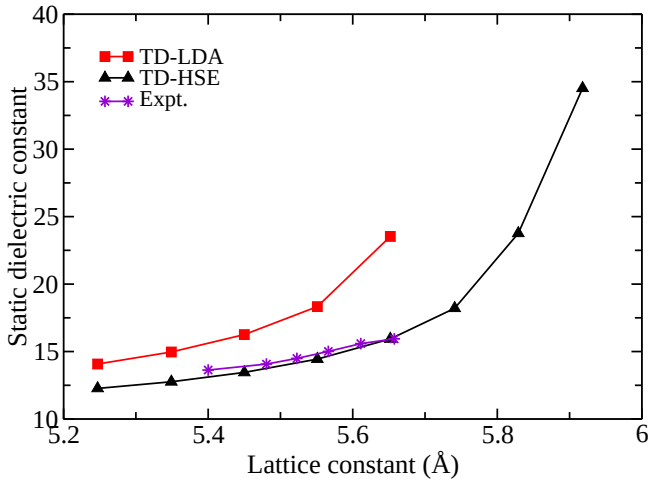

Figure B.4: Calculated static dielectric constants as a function of the lattice constant (Å) of germanium from the TD-HSE and TD-LDA periodic calculations. The experimental data are taken from Ref. [267] by Cardona and co-authors.

Table B.1: Calculated atomic static polarizabilities (bohr^3) as a function of lattice constant a_0 (Å) for C, Si, and Ge using the TD-HSE and TD-LDA approaches from periodic and cluster calculations.

	a_0	TD-HSE[a]	TD-LDA[a]	TD-LDA[b]
C	3.471	5.06	5.21	4.64
	3.506	5.22	5.38	4.78
	3.542	5.41	5.56	4.94
	3.578	5.60	5.76	5.10
	3.614	5.79	5.96	5.27
	3.650	5.99	6.16	5.43
	3.685	6.19	6.37	5.59
Si	5.295	23.12	23.93	24.38
	5.350	23.85	24.70	25.02
	5.404	24.61	25.50	25.67
	5.459	25.41	26.34	26.34
	5.514	26.25	27.23	27.04
	5.568	27.11	28.13	27.80
	5.623	28.03	29.10	28.61
Ge	5.247	22.97	23.66	24.93
	5.349	24.56	25.37	26.30
	5.450	26.27	27.24	27.82
	5.551	28.16	29.36	29.40
	5.652	30.28	32.09	31.13
	5.741	32.45	—	32.74
	5.829	35.24	—	34.49

[a] Periodic calculation
[b] Cluster calculation

Table B.2: Calculated atomic C_6 coefficients (hartree·bohr^6) as a function of lattice constant (Å) for C, Si, and Ge using the TD-HSE and TD-LDA approaches from periodic and cluster calculations.

	a_0	TD-HSE^a	TD-LDA^a	TD-LDA^b
C	3.471	14.68	14.80	15.54
	3.506	15.39	15.51	16.11
	3.542	16.17	16.29	16.75
	3.578	16.99	17.10	17.45
	3.614	17.84	17.95	18.17
	3.650	18.72	18.84	18.89
	3.685	19.66	19.74	19.59
Si	5.295	148.84	152.95	161.00
	5.350	155.96	160.41	167.25
	5.404	163.31	168.09	173.54
	5.459	171.18	176.25	180.10
	5.514	179.45	184.79	186.97
	5.568	187.99	193.61	194.38
	5.623	197.16	203.13	202.39
Ge	5.247	154.70	159.16	177.21
	5.349	169.92	175.46	190.70
	5.450	186.45	192.73	205.78
	5.551	204.55	211.61	221.35
	5.652	224.49	231.89	238.31
	5.741	243.63	—	254.19
	5.829	263.88	—	271.26

[a] Periodic calculation
[b] Cluster calculation

C COHESIVE PROPERTIES

Relativistic effects on cohesive properties of heavy nuclear-mass solids:

Table C.1: The spin-orbit contributions to the lattice constants a_0 (Å), the cohesive energies E_0 (eV/atom), and the bulk moduli B_0 (GPa) of 11 metals (taken from Ref. [261]), among which As, Sb, Bi, and Ce are not studied in this thesis.

Solids	a_0	E_0	B_0
Ca	0.00	0.00	0.00
Sr	0.00	0.00	0.00
Ba	0.00	-0.01	0.00
As	0.00	0.02	0.00
Sb	0.00	0.05	-5.00
Bi	-0.10	0.51	1.00
Cu	0.00	0.00	0.00
Ag	0.00	-0.01	0.00
Au	0.03	-0.15	2.00
Ce	-0.02	0.05	1.00
Th	-0.01	0.12	1.00

DFT calculations:

Table C.2: Equilibrium lattice constants (Å) of 24 metals. Zero-point vibrational energies (ZPVE) were determined by calculating the phonon dispersion relation at a set of volumes, marked as "Corr.", and "Uncorr." refers to the non-ZPVE-corrected values. Experimental values with ZPVE are summarized in the last columns (at 0 K unless noted otherwise).

Solid	LDA		PBE		M06-L		Expt.
	Uncorr.	Corr.	Uncorr.	Corr.	Uncorr.	Corr.	
Li	3.366	3.387	3.440	3.464	3.417	3.442	3.477
Na	4.052	4.067	4.199	4.215	4.036	4.053	4.225
K	5.043	5.055	5.285	5.301	4.911	4.929	5.225
Rb	5.376	5.385	5.670	5.677	5.246	5.254	5.585
Ca	5.336	5.346	5.527	5.538	5.384	5.392	5.565
Sr	5.789	5.795	6.020	6.028	5.881	5.887	6.048
Ba	4.758	4.760	5.020	5.024	5.016	5.019	5.007
Al	3.985	3.998	4.044	4.057	3.953	3.962	4.032
Pb	4.879	4.884	5.030	5.033	5.057	5.061	4.905
Fe	2.747	2.750	2.828	2.832	2.863	2.868	2.861
V	2.924	2.929	2.997	3.001	2.998	3.002	3.028
Mo	3.111	3.114	3.160	3.163	3.162	3.165	3.144
W	3.134	3.136	3.182	3.184	3.182	3.184	3.162
Nb	3.247	3.250	3.302	3.305	3.313	3.316	3.296
Ta	3.250	3.253	3.319	3.321	3.332	3.334	3.301
Ni	3.423	3.429	3.520	3.526	3.495	3.500	3.513
Cu	3.521	3.527	3.631	3.638	3.594	3.601	3.603
Rh	3.754	3.758	3.830	3.834	3.820	3.824	3.798
Ir	3.813	3.815	3.871	3.874	3.857	3.860	3.835
Pd	3.842	3.846	3.943	3.948	3.937	3.942	3.881
Pt	3.895	3.897	3.971	3.974	3.957	3.960	3.916
Au	4.054	4.058	4.159	4.164	4.157	4.162	4.065
Ag	4.004	4.009	4.149	4.156	4.153	4.160	4.069
Th	4.885	4.887	5.029	5.032	5.111	5.114	5.074

Li(20 K) [283], Na(5 K) [284], K(5 K) [284], Rb(5 K) [284], Ca [285], Sr [285], Ba [285], Al [96, 97], Pb(5 K) [286, 287], Fe [98, 99], V [98, 99], Mo [98, 99], W [98, 99], Nb [98, 99], Ta [98, 99], Ni(10 K) [287, 288], Cu [96, 97], Rh [96, 97], Ir(5 K) [286], Pd [96, 97], Pt [98, 99], Au(5 K) [286], Ag [96, 97], Th [98, 99].

Table C.3: Equilibrium lattice constants (Å) of 40 non-metallic solids.

Solid	LDA		PBE		M06-L		Expt.
	Uncorr.	Corr.	Uncorr.	Corr.	Uncorr.	Corr.	
LiF	3.913	3.944	4.066	4.104	3.973	4.008	4.010
LiCl	4.966	4.994	5.150	5.182	5.127	5.158	5.106
NaF	4.504	4.528	4.701	4.729	4.578	4.604	4.609
NaCl	5.469	5.491	5.699	5.722	5.579	5.603	5.595
MgO	4.164	4.180	4.257	4.274	4.203	4.219	4.207
MgS	5.139	5.153	5.237	5.252	5.189	5.202	5.202
TiC	4.261	4.271	4.332	4.343	4.311	4.321	4.330
ZrC	4.642	4.651	4.709	4.718	4.705	4.714	4.696
HfC	4.573	4.582	4.650	4.659	4.643	4.652	4.638
VC	4.088	4.099	4.154	4.166	4.119	4.131	4.160
NbC	4.427	4.434	4.484	4.493	4.461	4.469	4.470
TiN	4.172	4.182	4.246	4.257	4.248	4.259	4.239
ZrN	4.525	4.535	4.595	4.605	4.613	4.624	4.585
HfN	4.469	4.477	4.547	4.557	4.565	4.574	4.519
VN	4.042	4.051	4.115	4.127	4.111	4.123	4.135
NbN	4.356	4.362	4.421	4.428	4.425	4.432	4.379
C	3.532	3.545	3.572	3.585	3.551	3.564	3.567
Si	5.405	5.414	5.470	5.479	5.427	5.436	5.430
Ge	5.625	5.630	5.761	5.769	5.787	5.796	5.652
Sn	6.474	6.480	6.655	6.663	6.720	6.728	6.482
AlP	5.434	5.444	5.508	5.518	5.460	5.469	5.458
AlAs	5.630	5.637	5.731	5.738	5.711	5.717	5.652
AlSb	6.108	6.116	6.224	6.231	6.222	6.229	6.128
BN	3.582	3.595	3.625	3.639	3.601	3.615	3.607
BP	4.492	4.504	4.549	4.562	4.519	4.531	4.538
AsB	4.733	4.744	4.811	4.823	4.793	4.805	4.777
GaN	4.460	4.469	4.549	4.560	4.541	4.552	4.520
GaP	5.398	5.406	5.509	5.518	5.505	5.513	5.442
GaAs	5.607	5.612	5.748	5.755	5.772	5.779	5.641
GaSb	6.052	6.058	6.221	6.227	6.269	6.276	6.082
InP	5.828	5.835	5.964	5.973	5.958	5.967	5.861
InAs	6.027	6.033	6.192	6.198	6.232	6.238	6.036
InSb	6.451	6.454	6.643	6.651	6.698	6.705	6.469
SiC	4.330	4.341	4.381	4.392	4.334	4.345	4.358
ZnS	5.299	5.308	5.445	5.456	5.454	5.464	5.404
ZnSe	5.569	5.575	5.738	5.745	5.765	5.773	5.667
ZnTe	5.997	6.004	6.188	6.196	6.239	6.246	6.102
CdS	5.761	5.768	5.930	5.941	5.949	5.958	5.818
CdSe	6.011	6.017	6.197	6.203	6.248	6.254	6.050
CdTe	6.412	6.418	6.620	6.627	6.698	6.706	6.480

LiF [289], LiCl [289], NaF [289], NaCl [289], MgO [289], MgS [290], TiC [291], ZrC [291], HfC [291], VC [291, 292], NbC [291], TiN [291], ZrN [291], HfN [291], VN [293, 294], NbN [291, 295], C [80], Si [296], Ge [296], Sn [142], SiC [142], AlP [297], AlAs [297], AlSb [297], BN [142], BP [142], BAs [298], GaN [142], GaP [297], GaAs [297], GaSb [297], InP [297], InAs [297], InSb [297], ZnS(4.2 K) [299], ZnSe [300], ZnTe [301], CdS [302], CdSe [302], CdTe [302]

Table C.4: Equilibrium bulk moduli (GPa) of 24 metals

Solid	LDA		PBE		M06-L		Expt.
	Uncorr.	Corr.	Uncorr.	Corr.	Uncorr.	Corr.	
Li	15.2	14.2	14.0	13.4	13.2	12.6	12.8
Na	9.1	8.9	7.8	7.6	8.2	8.1	7.5
K	4.5	4.7	3.6	3.6	5.9	6.1	3.7
Rb	3.6	3.6	2.8	2.8	5.1	5.1	3.1
Ca	18.8	18.5	17.4	17.1	22.0	21.7	18.4
Sr	14.3	14.3	11.7	11.6	16.8	16.7	12.4
Ba	10.3	10.2	8.9	8.8	11.7	11.6	9.3
Al	83.7	81.3	77.5	75.9	116.1	114.9	79.4
Pb	53.7	52.6	40.6	40.1	39.7	39.1	48.8
Fe	252.1	252.7	189.8	185.0	158.4	152.2	173.0
V	209.1	207.0	179.6	177.9	191.3	188.8	157.0
Mo	293.0	290.2	260.5	257.9	270.0	267.4	265.3
W	335.9	334.3	300.8	299.2	316.5	315.0	314.2
Nb	195.2	192.4	172.8	170.6	176.6	174.6	174.0
Ta	211.9	210.5	190.2	189.3	199.6	198.8	194.2
Ni	256.7	251.6	198.6	195.6	217.8	214.9	187.6
Cu	187.3	184.1	140.4	137.8	158.9	156.2	142.3
Rh	317.8	315.0	257.5	254.6	265.8	262.8	268.7
Ir	403.4	400.8	347.2	344.6	368.8	366.2	383.0
Pd	226.9	224.2	169.0	166.6	168.0	165.5	195.0
Pt	307.4	305.3	249.1	246.9	260.5	258.3	277.0
Au	194.6	192.8	143.0	141.0	140.8	138.8	180.9
Ag	138.7	135.6	90.7	89.0	89.0	87.3	110.9
Th	63.3	63.8	54.5	54.4	54.5	54.4	58.0

Li [303], Na [304], K [305], Rb [306], Ca [285], Sr [285], Ba [285], Al [307], Pb [308], Fe [309, 310], V [311], Mo [312], W [312], Nb [313–315], Ta [312], Ni [309, 310], Cu [316, 317], Rh(4.2 K) [318], Ir [319], Pd [320], Pt [321, 322], Au [317], Ag [317], Th [322, 323].

Table C.5: Equilibrium bulk moduli (GPa) of 40 non-metallic solids

Solid	LDA		PBE		M06-L		Expt.
	Uncorr.	Corr.	Uncorr.	Corr.	Uncorr.	Corr.	
LiF	85.4	79.2	67.2	61.6	76.8	70.8	69.8
LiCl	40.8	39.7	31.9	30.0	33.4	31.5	35.4
NaF	61.7	58.8	45.1	42.4	53.1	50.2	51.4
NaCl	32.2	31.3	23.9	23.2	27.1	26.2	28.5
MgO	171.7	166.9	148.3	144.1	164.0	159.2	168.8
MgS	82.8	81.0	73.9	71.9	80.2	78.3	78.9
TiC	282.6	277.1	250.8	245.2	268.6	263.1	244.0
ZrC	246.6	242.5	222.0	218.1	230.0	226.2	225.5
HfC	260.2	255.2	233.7	230.8	246.7	243.8	242.7
VC	346.8	341.3	306.1	301.4	329.6	324.1	303.0
NbC	333.4	324.5	300.3	289.9	316.8	306.7	302.0
TiN	320.7	313.9	277.7	271.2	282.7	276.3	289.0
ZrN	283.7	277.8	249.4	244.1	244.9	240.0	215.0
HfN	301.7	296.1	262.8	256.5	260.9	254.6	306.0
VN	367.2	353.3	315.4	302.2	318.2	304.9	268.0
NbN	351.0	345.4	307.7	299.2	303.6	294.7	292.0
C	467.0	456.8	433.2	423.0	452.3	441.9	443.0
Si	96.2	94.6	88.9	87.7	98.3	96.8	99.2
Ge	72.4	70.2	59.0	56.9	58.3	56.5	75.8
Sn	44.9	43.8	35.8	35.3	34.9	34.5	53.0
AlP	89.4	87.4	81.9	80.9	90.1	88.5	86.0
AlAs	75.0	74.2	66.7	65.5	70.4	69.4	78.1
AlSb	56.0	55.8	49.2	49.5	51.7	51.9	59.3
BN	402.1	392.8	371.6	361.1	390.0	379.9	378.0
BP	175.2	171.5	161.6	158.0	169.6	166.0	173.0
AsB	146.6	143.8	130.9	127.8	133.8	130.9	148.0
GaN	201.6	197.7	171.8	167.6	178.9	172.9	200.0
GaP	89.1	87.4	76.1	74.9	80.5	79.5	88.7
GaAs	74.2	74.0	61.0	59.9	61.5	60.3	76.9
GaSb	55.5	55.1	43.5	44.0	44.5	42.9	56.3
InP	70.8	68.6	59.1	58.2	63.6	62.6	72.5
InAs	59.9	59.1	48.2	47.7	48.3	48.0	58.0
InSb	46.5	44.0	36.4	35.7	36.3	35.8	46.5
SiC	228.7	225.2	211.7	208.1	225.1	221.6	225.0
ZnS	86.4	84.6	69.6	68.5	74.0	73.1	77.2
ZnSe	71.5	71.4	56.8	55.6	58.2	57.3	64.7
ZnTe	55.4	54.9	43.4	43.2	43.1	42.8	52.8
CdS	68.0	64.3	53.6	52.9	57.7	56.7	64.3
CdSe	58.0	57.9	45.0	44.5	46.1	45.6	55.0
CdTe	46.2	48.2	35.3	34.6	35.2	34.8	44.5

LiF [324], LiCl [325], NaF [325], NaCl [326], MgO [327], MgS [290], TiC [328], ZrC [328], HfC (296 K)[329, 330], VC [331], NbC [266], TiN [332], ZrN(300 K) [295], HfN(300 K) [295], VN(300 K) [333], NbN(300 K) [295], C [96, 97], Si(77 K) [334], Ge(4.2 K) [335], Sn(90 K) [336, 337], SiC [338], AlP [289, 339], AlAs [339, 340], AlSb [339, 340], BN [341], BP [342], BAs [298], GaN [289], GaP [339, 340], GaAs [343], GaSb [339, 340], InP [339, 340], InAs [339, 340], InSb [339, 340], ZnS [344], ZnSe [344], ZnTe [344], CdS [302], CdSe [302], CdTe [344].

Table C.6: Equilibrium cohesive energies (eV/atom) of 24 metals. The experimental values are taken from Ref. [24] at 0 K.

Solid	LDA		PBE		M06-L		Expt.
	Uncorr.	Corr.	Uncorr.	Corr.	Uncorr.	Corr.	
Li	−1.80	−1.76	−1.61	−1.57	−1.88	−1.85	−1.63
Na	−1.25	−1.23	−1.09	−1.07	−1.45	−1.43	−1.11
K	−1.03	−1.02	−0.88	−0.87	−1.34	−1.33	−0.93
Rb	−0.94	−0.93	−0.79	−0.79	−1.31	−1.30	−0.85
Ca	−2.20	−2.18	−1.91	−1.89	−2.50	−2.48	−1.84
Sr	−1.89	−1.88	−1.62	−1.60	−2.24	−2.23	−1.72
Ba	−2.20	−2.19	−1.83	−1.82	−2.40	−2.39	−1.90
Al	−4.00	−3.96	−3.43	−3.39	−4.24	−4.20	−3.39
Pb	−3.78	−3.77	−2.96	−2.95	−3.60	−3.59	−2.03
Fe	−6.40	−6.35	−4.89	−4.82	−4.96	−4.92	−4.28
V	−6.74	−6.71	−5.36	−5.32	−6.18	−6.15	−5.31
Mo	−8.09	−8.05	−6.28	−6.25	−6.95	−6.92	−6.82
W	−10.23	−10.19	−8.44	−8.41	−9.88	−9.85	−8.90
Nb	−8.50	−8.47	−6.99	−6.97	−7.91	−7.88	−7.57
Ta	−9.59	−9.56	−8.13	−8.11	−8.73	−8.71	−8.09
Ni	−6.09	−6.05	−4.74	−4.70	−4.95	−4.91	−4.44
Cu	−4.54	−4.51	−3.50	−3.47	−4.28	−4.24	−3.49
Rh	−7.58	−7.55	−5.72	−5.68	−5.58	−5.55	−5.75
Ir	−9.32	−9.29	−7.36	−7.33	−7.11	−7.08	−6.94
Pd	−5.06	−5.02	−3.71	−3.68	−4.08	−4.05	−3.89
Pt	−7.15	−7.12	−5.55	−5.53	−5.80	−5.78	−5.84
Au	−4.38	−4.36	−3.10	−3.08	−3.61	−3.60	−3.81
Ag	−3.63	−3.60	−2.51	−2.49	−3.17	−3.15	−2.95
Th	−7.54	−7.53	−6.36	−6.35	−6.81	−6.80	−6.20

Table C.7: Equilibrium cohesive energies (eV/atom) of 40 non-metallic solids

Solid	LDA		PBE		M06-L		Expt.
	Uncorr.	Corr.	Uncorr.	Corr.	Uncorr.	Corr.	
LiF	−4.92	−4.86	−4.32	−4.27	−4.53	−4.47	−4.40
LiCl	−3.82	−3.78	−3.37	−3.33	−3.79	−3.75	−3.55
NaF	−4.36	−4.31	−3.82	−3.78	−4.08	−4.04	−3.93
NaCl	−3.48	−3.45	−3.10	−3.07	−3.59	−3.56	−3.33
MgO	−5.80	−5.72	−4.95	−4.88	−5.23	−5.16	−5.12
MgS	−4.31	−4.27	−3.68	−3.64	−4.06	−4.02	−4.00
TiC	−8.63	−8.55	−7.40	−7.31	−7.79	−7.71	−7.16
ZrC	−9.10	−9.03	−7.88	−7.81	−8.24	−8.17	−7.93
HfC	−9.26	−9.19	−8.07	−8.00	−8.31	−8.25	−8.11
VC	−8.34	−8.27	−7.04	−6.98	−7.32	−7.25	−6.94
NbC	−9.34	−9.27	−7.95	−7.89	−8.26	−8.19	−8.26
TiN	−8.29	−8.21	−6.99	−6.92	−7.26	−7.19	−6.69
ZrN	−8.76	−8.70	−7.46	−7.40	−7.72	−7.66	−7.52
HfN	−8.80	−8.74	−7.51	−7.46	−7.64	−7.58	−7.62
VN	−7.63	−7.57	−6.28	−6.23	−6.38	−6.33	−6.25
NbN	−8.52	−8.49	−7.07	−7.04	−7.24	−7.21	−7.50
C	−8.94	−8.76	−7.72	−7.55	−7.48	−7.30	−7.37
SiC	−7.40	−7.28	−6.40	−6.30	−6.44	−6.32	−6.36
Si	−5.30	−5.23	−4.56	−4.50	−4.69	−4.63	−4.63
Ge	−4.59	−4.55	−3.73	−3.69	−3.82	−3.79	−3.87
Sn	−3.95	−3.93	−3.17	−3.14	−3.36	−3.34	−3.14
AlP	−4.81	−4.75	−4.08	−4.03	−4.22	−4.16	−4.26
AlAs	−4.46	−4.42	−3.67	−3.63	−3.81	−3.77	−3.78
AlSb	−3.97	−3.94	−3.24	−3.20	−3.41	−3.38	−3.30
BN	−8.05	−7.89	−6.94	−6.78	−6.76	−6.60	−6.60
BP	−6.23	−6.13	−5.29	−5.19	−5.20	−5.09	−5.04
AsB	−5.61	−5.53	−4.63	−4.55	−4.62	−4.54	−4.70
GaN	−5.38	−5.30	−4.37	−4.30	−4.34	−4.26	−4.48
GaP	−4.32	−4.27	−3.47	−3.42	−3.54	−3.50	−3.56
GaAs	−4.04	−4.00	−3.15	−3.12	−3.26	−3.23	−3.31
GaSb	−3.66	−3.64	−2.81	−2.78	−2.97	−2.94	−3.00
InP	−3.96	−3.92	−3.13	−3.09	−3.27	−3.23	−3.43
InAs	−3.74	−3.71	−2.86	−2.84	−3.04	−3.02	−3.05
InSb	−3.45	−3.43	−2.61	−2.59	−2.86	−2.84	−2.79
ZnS	−3.71	−3.67	−2.89	−2.85	−3.05	−3.02	−3.17
ZnSe	−3.37	−3.34	−2.56	−2.53	−2.63	−2.60	−2.63
ZnTe	−2.95	−2.93	−2.08	−2.06	−2.19	−2.17	−2.41
CdS	−3.32	−3.28	−2.55	−2.52	−2.76	−2.73	−2.78
CdSe	−3.07	−3.04	−2.31	−2.29	−2.42	−2.40	−2.46
CdTe	−2.74	−2.72	−1.91	−1.89	−2.07	−2.05	−2.23

LiF [345], LiCl [345], NaF [345], NaCl [345], MgO [327], MgS [346, 347], TiC [345, 348], ZrC [345, 348, 349], HfC [345, 348], VC [345, 348], NbC [345, 348, 349], TiN [350], ZrN [349], HfN [351], VN [350], NbN [349], C [24], Si [24], Ge [24], Sn [24], SiC [157, 345], AlP [352], AlAs [352], AlSb [353], BN [157, 345], BP [353], BAs(300 K) [354], GaN [157, 345], GaP [157, 345], GaAs [340], GaSb [355], InP [355], InAs [355], InSb [355], ZnS [353, 356], ZnSe [353, 356], ZnTe [353, 356], CdS [353], CdSe [353], CdTe [353].

Comparison between DFT and DFT+vdW approaches:

Table C.8: Calculated cohesive properties of C, Si, and Ge using PBE and PBE+vdW$^{\text{TS+SCS}}$: lattice constants a_0 (Å), cohesive energies E_0 (eV/atom), and bulk moduli B_0 (GPa). The quasi-harmonic zero-point energy obtained from the PBE phonon spectrum is included for each method. The experimental data are shown for comparison.

		a_0	E_0	B_0
C	PBE	3.585	−7.55	423
	PBE+vdW$^{\text{TS+SCS}}$	3.577	−7.73	428
	Expt.	3.567	−7.37	443
Si	PBE	5.480	−4.50	88
	PBE+vdW$^{\text{TS+SCS}}$	5.439	−4.78	94
	Expt.	5.430	−4.62	99
Ge	PBE	5.769	−3.69	57
	PBE+vdW$^{\text{TS+SCS}}$	5.709	−3.95	64
	Expt.	5.652	−3.87	76

Table C.9: Calculated cohesive properties of the IIIA–VA compounds using PBE and PBE+vdW$^{\text{TS+SCS}}$: lattice constants a_0 (Å), cohesive energies E_0 (eV/atom), and bulk moduli B_0 (GPa).

		a_0	E_0	B_0
BN	PBE	3.639	−6.79	361
	PBE+vdW$^{\text{TS+SCS}}$	3.632	−6.97	368
	Expt.	3.607	−6.60	378
BP	PBE	4.562	−5.19	158
	PBE+vdW$^{\text{TS+SCS}}$	4.545	−5.43	162
	Expt.	4.538	−5.04	173
BAs	PBE	4.823	−4.55	128
	PBE+vdW$^{\text{TS+SCS}}$	4.801	−4.80	133
	Expt.	4.777	−4.70	148

Table C.10: Calculated cohesive properties of the IIIA–VA compounds using PBE and PBE+vdW$^{\text{TS+SCS}}$: lattice constants a_0 (Å), cohesive energies E_0 (eV/atom), and bulk moduli B_0 (GPa).

		a_0	E_0	B_0
AlP	PBE	5.518	−4.03	81
	PBE+vdW$^{\text{TS+SCS}}$	5.488	−4.27	86
	Expt.	5.458	−4.26	86
AlAs	PBE	5.738	−3.64	66
	PBE+vdW$^{\text{TS+SCS}}$	5.695	−3.89	71
	Expt.	5.652	−3.78	78
AlSb	PBE	6.231	−3.20	50
	PBE+vdW$^{\text{TS+SCS}}$	6.176	−3.44	53
	Expt.	6.128	−3.30	59

Table C.11: Calculated cohesive properties of the IIIA–VA compounds using PBE and PBE+vdW$^{\text{TS+SCS}}$: lattice constants a_0 (Å), cohesive energies E_0 (eV/atom), and bulk moduli B_0 (GPa).

		a_0	E_0	B_0
GaN	PBE	4.559	−4.30	168
	PBE+vdW$^{\text{TS+SCS}}$	4.564	−4.42	169
	Expt.	4.520	−4.48	200
GaP	PBE	5.518	−3.43	75
	PBE+vdW$^{\text{TS+SCS}}$	5.485	−3.67	81
	Expt.	5.442	−3.56	89
GaAs	PBE	5.755	−3.12	60
	PBE+vdW$^{\text{TS+SCS}}$	5.710	−3.35	65
	Expt.	5.641	−3.31	77
GaSb	PBE	6.227	−2.78	44
	PBE+vdW$^{\text{TS+SCS}}$	6.159	−3.03	49
	Expt.	6.082	−3.00	56

Table C.12: Calculated cohesive properties of the IIIA–VA compounds using PBE and PBE+vdW$^{\text{TS+SCS}}$: lattice constants a_0 (Å), cohesive energies E_0 (eV/atom), and bulk moduli B_0 (GPa).

		a_0	E_0	B_0
InP	PBE	5.973	−3.11	58
	PBE+vdW$^{\text{TS+SCS}}$	5.929	−3.32	63
	Expt.	5.861	−3.43	73
InAs	PBE	6.192	−2.86	48
	PBE+vdW$^{\text{TS+SCS}}$	6.142	−3.08	53
	Expt.	6.036	−3.05	58
InSb	PBE	6.651	−2.60	36
	PBE+vdW$^{\text{TS+SCS}}$	6.576	−2.83	39
	Expt.	6.469	−2.79	47

Table C.13: Calculated cohesive properties of the IIB–VIA compounds using PBE and PBE+vdW$^{\text{TS+SCS}}$: lattice constants a_0 (Å), cohesive energies E_0 (eV/atom), and bulk moduli B_0 (GPa).

		a_0	E_0	B_0
ZnS	PBE	5.456	−2.86	69
	PBE+vdW$^{\text{TS+SCS}}$	5.413	−3.07	74
	Expt.	5.404	−3.17	77
ZnSe	PBE	5.745	−2.54	56
	PBE+vdW$^{\text{TS+SCS}}$	5.688	−2.76	62
	Expt.	5.667	−2.62	65
ZnTe	PBE	6.196	−2.07	43
	PBE+vdW$^{\text{TS+SCS}}$	6.120	−2.29	48
	Expt.	6.102	−2.41	53
CdS	PBE	5.941	−2.52	53
	PBE+vdW$^{\text{TS+SCS}}$	5.877	−2.74	57
	Expt.	5.818	−2.78	64
CdSe	PBE	6.207	−2.28	45
	PBE+vdW$^{\text{TS+SCS}}$	6.134	−2.50	49
	Expt.	6.050	−2.46	55
CdTe	PBE	6.627	−1.88	35
	PBE+vdW$^{\text{TS+SCS}}$	6.552	−2.09	39
	Expt.	6.480	−2.23	45

D EXTRA DETAILS OF THE DFT+VDW APPROACH

Damping function forms:

(1) WY1 and WY2 [195]:

$f_{\rm damp}^{\rm WY1}(R) = \left(1 - \exp\left[-c_{\rm damp}\left(\frac{R}{R_{\rm m}}\right)^3\right]\right)^2$;

$f_{\rm damp}^{\rm WY2}(R) = \frac{1}{1+\exp\left[-\beta\left(\frac{R}{R_{\rm m}}-1\right)\right]}$,

$c_{\rm damp} = 3.54$ and $R_{\rm m}$ is the sum of the atomic vdW radii, and $\beta = 23$.

(2) DFT-D1/2 [70]:

$f_{\rm damp}(R) = \frac{s_6}{1+\exp\left[-d\left(\frac{r_{ij}}{s_R R_{ij}^0}-1\right)\right]}$,

$d = 23$, $s_R = 1$, s_6 is a global scaling parameter, and R_{ij}^0 is the sum of the atomic vdW radii.

(3) DFT-D3 [189, 206]:

$f_{\rm damp}(R) = \frac{1}{1+6\left(\frac{r_{ij}}{s_{r,n} R_{ij}^0}\right)^{-\alpha_n}}$,

$s_{r,n}$ is the order-dependent scaling factor of the cutoff radii R_{ij}^0, α_n is the steepness parameter.

(4) EHFSK [204]:

$f_{\rm damp}(r_{ij}) = \left(1 - \exp\left[-d\left(\frac{r_{ij}}{R_{ij}^0}\right)^N\right]\right)^M$;

$d = 3$, $N = 7$, $M = 4$, $R_{ij}^0 = 3.8$ Å for the first row elements, and $R_{ij}^0 = 4.8$ Å for the second row elements.

(5) OBS [38]:

$f_{\rm damp}(r_{ij}) = 1 - \exp\left[-\lambda\left(\frac{r_{ij}}{R^0_{ij}}\right)^n\right]$;

$\lambda = 7.5 \times 10^{-4}$ and $n = 8$.

Table D.1: The s_R scaling factor used in the TS method for different density functionals.

Functional	PBE	HSE	B3LYP	TPSS	M06-L
s_R	0.94	0.96	0.84	0.86	1.27

Table D.2: The single oscillator parameters for diamond- and zincblende-structure crystals [220].

Crystal	E_0 (eV)	$E_{\rm d}$ (eV)
C	10.9	49.7
β-SiC	7.6	42.0
Si	4.0	44.4
Ge	2.7	41.0
GaP	4.5	36.0
GaAs	3.6	33.5
ZnS	6.4	26.1
ZnSe	5.5	27.0
ZnTe	4.3	27.0
CdTe	4.1	25.7

Table D.3: Calculated static polarizabilities (bohr^3) as a function of lattice constant (Å) for C, Si, and Ge using the TD-HSE and TS+SCS approaches.

C			Si			Ge		
a_0	TS+SCS	TD-HSE	a_0	TS+SCS	TD-HSE	a_0	TS+SCS	TD-HSE
3.424	6.55	4.84	5.041	20.92	20.06	5.247	23.55	22.97
3.460	6.68	5.00	5.144	21.71	21.23	5.349	24.39	24.56
3.496	6.81	5.17	5.243	22.46	22.44	5.450	25.20	26.27
3.531	6.94	5.35	5.338	23.16	23.69	5.551	26.00	28.16
3.567	7.06	5.54	5.430	23.83	24.98	5.652	26.78	30.28
3.603	7.19	5.73	5.519	24.47	26.33	5.741	27.45	32.45
3.638	7.31	5.93	5.606	25.07	27.73	5.829	28.10	35.24
3.674	7.43	6.13	5.689	25.64	29.20	5.918	28.74	38.31

Table D.4: Calculated dispersion coefficients (hartree·bohr^6) as a function of lattice constant (Å) for C, Si, and Ge using the TD-HSE and TS+SCS approaches.

C			Si			Ge		
a_0	TS+SCS	TD-HSE	a_0	TS+SCS	TD-HSE	a_0	TS+SCS	TD-HSE
3.424	20.15	13.76	5.041	141.46	120.17	5.247	169.06	154.70
3.460	20.70	14.45	5.144	148.78	130.98	5.349	177.22	169.92
3.496	21.24	15.17	5.243	155.79	142.38	5.450	185.26	186.45
3.531	21.79	15.93	5.338	162.47	154.37	5.551	193.21	204.55
3.567	22.33	16.73	5.430	168.91	166.98	5.652	201.07	224.49
3.603	22.87	17.56	5.519	175.08	180.23	5.741	207.91	243.63
3.638	23.42	18.42	5.605	180.97	194.15	5.829	214.57	263.88
3.674	23.96	19.36	5.689	186.65	208.82	5.918	221.23	285.23

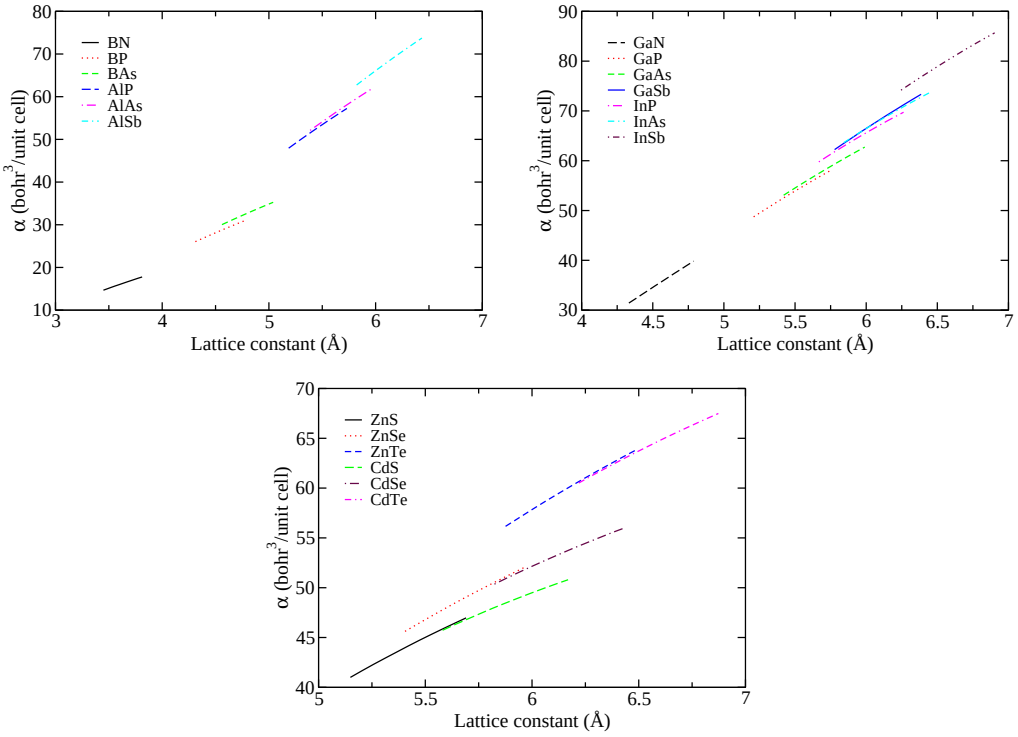

Figure D.1: Calculated static polarizabilities as a function of lattice constant for the IIIA–VA and IIB–VIA groups crystals using the TS+SCS model.

E ABBREVIATIONS

ACFDT	Adiabatic-connection fluctuation-dissipation theorem
BOA	Born-Oppenheimer approximation
B3LYP	Becke-3-Lee-Yang-Parr
BZ	Brillouin zone
BSE	Bethe-Salpeter equation
CC	Coupled cluster
CCSD(T)	Coupled cluster singles, doubles and perturbative triples
CE	Cluster extrapolation
CM	Clausius-Mossotti relation
DFA	Density-functional approximation
DFT	Density-functional theory
DOSD	Dipole oscillator strength distribution
EOS	Equation of state
EXX	Exact exchange
GGA	Generalized gradient approximation
HF	Hartree-Fock
HK	Hohenberg-Kohn
HA	Harmonic approximation
HSE	Heyd-Scuseria-Ernzerhof
KS	Kohn-Sham
KS-DFT	Kohn-Sham density-functional theory
LDA	Local-density approximation
LFE	Local field effect
MAE	Mean absolute error
MARE	Mean absolute relative error
MBPT	Many-body perturbation theory
ME	Mean error
MGGA	meta-generalized gradient approximation
MRE	Mean relative error

NQ	Nanoquanta kernel
PBC	Periodic boundary condition
PBE	Perdew-Burke-Enzerhof
QMC	Quantum Monte Carlo
QHO	Quantum harmonic oscillator
RMSD	Root-mean-square deviation
RPA	Random-phase approximation
RPBE	Revised PBE
SIE	Self-interaction error
SO	Single oscillator
TDDFT	Time-dependent density-functional theory
TF	Thomas-Fermi
TPSS	Tao-Perdew-Staroverov-Scuseria
TS	Tkatchenko/Scheffler
UEG	Uniform electron gas
vdW	van der Waals
XC	Exchange-correlation
XDM	Exchange-dipole moment
ZPVE	Zero-point vibrational energy

F SYMBOLS

$\hat{H}$	Hamilton operator
∇^2	Laplacian operator
n_0	Ground-state electron density
ψ	Wave function
$\mathbf{D}$	Electric displacement
$\mathbf{E}$	Electric field
χ_e	Electric susceptibility
L	Lorentz factor
ϵ	Fermi energy
$\mathbf{P}$	Polarization
f_{0n}	Oscillator strength of transition from ground state 0 to excited state n
α	Polarizability
ε	Relative permittivity or dielectric constant
ω	Frequency
V	Volume
f_{damp}	Damping function
s_R	Scaling parameter in the TS method

CURRICULUM VITAE

For reasons of data protection, my curriculum vitae is not published in the online version.

PUBLICATIONS, POSTER, TALKS

PUBLICATIONS

- W. Liu, V.G. Ruiz, G.-X. Zhang, B. Santra, X. Ren, M. Scheffler, and A. Tkatchenko, Structure and Energetics of Benzene Adsorbed on Transition-metal Surfaces: Density-functional Theory with van der Waals Interactions Including Collective Substrate Response, New J. Phys. **15**, 053043 (2013).

- G.-X. Zhang, A. Tkatchenko, J. Paier, H. Appel, and M. Scheffler, van der Waals Interactions in Ionic and Semiconductor Solids, Phys. Rev. Lett. **107**, 245501 (2011).

- G.-X. Zhang, Y. Xie, H.-T. Yu, and H.-G. Fu, First-Principles Calculations of the Stability and Electronic Properties of the $PbTiO_3$ (110) Polar Surface, J. Comput. Chem. **30**, 1785 (2009).

- Y. Xie, H.-T. Yu, G.-X. Zhang, and H.-G. Fu, Lattice Dynamics Investigation on Different Transition Behaviors of Cubic $BaTiO_3$ and $SrTiO_3$ by First-Principles Calculations, J. Phys.: Condens. Matter **20**, 215215 (2008).

- Y. Xie, H.-T. Yu, G.-X. Zhang, H.-G. Fu, and J.-Z. Sun, First-Principles Investigation of Stability and Structural Properties of the $BaTiO_3$ (110) Polar Surface, J. Phys. Chem. C **111** 6343 (2007).

- Y. Xie, H.-G. Fu, H.-T. Yu, G.-X. Zhang, and J.-Z. Sun, A First-Principles Investigation into the Ferroelectric and Antiferrodistortive Instabilities of Cubic $SrTiO_3$, J. Phys.: Condens. Matter **19**, 506213 (2007).

- B. Schatschneider, J.-J. Liang, A.M. Reilly, N. Marom, G.-X. Zhang, and A. Tkatchenko, Electrodynamic Response and Stability of Molecular Crystals, Phys. Rev. B **87**, 060104(R) (2013).

POSTER

- Psi-*k* conference, Berlin, Germany, September 2010
- ICTP, Trieste, Italy, January 2011
- IPAM, Los Angeles, CA, USA, May 2011
- Fachbeirat, Berlin, Germany, October 2011

TALKS

- DPG Frühjahrstagung, Regensburg, Germany, March 2010
- DPG Frühjahrstagung, Dresden, Germany, March 2011
- APS, Dallas, Texas, USA, March 2011
- CompSurf 2011, Santa Barbara, CA, USA, August 2011
- DPG Frühjahrstagung, Berlin, Germany, March 2012
- DPG Frühjahrstagung, Regensburg, Germany, March 2013
- APS, Baltimore, Maryland, USA, March 2013

PUBLICATIONS RELATED TO THIS THESIS

- G.-X. Zhang, A. Tkatchenko, J. Paier, H. Appel, and M. Scheffler, van der Waals Interactions in Ionic and Semiconductor Solids, Phys. Rev. Lett. **107**, 245501 (2011).
- G.-X. Zhang, A. M. Reily, A. Tkatchenko, and M. Scheffler, Correlations between Cohesive Properties: Experiment versus (Semi-)local Density Functionals, in preparation.

EIDESSTATTLICHE VERSICHERUNG

Ich versichere hiermit, alle Hilfsmittel und Hilfen angegeben und die Arbeit auf dieser Grundlage selbstständig verfasst zu haben. Die Arbeit ist weder in einem früheren Promotionsverfahren angenommen noch als ungenügend beurteilt worden.

Berlin, 23. Januar 2014

ACKNOWLEDGEMENTS

First of all, I must thank my group leader and the most essential person in this doctoral work, Alexandre Tkatchenko. Many thanks! Vielen Dank! Alex, I appreciate that you helped me get through each step of my Ph.D., in particular at the start of this work, and that you taught me being motivated and positive thinking, from which I'll benefit the whole life. Without your guidance, I'm sure it will be much harder for me to achieve my Ph.D. and I am very grateful.

Then, I must thank my supervisor Matthias Scheffler for providing me the opportunity to work on such a challenging and exciting topic, and to discuss with so many experts in different fields. Thank you so much for guiding my doctoral thesis and giving me advices for improving my scientific skills. Vielen Dank! I appreciate the time during the past years in Berlin. The scientific atmosphere at the FHI is extremely challenging and fruitful and Berlin is a great city that I would prefer living outside China.

I would like to acknowledge my second supervisor Felix von Oppen and the committee of my Ph.D. defense.

A special thanks goes to Anthony M. Reilly, with whom I discussed parts of the work presented here. Anthony, thanks for carefully proofreading my thesis. Thanks to our collaborators Heiko Appel and Joachim Paier. Moreover, I would like to thank Norina Richter for helping the German abstract, and Franziska Schubert, Victor Ruiz, Wei Liu, Igor Poltavskyi, and Jan Hermann for providing their comments. I must acknowledge my officemate Vivekanand Gobre for guiding me to programming. Fabio, thank you for sharing your experience of thesis submission, and you are a great officemate and friend. I appreciate the help I obtained from other former and current members of the theory department of FHI, in particular to Jörg, Claudia, Xinguo, Hong, Mariana, Marco, Mathis, and Katja, and a special thanks goes to our secretaries Gaby, Julia, Birgit, and Carmen, as well as, Steffen.

Thanks to all my friends that I met during my Ph.D. time. A huge thanks to my German sisters, Norina, Franziska, and Claudia. I would like to thank my flatmates Xin Yu and Shuangyan He, and the Chinese community, in particular to Bo Li, Xiaoying Sun, Chuangzhu Wu, Juan Li, Xuerong Shi, Yingna Sun, Bing Yang, Lili Sun, Xunhua Zhao, Yan Zhang, Javier Carrasco, and many others.

Finally, my biggest thanks goes to my family and friends in China for their permanent support, especially to my parents Jing-Jun and Hui, and my brother Guo-Qiang. I cannot imagine how could I get through the life outside China without your encouragement and understanding. Thank you very much. Yan Zhu, Jing-Hua Wang, and Yu Zhang, many thanks for your friendship. I would like to acknowledge my former supervisor Hai-Tao Yu and Ying Xie for their advices. And to my cousin Ying-Chun who had passed away.

BIBLIOGRAPHY

BIBLIOGRAPHY

[1] N. W. ASHCROFT and N. D. MERMIN, *Solid State Physics*, Holt, Reinhart & Winston, New York, 1976.

[2] J. E. MAYER, *J. Chem. Phys.* **1**, 270 (1933).

[3] A. MAY, *Phys. Rev.* **52**, 339 (1937).

[4] F. HAJJ, *J. Chem. Phys.* **44**, 4618 (1966).

[5] D. W. LYNCH, *J. Phys. Chem. Solids* **28**, 1941 (1967).

[6] J. K. JAIN, J. SHANKER, and D. P. KHANDELWAL, *Phys. Rev. B* **13**, 2692 (1976).

[7] P. S. BAKHSHI, S. C. GOYAL, and J. SHANKER, *J. Inorg. Nucl. Chem.* **39**, 546 (1977).

[8] S. GRIMME, *WIREs Rev. Comput. Mol. Sci.* **1**, 211 (2011).

[9] E. R. JOHNSON, I. D. MACKIE, and G. A. DILABIO, *J. Phys. Org. Chem.* **22**, 1127 (2009).

[10] A. TKATCHENKO, L. ROMANER, O. T. HOFMANN, E. ZOJER, C. AMBROSCH-DRAXL, and M. SCHEFFLER, *MRS Bulletin* **35**, 435 (2010).

[11] J. KLIMEŠ and A. MICHAELIDES, *J. Chem. Phys.* **137**, 120901 (2012).

[12] R. EISENSCHITZ and F. LONDON, *Z. Physik* **60**, 491 (1930).

[13] F. LONDON, *Trans. Faraday Soc.* **33**, 8 (1937).

[14] A. J. STONE, *The Theory of Intermolecular Forces*, Oxford Unversity Press, USA, 2th edition, 2013.

[15] I. G. KAPLAN, *Intermolecular Interactions*, John Wiley & Sons. Ltd, 2006.

[16] X. CHU and A. DALGARNO, *J. Chem. Phys.* **121**, 4083 (2004).

[17] P. W. FOWLER, P. J. KNOWLES, and N. C. PYPER, *Mol. Phys.* **56**, 83 (1985).

[18] P. W. FOWLER and P. A. MADDEN, *Phys. Rev. B* **29**, 1035 (1984).

[19] N. C. PYPER and P. POPELIER, *J. Phys.: Condens. Matter* **9**, 471 (1997).

[20] A. TKATCHENKO, R. A. DISTASIO, R. CAR, and M. SCHEFFLER, *Phys. Rev. Lett.* **108**, 236402 (2012).

[21] V. BLUM, R. GEHRKE, F. HANKE, P. HAVU, V. HAVU, X. REN, K. REUTER, and M. SCHEFFLER, *Comput. Phys. Commun.* **180**, 2175 (2009).

[22] A. TKATCHENKO and M. SCHEFFLER, *Phys. Rev. Lett.* **102**, 073005 (2009).

[23] W. L. BRAGG, *Nature* **90**, 410 (1912).

[24] C. KITTEL, *Introduction to Solid State Physics*, John Wiley & Sons., New York, 7th edition, 1996.

[25] A. M. REILLY and A. TKATCHENKO, *J. Phys. Chem. Lett.* **4**, 1028 (2013).

[26] J. R. TESSMAN, A. H. KAHN, and W. SHOCKLEY, *Phys. Rev.* **92**, 890 (1953).

[27] N. F. MOTT and H. JONES, *The Theory of the Properties of Metals and Alloys*, New York, 1936.

[28] J. DE SMEDT, W. H. KEESOM, and H. H. MOOY, *Proc. Roy. Amsterdam Acad.* **33**, 255 (1930).

[29] F. E. SIMON and C. VON SIMSON, *Z. Physik* **25**, 160 (1924).

[30] J. DE SMEDT and W. H. KEESOM, *Physica* **5**, 344 (1925).

[31] W. H. KEESOM and H. H. MOOY, *Nature* **125**, 889 (1930).

[32] G. NATTA and A. NASINI, *Nature* **125**, 457 (1930).

[33] H. MARGENAU, *Phys. Rev.* **38**, 747 (1931).

[34] H. MARGENAU, *Rev. Mod. Phys.* **11**, 1 (1939).

[35] G. L. POLLACK, *Rev. Mod. Phys.* **36**, 748 (1964).

[36] K. F. NIEBEL and J. A. VENABLES, *in Rare Gas Solids*, volume I, Academic Press, New York, 1976.

[37] J. A. BARKER, *in Rare Gas Solids*, volume I, Academic Press, New York, 1976.

[38] F. ORTMANN, F. BECHSTEDT, and W. G. SCHMIDT, *Phys. Rev. B* **73**, 205101 (2006).

[39] T. KIHARA and S. KOBA, *J. Phys. Soc. Jpn.* **7**, 348 (1952).

[40] J. JANSEN and M. D. DAWSON, *J. Chem. Phys.* **23**, 482 (1955).

[41] R. A. AZIZ, *J. Chem. Phys.* **99**, 4518 (1993).

[42] O. G. PETERSON, D. N. BATCHELDER, and R. O. SIMMONS, *Phys. Rev.* **150**, 703 (1966).

[43] T. BRICHENO and J. A. VENABLES, *J. Phys. C: Solid State Phys.* **9**, 4095 (1976).

[44] M. J. ELROD and R. J. SAYKALLY, *Chem. Rev.* **94**, 1975 (1994).

[45] B. M. AXILROD and E. TELLER, *J. Chem. Phys.* **11**, 299 (1943).

[46] Y. MUTO, *Proc. Phys. Math. Soc. Jpn.* **17**, 629 (1943).

[47] L. JANSEN, *Phys. Rev.* **135**, A1292 (1964).

[48] L. JANSEN, *Adv. Quantum Chem.* **2**, 119 (1966).

[49] G. DOTELLI and L. JANSEN, *Phys. A* **234**, 151 (1996).

[50] V. F. LOTRICH and K. SZALEWICZ, *Phys. Rev. Lett.* **79**, 1301 (1997).

[51] K. ROŚCISZEWSKI, B. PAULUS, P. FULDE, and H. STOLL, *Phys. Rev. B* **60**, 7905 (1999).

[52] K. ROŚCISZEWSKI, B. PAULUS, P. FULDE, and H. STOLL, *Phys. Rev. B* **62**, 5482 (2000).

[53] A. TKATCHENKO and O. A. VON LILIENFELD, *Phys. Rev. B* **78**, 045116 (2008).

[54] M. BORN and J. E. MAYER, *Zeits. f. Physik* **75**, 1 (1932).

[55] J. E. MAYER and R. B. LEVY, *J. Chem. Phys.* **1**, 647 (1933).

[56] J. E. MAYER, *J. Chem. Phys.* **1**, 327 (1933).

[57] J. C. PHILLIPS, *Rev. Mod. Phys.* **42**, 317 (1970).

[58] M. F. C. LADD, *J. Chem. Phys.* **60**, 1954 (1974).

[59] J. SHANKER, G. G. AGRAWAL, and R. P. SINGH, *J. Chem. Phys.* **69**, 670 (1978).

[60] J. UPADHYAYA, *Phys. Lett. A* **73**, 238 (1979).

[61] G. D. MAHAN, *Solid State Ionics* **1**, 29 (1980).

[62] P. W. FOWLER and P. A. MADDEN, *Mol. Phys.* **49**, 913 (1983).

[63] P. W. FOWLER and P. A. MADDEN, *J. Phys. Chem.* **89**, 2581 (1985).

[64] N. C. PYPER, *Phil. Trans. R. Soc. Lond. A* **352**, 89 (1995).

[65] N. C. PYPER, *Mol. Phys.* **95**, 1 (1998).

[66] M. WILSON, P. A. MADDEN, P. JEMMER, P. W. FOWLER, and A. BATANA, *Mol. Phys.* **96**, 1457 (1999).

[67] E. BICHOUTSKAIA and N. C. PYPER, *J. Phys. Chem. C* **111**, 9548 (2007).

[68] M. P. HOUSDEN and N. C. PYPER, *J. Phys.: Condens. Matter* **20**, 085222 (2008).

[69] K. DOLL and H. STOLL, *Phys. Rev. B* **56**, 10121 (1997).

[70] S. GRIMME, *J. Comput. Chem.* **27**, 1787 (2006).

[71] J. KLIMEŠ, D. R. BOWLER, and A. MICHAELIDES, *Phys. Rev. B* **83**, 195131 (2011).

[72] G.-X. ZHANG, A. TKATCHENKO, J. PAIER, H. APPEL, and M. SCHEFFLER, *Phys. Rev. Lett.* **107**, 245501 (2011).

[73] J. FRIEDEL, *Proc. Phys. Soc. B* **65**, 769 (1952).

[74] J. J. REHR, E. ZAREMBA, and W. KOHN, *Phys. Rev. B* **12**, 2062 (1975).

[75] D. D. RICHARDSON and J. MAHANTY, *J. Phys. C: Solid State Phys.* **10**, 3971 (1977).

[76] E. ZAREMBA and W. KOHN, *Phys. Rev. B* **13**, 2270 (1976).

[77] J. A. MORIARTY, *Phys. Rev. B* **10**, 3075 (1974).

[78] J. TAO, J. P. PERDEW, and A. RUZSINSZKY, *Phys. Rev. B* **81**, 233102 (2010).

[79] J. WELLENDORFF and T. BLIGAARD, *Top. Catal.* **54**, 1143 (2011).

[80] S. STOUPIN and Y. V. SHVYD'KO, *Phys. Rev. Lett.* **104**, 085901 (2010).

[81] A. ARESTI, L. GARBATO, and A. RUCCI, *J. Phys. Chem. Solids* **45**, 361 (1984).

[82] H. SCHLOSSER, *J. Phys. Chem. Solids* **53**, 855 (1992).

[83] H. SCHLOSSER, *phys. status solidi (b)* **179**, K1 (1993).

[84] A. L. IVANOVSKII, *Prog. Mater. Sci.* **57**, 184 (2012).

[85] O. L. ANDERSON and J. E. NAFE, *J. Geophys. Res.* **70**, 3950 (1965).

[86] M. L. COHEN, *Phys. Rev. B* **32**, 7988 (1985).

[87] P. K. LAM and M. L. COHEN, *Phys. Rev. B* **35**, 9190 (1987).

[88] F. BIRCH, *Phys. Rev.* **71**, 809 (1947).

[89] W. KOHN and L. J. SHAM, *Phys. Rev.* **140**, A1133 (1965).

[90] J. P. PERDEW, A. RUZSINSZKY, J. TAO, V. STAROVEROV, G. SCUSERIA, and G. CSONKA, *J. Chem. Phys.* **123**, 62201 (2005).

[91] A. J. COHEN, P. MORI-SÁNCHEZ, and W. YANG, *Chem. Phys.* **112**, 289 (2012).

[92] K. BURKE, *J. Chem. Phys.* **136**, 150901 (2012).

[93] A. J. COHEN, P. MORI-SNCHEZ, and W. YANG, *Science* **321**, 792 (2008).

[94] J. P. PERDEW, K. BURKE, and M. ERNZERHOF, *Phys. Rev. Lett.* **77**, 3865 (1996).

[95] J. TAO, J. P. PERDEW, V. N. STAROVEROV, and G. E. SCUSERIA, *Phys. Rev. Lett.* **91**, 146401 (2003).

[96] V. N. STAROVEROV, G. E. SCUSERIA, J. TAO, and J. P. PERDEW, *Phys. Rev. B* **69**, 075102 (2004).

[97] V. N. STAROVEROV, G. E. SCUSERIA, J. TAO, and J. P. PERDEW, *Phys. Rev. B* **78**, 239907 (2008).

[98] P. HAAS, F. TRAN, and P. BLAHA, *Phys. Rev. B* **79**, 085104 (2009).

[99] P. HAAS, F. TRAN, and P. BLAHA, *Phys. Rev. B* **79**, 209902 (R) (2009).

[100] P. HAAS, F. TRAN, P. BLAHA, L. S. PEDRORA, A. J. R. SILVA, M. M. ODASHIMA, and K. CAPELLE, *Phys. Rev. B* **81**, 125136 (2010).

[101] S. K. GHOSH and R. G. PARR, *Phys. Rev. A* **34**, 785 (1986).

[102] A. D. BECKE and M. E. ROUSSEL, *Phys. Rev. A* **39**, 3761 (1989).

[103] A. D. BECKE, *J. Chem. Phys.* **98**, 1372 (1993).

[104] A. D. BECKE, *J. Chem. Phys.* **98**, 5648 (1993).

[105] A. D. BECKE, *J. Chem. Phys.* **104**, 1040 (1996).

[106] O. A. VYDROV and G. E. SCUSERIA, *J. Chem. Phys.* **125**, 234109 (2006).

[107] J. HARL and G. KRESSE, *Phys. Rev. Lett.* **103**, 056401 (2009).

[108] J. HARL, L. SCHIMKA, and G. KRESSE, *Phys. Rev. B* **81**, 115126 (2010).

[109] J. KLIMEŠ, D. R. BOWLER, and A. MICHAELIDES, *J. Phys.: Condens. Matter* **22**, 022201 (2010).

[110] G. H. BOOTH, A. GRÜNEIS, G. KRESSE, and A. ALAVI, *Nature* **493**, 365 (2013).

[111] J. ČÍŽEK, *J. Chem. Phys.* **45**, 4256 (1966).

[112] J. ČÍŽEK and J. PALDUS, *Int. J. Quant. Chem.* **5**, 359 (1971).

[113] G. D. PURVIS and R. J. BARTLETT, *J. Chem. Phys.* **76**, 1910 (1982).

[114] J. NOGA and R. J. BARTLETT, *J. Chem. Phys.* **86**, 7041 (1987).

[115] D. BOHM and D. PINES, *Phys. Rev.* **82**, 625 (1951).

[116] D. PINES and D. BOHM, *Phys. Rev.* **85**, 338 (1952).

[117] D. BOHM and D. PINES, *Phys. Rev.* **92**, 609 (1953).

[118] F. SCHWABEL, *Advanced Quantum Mechanics*, Springer, 4th edition, 2008.

[119] P. HAO, Y. FANG, J. SUN, G. I. CSONKA, P. H. T. PHILIPSEN, and J. P. PERDEW, *Phys. Rev. B* **85**, 014111 (2012).

[120] M. BORN and R. OPPENHEIMER, *Ann. der Physik* **84**, 457 (1927).

[121] L. H. THOMAS, *Math. Proc. Cambridge* **23**, 542 (1927).

[122] E. FERMI, *Rend. Accard. Naz. Lincei* **6**, 602 (1927).

[123] P. HOHENBERG and W. KOHN, *Phys. Rev.* **136**, B864 (1964).

[124] I. N. LEVINE, *Quantum Chemistry*, Prentice-Hall of India Private Limited, 2006.

[125] http://en.wikipedia.org/wiki/Kohn Sham equations, 2013.

[126] O. A. VYDROV, *Correcting the Self-Interaction Error of Approximate Density Functionals*, PhD thesis, Rice University, Houston, Texas, 2007.

[127] J. P. PERDEW and K. SCHMID, *in Density Functional Theory and Its Application to Materials*, AIP, Melville, New York, 2001.

[128] P. A. M. DIRAC, *Math. Proc. Cambridge* **26**, 376 (1930).

[129] D. M. CEPERLEY and B. J. ALDER, *Phys. Rev. Lett.* **45**, 566 (1980).

[130] S. H. VOSKO, L. WILK, and M. NUSAIR, *Can. J. Phys.* **58**, 1200 (1980).

[131] J. P. PERDEW and A. ZUNGER, *Phys. Rev. B* **23**, 5048 (1981).

[132] J. P. PERDEW and Y. WANG, *Phys. Rev. B* **45**, 13244 (1992).

[133] K. BURKE, J. P. PERDEW, and M. ERNZERHOF, *J. Chem. Phys.* **109**, 3760 (1998).

[134] R. O. JONES and O. GUNNARSSON, *Rev. Mod. Phys.* **61**, 689 (1989).

[135] V. N. STAROVEROV, G. E. SCUSERIA, J. TAO, and J. P. PERDEW, *J. Chem. Phys.* **119**, 12129 (2003).

[136] J. SUN, M. MARSMAN, G. I. CSONKA, A. RUZSINSZKY, P. HAO, Y.-S. KIM, G. KRESSE, and J. P. PERDEW, *Phys. Rev. B* **84**, 035117 (2011).

[137] J. P. PERDEW, J. A. CHEVARY, S. H. VOSKO, K. A. JACKSON, M. R. PEDERSON, D. J. SINGH, and C. FIOLHAIS, *Phys. Rev. B* **46**, 6671 (1992).

[138] Y. ZHANG and W. YANG, *Phys. Rev. Lett.* **80**, 890 (1998).

[139] B. HAMMER, L. B. HANSEN, and J. K. NØRSKOV, *Phys. Rev. B* **59**, 7413 (1999).

[140] J. P. PERDEW, A. RUZSINSZKY, G. I. CSONKA, O. A. VYDROV, G. E. SCUSERIA, L. A. CONSTANTIN, X. ZHOU, and K. BURKE, *Phys. Rev. Lett.* **100**, 136406 (2008).

[141] G. I. CSONKA, J. P. PERDEW, A. RUZSINSZKY, P. H. T. PHILIPSEN, S. LEBÈGUE, J. PAIER, O. A. VYDROV, and J. G. ÁNGYÁN, *Phys. Rev. B* **79**, 155107 (2009).

[142] L. SCHIMKA, J. HARL, and G. KRESSE, *J. Chem. Phys.* **134**, 024116 (2011).

[143] J. P. PERDEW, A. RUZSINSZKY, G. I. CSONKA, L. A. CONSTANTIN, and J. SUN, *Phys. Rev. Lett.* **103**, 026403 (2009).

[144] J. P. PERDEW, A. RUZSINSZKY, G. I. CSONKA, L. A. CONSTANTIN, and J. SUN, *Phys. Rev. Lett.* **106**, 179902(E) (2011).

[145] Y. ZHAO and D. G. TRUHLAR, *J. Chem. Phys.* **125**, 194101 (2006).

[146] Y. ZHAO and D. G. TRUHLAR, *J. Chem. Phys.* **128**, 184109 (2008).

[147] Y. ZHAO and D. G. TRUHLAR, *Theor. Chem. Acc.* **120**, 215 (2008).

[148] Y. ZHAO and D. G. TRUHLAR, *J. Phys. Chem. A* **110**, 13126 (2006).

[149] C. T. LEE, W. T. YANG, and R. G. PARR, *Phys. Rev. B* **37**, 785 (1988).

[150] J. HEYD, G. E. SCUSERIA, and M. ERNZERHOF, *J. Chem. Phys.* **124**, 219906(E) (2006).

[151] J. HEYD, G. E. SCUSERIA, and M. ERNZERHOF, *J. Chem. Phys.* **118**, 8207 (2003).

[152] J. HEYD and G. E. SCUSERIA, *J. Chem. Phys.* **121**, 1187 (2004).

[153] J. HEYD, J. E. PERALTA, G. E. SCUSERIA, and R. L. MARTIN, *J. Chem. Phys.* **123**, 174101 (2005).

[154] T. M. HENDERSON, J. PAIER, and G. E. SCUSERIA, *phys. status solidi (b)* **248**, 767 (2011).

[155] J. PAIER, M. MARSMAN, K. HUMMER, G. KRESSE, I. C. GERBER, and J. G. ÁNGYÁN, *J. Chem. Phys.* **124**, 154709 (2006).

[156] A. V. KRUKAU, O. A. VYDROV, A. F. IZMAYLOV, and G. E. SCUSERIA, *J. Chem. Phys.* **125**, 224106 (2006).

[157] J. PAIER, M. MARSMAN, and G. KRESSE, *J. Chem. Phys.* **127**, 024103 (2007).

[158] M. MARSMAN, J. PAIER, A. STROPPA, and G. KRESSE, *J. Phys.: Condens. Matter* **20**, 064201 (2008).

[159] J. P. PERDEW, M. ERNZERHOF, and K. BURKE, *J. Chem. Phys.* **105**, 9982 (1996).

[160] X. REN, P. RINKE, C. JOAS, and M. SCHEFFLER, *J. Mater. Sci.* **47**, 7447 (2012).

[161] H. ESHUIS, J. E. BATES, and F. FURCHE, *Theor. Chem. Acc.* **131**, 1084 (2012).

[162] X. REN, A. TKATCHENKO, P. RINKE, and M. SCHEFFLER, *Phys. Rev. Lett.* **106**, 153003 (2011).

[163] X. REN, P. RINKE, G. E. SCUSERIA, and M. SCHEFFLER, *Phys. Rev. B* **88**, 035120 (2013).

[164] D. R. HARTREE, *Math. Proc. Cambridge* **24**, 89 (1928).

[165] V. FOCK, *Z. Physik* **61**, 126 (1930).

[166] C. MØLLER and M. S. PLESSET, *Phys. Rev.* **46**, 618 (1934).

[167] J. S. BINKLEY and J. A. POPLE, *Int. J. Quant. Chem.* **9**, 229 (1975).

[168] H. C. HAMAKER, *Physica* **4**, 1058 (1937).

[169] M. C. STRUENSEE, *Uses of Dipole Oscillator Strength Sum Rules in Second Order Perturbation Theory*, PhD thesis, University of Texas at Austin, 1984.

[170] H. B. G. CASIMIR and D. POLDER, *Phys. Rev.* **73**, 360 (1948).

[171] A. DALGARNO, *Adv. Phys.* **11**, 281 (1962).

[172] H. SUTTER and R. H. COLE, *J. Chem. Phys.* **52**, 132 (1970).

[173] V. A. MALTSEV, O. A. NERUSHEV, and S. A. NOVOPASHIN, *Chem. Phys. Lett.* **212**, 480 (1993).

[174] A. SALOP, E. POLLACK, and B. BEDERSON, *Phys. Rev.* **124**, 1431 (1961).

[175] G. E. CHAMBERLAIN and J. C. ZORN, *Phys. Rev.* **129**, 677 (1963).

[176] L. SCHIMKA, J. HARL, G. A. STROPPA, A, M. MARSMAN, F. MITTENDORFER, and G. KRESSE, *Nat. Mater.* **9**, 741 (2010).

[177] J. PAIER, B. G. JANESKO, T. M. HENDERSON, G. E. SCUSERIA, A. GRÜNEIS, and G. KRESSE, *J. Chem. Phys.* **132**, 094103 (2010).

[178] X. REN, P. RINKE, V. BLUM, J. WIEFERINK, A. TKATCHENKO, A. SANFILIPPO, K. REUTER, and M. SCHEFFLER, *New J. Phys.* **14**, 053020 (2012).

[179] M. DION, H. RYDBERG, E. SCHRÖDER, D. C. LANGRETH, and B. I. LUNDQVIST, *Phys. Rev. Lett.* **92**, 246401 (2004).

[180] O. A. VYDROV and T. VAN VOORHIS, *Phys. Rev. Lett.* **103**, 063004 (2009).

[181] K. LEE, E. D. MURRAY, L. KONG, B. I. LUNDQVIST, and D. C. LANGRETH, *Phys. Rev. B* **82**, 081101(R) (2010).

[182] O. A. VYDROV and T. V. VOORHIS, *J. Chem. Phys.* **133**, 244103 (2010).

[183] O. A. VYDROV and T. V. VOORHIS, *J. Chem. Phys.* **130**, 104105 (2009).

[184] O. A. VYDROV and T. V. VOORHIS, *J. Chem. Phys.* **132**, 164113 (2010).

[185] O. A. VYDROV and T. V. VOORHIS, *Phys. Rev. A* **81**, 062708 (2010).

[186] D. LU, H.-V. NGUYEN, and G. GALLI, *J. Chem. Phys* **133**, 154110 (2010).

[187] D. C. LANGRETH, B. I. LUNDQVIST, S. D. CHAKAROVA-KÄCK, V. R. COOPER, M. DION, P. HYLDGAARD, A. KELKKANEN, J. KLEIS, L. KONG, S. LI, P. G. MOSES, E. MURRAY, A. PUZDER, H. RYDBERG, E. SCHRÖDER, and T. THONHAUSER, *J. Phys.: Condens. Matter* **21**, 084203 (2009).

[188] S. GRIMME, *J. Comput. Chem.* **25**, 1463 (2004).

[189] S. GRIMME, J. ANTONY, S. EHRLICH, and H. KRIEG, *J. Chem. Phys.* **132**, 154104 (2010).

[190] A. D. BECKE and E. R. JOHNSON, *J. Chem. Phys.* **122**, 154104 (2005).

[191] A. D. BECKE and E. R. JOHNSON, *J. Chem. Phys.* **123**, 154101 (2005).

[192] A. D. BECKE and E. R. JOHNSON, *J. Chem. Phys.* **127**, 154108 (2007).

[193] G. D. ZEISS and W. J. MEATH, *Mol. Phys.* **33**, 1155 (1977).

[194] D. J. MARGOLIASH and W. J. MEATH, *J. Chem. Phys.* **68**, 1426 (1978).

[195] Q. WU and W. T. YANG, *J. Chem. Phys.* **116**, 515 (2002).

[196] E. R. JOHNSON and A. D. BECKE, *J. Chem. Phys.* **123**, 024101 (2005).

[197] E. R. JOHNSON and A. D. BECKE, *J. Chem. Phys.* **124**, 174104 (2006).

[198] F. L. HIRSHFELD, *Theor. Chim. Acta.* **44**, 129 (1977).

[199] A. OLASZ, K. VANOMMESLAEGHE, A. KRISHTAL, T. VESZPRÉMI, C. V. ALSENOY, and P. GEERLINGS, *J. Chem. Phys.* **127**, 224105 (2007).

[200] F. O. KANNEMANN and A. D. BECKE, *J. Chem. Theory Comput.* **6**, 1081 (2010).

[201] S. N. STEINMANN and C. CORMINBOEUF, *J. Chem. Phys.* **134**, 044117 (2011).

[202] K. T. TANG, *Phys. Rev.* **177**, 108 (1969).

[203] T. BRINCK, J. S. MURRAY, and P. POLITZER, *J. Chem. Phys.* **98**, 4305 (1993).

[204] M. ELSTNER, P. HOBZA, T. FRAUENHEIM, S. SUHAI, and E. KAXIRAS, *J. Chem. Phys.* **114**, 5149 (2001).

[205] P. JUREČKA, J. ČERNÝ, P. HOBZA, and D. SALAHUB, *J. Comput. Chem.* **28**, 555 (2007).

[206] J.-D. CHAI and M. HEAD-GORDON, *Phys. Chem. Chem. Phys.* **10**, 6615 (2008).

[207] S. GRIMME, S. EHRLICH, and L. GOERIGK, *J. Comput. Chem.* **32**, 1456 (2011).

[208] P. JUREČKA, J. ŠPONER, J. ČERNÝ, and P. HOBZA, *Phys. Chem. Chem. Phys.* **8**, 1985 (2006).

[209] V. G. RUIZ, W. LIU, E. ZOJER, M. SCHEFFLER, and A. TKATCHENKO, *Phys. Rev. Lett.* **108**, 146103 (2012).

[210] http://en.wikipedia.org/wiki/Polarization density, 2013.

[211] J. D. JACKSON, *Classical Electrodynamics*, John Wiley & Sons., New York, 1975.

[212] M. S. DRESSELHAUS, Solid State Physics (Part II): Optical Properties of Solids [PDF document]. Retrieved from Lecture Notes Online Web site: http://bookos.org/book/453978/572abc, 2001.

[213] N. F. MOTT and M. J. LITTLETON, *Trans. Faraday Soc.* **34**, 485 (1938).

[214] N. F. MOTT and R. W. GURNEY, *Electronic Processes in Ionic Crystals*, Oxford Unversity Press, London, 1948.

[215] C. G. DARWIN, *Proc. Roy. Soc. Lond. A* **17**, 146 (1934).

[216] C. G. DARWIN, *Proc. Roy. Soc. Lond. A* **182**, 152 (1943).

[217] B. R. A. NIJBOER and F. W. DE WETTE, *Physica* **24**, 422 (1958).

[218] F. W. DE WETTE and G. E. SCHACHER, *Phys. Rev.* **137**, 78 (1965).

[219] I. M. BOSWARVA, *Phys. Rev. B* **1**, 1698 (1970).

[220] S. H. WEMPLE and M. DIDOMENICO, *Phys. Rev. B* **3**, 1338 (1971).

[221] F. CLARO, *Phys. Rev. B* **25**, 2483 (1982).

[222] R. BONNEVILLE, *Phys. Rev. B* **21**, 368 (1980).

[223] R. BONNEVILLE and G. FISHMAN, *Phys. Rev. B* **22**, 2008 (1980).

[224] R. BONNEVILLE, *Phys. Rev. B* **26**, 513 (1982).

[225] A. JIEMCHOOROJ, B. E. SERNELIUS, and P. NORMAN, *Phys. Rev. A* **69**, 044701 (2004).

[226] S. BOTTI, A. CASTRO, X. ANDRADE, A. RUBIO, and M. A. L. MARQUES, *Phys. Rev. B* **78**, 035333 (2008).

[227] E. RUNGE and E. K. U. GROSS, *Phys. Rev. Lett.* **52**, 997 (1984).

[228] M. A. L. MARQUES and E. K. U. GROSS, *Time-Dependent Density Functional Theory, in A Primer in Density Functional Theory*, Springer, 2003.

[229] M. A. L. MARQUES, C. A. ULLRICH, F. NOGUERIA, A. RUBIO, K. BURKE, and E. K. U. GROSS, editors, *Time-Dependent Density Functional Theory*, Springer, Berlin Heidelberg, 2006.

[230] P. ELLIOTT, F. FURCHE, and K. BURKE, *Excited States from Time-Dependent Density Functional Theory*, volume 26, Reviews in Computational Chemistry, 2009.

[231] J. PAIER, M. MARSMAN, and G. KRESSE, *Phys. Rev. B* **78**, 121201 (2008).

[232] S. L. ADLER, *Phys. Rev.* **126**, 413 (1962).

[233] N. WISER, *Phys. Rev.* **129**, 62 (1963).

[234] G. ONIDA, L. REINING, and A. RUBIO, *Rev. Mod. Phys.* **74**, 601 (2002).

[235] L. HEDIN, *Phys. Rev.* **139**, A796 (1965).

[236] S. ALBRECHT, L. REINING, R. DEL SOLE, and G. ONIDA, *Phys. Rev. Lett.* **80**, 4510 (1998).

[237] R. DEL SOLE, G. ADRAGNA, V. OLEVANO, and L. REINING, *Phys. Rev. B* **67**, 045207 (2003).

[238] G. ADRAGNA, R. DEL SOLE, and A. MARINI, *Phys. Rev. B* **68**, 165108 (2003).

[239] L. REINING, V. OLEVANO, A. RUBIO, and G. ONIDA, *Phys. Rev. Lett.* **88**, 066404 (2002).

[240] F. SOTTILE, V. OLEVANO, and L. REINING, *Phys. Rev. Lett.* **91**, 056402 (2003).

[241] S. SHARMA, J. K. DEWHURST, A. SANNA, and E. K. U. GROSS, *Phys. Rev. Lett.* **107**, 186401 (2011).

[242] A. MARINI, R. DEL SOLE, and A. RUBIO, *Phys. Rev. Lett.* **91**, 256402 (2003).

[243] S. BOTTI, F. SOTTILE, N. VAST, V. OLEVANO, L. REINING, H.-C. WEISSKER, A. RUBIO, G. ONIDA, R. DEL SOLE, and R. W. GODBY, *Phys. Rev. B* **69**, 155112 (2004).

[244] F. BRUNEVAL, F. SOTTILE, V. OLEVANO, R. DEL SOLE, and L. REINING, *Phys. Rev. Lett.* **94**, 186402 (2005).

[245] G. KRESSE and J. FURTHMÜLLER, *Comput. Mater. Sci.* **6**, 15 (1996).

[246] G. KRESSE and J. FURTHMÜLLER, *Phys. Rev. B* **54**, 11169 (1996).

[247] R. STERNHEIMER, *Phys. Rev.* **84**, 244 (1951).

[248] B. WALKER, A. M. SAITTA, R. GEBAUER, and S. BARONI, *Phys. Rev. Lett.* **96**, 113001 (2006).

[249] X. ANDRADE, S. BOTTI, M. A. L. MARQUES, and A. RUBIO, *J. Chem. Phys.* **126**, 184106 (2007).

[250] X. ANDRADE, *Linear and Non-linear Response Phenomena of Molecular Systems within Time-dependent Density Functional Teory*, PhD thesis, University of the Basque Country, 2010.

[251] M. A. L. MARQUES, A. CASTRO, G. F. BERTSCH, and A. RUBIO, *Comput. Phys. Comm.* **151**, 60 (2003).

[252] A. CASTRO, M. A. L. MARQUES, H. APPEL, M. OLIVEIRA, C. A. ROZZI, X. ANDRADE, F. LORENZEN, E. K. U. GROSS, and A. RUBIO, *phys. status solidi (b)* **243**, 2465 (2006).

[253] A. TOGO, F. OBA, and I. TANAKA, *Phys. Rev. B* **78**, 134106 (2008).

[254] K. PARLINSKI, Z. Q. LI, and Y. KAWAZOE, *Phys. Rev. Lett.* **78**, 4063 (1997).

[255] S. BARONI, S. DE GIRONCOLI, A. DAL CORSO, and P. GIANNOZZI, *Rev. Mod. Phys.* **73**, 515 (2001).

[256] G. KERN, G. KRESSE, and J. HAFNER, *Phys. Rev. B* **59**, 8551 (1999).

[257] K. ROŚCISZEWSKI and B. PAULUS, *Mol. Phys.* **108**, 2147 (2010).

[258] B. GRABOWSKI, T. HICKEL, and J. NEUGEBAUER, *Phys. Rev. B* **76**, 024309 (2007).

[259] H. J. MONKHORST and J. D. PACK, *Phys. Rev. B* **13**, 5188 (1976).

[260] E. VAN LENTHE, E. J. BAERENDS, and J. G. SNIJDERS, *J. Chem. Phys.* **101**, 9783 (1994).

[261] P. H. T. PHILIPSEN and E. J. BAERENDS, *Phys. Rev. B* **61**, 1773 (2000).

[262] P. BLAHA, K. SCHWARZ, G. K. H. MADSEN, D. KVASNICKA, and J. LUITZ, *WIEN2k, An Augmented Plane Wave Plus Local Orbitals Program for Calculating Crystal Properties*, Vienna University of Technology, Austria, 2001.

[263] http://phonopy.sourceforge.net/FHI-aims.html.

[264] A. B. ALCHAGIROV, J. P. PERDEW, J. C. BOETTGER, R. C. ALBERS, and C. FIOLHAIS, *Phys. Rev. B* **63**, 224115 (2001).

[265] D. DZIVENKO, A. ZERR, N. GUIGNOT, M. MEZOUAR, and R. RIEDEL, *Euro. Phys. Lett.* **92**, 66001 (2010).

[266] K. K. KORIR, G. O. AMOLO, N. W. MAKAU, and D. P. JOUBERT, *Diam. Relat. Mater.* **20**, 157 (2011).

[267] A. R. GOÑI, K. SYASSEN, and M. CARDONA, *Phys. Rev. B* **41**, 10104 (1990).

[268] J. A. VAN VECHTEN, *Phys. Rev.* **182**, 891 (1969).

[269] H. R. PHILLIP and E. A. TAFT, *Phys. Rev.* **136**, A1445 (1964).

[270] P. LAUTENSCHLAGER, M. GARRIGA, L. VINA, and M. CARDONA, *Phys. Rev. B* **36**, 4821 (1987).

[271] S. T. PANTELIDES, *Phys. Rev. Lett.* **35**, 250 (1975).

[272] P. Y. YU and M. CARDONA, *Fundamentals of Semiconductors*, Springer-Verlag, Berlin, 2001.

[273] H. JEX, *phys. status solidi (b)* **45**, 343 (1971).

[274] D. W. OXTOBY and W. M. GELBART, *Mol. Phys.* **29**, 1569 (1975).

[275] B. U. FELDERHOF, *Physica* **76**, 486 (1974).

[276] J. APPLEQUIST, J. R. CARL, and K. K. FUNG, *J. Am. Chem. Soc.* **94**, 2952 (1972).

[277] J. APPLEQUIST, *Acc. Chem. Res.* **10**, 79 (1977).

[278] B. T. THOLE, *Chem. Phys.* **59**, 341 (1981).

[279] A. MAYER, *Phys. Rev. B* **71**, 235333 (2005).

[280] A. MAYER, *Phys. Rev. B* **75**, 045407 (2007).

[281] R. R. BIRGE, *J. Chem. Phys.* **72**, 5312 (1980).

[282] B. SANTRA, J. C. V. KLIMEŠ, D. ALFÈ, A. TKATCHENKO, B. SLATER, A. MICHAELIDES, R. CAR, and M. SCHEFFLER, *Phys. Rev. Lett.* **107**, 185701 (2011).

[283] R. BERLINER and S. A. WERNER, *Phys. Rev. B* **34**, 3586 (1986).

[284] C. S. BARRETT, *Acta Cryst.* **9**, 671 (1956).

[285] M. S. ANDERSON, C. A. SWENSON, and D. T. PETERSON, *Phys. Rev. B* **41**, 3329 (1990).

[286] Y. S. TOULOUKIAN, R. K. KIRBY, R. E. TAYLOR, and P. D. DESAI, *Thermophysical Properties of Matter*, volume 12, IFI/Plenum, New York, 1975.

[287] R. GAUDOIN and W. M. C. FOULKES, *Phys. Rev. B* **66**, 052104 (2002).

[288] M. KRESCH, O. DELAIRE, R. STEVENS, J. Y. Y. LIN, and B. FULTZ, *Phys. Rev. B* **75**, 104301 (2007).

[289] K. H. HELLWEGE, editor, *Landolt-Börnstein, New Series, Group III*, Springer, Berlin, 1966.

[290] S. M. PEIRIS, A. J. CAMPBELL, and D. L. HEINZ, *J. Phys. Chem. Solids* **55**, 413 (1994).

[291] E. I. ISAEV, R. AHUJA, S. I. SIMAK, A. I. LICHTENSTEIN, Y. K. VEKILOV, B. JOHANSSON, and I. A. ABRIKOSOV, *Phys. Rev. B* **72**, 064515 (2005).

[292] W. K. SCHUBERT, R. N. SHELTON, and E. L. WOLF, *Phys. Rev. B* **23**, 5097 (1981).

[293] N. A. CHRISTENSEN and P. ROEHAMMER, *J. Cryst. Growth* **38**, 281 (1977).

[294] B. R. ZHAO, L. CHEN, H. L. LUO, M. D. JACK, and D. P. MULLIN, *Phys. Rev. B* **29**, 6198 (1984).

[295] X.-J. CHEN, V. V. STRUZHKIN, Z. WU, M. SOMAYAZULU, J. QIAN, S. KUNG, A. N. CHRISTENSEN, Y. ZHAO, R. E. COHEN, H.-K. MAO, and R. J. HEMLEY, *Proc. Nat. Acad. Sci. U.S.A.* **102**, 3198 (2005).

[296] R. R. REEBER and K. WANG, *Mater. Chem. Phys.* **46**, 259 (1996).

[297] I. VURGAFTMAN, J. R. MEYER, and L. R. RAM-MOHAN, *J. Appl. Phys.* **89**, 5815 (2001).

[298] R. G. GREENE, H. LUO, A. L. RUOFF, S. S. TRAIL, and F. J. DISALVO, *Phys. Rev. Lett.* **73**, 2476 (1994).

[299] R. R. REEBERT, *phys. status solidi (a)* **32**, 321 (1975).

[300] G.-D. LEE, M. H. LEE, and J. IHM, *Phys. Rev. B* **52**, 1459 (1995).

[301] L. LEY, R. A. POLLAK, F. R. MCFEELY, S. P. KOWALCZYK, and D. A. SHIRLEY, *Phys. Rev. B* **9**, 600 (1974).

[302] S. SARKAR, S. PAL, P. SARKAR, A. L. ROSA, and T. FRAUENHEIM, *J. Chem. Theory Comput.* **7**, 2262 (2011).

[303] R. A. FELICE, J. TRIVISONNO, and D. E. SCHUELE, *Phys. Rev. B* **16**, 5173 (1977).

[304] M. E. DIEDERICH and J. TRIVISONNO, *J. Phys. Chem. Solids* **27**, 637 (1966).

[305] W. R. MARQUARDT and J. TRIVISGNNO, *J. Phys. Chem. Solids* **26**, 273 (1965).

[306] E. J. GUTMAN and J. TRIVISONNO, *J. Phys. Chem. Solids* **28**, 805 (1967).

[307] G. N. KAMM and G. A. ALERS, *J. Appl. Phys.* **35**, 327 (1964).

[308] D. L. WALDORF and G. A. ALERS, *J. Appl. Phys.* **33**, 3266 (1962).

[309] O. L. ANDERSON, *in Physical Acoustics*, volume III-B, Academic, New York, 1965.

[310] V. L. MORUZZI and P. M. MARCUS, *Phys. Rev. B* **48**, 7665 (1993).

[311] G. A. ALERS, *Phys. Rev.* **119**, 1532 (1960).

[312] F. H. FEATHERSTON and J. R. NEIGHBOURS, *Phys. Rev.* **130**, 1324 (1963).

[313] G. A. ALERS and D. L. WALDORF, *Phys. Rev. Lett.* **6**, 677 (1961).

[314] K. A. JONES, S. C. MOSS, and R. M. ROSE, *Acta Met.* **17**, 365 (1969).

[315] W. C. HUBBELL and F. R. BROTZEN, *J. Appl. Phys.* **43**, 3306 (1972).

[316] W. C. OVERTON and J. GAFFNEY, *Phys. Rev.* **98**, 969 (1955).

[317] W. B. HOLZAPFEL, M. HARTWIG, and W. SIEVERS, *J. Phys. Chem. Ref. Data* **30**, 515 (2001).

[318] E. WALKER, J. ASHKENAZI, and M. DACOROGNA, *Phys. Rev. B* **24**, 2254 (1981).

[319] H. CYNN, J. E. KLEPEIS, C.-S. YOO, and D. A. YOUNG, *Phys. Rev. Lett.* **88**, 135701 (2002).

[320] D. K. HSU and R. G. LEISURE, *Phys. Rev. B* **20**, 1339 (1979).

[321] R. E. MACFARLANE, J. A. RAYNE, and C. K. JONES, *Phys. Letts.* **20**, 234 (1966).

[322] G. SIMMONS and H. WANG, *Single Crystal Elastic Constants and Calculated Aggregate Properties: A Handbook*, MIT Press, Cambridge, Massachusetts, 2th edition, 1971.

[323] G. BELLUSSI, U. BENEDICT, and W. B. HOLZAPFEL, *J. Less-Common Met.* **78**, 147 (1981).

[324] C. V. BRISCOE and C. F. SQUIRE, *Phys. Rev.* **106**, 1175 (1957).

[325] J. T. LEWIS, A. LEHOCZKY, and C. V. BRISCOE, *Phys. Rev.* **161**, 877 (1967).

[326] H. SPETZLER, C. G. SAMMIS, and R. J. O'CONNELL, *J. Phys. Chem. Solids* **33**, 1727 (1972).

[327] A. J. COHEN and R. G. GORDON, *Phys. Rev. B* **14**, 4593 (1976).

[328] R. CHANG and L. J. GRAHAM, *J. Appl. Phys.* **37**, 3778 (1966).

[329] W. WEBER, *Phys. Rev. B* **8**, 5082 (1973).

[330] H. L. BROWN, P. E. ARMSTRONG, and C. P. KEMPTER, *J. Chem. Phys.* **45**, 547 (1966).

[331] V. A. GUBANOV, A. L. IVANOVSKY, and V. P. ZHUKOV, *Electronic Structure of Refractory Carbides and Nitrides*, Cambridge University Press, Cambridge, 1994.

[332] V. ZHUKOV, V. GUBANOV, O. JEPSEN, N. CHRISTENSEN, and O. ANDERSEN, *J. Phys. Chem. Solids* **49**, 841 (1988).

[333] J. O. KIM, J. D. ACHENBACH, P. B. MIRKARIMI, M. SHINN, and S. A. BARNETT, *J. Appl. Phys.* **72**, 1805 (1992).

[334] J. J. HALL, *Phys. Rev.* **161**, 756 (1967).

[335] L. J. BRUNER and R. W. KEYES, *Phys. Rev. Lett.* **7**, 55 (1961).

[336] D. L. PRICE and J. M. ROWE, *Solid State Commun.* **7**, 1433 (1969).

[337] C. J. BUCHENAUER, M. CARDONA, and F. H. POLLAK, *Phys. Rev. B* **3**, 1243 (1971).

[338] R. D. CARNAHAN, *J. Am. Ceram. Soc.* **51**, 223 (1968).

[339] J. TAN, Y. LI, and G. JI, *Comput. Mater. Sci.* **58**, 243 (2012).

[340] W. A. HARRISON, *Electronic Structure and the Properties of Solids*, Freeman, New York, 1980.

[341] F. AGUADO and V. G. BAONZA, *Phys. Rev. B* **73**, 024111 (2006).

[342] W. WETTLING and J. WINDSCHEIF, *Solid State Commun.* **50**, 33 (1984).

[343] R. I. COTTAM and G. A. SAUNDERS, *J. Phys. C: Solid State Phys.* **6**, 2105 (1973).

[344] J. G. COLLINS, G. K. WHITE, J. A. BIRCH, and T. F. SMITH, *J. Phys. C: Solid State Phys.* **13**, 1649 (1980).

[345] M. W. CHASE, JR., editor, *NIST-JANAF Thermochemical Tables*, AIP, New York, 4 edition, 1998.

[346] K. P. THAKUR and J. D. PANDEY, *J. Inorg. Nucl. Chem.* **37**, 645 (1975).

[347] R. SANDERSON, *Inorganic Chemistry*, Reinhold, New York, 1967.

[348] F. VINES, C. SOUSA, P. LIU, J. A. RODRIGUEZ, and F. ILLAS, *J. Chem. Phys.* **122**, 174709 (2005).

[349] A. F. GUILLERMET, J. HÄGLUND, and G. GRIMVALL, *Phys. Rev. B* **45**, 11557 (1992).

[350] J. HÄGLUND, G. GRIMVALL, T. JARLBORG, and A. F. GUILLERMET, *Phys. Rev. B* **43**, 14400 (1991).

[351] A. F. GUILLERMET, J. HÄGLUND, and G. GRIMVALL, *Phys. Rev. B* **48**, 11673 (1993).

[352] W. A. HARRISON, *Electronic Structure and the Properties of Solids*, Dover, New York, 1989.

[353] W. MARTIENSSEN, editor, *Landolt-Börnstein, Numerical Data and Functional Relationships in Science and Technology-Crystal and Solid State Physics - New Series*, Springer, Berlin, 2005.

[354] H. DUMONT and Y. MONTEIL, *J. Cryst. Growth* **290**, 410 (2006).

[355] T. SOMA, *J. Phys. C: Solid State Phys.* **11**, 2669 (1978).

[356] S. SAHA, S. PAL, P. SARKAR, A. L. ROSA, and T. FRAUENHEIM, *J. Comput. Chem.* **33**, 1165 (2012).